

---

# **The Iron-Boron System: Ordered Structures and Point Defects**

---

Dissertation

zur

Erlangung des Grades eines

Doktors der Naturwissenschaften

in der Fakultät für Physik und Astronomie

der Ruhr-Universität Bochum von

Arthur Bialon

aus

Tichau

Bochum 2013

Das Verfassen der vorliegenden Dissertation in englischer Sprache wurde vom Dekanat mit dem Schreiben vom 17.12.2012 genehmigt.

Die Genehmigung zur Vorabveröffentlichung von Teilen dieser Dissertation wurde vom Dekanat mit den Schreiben vom 17.12.2012 und 27.03.2013 erteilt. Die Publikationen sind am Ende der Dissertation aufgeführt.

Erster Gutachter:	Prof. Dr. Ralf Drautz
Zweiter Gutachter:	Prof. Dr. Jörg Neugebauer
Tag der Disputation:	27.06.2013

# Contents

<b>1. Introduction</b>	<b>15</b>
<b>2. Structure Maps</b>	<b>23</b>
2.1. Introduction . . . . .	23
2.2. Previous Structure Maps . . . . .	25
2.2.1. Atomic Properties . . . . .	25
2.2.2. Mendeleev Number . . . . .	27
2.2.3. Local Environment . . . . .	29
2.3. New Structure Maps for d-p Compounds . . . . .	31
2.3.1. Verification of Experimental Data Set . . . . .	31
2.3.2. Trends in Volume . . . . .	39
2.3.3. Trends in Coordination Number . . . . .	40
2.3.4. New Order Parameters . . . . .	45
2.3.5. Restriction to the d-p System . . . . .	47
2.3.6. Estimation of Polyhedron Volumes . . . . .	49
2.3.7. Binary Structure Maps . . . . .	50
2.3.8. Pseudobinary Structure Maps . . . . .	56
2.4. Summary . . . . .	63
<b>3. Electronic Structure Calculations</b>	<b>65</b>
3.1. Schrödinger Equation . . . . .	66
3.2. Hartree and Hartree-Fock Approximations . . . . .	66
3.2.1. Hartree Approximation . . . . .	66
3.2.2. Hartree-Fock Approximation . . . . .	68
3.3. Density Functional Theory . . . . .	69
3.3.1. Thomas-Fermi Approximation . . . . .	69
3.3.2. Hohenberg-Kohn Theorem . . . . .	70
3.3.3. Kohn-Sham Equations . . . . .	71
3.4. Exchange and Correlation in DFT . . . . .	74
3.4.1. Local Density Approximation . . . . .	74
3.4.2. Generalized Gradient Approximation . . . . .	74
3.5. Basis Sets and k-point Sampling . . . . .	75
3.5.1. Basis Sets . . . . .	75
3.5.2. k-point Sampling . . . . .	76
3.6. Pseudopotentials . . . . .	76
3.7. Limitations of DFT . . . . .	78

3.8. Computational Details . . . . .	79
<b>4. Iron-Boron Binary Compounds</b>	<b>81</b>
4.1. Introduction . . . . .	81
4.2. Heat of Formation . . . . .	83
4.3. Phase Stability . . . . .	84
4.4. Possible Routes for Synthesis . . . . .	89
4.5. Mechanical Properties . . . . .	91
4.6. Summary . . . . .	93
<b>5. Boron Point Defects in <math>\alpha</math>-Iron</b>	<b>95</b>
5.1. Introduction . . . . .	95
5.1.1. Impact on Mechanical Properties . . . . .	95
5.1.2. Solution Character of Boron in Ferrite . . . . .	98
5.2. Single Boron Point Defect . . . . .	100
5.2.1. Supercell Construction . . . . .	100
5.2.2. Solution Behavior . . . . .	101
5.2.3. Migration Barriers . . . . .	102
5.2.4. Influence on Elastic Properties . . . . .	105
5.3. Point Defect Interaction . . . . .	111
5.3.1. Supercell Construction . . . . .	111
5.3.2. Boron - Boron . . . . .	112
5.3.3. Boron - Vacancy . . . . .	115
5.3.4. Boron - Hydrogen . . . . .	116
5.3.5. Boron - Carbon, Nitrogen, Oxygen . . . . .	117
5.3.6. Boron - Aluminum, Silicon, Phosphorus, Sulfur . . . . .	121
5.4. Trends in Point Defect Interaction . . . . .	122
5.4.1. Geometric Factor . . . . .	124
5.4.2. Mechanical and Chemical Contribution . . . . .	125
5.4.3. Point Defects in Similar Sites . . . . .	126
5.4.4. Point Defects in Different Sites . . . . .	130
5.5. Summary . . . . .	134
<b>6. Impact on Steel Design</b>	<b>137</b>
<b>7. Conclusion</b>	<b>141</b>
<b>A. Appendix</b>	<b>145</b>
A.1. Atomic Properties-Based Structure Maps . . . . .	145
A.2. Predictive Ability of Structure Maps . . . . .	147
A.3. High-Throughput Environment . . . . .	149
A.4. Convergence Tests & Exchange Correlation Functional . . . . .	152
A.5. List of Binary Compounds . . . . .	157
A.6. Nudged Elastic Band Method . . . . .	162
A.7. Calculation of Elastic Constants . . . . .	164

A.7.1. Theoretical Background . . . . .	164
A.7.2. Convergence Test for Elastic Constants . . . . .	167
<b>Bibliography</b>	<b>169</b>
<b>Curriculum Vitae</b>	<b>199</b>



## List of Tables

2.1.	List of prior schemes for structure maps, including system and composition, the atomic properties used for the axes and the crystal structures. . . . .	27
2.2.	List of important compositions and corresponding crystal structures, denoted by Pearson symbol, prototype and number of appearance. . . . .	33
4.1.	Comparison of the calculated $E_f$ for tI12-Fe <sub>2</sub> B and oP8-FeB with experimental and other theoretical values. . . . .	88
4.2.	Calculated single-crystal elastic constants $C_{ij}$ , the bulk, shear, and Young's moduli and Poisson ratio for known and predicted Fe-B phases. . . . .	91
5.1.	Formation energy and differences of the formation energies for substitutional, octahedral and tetrahedral sites. . . . .	102
5.2.	Calculated migration barriers for boron in a $3 \times 3 \times 3$ supercell using the NEB method. Values for carbon, nitrogen and oxygen are listed for comparison. . . .	104
5.3.	Fit for the elastic constants, relative volume modification and reduction of magnetic moment of ferritic Fe-X alloys as a function of defect concentration. .	109
5.4.	Interaction energies for single-type dumbbells and $OH-\square-OH$ complexes. . . .	119
5.5.	Formation energy difference between substitutional and interstitial point defects fluorine, neon, chlorine and argon in $\alpha$ -iron. . . . .	124
A.1.	List of binary compounds considered in the investigation of phase stability in the Fe-B system. . . . .	161
A.2.	Applied parametrized strains to determine the three independent elastic constants for the cubic unit cell. . . . .	165
A.3.	Applied parametrized strains to determine the six independent elastic constants for the tetragonal unit cell. . . . .	166
A.4.	Applied parametrized strains to determine the nine independent elastic constants for the orthorhombic unit cell. . . . .	166
A.5.	Applied parametrized strains to determine the five independent elastic constants for the hexagonal unit cell. . . . .	167

## *List of Tables*

---



## List of Figures

1.1. Crystal structure of bcc and fcc and Fe-C phase diagram. . . . .	16
1.2. Microstructures of ferrite, pearlite, bainite and martensite in steels. . . . .	17
1.3. Elongation versus tensile strength for various steel types. . . . .	18
1.4. List of important elements of the periodic table in steel manufacturing. . . . .	19
2.1. Schematic illustration of a structure map. . . . .	24
2.2. Elements put in sequential order by one-dimensional string running through modified periodic table . . . . .	28
2.3. The Pettifor structure map for $AB$ compounds. . . . .	29
2.4. Schematic illustration of a nearest neighbor histogram. . . . .	30
2.5. Considered transition metals and p-block elements. . . . .	32
2.6. Compounds built of the same coordination polyhedra. . . . .	35
2.7. Distribution of 1:1 compounds in the binary d-p systems. . . . .	36
2.8. Distribution of 2:1 and 1:2 compounds in the binary d-p systems. . . . .	38
2.9. Polyhedron volumes for p and d sites for common compositions. . . . .	39
2.10. Distribution of coordination numbers for the Wyckoff sites. . . . .	41
2.11. Global versus local composition of binary d-p compounds with B/C/N/O. . . . .	43
2.12. Global versus local composition of binary d-p compounds with Al/Si/P/S. . . . .	44
2.13. Variation of the axis ratios of hP3-AlB <sub>2</sub> and oS8-TiI for different chemical systems and influence on the coordination number. . . . .	47
2.14. Correlation between d ground state volume and polyhedron volumes for the p- and d-sites in the d-Si systems. . . . .	49
2.15. Structure map for 1:1 composition. . . . .	50
2.16. Structure map for 1:1 composition explicitly including defect structures. . . . .	52
2.17. Structure map for a d:p ratio of 2:1. . . . .	53
2.18. Structure map for a d:p ratio of 1:2. . . . .	54
2.19. Structure map for a d:p ratio of 3:1 and 1:3. . . . .	55
2.20. Structure map for d:p ratio of 3:2/2:3, 3:4 and 5:3. . . . .	56
2.21. Structure map for the less important compositions. . . . .	57
2.22. Pseudobinary structure map for the 1:1 composition. . . . .	58
2.23. Pseudobinary structure map for a d:p ratio of 2:1. . . . .	59
2.24. Pseudobinary structure map for a d:p ratio of 1:2. . . . .	60
2.25. Pseudobinary structure map for a d:p ratio of 3:1 and 1:3. . . . .	61
2.26. Pseudobinary structure map for d:p ratio of 3:2/2:3, 3:4 and 5:3. . . . .	62

3.1. Schematic representation of the self-consistent loop for the solution of Kohn-Sham equations. . . . .	73
3.2. Schematic illustration of the all-electron and pseudoelectron potentials and the corresponding wavefunctions. . . . .	77
4.1. Fe-B phase diagram and crystal structures of known stable and metastable compounds. . . . .	82
4.2. Stability of binary Fe-B compounds and Influence of the xc functional of the stability of competing 1:1 and boron-rich compounds. . . . .	85
4.3. Crystal structures and nearest neighbor histograms for t112-Fe <sub>2</sub> B, oP8-, oS8, t116-FeB, oP6-, hP6-, oP12-FeB <sub>2</sub> and oP10-FeB <sub>4</sub> . . . . .	87
4.4. Relative stability, volume per atom and monoclinic distortion of pseudobinary oP10-Fe <sub>x</sub> Cr <sub>1-x</sub> B <sub>4</sub> compound and total and projected density of states for lowest energy compounds. . . . .	90
5.1. Viable point defects sites in bcc. . . . .	101
5.2. Migration path of boron for the substitutional and interstitial configurations with final states in first and second nearest-neighbor position and the dissociative mechanism. . . . .	103
5.3. Calculated elastic constants $C_{11}$ , $C_{12}$ and $C_{44}$ and directional-dependence of Young's modulus $Y$ of ferritic Fe-X (X=B, □, Al, Si, P, S) alloys as function of defect concentration. . . . .	107
5.4. Relative lattice parameter modification and reduction of normalized total magnetic moment of ferritic Fe-X alloys as function of defect concentration and charge density difference of $2 \times 2 \times 2$ and $3 \times 3 \times 3$ supercells containing a vacancy or substitutional boron. . . . .	109
5.5. Interaction energy versus point defect separation for B-B and B-□ $SB-SB$ , B-B $SB-OH$ and $OH-OH$ . . . . .	113
5.6. Formation energy of boron complexes with up to six atoms incorporated into a vacant site in $\alpha$ -iron. . . . .	114
5.7. Interaction energy versus point defect separation for B-H $SB-TH$ and $OH-TH$ . . . . .	116
5.8. Interaction energy versus point defect separation for B-B/C/N/O $SB-OH$ and $OH-OH$ . . . . .	117
5.9. Local magnetic moments of point defects and the nearest-neighbor host iron atoms. . . . .	120
5.10. Interaction energy versus point defect separation for B-Al/Si/P/S $SB-SB$ and $OH-SB$ . . . . .	121
5.11. Interaction energies of boron with a second point defect for the closest arrangements as obtained from ionic relaxation. . . . .	123
5.12. Geometric factor $\overline{\Delta V}$ versus interaction energy for configurations with point defects in similar sites and with dumbbell formation. . . . .	128
5.13. Decomposition of the interaction energy into mechanical and chemical contribution and □-□ interaction energy for 1NN and 2NN $SB-SB$ and $OH-OH$ configurations. . . . .	129

5.14. Tabulated covalent and effective radii for s-block and p-block elements in $\alpha$ -iron.	130
5.15. Decomposition of interaction energy into mechanical and chemical contribution for $SB-OH/TH$ configurations. . . . .	132
5.16. Variation in the charge density evoked by incorporation of point defects aligned along $\langle 100 \rangle$ . . . . .	134
A.1. Order parameters based solely on atomic properties. . . . .	146
A.2. Location of hypothetical compounds in binary 1:1 structure map in d-Si systems.	147
A.3. Schematic representation of the high-throughput environment strucscan. . . .	150
A.4. Convergence tests of k-point density and plane wave cutoff for Fe/B/C/N/O/H for PBE. . . . .	153
A.5. Convergence tests of k-point density and plane wave cutoff for Fe/B/C/N/O/H for LDA. . . . .	154
A.6. Convergence tests of k-point density and plane wave cutoff for Al/Si/P/S for PBE. . . . .	155
A.7. Crystal structures of bcc, fcc and hcp and stability sequence of the crystal structures with varying initial magnetic configurations for LDA and PBE. . . .	156
A.8. The nudged elastic band force $\vec{F}_i^{NEB}$ comprises of the spring force $\vec{F}_i^{S  }$ parallel and the potential force $\vec{F}_i^{\perp}$ perpendicular to the tangent. . . . .	162
A.9. Convergence tests with respect to k-point density and plane wave cutoff for elastic constants of ferromagnetic bcc iron. . . . .	167

## *List of Figures*

---

*"Alles Denken ist ja Kunst."  
Carl von Clausewitz  
Vom Kriege*

## Acknowledgments

This thesis could not have been written without the help and input of people which contributed in many different ways.

First of all I would like to thank Prof. Ralf Drautz, head of the Department of Atomistic Modelling and Simulation (AMS) at the Interdisciplinary Centre for Advanced Materials Simulation (ICAMS), and Dr. Thomas Hammerschmidt, head of the Bond-Order Potential Development and Large Scale Atomistic Simulation group, for the opportunity to work at ICAMS and their support during the project. I would also like to thank Prof. Jörg Neugebauer, director of the Computational Materials Design Department of the Max Planck Institute for Iron Research, for reviewing this doctoral thesis, and Dr. Nicholas Hatcher for proofreading.

Furthermore, I would like to thank Dr. Aleksey Kolmogorov and Dr. Roxana Margine from the University of Oxford for the fruitful discussions and their support.

I would also like to thank my colleagues at the AMS who always spared some of their time for my questions. Special thanks go to Marco Rožgic, Thomas Schablitzki, Dr. Miroslav Čák, Aenne Köster and Dr. Christoph Begau for the awesome time.

I would like to thank the IT department, Lothar Merl, Niklas Caesar, Klaus Kühnberger and Vladimir Lenz, for their efforts to keep 'Vulcan' and all the personal computers running.

And my family, thank you for never questioning my actions, decisions and plans for the future.

Furthermore, I would like to thank nature simply for creating boron. Such an interesting element. And the steel industry. For using it.

# 1. Introduction

*"Oh, my dear, the questions never end. A lifetime is simply a series of endless questions to be answered."*

*Randall N. Bills*

*MechWarrior Dark Age # 27: Pandora's Gambit*

Modern steels are nowadays widely used in power plants [1–6], for structural applications [7–13], including shipbuilding [12], offshore structures [13, 14], e.g. sea platform, gas and oil pipeline fabrication [15, 16]. They are also used for railway purposes [17], in the automotive industry [18–21], in engineering machinery like cutting tools [22–24], for armored protection [25–31] and, of course, in the household [32], to name but a few examples.

In general, a steel is an alloy that consists mainly of iron with carbon addition in the range of a few weight percent. Iron itself exhibits good ductility, but hardness and strength are rather low. The ground state of iron is the bcc crystal structure, also referred to as  $\alpha$ -iron or ferrite (Fig. 1.1(a)). It transforms to the fcc crystal structure, also referred to as  $\gamma$ -iron or austenite (Fig. 1.1(b)), above 912°C. The addition of carbon alters the mechanical properties which is attributed to both the influence of carbon as solute element in the matrix and the formation of precipitates. One of the most important precipitates is the carbide  $\text{Fe}_3\text{C}$  (Fig. 1.2(a)), as listed in the Fe-C phase diagram (Fig. 1.1(c)), and is called cementite. A lamellar mixture of cementite and ferrite is referred to as pearlite (Fig. 1.2(b)). These three phases are the common constituents of the so-called plain carbon steels. The mechanical properties of these steels are determined by the carbon content and the heat treatment during fabrication, which determines the type of host matrix and appearance of carbides in the microstructure of the steels. Other important microstructures are bainite and martensite (Fig. 1.2(c,d)). Bainite is formed in the temperature range between 250 and 550°C. The microstructure consist of ferrite plates with parallel alignment which are accumulated in larger structures referred to as sheaves. The sheaves are separated by low-misorientation boundaries or cementite particles. Martensite is formed if austenitic steel is subject to rapid quenching. The transformation is displacive, the austenitic lattice is deformed into the martensitic structure. This phase is of importance because the formation of martensite makes the steel harder, but simultaneously increases the brittleness.

Plain carbon steels represent only one type of steels. Other steel types have been developed to have specific mechanical properties, in order to make the material suitable for specific environments and applications. Thus, the actual mechanical properties of the steel may be used for the classification of the various steel types. An example is the usage of the elongation and

## 1. Introduction

tensile strength as measure (Fig. 1.3). Designations of the various steel types are interstitial-free (low content of interstitial elements), mild (carbon steels with low alloy content) or

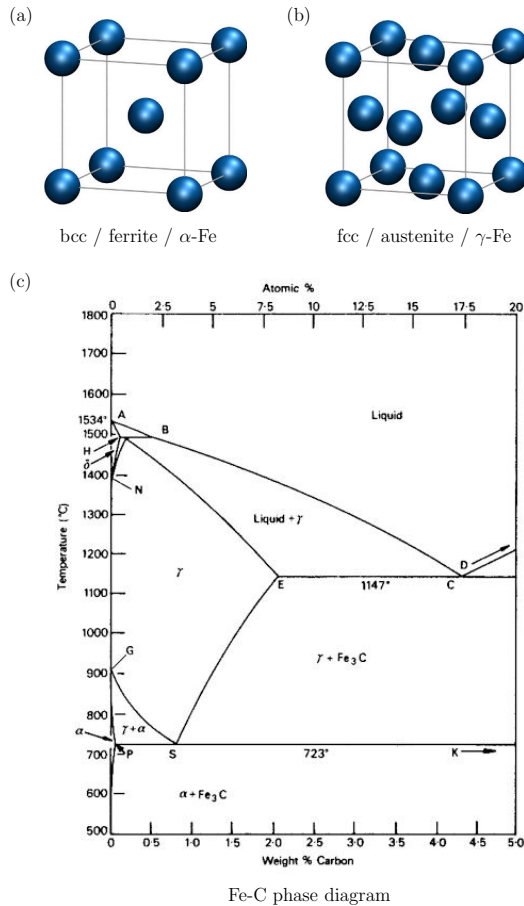


Figure 1.1.: Crystal structure of (a) bcc and (b) fcc and (c) Fe-C phase diagram (from Ref. [33]).

bake-hardening (application of temperature in order to increase strength) steels. Manganese-carbon steels represent an important steel type, as well as high-strength low-alloy (HSLA) steels that incorporate additional elements compared to the mild steel. The latter is also referred to as micro-alloyed steel. Duplex-phase (DP) steels have a host matrix consisting of both ferrite and austenite. In complex-phase (CP) steels also bainite and martensite appear in the microstructure, the latter being the hardest phase, but also the most brittle one. Martensitic or transformation-induced plasticity (TRIP) steels contain a larger amount of martensite in the microstructure. TWIP (twinning-induced plasticity) steels are austenitic steels that obtain their exceptional mechanical properties by deformations that results in twinning. This leads to a finer microstructure which improves the mechanical properties. HFP (hot-press forming) steels are processed in the austenitic state in a forming press with water-cooled dies that quench the material into the martensitic state. Extra advanced high-strength steels (X-AHSS) are under development in order to outclass the mechanical properties of the conventional advanced high-strength steels, i.e. DP, CP, TRIP, HFP and martensitic steels [34].

It is exactly this ability of adjusting the mechanical properties that makes steels so important. The steel can be tailored in order to match specific requirements that make the material suitable for many operational environments. Steels used in power plants are exposed to heat, thus the material requires good creep properties [3–6], in terms of a high stability of the microstructure, in order to prevent the materials' failure. For structural applications, the steels require high strength [8–13], wear resistance [11], good weldability [12, 13] and toughness [13]. In the case of shipbuilding, sea platform and oil pipelines fabrication the steels require a good corrosion resistance [14–16] as well as good weldability [39]. The former is also required for steels used in the household [32]. Steels used in the automotive industry require good corrosion resistance [18] besides high strength [19–21] if the materials is used in the chassis. Low strength ultra-soft steels are required for parts with a complex geometry. For cutting



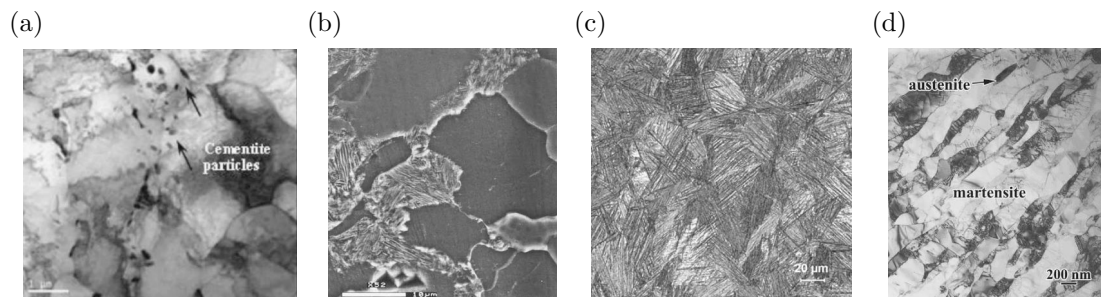


Figure 1.2.: Transmission electron microscopy micrographs of cementite particles in ferrite (a) (from Ref. [35]) and martensite (d) (from Ref. [36]). Optical micrographs of ferrite and pearlite (b) (from Ref. [37]) and bainite (c) (from Ref. [38]).

tools, the steels require a high hardness and wear resistance [24]. For armored protection, the steels require good ballistic performance, in order to withstand the impact of a high-velocity projectile. Obvious required properties are therefore good hardness and impact properties, but recent investigations also highlight the importance of the microstructure on the ballistic performance [29–31]. The ability to tailor the material in order to exhibit specific and required properties is due to variations of the chemical composition of the basic material and varying process parameters in manufacturing.

The chemical composition denotes the type and concentration of additional elements apart from the main ingredients iron and carbon. However, these additional elements may not only consist of elements which are added on purpose, in order to modify the operational characteristics in an usually beneficial way. Already present traces of impurities in the material may exhibit a detrimental impact on the mechanical properties, although their impact can be usually negated by the addition of specific elements, which have a high affinity towards the impurity elements. In the case of elements added on purpose, the impact on the steel usually depends on the additive itself. Examples are the formation of specific precipitates which may improve the hardness if the precipitates are very small. Or the precipitates reduce the solute amount of specific elements which usually would deteriorate the mechanical properties. Additives may also alter the microstructure by affecting the grain growth or the transformation from austenite to ferrite. Some additives can also stabilize austenite at room temperature or are able to prevent segregation of detrimental elements via a site competition effect. The common additive elements in steel production are summarized in Fig. 1.4 among the common impurities, which have a detrimental effect on the operational characteristics, and elements where the actual impact, either overall beneficial or detrimental, depends on the nominal concentration, the distribution and preferred site in the crystal lattice.

The common additive elements with a beneficial impact on the operational characteristics are mostly 3d, a few early 4d transition metals, and tungsten from the 5d row. Titanium, vanadium and niobium, for example, may be used to affect the grain growth, thus influencing the grain size [40–42]. Addition of chromium and molybdenum exhibits a significant contri-

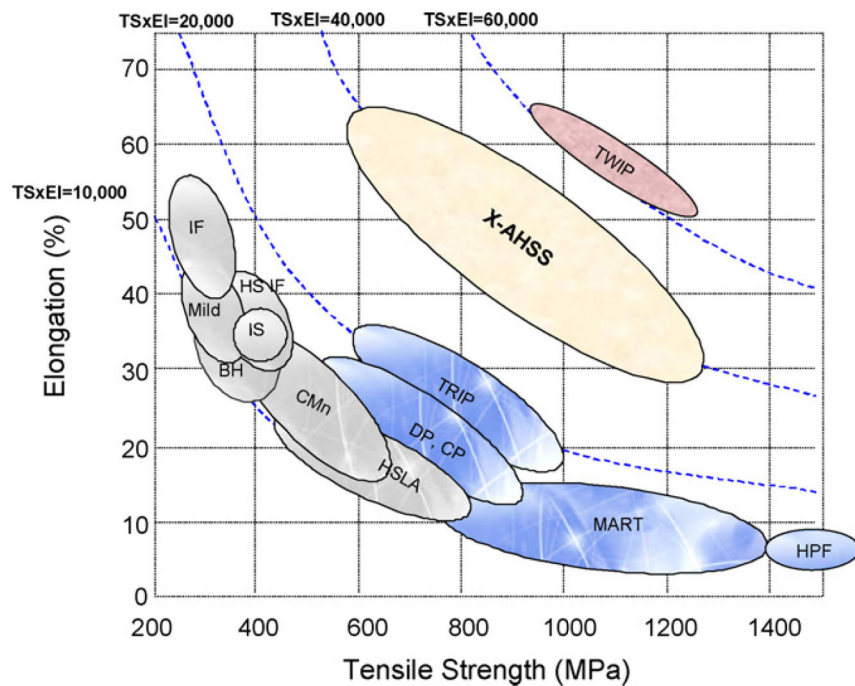


Figure 1.3.: Elongation versus tensile strength for various steel types (from Ref. [34]).

tribution to corrosion [43, 44] and wear resistance [45, 46]. Tungsten improves also the wear resistance [47] as well as creep strength [48] and hardness [49]. Addition of manganese improves the hardenability [50] and acts as deoxidizer. Nickel enhances the toughness [51, 52]. Common additive elements in the p-block of the periodic table are predominantly the first and second row elements. Aluminum affects the grain growth, leading to grain refinement [53, 54], and acts as deoxidizer similar to silicon, which additionally enhances the hardness [55, 56]. Addition of lead increases the machinability [57–60]. Cerium from the lanthanide series removes sulfur from solid solution [61] and improves the corrosion resistance of stainless steels by the formation of stable oxides [62, 63]. Common impurities are hydrogen which promotes embrittlement [64–68], oxygen which causes corrosion [69, 70], and sulfur which decreases ductility [71] if segregated to grain boundaries and enhances the corrosion process [72]. Helium becomes important if the material is subject to irradiation (e.g. steels used in nuclear power plants) and causes a loss of ductility [73] and promotes intergranular cracking [74]. Tin and antimony also promote intergranular cracking if segregated to grain boundaries [75, 76]. The elements nitrogen and phosphorus are examples which do not fall clearly into one of the two categories, and their actual impact on the mechanical properties often depends on additional factors, e.g. the nominal concentration, the location or distribution within the material and the actual form, i.e. whether it is still present as solute within the host matrix or bound in precipitates. Solute nitrogen makes steels brittle but nitrogen-containing precipitates increase the toughness [77]. Nitrogen-containing coatings improve the corrosion resistance [78]. Phosphorus causes embrittlement if present at grain boundaries [79], but simultaneously the presence

1 IA																		18 VIIIA																																																							
1	1.0079																	2	4.0025																																																						
	H Hydrogen																	He Helium																																																							
2 IIA																																																																									
3	6.941			4			9.0122											5	10.811			6	12.011			7	14.007			8	15.999			9	18.998			10	20.180																																		
	Li Lithium			Be Beryllium																					B Boron			C Carbon			N Nitrogen			O Oxygen			F Fluorine			Ne Neon																																	
11	22.990			12			24.305											13	26.982			14	28.086			15	30.974			16	32.065			17	35.453			18	39.948																																		
	Na Sodium			Mg Magnesium																					Al Aluminum			Si Silicon			P Phosphorus			S Sulphur			Cl Chlorine			Ar Argon																																	
19	39.098			20			40.078			21	44.956			22	47.867			23	50.942			24	51.996			25	54.938			26	55.845			27	58.933			28	58.693			29	63.546			30	65.39			31	69.723			32	72.64			33	74.922			34	78.96			35	79.904			36	83.8		
	K Potassium			Ca Calcium			Sc Scandium			Ti Titanium			V Vanadium			Cr Chromium			Mn Manganese			Fe Iron			Co Cobalt			Ni Nickel			Cu Copper			Zn Zinc			Ga Gallium			Ge Germanium			As Arsenic			Se Selenium			Br Bromine			Kr Krypton																					
37	85.468			38			87.62			39	88.906			40	91.224			41	92.906			42	95.94			43	96			44	101.07			45	102.91			46	106.42			47	107.87			48	112.41			49	114.82			50	118.71			51	121.76			52	127.6			53	126.9			54	131.29		
	Rb Rubidium			Sr Strontium			Y Yttrium			Zr Zirconium			Nb Niobium			Mo Molybdenum			Tc Technetium			Ru Ruthenium			Rh Rhodium			Pd Palladium			Ag Silver			Cd Cadmium			In Indium			Sn Tin			Sb Antimony			Te Tellurium			I Iodine			Xe Xenon																					
55	132.91			56			137.33			57-71			72	178.49			73	180.95			74	183.84			75	186.21			76	190.23			77	192.22			78	195.08			79	196.97			80	200.59			81	204.38			82	207.2			83	208.98			84	209			85	210			86	222			
	Cs Cesium			Ba Barium			La-Lu Lanthanide			Hf Hafnium			Ta Tantalum			W Tungsten			Re Rhenium			Os Osmium			Ir Iridium			Pt Platinum			Au Gold			Hg Mercury			Tl Thallium			Pb Lead			Bi Bismuth			Po Polonium			At Astatine			Rn Radon																					
87	223			88			226			89-103			104	261			105	262			106	266			107	264			108	277			109	268			110	281			111	280			112	285			113	284			114	289			115	288			116	293			117	292			118	294			
	Fr Francium			Ra Radium			Ac-Lr Actinide			Rf Rutherfordium			Db Dubnium			Sg Seaborgium			Bh Bohrium			Hs Hassium			Mt Meitnerium			Ds Darmstadtium			Rg Roentgenium			Uub Ununbium			Uut Ununtrium			Uuq Ununquadium			Uup Ununpentium			Uuh Ununhexium			Uus Ununseptium			Uuo Ununoctium																					
57	138.91			58	140.12			59	140.91			60	144.24			61	145			62	150.36			63	151.96			64	157.25			65	158.93			66	162.50			67	164.93			68	167.26			69	168.93			70	173.04			71	174.97																
	La Lanthanum			Ce Cerium			Pr Praseodymium			Nd Neodymium			Pm Promethium			Sm Samarium			Eu Europium			Gd Gadolinium			Tb Terbium			Dy Dysprosium			Ho Holmium			Er Erbium			Tm Thulium			Yb Ytterbium			Lu Lutetium																														
89	227			90	232.04			91	231.04			92	238.03			93	237			94	244			95	243			96	247			97	247			98	251			99	252			100	257			101	258			102	259			103	262																
	Ac Actinium			Th Thorium			Pa Protactinium			U Uranium			Np Neptunium			Pu Plutonium			Am Americium			Cm Curium			Bk Berkelium			Cf Californium			Es Einsteinium			Fm Fermium			Md Mendelevium			No Nobelium			Lr Lawrencium																														

Figure 1.4.: Important elements of the periodic table in steel manufacturing. Additives apart from the main constituents (blue) may have an overall beneficial impact (green) or the impact is dependent on additional factors and can be either detrimental or beneficial (yellow). Impurities have an overall detrimental impact (red) on the mechanical properties.

at grain boundaries is attributed to improve the hardenability [80]. Relative good strength and toughness are achieved if the fabrication process ensures phosphorus to be finely dispersed and the grain size to be small [81].

The microstructure of the steel is determined by the fabrication process that includes heat treatment, i.e. applied temperature, holding time, cooling rate etc., and mechanical deformation during processing, e.g. (hot) rolling. Usually, the fabrication process consists of several steps, which may include different applied temperatures, distracted by cooling sequences and applications of mechanical deformation. These procedures influence the microstructure by affecting the basic host matrix, the grain size and the formation and size of precipitates. It also affects the diffusion of the elements in the material, thus determining the distribution in the steel.

As both the chemical composition and the fabrication process determine the microstructure and thus the mechanical properties of the steel, the design of new steels is a complicated task. Slight variations in the concentration of a given additive or the parameters controlling heat treatment may result in noticeable differences in the final microstructure of the steel. This includes the crystal structure of the iron host matrix, the size of the grains and the existence of precipitates in the host matrix or at grain boundaries, which effectively influence the mechanical properties. In order to achieve the optimum impact on the mechanical properties, a detailed

## 1. Introduction

---

knowledge of the behavior of specific additives is required with respect to, e.g, the diffusivity and precipitation behavior, factors that are influenced by the chemical composition of the raw material as well as the fabrication process. In this investigation, we focus on one of the specific additives, namely boron.

Boron is one of the common additive elements in steel production, and although it is usually added in very small quantities, often in the range of 100 parts per million (ppm) or less, it is found to have a large impact on the mechanical properties of the steel [82]. However, the usage of boron is not only restricted to these low contents, but relative large amounts of boron may be used to form transition metal borides, which are used as hard and protective coatings on the steel surfaces or alter the mechanical properties of the steel. Its attractiveness as alloying element stems also from its ability to achieve the same effect on some mechanical properties with less additive content compared to other alloying elements [83,84]. In addition, in times of increasing costs for resources, boron is still a relative cheap alloying element [82,85], especially compared to some of the transition metals usually used as alloying elements.

Iron borides in particular are widely used as hard and protective coatings on steel surfaces in order to improve the wear and corrosion resistance of the steel [86–92]. The coating is produced via the process of boriding (or boronizing) which includes the deposition of boron on the surface and an additional heat treatment, e.g. in the form of laser irradiation [90] or a thermochemical process [91], in order to form the borides on the steel surfaces. Iron borides formed in the microstructure of steels, in contrast, can alter the mechanical properties in a direct or indirect way. As an example for a direct influence, the formation of borides in high boron steels improves the tensile strength [93]. Indirectly, the formation of borides depletes the amount of boron in solid solution, thus properties dependent on this amount will be affected.

The addition of low boron contents is known to improve the hardenability of low-carbon and low-alloy steels [82,94–108], the ductility at room [109] and high temperature [110–115], the (fracture) toughness [116,117] and the creep behavior of both ferritic [118–124] and austenitic stainless steels [125–131]. Furthermore, boron additions also improve the corrosion resistance [132–134] and result in microstructure modification, e.g. refinement of austenitic [135] and ferritic [136–138] grains. The variety of effects on the operational characteristics of the steels arise from several different mechanisms, which require boron to be present as a solute element or bound in precipitates and located appropriately in the microstructure.

Boron has the tendency to segregate to austenitic grain boundaries [139–141], although the boron content at grain boundaries depends strongly on the applied temperature and holding time [142–144] as well as the cooling rate [144,145]. If present as solute element, it improves the hardenability of low-carbon and low-alloy steels [101] by retarding the ferritic/pearlitic transformation, thus increasing the time range for the bainitic and martensitic transformation [102,103]. The mechanism responsible for an improvement of ductility by boron addition depends on the type of host matrix. Below the austenite-ferrite transformation temperature, the beneficial impact is attributed to intragranular formation of  $\text{Fe}_{23}(\text{B,C})_6$  particles, acting as nucleation sites for ferrite [111], or other carbides, that influence the microstructure [112]. In austenite, the beneficial impact is attributed to enhanced grain boundary cohesion due to boron segregation [113] and the promotion of precipitate formation [114]. Improvement of

---

toughness by boron addition is due to microstructure evolution, where boron additions lead to a finer substructure of the steel [117]. With regard to creep resistance, the improvement in ferritic steels by boron addition is attributed to boron enrichment of  $M_{23}C_6$  carbides near prior austenite grain boundaries, thus suppressing the coarsening of the carbides during creep and maintaining a homogeneous distribution of fine  $M_{23}C_6$  carbides [120–123]. In austenitic steels, the beneficial impact is primarily due to boronitride formation [125, 126, 146]. We will discuss the different mechanisms in detail in section 5 of this thesis.

Despite the variety of impacts of boron addition on some of the mechanical properties of the steel, the similarity is in the dependence on the nominal boron content, the distribution and the nature of boron, whether it is present as solute element or bound in precipitates, in order to achieve a beneficial impact. As both the boron distribution and boron nature depend not only on the fabrication process, primarily the heat treatment, but also on the presence of specific additional elements in the raw material, it is therefore not surprising that, apart from varying nominal boron contents in the literature in order to achieve optimum impact on the properties, the overall impact of boron addition on the properties is still controversial [82, 104–106]. Slight deviations in boron content, the chemical composition of the raw material and differences in the fabrication process may change the impact on the mechanical properties, even in a detrimental way.

Based on the usage in the steel production, as outlined before, we will investigate the ordered Fe-B compounds as well as the behavior of boron point defects in an iron host matrix. We will restrict ourselves only to the class of ferritic steels, where the iron host matrix adopts the bcc structure. The ordered compounds are investigated via the structure map approach and density functional theory (DFT) calculations. The former method represents a classification scheme and is in our investigation used to identify the governing factors that drive the compound formation. The latter method addresses geometric, electronic and thermodynamic properties of the compounds. DFT calculations are also applied in the investigation of boron point defects in the iron host matrix. So far, a considerable number of DFT studies were devoted to the behavior of boron point defects at grain boundaries [147–154], but corresponding studies addressing boron point defects in bulk iron are rather sparse [155, 156]. Our aim is to gain insight into the behavior of boron point defects and whether and to which extent its behavior differs from its nearest neighbors in the periodic table. As the influence of boron on the mechanical properties is to a great extent determined by the distribution, we focus on the factors that influence the distribution, namely the boron migration and interactions with other point defects.

This thesis is structured as follows: Section 2 addresses the question of compound formation via the structure map approach. After reviewing previous work on this topic, we first introduce the concept of a polyhedron analysis, decompose the crystal structures into the coordination polyhedra and present new structure maps for transition metal - sp-valent systems using the available information from the polyhedron decomposition. Section 3 reviews the theoretical background of density functional theory. In section 4 the binary Fe-B system is investigated via DFT with respect to compound formation. Investigating not only the known stable and metastable compounds, we also address the question of new viable ground states in the Fe-B

system, and discuss potential synthesis routes. Section 5 is devoted to the behavior of boron point defects in ferrite, addressing the solution behavior, the migration, the impact on the elastic properties of ferrite with varying boron content and the interaction of boron with other point defects. Regarding the interaction, we predominantly focus on important elements in the steel manufacturing that are located in the p-block of the periodic table (c.f. Fig. 1.4) as well as hydrogen. Section 6 reflects the results with respect to the design of new steels. The conclusions are then summarized in section 7. Details of the methodology are summarized in the appendix.

## 2. Structure Maps

*"Deleting complications to try and find simplistic patterns, simplistic solutions to puzzles, was a human approach."*

Neal Asher  
The Technician

### 2.1. Introduction

The properties of steels and compound materials in general are a consequence of their chemical composition and microstructure. While the microstructure is to a large degree determined by the fabrication process, the chemistry of compound formation is fully determined by the constituent elements. The elements differ in the number of protons within the core, generally assigned as atomic number, and the corresponding number of electrons to achieve charge neutrality. The electrons, or more precisely the electronic configuration of occupied and unoccupied states, will determine not only elemental properties like, e.g., the volume or the electronegativity, but also the corresponding crystal structure. However, the ambient conditions are likely to influence the crystal structure. Examples are extreme temperature conditions or the application of pressure which may not only promote phase transitions, but also changes of the energetically preferred crystal structure.

Extending the concept to a mixture of two or more elements or constituents, three questions regarding the crystal structures are raised [157]:

1. Will the mixture form a compound?
2. If compound formation occurs, at which compositions will the compounds appear?
3. Which crystal structures will the compounds adopt, dependent on the composition?

The third question refers to the observation that the same crystal structure can be adopted by different chemical systems. For example, the prototypical NaCl-type crystal structure is not only observed in the name-giving Na-Cl system, but also e.g. in Mn-O. However, due to the different atomic size the cell volume and the internal coordinates of the atoms will vary, but the symmetry of the cell, i.e. the Wyckoff positions and the space group, remains unchanged.

In the past years, several attempts have been made to find simple guidelines, or more precisely order parameters, based on tabulated or derived atomic properties or other scales that provide insight into whether a mixture of two or more elements is expected to form compounds and which crystal structure will be adopted. These order parameters are either quantities chosen

## 2. Structure Maps

from a representative scale, defined to clearly identify a given element, or derived quantities based on the atomic properties of the constituent elements in the mixture or crystal structure.

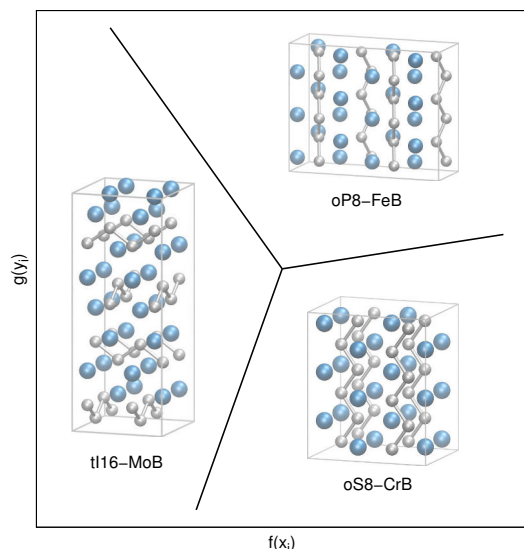


Figure 2.1.: Schematic illustration of a structure map. Order parameters are derived from atomic properties so that the different prototypes appear in well-defined regions.

The likeliness of compound formation or the adopted prototypical crystal structure is then plotted by a two- or three-dimensional diagram with the axes defined by the corresponding order parameters. By definition, well chosen order parameters will yield firstly well defined areas consisting of the same data points (compound formation or prototype) and secondly a minimum of overlap between the different areas. A schematic representation of a structure map is given in Fig. 2.1. The order parameters are calculated from tabulated or derived atomic properties. Adequate order parameters assign the different prototypes to well-defined regions in the structure map. Ideally there is no overlap between different prototypes.

Identified guidelines may support efforts made in materials science, as the design of new materials is still a difficult and time-consuming task. Simple correlations or rules may introduce several applications in the design process. For example, cheaper elements could be identified to substitute an expensive element without changing the crystal structure, as often mechanical or physical properties tend to correlate with the underlying crystal structure. Furthermore, the rules could be used to predict the crystal structures of given mixtures of binary or multicomponent systems, if the system is known or expected to form compounds. This would be advantageous especially for multicomponent systems that are increasingly difficult to sample both, theoretically and experimentally.

This section is structured as follows: We will first summarize previous approaches to find order parameters using either tabulated or derived atomic properties or other scales for the classification of both the likeliness of compound formation and the adopted prototype. This will be followed by an introduction into the concept of analyzing the atomic environment in a crystal structure by the local polyhedra formed by the neighboring atoms. We will then present the results for the identified order parameters, based on a polyhedra analysis of the crystal structures, for a specific system: the binary transition metal - sp valent system. For simplicity we will refer to this system as d-p system for the rest of the study. We will further extend our approach to ternary systems, that have either two different d or p elements (i.e. d-d-p or d-p-p), whereas we restrict the discussion of the ternary compounds to the crystal structures that are adopted in the binary system. In the ternary systems, these crystal structures appear



with mixed d or p elements at the Wyckoff sites. We further briefly discuss the predictive ability of our structure maps.

## 2.2. Previous Structure Maps

### 2.2.1. Atomic Properties

In the 1960s until the 1980s the concept of order parameters and structure maps was established and applied to several classes of compounds, as summarized in Tab. 2.1. The majority of proposed order parameters are based on tabulated or derived atomic properties, and many investigations use order parameters based on the electronic configuration (e.g. number of valence electrons), the atomic size or an electronegativity scale. The only exception in Tab. 2.1 is the study by Phillips *et al.* [158] that used ionicity values determined from the compounds as order parameters. The majority also used only two axes for the structure maps, except the studies by Villars [159–161] that use three axes. A discussion regarding the general success of the majority of structure maps listed in Tab. 2.1 is given in Ref. [159]. Deviations from ideal separation appeared in many of the studies. Possible deviations were overlapping domains of different compounds in the structure maps or the placement of single points that belong to one compound into the domain of another. However, in some cases the overlapping domains of different compounds were attributed to close geometrical relationships.

Class <sup>1</sup>	Coordinates <sup>2</sup>	Structures	Ref.
$X^8Y^{N-8}$	$E_h$ vs $C$	NaCl, c-ZnS, h-ZnS	[158]
AB	$\Sigma N_{ve}$ vs $ (r_p + r_s)_A - (r_p + r_s)_B $ vs $ \Delta X^{MB} $	AsLi, AuCd, FeB, GeS, MnP, AlEr, CrB, AuCu, $\gamma$ -CuTi, NaPb, WC, c-ZnS, h-ZnS, HgS, TiAs, CsCl, FeSi, GeK, NaCl, NaTi	[159]
AB <sub>2</sub>	$\Sigma N_{ve}$ vs $(r_p + r_s)_A - (r_p + r_s)_B$ vs $\Delta X^{MB}$	VO <sub>2</sub> , CaF <sub>2</sub> , AlHo <sub>2</sub> , V <sub>2</sub> C, PbCl <sub>2</sub> , Co <sub>2</sub> Si, MoPt <sub>2</sub> , Si <sub>2</sub> Zr, CeCu <sub>2</sub> , $\alpha$ -GdSi <sub>2</sub> , Cu <sub>2</sub> Sb, TiO <sub>2</sub> , CaC <sub>2</sub> , MoSi <sub>2</sub> , CuAl <sub>2</sub> , Si <sub>2</sub> Th, AlB <sub>2</sub> , Cd <sub>2</sub> Ce, CdI <sub>2</sub> , CaIn <sub>2</sub> , CrSi <sub>2</sub> , MgZn <sub>2</sub> , MgNi <sub>2</sub> ,	[160]

<sup>1</sup>X, Y non-transition elements; Z main group cations; W main group anion; T, U transition metals; M, N s, p, d elements; A, B s, p, d, f elements; H halide, nitride, cyanide, nitrite; I d, f element; J p, d element

<sup>2</sup> $C$  average ionic energy gap;  $E_h$  average covalent energy gap;  $\Delta E$  difference between the transition metal and main group valence energy levels;  $\bar{n}$  average principal quantum number;  $\bar{N}_g$  average group number;  $\Delta N_g$  difference in group number;  $\bar{N}_v$  average number of holes in d band;  $\Sigma N_{ve}$  sum of valence electrons;  $\bar{N}$  average electron concentration;  $r_e$  tabulated atomic radii;  $R_s, R_p$  pseudopotential radii after St. John and Bloch [162];  $r_s, r_p$  pseudopotential radii after Zunger [163];  $\Delta V/V$  size factor difference;  $\Delta X^G$  difference in electronegativity after Gordy and Thomas [164];  $\Delta X^{MB}$  difference in electronegativity after Martynov and Batsanov [165];  $\Delta X^{WB}$  difference in electronegativity after Watson and Bennett [166];

## 2. Structure Maps

AB <sub>3</sub>	$\Sigma N_{ve}$ vs $(r_p + r_s)_A - (r_p + r_s)_B$ vs $\Delta X^{MB}$	c-FeS <sub>2</sub> , o-FeS <sub>2</sub> , MgCu <sub>2</sub> ZrSe <sub>3</sub> , AlCl <sub>3</sub> , $\beta$ -Cu <sub>3</sub> Ti, Fe <sub>3</sub> C, YF <sub>3</sub> , Br <sub>3</sub> Pu, CuTi <sub>3</sub> , CoGa <sub>3</sub> , Al <sub>3</sub> Ti, Ni <sub>3</sub> P, AsNa <sub>3</sub> , Ni <sub>3</sub> Sn, Cl <sub>3</sub> U, Ni <sub>3</sub> Ti, D <sub>3</sub> Ho, LaF <sub>3</sub> , FeCl <sub>3</sub> , AuCu <sub>3</sub> , Cr <sub>3</sub> Si, As <sub>3</sub> Co, BiF <sub>3</sub>	[161]
A <sub>3</sub> B <sub>5</sub>		Ge <sub>3</sub> Rh <sub>5</sub> , U <sub>3</sub> S <sub>5</sub> , Nb <sub>3</sub> P <sub>5</sub> , Pu <sub>3</sub> Pd <sub>5</sub> , Rh <sub>3</sub> Pu <sub>5</sub> , B <sub>3</sub> Cr <sub>5</sub> , Si <sub>3</sub> W <sub>5</sub> , Th <sub>3</sub> Pd <sub>5</sub> , Si <sub>3</sub> Mn <sub>5</sub>	
X <sup>8</sup> Y <sup>N-8</sup>	$ (R_p + R_s)_X - (R_p + R_s)_Y $ vs $ (R_p - R_s)_X + (R_p - R_s)_Y $	C, NaCl, CsCl, c-ZnS, h-ZnS	[162]
MN	$ (r_p + r_s)_M - (r_p + r_s)_N $ vs $ (r_p - r_s)_M + (r_p - r_s)_N $	NaCl, CsCl, NiAs, PbO, CuTi, GeS, CuCd, FeSi, FeB, MnP, NaTi, CrB, CoSn, SeTi, MoP, KGe, LiO, AuCu, AsGe, NaSi, NS, NaHg, KO, SiP, RbO, NaP, HgCl, LiGe, TlTe, NaPb	[163]
TU	$\bar{N}_v$ vs $ \Delta X^{WB} $	AuCd, AuCu, CrB, CsCl, $\gamma$ -CuTi, $\sigma$ -FeCr	[166]
TU <sub>2</sub>		MgCu <sub>2</sub> , MgZn <sub>2</sub> , CuAl <sub>2</sub> , MoSi <sub>2</sub> , NiTi <sub>2</sub> , $\sigma$ -FeCr, MoPt <sub>2</sub>	
TU <sub>3</sub>		AuCu <sub>3</sub> , CuTi <sub>3</sub> , TiAl <sub>3</sub> , SnNi <sub>3</sub> , TiNi <sub>3</sub> , WO <sub>3</sub> , $\sigma$ -FeCr	
XY	$\bar{n}$ vs $ \Delta X^G $	NaCl, c-ZnS, h-ZnS	[167]
XZ		NaCl, CsCl, c-ZnS, h-ZnS	
XT		NiAs, NaCl, MnP	
XW <sub>2</sub>		CaF <sub>2</sub> , TiO <sub>2</sub> , CdI <sub>2</sub> , MoS <sub>2</sub> , NbS <sub>2</sub> , PbCl <sub>2</sub>	
XW <sub>3</sub>		AlFe <sub>3</sub> , CoAs <sub>3</sub> , CrCl <sub>3</sub> , $\alpha$ -ReO <sub>3</sub> , LaF <sub>3</sub> , AlF <sub>3</sub>	
X <sub>2</sub> W <sub>3</sub>		$\alpha$ -Al <sub>2</sub> O <sub>3</sub> , La <sub>2</sub> O <sub>3</sub> , Mn <sub>2</sub> O <sub>3</sub> , Bi <sub>2</sub> Te <sub>3</sub> , Sb <sub>2</sub> S <sub>3</sub>	
TU	$\bar{N}_g$ vs $\Delta N_g$	CrB, AuCu, AuCd, CsCl, Mg, FeB, Fe <sub>7</sub> W <sub>6</sub> , $\gamma$ -CuTi, $\alpha$ -FeCr	[168]
XT	$\Sigma N_{ve}$ vs $\Delta E$	CsCl, NiAs, CuS, AuCd, NbPb, FeSi, FeB, MnP, CrB, CoSn, MoP, CuAu, NaCl, ZnS, TiAs, NbAs, NiS, CuTe, PdS, PtS, CoGe, PbO	[169]
X <sub>2</sub> T		TiO <sub>2</sub> , IrSe <sub>2</sub> , CdI <sub>2</sub> , PdS <sub>2</sub> , o-FeS <sub>2</sub> , c-FeS <sub>2</sub> , HfGa <sub>2</sub> , CuP <sub>2</sub> ,	

		MoSi <sub>2</sub> , PdP <sub>2</sub> , ReS <sub>2</sub> , FeAsS, FeAs <sub>2</sub> , AuSn <sub>2</sub> , CuAl <sub>2</sub> , PdSn <sub>2</sub> , CaF <sub>2</sub> , NbAs <sub>2</sub> , PbCl <sub>2</sub> TiAs <sub>2</sub> , CrSi <sub>2</sub> , CuMg <sub>2</sub> , TiSi <sub>2</sub> , ZrSi <sub>2</sub> , GdSi <sub>2</sub> , Cu <sub>2</sub> Sb, CaCl <sub>2</sub> , Cu <sub>2</sub> Mg, RuB <sub>2</sub> , ReB <sub>2</sub> , CaC <sub>2</sub> , MoP <sub>2</sub> , AlB <sub>2</sub> , MgZn <sub>2</sub> , ZrGa <sub>2</sub> , FeSi <sub>2</sub> , PbFCl, AuTe <sub>2</sub> , PdBi <sub>2</sub>	
A <sub>2</sub> BH <sub>4</sub>	( $r_p + r_s$ ) <sub>A</sub> vs ( $r_p + r_s$ ) <sub>B</sub>	Al <sub>2</sub> MgO <sub>4</sub> , Th <sub>3</sub> P <sub>4</sub> , Fe <sub>2</sub> CaO <sub>4</sub> , K <sub>2</sub> SO <sub>4</sub> , Cr <sub>3</sub> S <sub>4</sub> , Al <sub>2</sub> BeO <sub>4</sub> , K <sub>2</sub> MgF <sub>4</sub> , Mn <sub>3</sub> O <sub>4</sub> , Ag <sub>2</sub> HgI <sub>4</sub> , Li <sub>2</sub> WO <sub>4</sub> , Y <sub>2</sub> CrS <sub>4</sub> , Yb <sub>3</sub> S <sub>4</sub> , Pb <sub>3</sub> O <sub>4</sub> , Al <sub>2</sub> BaO <sub>4</sub> , Sr <sub>2</sub> PbO <sub>4</sub> , Na <sub>2</sub> SO <sub>4</sub> , K <sub>2</sub> PtCl <sub>4</sub> , K <sub>2</sub> Pd(NO <sub>2</sub> ) <sub>4</sub> , Cr <sub>2</sub> CuO <sub>4</sub> , KHSO <sub>4</sub> , LiKSO <sub>4</sub> , KNaSO <sub>4</sub> , K <sub>2</sub> SO <sub>3</sub> (N <sub>2</sub> O <sub>2</sub> ), Na(MoO <sub>2</sub> )PO <sub>4</sub> , Ti <sub>2</sub> CaO <sub>4</sub> , Ba <sub>2</sub> TiO <sub>4</sub> , H <sub>2</sub> SO <sub>4</sub> , H <sub>2</sub> SeO <sub>4</sub> , Li <sub>2</sub> SO <sub>4</sub> , Na <sub>2</sub> CrO <sub>4</sub> , (NH <sub>4</sub> ) <sub>2</sub> CrO <sub>4</sub> , Na <sub>2</sub> S <sub>2</sub> O <sub>3</sub> , (NH <sub>4</sub> ) <sub>2</sub> S <sub>2</sub> O <sub>3</sub> , BaHPO <sub>4</sub> , CaHPO <sub>4</sub> , NaBePO <sub>4</sub> , NaH(PO <sub>3</sub> NH <sub>2</sub> ), K(UO <sub>2</sub> )VO <sub>4</sub> , Bi <sub>2</sub> PbS <sub>4</sub> , Sb <sub>2</sub> FeS <sub>4</sub> , As <sub>2</sub> PbS <sub>4</sub> , Sb <sub>2</sub> SnTe <sub>4</sub> , In <sub>2</sub> ZnS <sub>4</sub>	[170]
IJ <sub>5</sub>	$r_{e,A}/r_{e,B}$ vs $\Sigma N_{ve}$ vs $\Delta X^{MB}$	CaCu <sub>5</sub> , AuBe <sub>5</sub> , PrNi <sub>2</sub> Al <sub>3</sub> , YNi <sub>2</sub> Al <sub>3</sub> , SmAg <sub>3.5</sub> Al <sub>1.5</sub> , BaZn <sub>5</sub> , SmAg <sub>2.4</sub> Al <sub>2.6</sub> , Nd <sub>3</sub> Ni <sub>13</sub> B <sub>2</sub> , CeCo <sub>4</sub> B, CeCo <sub>3</sub> B <sub>2</sub> , LaRu <sub>3</sub> Si <sub>2</sub> , ErRh <sub>3</sub> Si <sub>2</sub> , ErIr <sub>3</sub> B <sub>2</sub> , Ce <sub>2</sub> Co <sub>7</sub> B <sub>3</sub> , Ce <sub>3</sub> Co <sub>11</sub> B <sub>4</sub>	[171]
T <sub>x</sub> U <sub>y</sub>	$\bar{N}$ vs $\bar{\Delta V}/V$	MgCu <sub>2</sub> , MgZn <sub>2</sub> , MgNi <sub>2</sub> , Cr <sub>3</sub> Si, $\sigma$ -FeCr, Ti <sub>5</sub> Re <sub>24</sub> , Cr <sub>0.16</sub> Mo <sub>0.38</sub> Co <sub>0.46</sub> , Mo <sub>3</sub> (Mo <sub>0.8</sub> Ni <sub>0.2</sub> ) <sub>5</sub> Ni <sub>6</sub> , W <sub>6</sub> Fe <sub>7</sub>	[172]

Table 2.1.: List of prior schemes for structure maps, including system and composition, the atomic properties used for the axes and the crystal structures.

### 2.2.2. Mendelev Number

Instead of using typical physical properties of the atoms, Pettifor proposed the chemical scale  $\chi$  and the closely related Mendelev number  $M$  as an appropriate coordinate to achieve the best structural separation within two-dimensional maps [173]. The scale was defined as an unique parameter by a single one-dimensional string running across the two-dimensional periodic table with the constraints to vary in ascending order (linearly for the Mendelev number  $M$ ) across the transition metals and the sp element series without hydrogen and the 2p elements as they behave chemically distinct from the elements in the same group (Fig. 2.2). The Pauling electronegativity scale for beryllium to fluorine has been used to set the magnitude of the



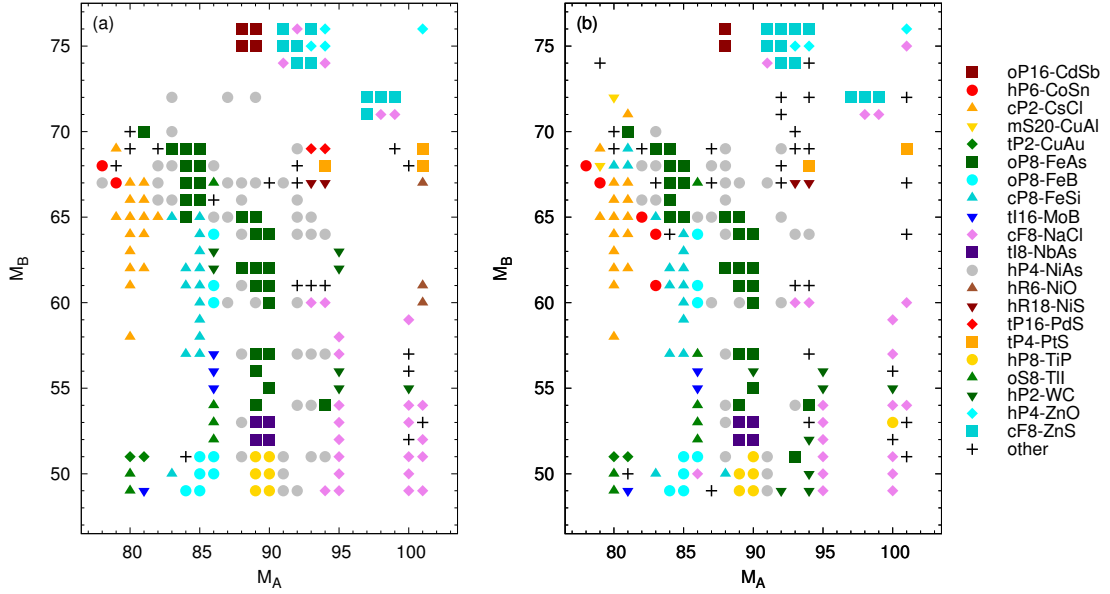


Figure 2.3.: Section of a Pettifor structure map for  $AB$  compounds, from (a) Ref. [177] and (b) compiled with a dataset from Ref. [178]. Crystal structures that appear only once are marked as 'other'.

prototype changed from a more frequently occurring crystal structure to a crystal structure that appears only once, marked as 'other', we observe also changes in the regions for the most important  $AB$  crystal structures. The cP2-CsCl region is reduced and now embraced by hP6-CoSn. We also note the slightly reduced oP8-FeAs and significantly reduced hP4-NiAs regions. The cF8-NaCl region in the bottom right corner shows more variation in different crystal structures. We also note the now misplaced oS8-TiI compound which in the original structure maps was resolved as tI16-MoB. However, there are also a few regions that are slightly improved. The cF8-NaCl, cF8-ZnS and hP4-ZnO region in the top right corner appears more ordered. hP2-WC compounds in the same row as cP8-FeSi have disappeared, thus reducing the spread of hP2-WC in the structure map. We further note the improved ordering of cP8-FeSi and hP4-NiAs next to cP2-CsCl.

The existence of such domains of structural stability were explained by a tight-binding model providing a microscopic, quantum-mechanical explanation [179, 180]. Despite the relatively simple model, neglecting the s states and taking only into account the p and d states, it was able to explain most of the observed stable domains of specific pd-bonded  $AB$  compounds.

### 2.2.3. Local Environment

The analysis of the atomic environment of constituent atoms in compounds was often limited to a few compounds containing specific elements, e.g. boron [181]. In order to generalize

a few of the known d-p compounds in terms of polyhedra-packing, Girgis and Villars [182] analyzed the existing compounds with respect to the existing coordination polyhedra of the constituent atoms, thus following the pioneering work by Frank and Kasper [183, 184] on the topologically close-packed phases adopted by transition metals. The main goal was not to determine all existing coordination polyhedra, but to identify the ones needed to build the underlying structure type.

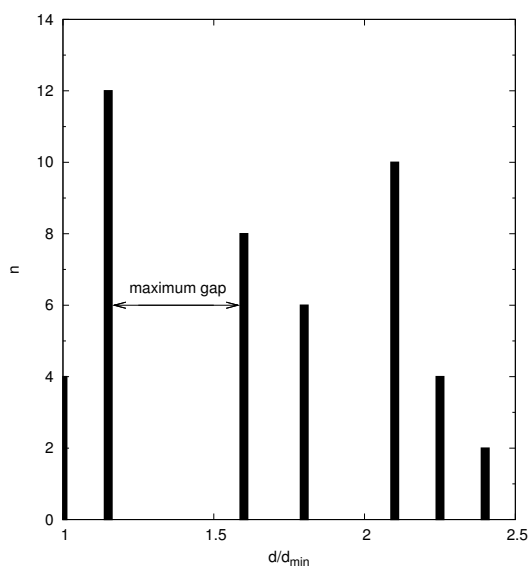


Figure 2.4.: Schematic illustration of a nearest neighbor histogram showing the normalized interatomic distances between an atom and its closest neighbors. The interatomic distances reveal a maximum gap. All atoms below the maximum gap belong to the atomic environment of the central atom.

Following Villars' work [159–161], Villars and Hulliger [185] presented an attempt to link the atomic properties of the constituent elements with geometrical properties of the crystallized compounds. Each prototype has been analyzed in order to determine the coordination polyhedra, i.e. the geometrical construct formed around a central atom by its neighbors. In order to determine the closest or nearest neighbors of a central atom that form the coordination polyhedron, the authors used the maximum gap rule introduced by Brunner and Schwarzenbach [186] (Fig. 2.4). In this method, the calculated interatomic distances between each atom and its closest neighbors are investigated with respect to a maximum gap. All atoms below the maximum gap are the nearest neighbors of the central atom. This is also referred to as atomic environment of the central atom. The coordination polyhedron is then determined by the atoms of the atomic environment.

The authors considered all binary, ternary and quaternary compounds with the same coordination polyhedron on every atomic site, thus

the structures have been designated as single-environmental types. Weakly distorted polyhedra were assigned with their undistorted versions, thus reducing the number of distinct coordination polyhedra found in the dataset to eight. The order parameter from prior studies [160, 161] were modified to explicitly include the stoichiometry.

In a series of subsequent studies, Daams, van Vucht and Villars extended the analysis of the geometrical features to cubic intermetallic compounds [187], followed by Daams and Villars investigating the rhombohedral [188], hexagonal [189] and tetragonal [190] intermetallic structure types. As the maximum gap rule was found to yield inconsistent results in some cases, the authors proposed the maximum convex volume rule [187] to identify the nearest neighbors where the maximum gap rule failed. Here, the coordination polyhedra is defined as the maxi-

mum volume around one central atom enclosed by convex faces with all the coordinating atoms lying at the intersections of at least three faces. Slightly distorted polyhedra were assigned to their undistorted version, referred to as atomic environment type (AET). In a few crystal structure types (often hydrogen containing ones or metals in combination with p elements) the polyhedra analysis identified irregular AETs (IAET) which can not be described by a convex volume.

The analysis of the underlying datasets separated into cubic, rhombohedral, hexagonal and tetragonal intermetallic structure types revealed that among all the possible AET most of the crystal structure types consisted of a given set of only a few AETs. The number of most frequently occurring ones among the different cell types was consistently in the range of approximately 20 AETs. Some of the AETs were found to be preferred in all the different cell types, whereas especially the IAETs were often found to occur only in one cell type. The AETs found in the corresponding crystal structure types were then used to define a generic term to replace the prototype classification. The number of different coordination polyhedra found within a structure was used to determine the environment type. Based on this classification, the structures were then assigned to a coordination type, using the number and kind of the AETs as selection criterion. This classification by the environment type significantly reduces the number of different entries compared to the classification according to prototype.

Villars and Daams [191] extended the same approach to the chemical elements, including not only the known ground states but also the low/high-temperature and high-pressure modifications. As the structure is determined by the bonding situation, the authors expected to find both the same AETs for different elements having the same bonding situation and a tendency towards single-environmental type, as higher order environmental types would imply varying bonding situations at different atomic sites. Indeed, the authors identified a set of seven most frequently occurring AETs among the periodic table. Using Zunger's pseudopotential radii and the number of valence electrons, and separating structures obtained under normal conditions from the low/high-temperature and high-pressure ones, the authors were able to explain the occurrence of a specific AET as a volume and bonding effect.

About a decade later, Villars and co-workers [192] presented new structure maps for *AB* compounds by combining the determination of the AETs with a new ordering scheme of the Mendeleev number that is different from Ref. [173]. Each binary compound was decomposed into the AETs of each constituent elements. For the simpler compounds, the decomposition listed one or two different AETs. Structures with three or more different AETs were designated as complex, and less frequently occurring AETs were grouped into a distinct class.

## 2.3. New Structure Maps for d-p Compounds

### 2.3.1. Verification of Experimental Data Set

The focus of this investigation are compounds that are formed by a transition metal and a p-block element. In order to obtain the required information for the dataset, we scanned the

## 2. Structure Maps

1 IA																		18 VIIIA																
1	1.0079																	2	4.002															
	<b>H</b>																		<b>He</b>															
	Hydrogen																		Helium															
2	6.941	9.0122																	5	10.811	6	12.011	7	14.007	8	15.999	9	18.998	10	20.18				
	<b>Li</b>	<b>Be</b>																		<b>B</b>	<b>C</b>	<b>N</b>	<b>O</b>	<b>F</b>	<b>Ne</b>									
	Lithium	Beryllium																		Boron	Carbon	Nitrogen	Oxygen	Fluorine	Neon									
3	22.990	24.305																	13	26.982	14	28.086	15	30.974	16	32.065	17	35.453	18	39.948				
	<b>Na</b>	<b>Mg</b>																		<b>Al</b>	<b>Si</b>	<b>P</b>	<b>S</b>	<b>Cl</b>	<b>Ar</b>									
	Sodium	Magnesium																		Aluminum	Silicon	Phosphorus	Sulphur	Chlorine	Argon									
4	39.098	40.078	21	44.956	22	47.867	23	50.942	24	51.996	25	54.938	26	55.845	27	58.933	28	58.693	29	63.546	30	65.39	31	69.723	32	72.64	33	74.922	34	78.96	35	79.904	36	83.8
	<b>K</b>	<b>Ca</b>	<b>Sc</b>	<b>Ti</b>	<b>V</b>	<b>Cr</b>	<b>Mn</b>	<b>Fe</b>	<b>Co</b>	<b>Ni</b>	<b>Cu</b>	<b>Zn</b>	<b>Ga</b>	<b>Ge</b>	<b>As</b>	<b>Se</b>	<b>Br</b>	<b>Kr</b>																
	Potassium	Calcium	Scandium	Titanium	Vanadium	Chromium	Manganese	Iron	Cobalt	Nickel	Copper	Zinc	Gallium	Germanium	Arsenic	Selenium	Bromine	Krypton																
5	85.468	87.62	39	88.906	40	91.224	41	92.906	42	95.94	43	96	44	101.07	45	102.91	46	106.42	47	107.87	48	112.41	49	114.82	50	118.71	51	121.76	52	127.6	53	126.9	54	131.29
	<b>Rb</b>	<b>Sr</b>	<b>Y</b>	<b>Zr</b>	<b>Nb</b>	<b>Mo</b>	<b>Tc</b>	<b>Ru</b>	<b>Rh</b>	<b>Pd</b>	<b>Ag</b>	<b>Cd</b>	<b>In</b>	<b>Sn</b>	<b>Sb</b>	<b>Te</b>	<b>I</b>	<b>Xe</b>																
	Rubidium	Strontium	Yttrium	Zirconium	Niobium	Molybdenum	Technetium	Ruthenium	Rhodium	Palladium	Silver	Cadmium	Indium	Tin	Antimony	Tellurium	Iodine	Xenon																
6	132.91	137.33	57-71	72	178.49	73	180.95	74	183.84	75	186.21	76	190.23	77	192.22	78	195.08	79	196.97	80	200.59	81	204.38	82	207.2	83	208.98	84	209	85	210	86	222	
	<b>Cs</b>	<b>Ba</b>	<b>La-Lu</b>	<b>Hf</b>	<b>Ta</b>	<b>W</b>	<b>Re</b>	<b>Os</b>	<b>Ir</b>	<b>Pt</b>	<b>Au</b>	<b>Hg</b>	<b>Tl</b>	<b>Pb</b>	<b>Bi</b>	<b>Po</b>	<b>At</b>	<b>Rn</b>																
	Cesium	Barium	Lanthanide	Hafnium	Tantalum	Tungsten	Rhenium	Osmium	Iridium	Platinum	Gold	Mercury	Thallium	Lead	Bismuth	Polonium	Astatine	Radon																
7	223	226	89-103	104	261	105	262	106	266	107	264	108	277	109	268	110	281	111	280	112	285	113	284	114	289	115	288	116	293	117	292	118	294	
	<b>Fr</b>	<b>Ra</b>	<b>Ac-Lr</b>	<b>Rf</b>	<b>Db</b>	<b>Sg</b>	<b>Bh</b>	<b>Hs</b>	<b>Mt</b>	<b>De</b>	<b>Rg</b>	<b>Uub</b>	<b>Uut</b>	<b>Uuq</b>	<b>Uup</b>	<b>Uuh</b>	<b>Uus</b>	<b>Uuo</b>																
	Francium	Radium	Actinide	Rutherfordium	Dubnium	Seaborgium	Bohrium	Hassium	Meitnerium	Darmstadtium	Roentgenium	Uunbium	Uutrium	Uunquadium	Uunpentium	Uunhexium	Uunseptium	Uunoctium																
	57	138.91	58	140.12	59	140.91	60	144.24	61	145	62	150.36	63	151.96	64	157.25	65	158.93	66	162.50	67	164.93	68	167.26	69	168.93	70	173.04	71	174.97				
	<b>La</b>	<b>Ce</b>	<b>Pr</b>	<b>Nd</b>	<b>Pm</b>	<b>Sm</b>	<b>Eu</b>	<b>Gd</b>	<b>Tb</b>	<b>Dy</b>	<b>Ho</b>	<b>Er</b>	<b>Tm</b>	<b>Yb</b>	<b>Lu</b>																			
	Lanthanum	Cerium	Praseodymium	Neodymium	Promethium	Samarium	Europium	Gadolinium	Terbium	Dysprosium	Holmium	Erbium	Thulium	Ytterbium	Lutetium																			
	89	227	90	232.04	91	231.04	92	238.03	93	237	94	244	95	243	96	247	97	247	98	251	99	252	100	257	101	258	102	259	103	262				
	<b>Ac</b>	<b>Th</b>	<b>Pa</b>	<b>U</b>	<b>Np</b>	<b>Pu</b>	<b>Am</b>	<b>Cm</b>	<b>Bk</b>	<b>Cf</b>	<b>Es</b>	<b>Fm</b>	<b>Md</b>	<b>No</b>	<b>Lr</b>																			
	Actinium	Thorium	Protactinium	Uranium	Neptunium	Plutonium	Americium	Curium	Berkelium	Californium	Einsteinium	Fermium	Mendelevium	Nobelium	Lawrencium																			

Figure 2.5.: The focus is on compounds that are formed by a transition metal (red) and a p-block element, excluding halogens and the noble gases. Elements in the p-block are classified as non-metallic (purple), semi-metallic (blue) and metallic (cyan). The separation between non-metallic and metallic elements runs approximately diagonal through the p-block.

Pearson's Crystal Database (PCD) [178] for entries. From the p-block elements, we exclude the halogens and the noble gases (Fig. 2.5). The number of entries that list compounds containing noble gases is negligible, as expected due to the completely filled shells of the noble gases. For the halogen-containing compounds, we also observe a reduced number of entries compared to the earlier p-block elements. Furthermore, the clear majority of these compounds crystallizes in structure types that are only observed in the transition metal - halogen system, i.e. these crystal structures are not observed in combination with a transition metal and an earlier p-block element. Thus, we exclude the halogens due to the limited number of entries in combination with the unique crystal structures that are only observed in the transition metal - halogen system. From the entries in the PCD we compiled a list of compounds that appear in the binary d-p system. These structure files were compared with the phase diagrams listed in [193]. This allowed us to exclude metastable, high-temperature and high-pressure compounds. Furthermore, we excluded compounds that were observed in thin films, compounds that list the crystal geometry obtained by calculations and compounds that contain defects, i.e. compounds with a non-integer composition due to partially occupied atomic sites. This includes also structure files of phases that have full occupation in the PCD files, but are explicitly listed as defect phases in the phase diagrams. For example, we excluded the hP4-NiAs phase in the Co-S [194], Co-Se [195] and Ni-Te [196] system which lists structure files in the PCD with perfect composition, but the corresponding phase diagram lists the compositions



$d_x p_y$	Pearson Symbol - Prototype (#)
4:1	cP5-Fe <sub>4</sub> N (4)
3:1	cP4-Cu <sub>3</sub> Au (12), cP8-Cr <sub>3</sub> Si (17), hP8-Mg <sub>3</sub> Cd (8), oP8-Cu <sub>3</sub> Ti (3), oP16-Fe <sub>3</sub> C (5), tI32-Ni <sub>3</sub> P (9), tP32-Ti <sub>3</sub> P (7)
5:2	hP42-Pd <sub>5</sub> Sb <sub>2</sub> (3)
7:3	hP20-Th <sub>7</sub> Fe <sub>3</sub> (4)
9:4	Cu <sub>9</sub> Al <sub>4</sub> (3)
2:1	hP6-Co <sub>1.75</sub> Ge (7), hP9-Fe <sub>2</sub> P (6), oP12-Co <sub>2</sub> Si (15), oS24-Pd <sub>2</sub> As (3), tI12-CuAl <sub>2</sub> (13), tP6-Cu <sub>2</sub> Sb (6)
5:3	hP16-Mn <sub>5</sub> Si <sub>3</sub> (24), oP16-Rh <sub>5</sub> Ge <sub>3</sub> (5), oS16-Pt <sub>5</sub> Ga <sub>3</sub> (3), tI32-Cr <sub>5</sub> B <sub>3</sub> (4), tI32-W <sub>5</sub> Si <sub>3</sub> (9)
3:2	oP20-Ni <sub>3</sub> Sn <sub>2</sub> (3), tP10-U <sub>3</sub> Si <sub>2</sub> (9), tP20-Zr <sub>3</sub> Al <sub>2</sub> (3)
13:9	mS44-Ni <sub>13</sub> Ga <sub>9</sub> (3)
11:8	Cr <sub>11</sub> Ge <sub>8</sub> (3)
5:4	hP18-Ti <sub>5</sub> Ga <sub>4</sub> (3), oP36-Sm <sub>5</sub> Ge <sub>4</sub> (5), tI18-Ti <sub>5</sub> Te <sub>4</sub> (8), tP36-Zr <sub>5</sub> Si <sub>4</sub> (3)
6:5	oI44-V <sub>6</sub> Si <sub>5</sub> (3)
11:10	tI84-Ho <sub>11</sub> Ge <sub>10</sub> (5)
1:1	cF8-NaCl (20), cF8-ZnS (6), cP2-CsCl (13), cP8-FeSi (13), hP2-WC (5), hP4-NiAs (23), hP4-ZnO (3), hP6-CoSn (4), oP8-FeAs (20), oP8-FeB (8), oS8-TiI (14), tP2-CuAu (3), tI16-MoB (3)
3:4	cF56-Fe <sub>3</sub> O <sub>4</sub> (5), hP14-Nb <sub>3</sub> Te <sub>4</sub> (3), mS14-Cr <sub>3</sub> S <sub>4</sub> (11), oI14-Ta <sub>3</sub> B <sub>4</sub> (6)
2:3	hP5-Ni <sub>2</sub> Al <sub>3</sub> (8), hR30-Al <sub>2</sub> O <sub>3</sub> (4), oF40-Zr <sub>2</sub> Al <sub>3</sub> (4), oP40-Ru <sub>2</sub> Ge <sub>3</sub> (3)
5:8	mS26-V <sub>5</sub> S <sub>8</sub> (6)
1:2	cF12-CaF <sub>2</sub> (7), cP12-FeS <sub>2</sub> (19), hP3-AlB <sub>2</sub> (12), hP3-CdI <sub>2</sub> (8), hP6-MoS <sub>2</sub> (4), hP9-CrSi <sub>2</sub> (6), mP12-CoSb <sub>2</sub> (8), mP12-VO <sub>2</sub> (3), mS18-NbTe <sub>2</sub> (3), oF24-TiSi <sub>2</sub> (3), oF48-Mg <sub>2</sub> Cu (3), oP6-FeAs <sub>2</sub> (9), oP6-FeS <sub>2</sub> (5), oP12-PbCl <sub>2</sub> (3), oS12-ZrSi <sub>2</sub> (6), tI6-MoSi <sub>2</sub> (3), tI12-CuAl <sub>2</sub> (13), tI24-HfGa <sub>2</sub> (4)
3:7	cl40-Ru <sub>3</sub> Sn <sub>7</sub> (6)
2:5	tP14-Hg <sub>5</sub> Mn <sub>2</sub> (3)
1:3	cl32-CoAs <sub>3</sub> (7), cP4-Cu <sub>3</sub> Au (6), mP8-ZrSe <sub>3</sub> (4), tI8-TiAl <sub>3</sub> (8), tI16-ZrAl <sub>3</sub> (4), tP16-IrIn <sub>3</sub> (3)
2:9	mP22-Co <sub>2</sub> Al <sub>9</sub> (3)
1:6	oS28-MnAl <sub>6</sub> (3)
1:12	cF52-UB <sub>12</sub> (3), cl26-WAl <sub>12</sub> (4)

Table 2.2.: List of important compositions and corresponding crystal structures, denoted by Pearson symbol and prototype. The number of appearances is given in brackets. Only structures which appear a minimum of three times for a given composition in the considered system are listed. These compounds will be used as the dataset for the structure maps.

$\text{Co}_{0.88}\text{S}$ ,  $\text{Co}_{0.88}\text{Se}$  and  $\text{Ni}_{0.8}\text{Te}$ , respectively. An exception is made if the stability range in the corresponding phase diagram contains the perfect composition. Thus, cF8-NaCl is excluded in, for example, the V-C [197] system, but kept in the Ti-C system [198]. However, we will test the performance of our order parameters with respect to the appearance of defects in the crystal structures. If phase diagrams list conflicting data, like two or more compounds for an identical composition, the corresponding structure files are also excluded. Structure files for binary systems, for which no phase diagram is listed in [193], are completely excluded. Furthermore, we added entries that list ternary systems, d-d-p or d-p-p, that adopt crystal structures observed in the binary systems. Here, the compounds appear with mixed d or p elements at the Wyckoff sites. Due to the significantly reduced number of available experimental phase diagrams for ternary systems in [193] compared to the binary systems, we dropped the comparison of the entries with the phase diagrams in order to exclude unwanted entries. Instead, we simply checked the entries for keywords in the structure files, that designated a compound as high-temperature, high-pressure or metastable phase. Furthermore, we excluded compounds where d and p elements mix at the same Wyckoff site. However, this represents clearly the minority of entries. Only about 22% of the entries list compounds with mixed d and p elements at the same Wyckoff site. We note that this behavior is predominantly observed for the p-block elements that are designated as semi-metallic and metallic, c.f. Fig. 2.5.

The structure files from the revised dataset were transformed into the standard structural input files for BOPfox [199,200]. The built-in polyhedron analysis [201] examined the structures with respect to the coordination number (i.e. the number of nearest-neighbors), the composition of the coordination polyhedron (i.e. the number of d and p elements in the coordination polyhedron without the central atom), and the corresponding polyhedron type. The algorithm to identify the nearest neighbors is based on a Voronoi construction [202]. The arrangement of the atoms that have been identified to represent the atomic environment are compared to a set of regular polyhedra in a database. The smallest polyhedron is the tetrahedron comprised of four atoms, the largest one contains 39 atoms. The resemblance of the atomic environment with the polyhedra in the database is calculated via a correlation method that consist of a sorted histogram containing the differences in the normalized distances of two, three and four atoms of the local environment. The histogram of the considered atom is compared with the histograms of the polyhedra in the database, that consist of the same number of atoms as the atomic environment. The resemblance for each value is calculated via a Gaussian function, summarized and normalized with respect to the number of entries. This resemblance factor  $R$  is defined in the range  $0 \leq R \leq 1$ . The larger the value of  $R$ , the greater the resemblance of a polyhedron with the reference polyhedron. Relating to the prior work by Daams, Villars and co-workers, this repetition of determining the coordination polyhedron is due to the following reasons: First, tests of the Voronoi construction revealed that this method is more robust than the maximum gap rule, thus giving coordination numbers for crystal structures where the maximum gap approach fails. Second, Daams, Villars and co-workers addressed only the cubic, rhombohedral, hexagonal and tetragonal crystal structures. To our knowledge, no publications addressing the orthorhombic, monoclinic and triclinic crystal structures are available. Third, in the available publications the authors do not list the compositions of the coordination polyhedra. For further analysis, we also calculated the volume of the coordination polyhedra

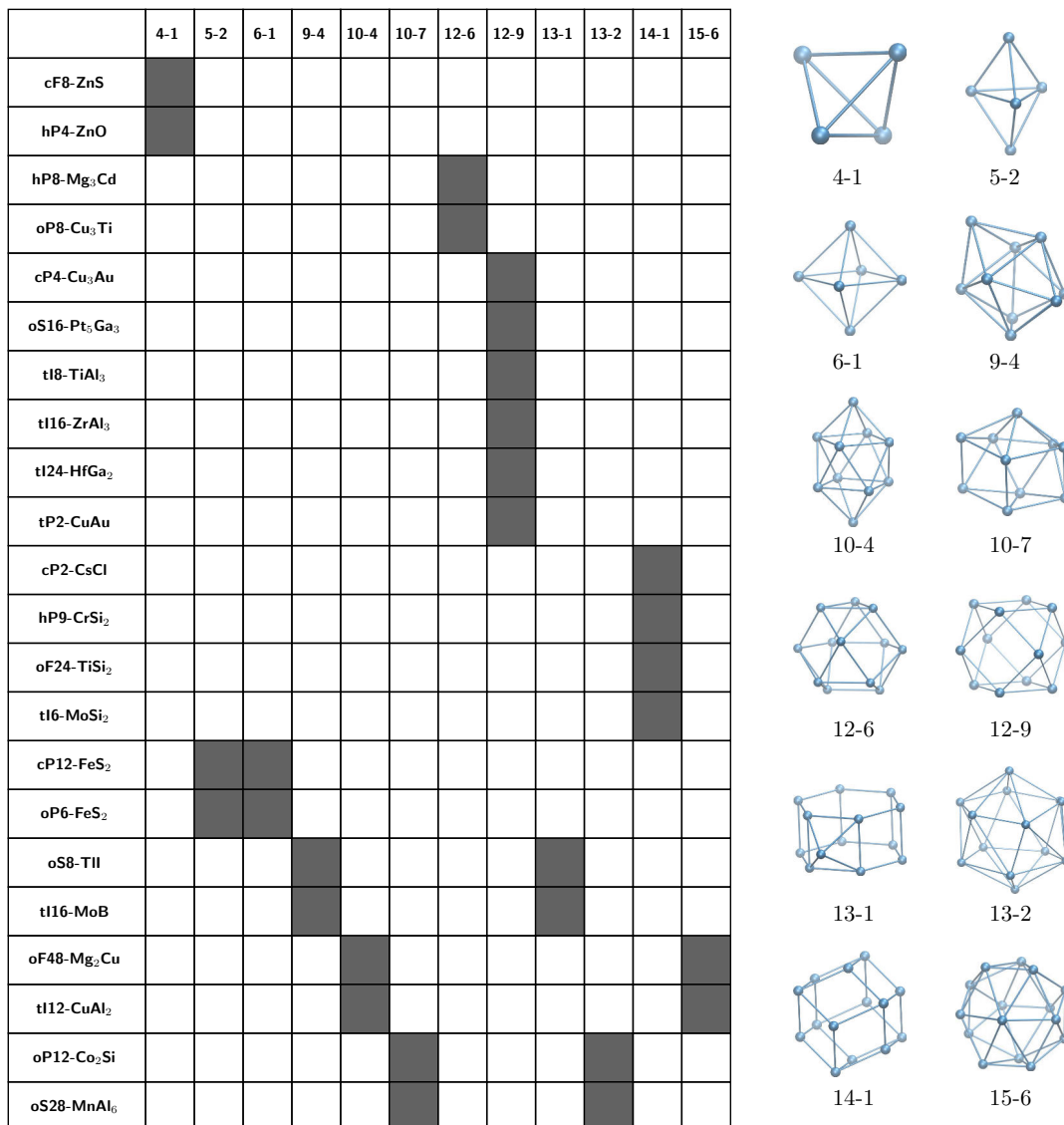


Figure 2.6.: Compounds which are built of the same coordination polyhedra (left panel). Schematic illustration of the listed coordination polyhedra (right panel).

with qhull-2011.1 [203].

Tab. 2.2 lists the most important compositions and corresponding crystal structures that appear in the binary d-p system, denoted by Pearson symbol and the prototype. The number of appearances in the considered system is given in brackets. Only structures which appear at least three times are listed, and will provide the dataset for the structure maps. This results in a total of 574 entries which crystallize in 83 different prototypes. 499 of these entries, which crystallize in 64 different prototypes, are representatives of the most frequently occurring d:p ratios: 1:1, 2:1/1:2, 3:1/1:3, 3:2/2:3, 3:4 and 5:3. Among these compositions, 216 entries

## 2. Structure Maps

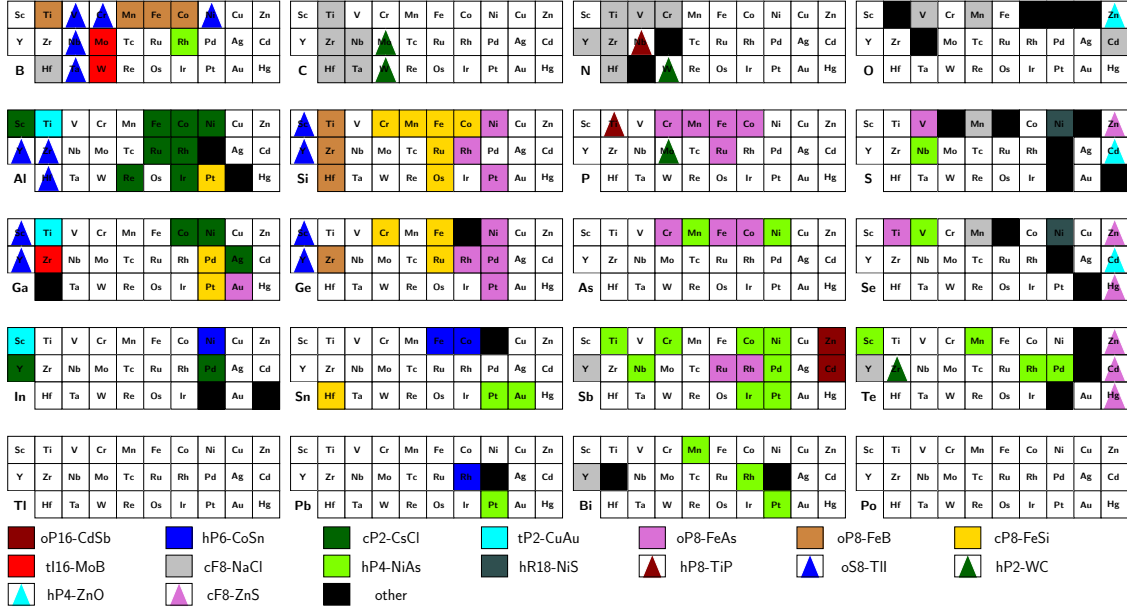


Figure 2.7.: Distribution of 1:1 compounds in the binary d-p systems. We separate according to p element. Structures that appear only once are marked as 'other'.

crystallize in prototypes that have only one or two representatives and are therefore excluded. We explicitly distinguish between the compounds with identical composition, but swapped ratio, as here the d and p elements occupy the opposite Wyckoff sites, thus the coordination polyhedra vary for the d and p elements. We also note that Tab. 2.2 is not symmetric with respect to the 1:1 composition. Compositions with both d- and p-rich compounds (e.g. 2:1/1:2 and 3:1/1:3) have usually a significantly larger number of entries for one d:p ratio, but not for the swapped one. Furthermore, the less common compositions usually appear only for the d- or p-rich compounds, but not for the opposite ones. Some of the compounds listed in Tab. 2.2 are built of the same coordination polyhedra. These are summarized in Fig. 2.6 among a schematic illustration of the corresponding coordination polyhedra<sup>1</sup>. The structural similarity of the cubic, hexagonal and tetragonal compounds in Fig. 2.6 that is due to the appearance of identical coordination polyhedra is in agreement with the findings in Refs. [185,187,189]. The only exception is hP9-CrSi<sub>2</sub> that according to our analysis is built of the same coordination polyhedra as cP2-CsCl and tI6-MoSi<sub>2</sub>, but Ref. [189] lists a coordination polyhedron that differs from cP2-CsCl and tI6-MoSi<sub>2</sub>. However, the coordination number is the same. This might be attributed to different approaches in order to determine the coordination polyhedra. We will refer to the structural similarity of the listed compounds when discussing the structure maps.

<sup>1</sup>4-1: tetrahedron, 5-2: triangular dipyramid, 6-1: octahedron, 9-4: triaugmented triangular prism, 10-4: gyroelongated square dipyramid, 10-7: sphenocorona, 12-6: triangular orthobicupola, 12-9: cuboctahedron, 13-1: augmented hexagonal prism, 13-2: observed in  $\chi$  phase, 14-1: rhombic dodecahedron, 15-6: Frank-Kasper CN15; index refers to entry in reference database implemented in BOPfox

The distribution of compounds with 1:1 composition (Fig. 2.7), one of the richest compositions with respect to the number and variety of compounds, presents a first insight into suitable order parameters for the structure maps. For the most frequently appearing compounds, boron reveals an oscillatory dependence on the corresponding d element and the resulting crystal structure, that follows  $\text{oP8-FeB} \rightarrow \text{oS8-TiB} \rightarrow \text{oP8-FeB} \rightarrow \text{oS8-TiB}$  for the 3d elements. 4d and 5d have only  $\text{oS8-TiB}$  and  $\text{tI16-MoB}$ .  $\text{oP8-FeB}$  and  $\text{oS8-TiB}$  appear also with aluminum, silicon, gallium and germanium, but far less frequent and shifted to the beginning of the d rows. These three compounds are also close in the Pettifor structure map (c.f. Fig. 2.3). One of the most important 1:1 compounds,  $\text{cF8-NaCl}$ , appears most frequently in the left of the d row with nitrogen or carbon, and to a lesser extent with oxygen. For the other p elements, the formation of these compounds is predominantly observed for manganese and yttrium. The appearance of the second-most important 1:1 compound,  $\text{cP2-CsCl}$ , is predominantly observed for early p elements with late d elements. Formation of  $\text{cP8-FeSi}$  is predominantly observed for silicon and germanium with d elements in the middle of the d-block. This compound competes with  $\text{oP8-FeAs}$ , that is formed with late d elements, and its appearance shifts to the left when going right in the p-block. This compound then competes with  $\text{hP4-NiAs}$ , that is formed with late and early d elements. The oscillatory dependence of compound formation on d elements is also observed for antimony. The compounds  $\text{cF8-ZnS}$  and  $\text{hP4-ZnO}$  are only found in the last d column. The distribution also shows that the first row p-block elements differ greatly from the remaining p elements with respect to the type of compound. The short overview of the distribution already highlights certain topics that have to be addressed with respect to the structure maps. First of all, the oscillatory dependence of compound formation on the d element is expected to occur also in the structure maps. Thus, a given compound might appear not only in one region of the structure map, but several separated regions. Ideally, these regions should be intersected by the compounds that also intersect in Fig. 2.7. Second, the distribution of some compounds appear somewhat arbitrarily, without a simple, intuitive rule of appearance. Separation into different regions for one and the same compounds might also have to be taken into account for these cases.

The 2:1 compounds appear to a lesser extent in the d-p systems (Fig. 2.8). Boron predominantly crystallizes in the  $\text{tI12-CuAl}_2$  structure, that is also found to a lesser extent for aluminum, silicon, gallium and germanium. This distribution is similar to the 1:1 compounds, as discussed above.  $\text{oP12-Co}_2\text{Si}$  appears predominantly for silicon, germanium and tin, and to a lesser extent for p elements to the left and right. This compound competes with  $\text{hP9-Fe}_2\text{P}$  that appears to the right for silicon, and appears more often in combination with phosphorus. The 1:2 compounds, on the contrary, crystallize in a larger number and variety than the 2:1 compounds. Boron favors to crystallize in  $\text{hP3-AlB}_2$ , predominantly with the early d elements. In contrast to the boron-containing 2:1 compounds, this structure is not adopted in combination with aluminum, silicon and germanium. Moreover, the tendency of adopting the same crystal structure is more pronounced for identical columns and to a far lesser extent for same rows. Exceptions are  $\text{cF12-CaF}_2$ ,  $\text{tI12-CuAl}_2$  and  $\text{cP12-FeS}_2$  that also appear in adjacent columns.  $\text{oP6-FeS}_2$  appears in close vicinity to  $\text{cP12-FeS}_2$ . We also note that some compounds may appear with reversed composition, e.g.  $\text{tI12-CuAl}_2$  that appear for both d:p ratios, 2:1 and 1:2.

## 2. Structure Maps

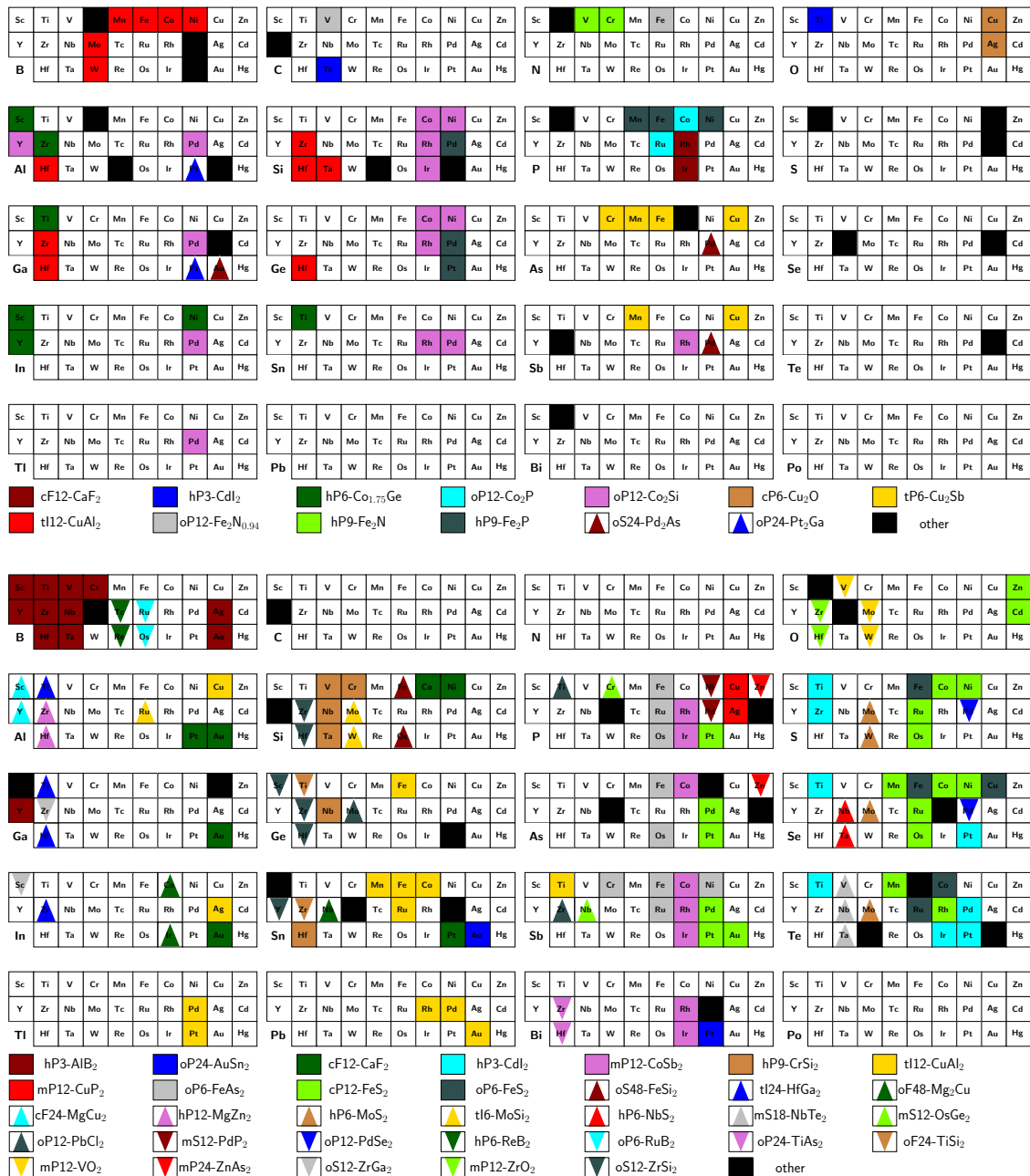


Figure 2.8.: Distribution of 2:1 (top) and 1:2 (bottom) compounds in the binary d-p systems. Structures that appear only once are marked as 'other'.

In summary, we discussed the distribution of the different compounds in the most important compositions 2:1, 1:1 and 1:2. Although we were able to highlight tendencies with respect to compound formation dependent of p and d element, none of these tendencies was thoroughly valid for all three compositions. This suggests that splitting the data might be necessary to

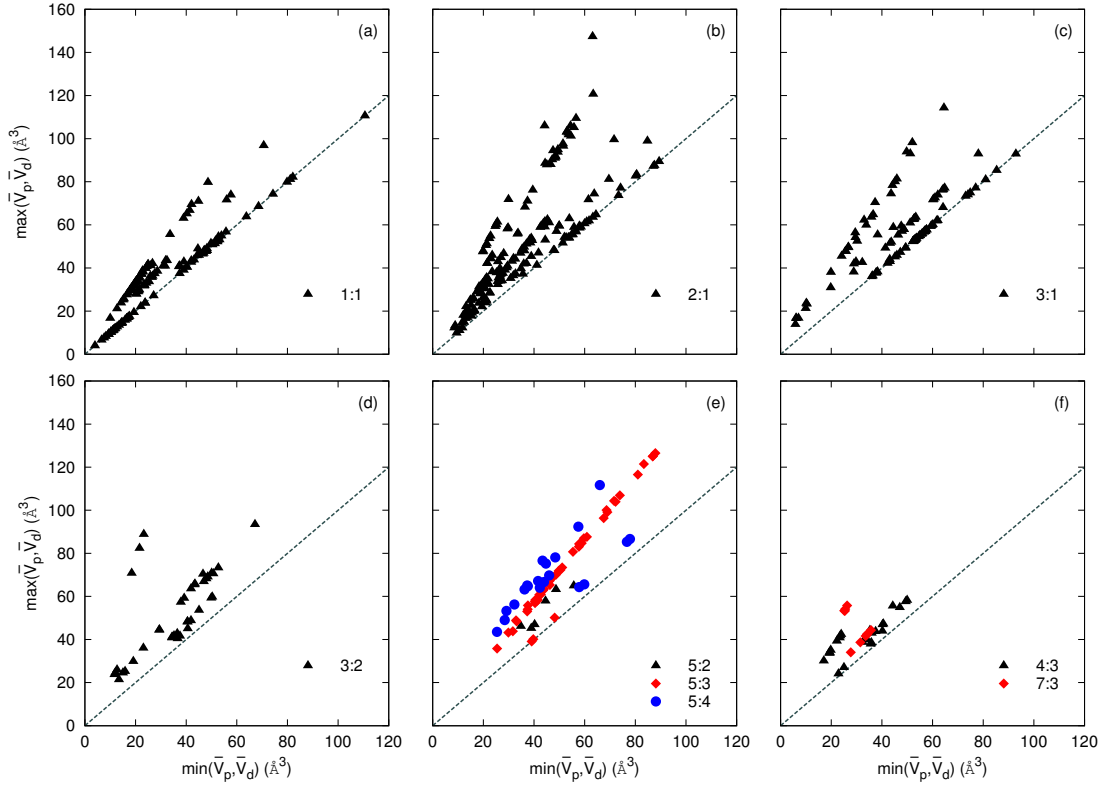


Figure 2.9.: Polyhedron volumes for p and d sites for common compositions: (a) 1:1, (b) 2:1, (c) 3:1, (d) 3:2, (e) 5:2,5:3,5:4, (f) 4:3,7:3. For compounds consisting of several p or d sites, the polyhedron volume is averaged.

produce structure maps with little overlap. We will address this question in the following sections.

### 2.3.2. Trends in Volume

As a first step, we analyzed the polyhedron volumes for the Wyckoff positions in the different crystal structures of the dataset. We differentiate between polyhedron volumes for the p and for the d sites. If a crystal structure has several Wyckoff positions occupied by a p or d element, respectively, we average the corresponding volumes. Instead of assigning the polyhedron volume of the d and p sites to the two axis, we rather use the minimum and maximum values of the two polyhedron volumes for the axis. This helps us to account for crystal structures where configurations also appear with swapped d and p elements, thus inverting the d:p ratio. An example is the  $\text{tl12-CuAl}_2$  compound, that appears for both a d:p ratio of 2:1 and 1:2, c.f. Fig. 2.8. Without using the minimum and maximum polyhedron volumes, configurations with swapped d and p sites would be mirrored with respect to the

identity.

Despite the number of different crystal structures, the polyhedron volumes of the p and d elements for the most common compositions (Fig. 2.9) align along only a few branches. Three distinct branches are found for the 1:1 composition (Fig. 2.9(a)), which are formed by thirteen different crystal structures. About five branches are identified for the 2:1 composition (Fig. 2.9(b)). Three branches are found for the compositions 3:1 (Fig. 2.9(c)), 3:2 (Fig. 2.9(d)) and 5:2, 5:3 and 5:4 (Fig. 2.9(e)). Only two branches are observed for the compositions 4:3 and 7:3 (Fig. 2.9(f)).

### 2.3.3. Trends in Coordination Number

Furthermore, we investigated potential tendencies in the coordination number for each of the considered p elements. In spite of the various crystal structures the d-p systems tend to crystallize in, an analysis of the coordination number might reveal the favorite coordination numbers for the specific p elements. This might already indicate why specific crystal structures and compositions only appear for some of the p elements. Furthermore, such an approach might reveal tendencies associated with the alloyed d element, and possibly the number of valence electrons of the d element.

We first investigated the distribution of the coordination numbers among the Wyckoff sites that are occupied by either the d or p element, and separate the histograms according to the p element (Fig. 2.10). We note that a separation according to the d element significantly reduces the information value of the histograms. We explicitly take into account all Wyckoff sites, and at this point we do not average over the d- and p-occupied Wyckoff sites. The appearance is normalized with respect to the total number of Wyckoff positions that are occupied by p or d elements, respectively.

The first row of the p-block in the periodic table is much more restrictive with respect to the coordination number than the remaining elements. Among the first row elements, nitrogen stands out due to its restriction to be only six-fold coordinated. Boron is less restrictive, but clearly favors to be nine-fold coordinated, while carbon prefers to be six-fold coordinated, although both elements allow other coordination numbers. The peak of nine-fold coordination for boron is due to the 1:1 compounds oP8-FeB, oS8-TiI and tI16-MoB that are observed in a number of TM-B systems (Fig. 2.7). The same compounds are responsible for the thirteen-fold peak for the transition metals. Also hP3-AlB<sub>2</sub> contributes to the nine-fold peak for the boron sites. The peaks for six-fold coordination for both carbon and nitrogen in the p and d sites is mainly attributed to the 1:1 compounds cF8-NaCl and hP2-WC. Oxygen does not clearly exhibit a favorite coordination number, the distribution is flattened compared to the other first row elements. This distribution should be attributed to the complex oxygen-rich phases in the Ti-O, V-O and Mo-O system, that have relative large, predominantly monoclinic or triclinic unit cells with a large number of Wyckoff sites with small multiplicities. Comparing the corresponding coordination numbers of the transition metals reveals the tendency to reduce



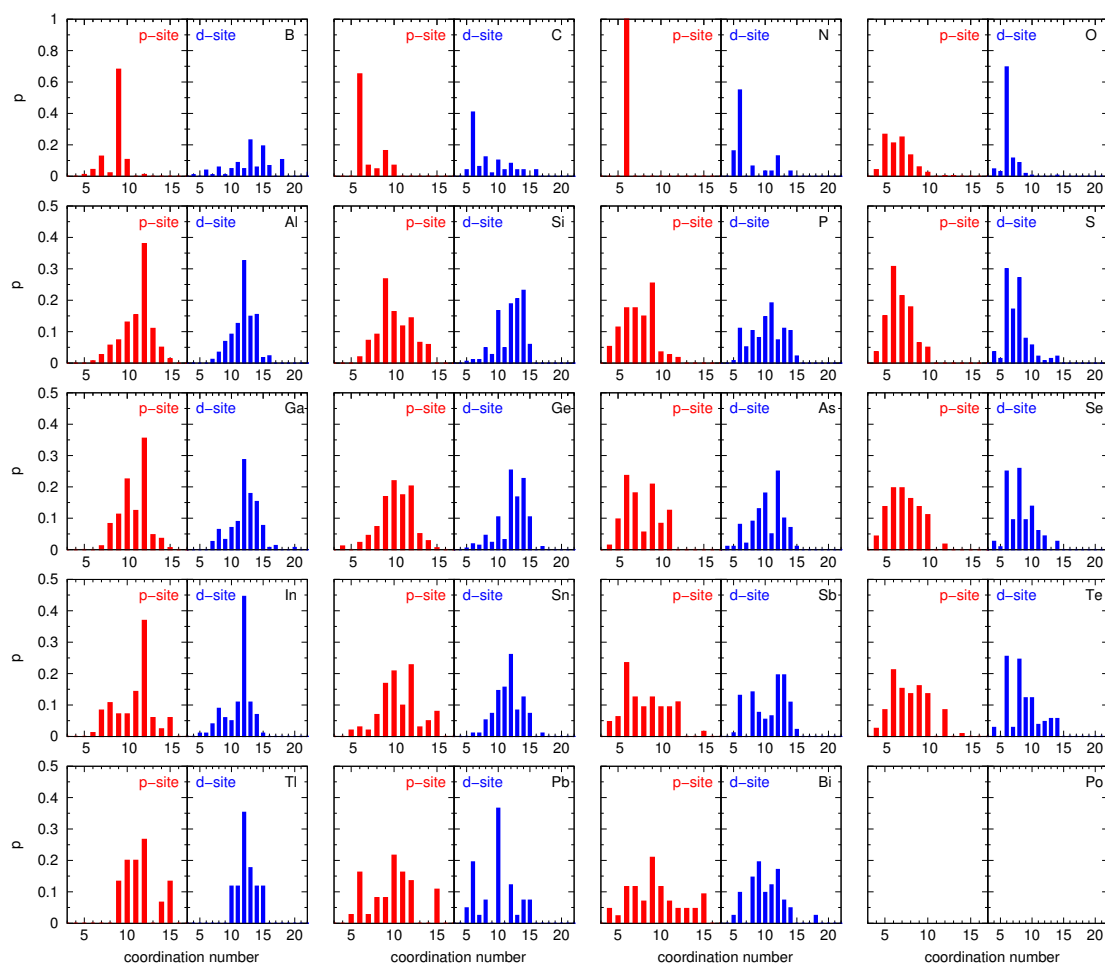


Figure 2.10.: Distribution of coordination numbers for all Wyckoff sites in the crystal structures, separated for the sites occupied by d and p elements. All values are normalized with respect to the number of Wyckoff sites. Polonium is omitted as [193] lists no phase diagram.

the coordination number with increasing number of valence electrons of the p-block element, as expected.

Elements in the second, third and fourth row of the p-block behave differently to the first row elements. The distribution of the coordination numbers is smeared out, although in most cases a favorite coordination number can be identified. Aluminum, gallium and indium exhibit a peak for twelve-fold coordination for both the p and d sites. Thallium in the fifth row resembles this tendency to a lesser extent. As expected, for the remaining elements in the second, third and fourth row, the coordination numbers and the relative appearance for both p and d sites tend to decrease with increasing number of valence electrons of the p-block elements. Sulfur, selenium and tellurium clearly favor six-fold coordination for the p sites, while for the d sites

both the six-fold and eight-fold coordination is favored.

The p-block elements of the fifth row do not show comparable tendencies in the coordination number. However, for these elements only a handful of phase diagrams are available [193], thus due to a lack of sufficient data points no evaluation can be given. Compound formation with thallium is only found for yttrium, palladium and platinum. Lead forms compounds with scandium, yttrium, zirconium, rhodium, palladium, platinum and gold. Bismuth forms compounds with titanium, manganese, nickel, yttrium, zirconium, rhodium, palladium, hafnium, iridium and platinum. Polonium has been omitted because no phase diagrams are listed for this element in [193].

We further compared the relationship between the global compound composition with the local composition that is found in the different coordination polyhedra for the p and d Wyckoff sites. Here, the term global compound composition refers to the normalized p content in the compound, while the term local composition refers to the normalized p content in the coordination polyhedron, that surrounds the d or p Wyckoff site, respectively. For the first row p-block elements (Fig. 2.11), the coordination polyhedra for the d sites in binary d-p compounds containing boron generally tend to resemble the global composition. However, some deviations are observed in the middle of the transition metal block for boron-rich compounds. On the contrary, the p site polyhedra have generally a much lower local composition compared to the global value. For carbon a different tendency is observed, as the compounds in the TM-C systems generally tend to ignore the global composition, and the p and d sites are mostly surrounded by d and p elements, respectively. This is due to the preference of cF8-NaCl and hP2-WC, which have the same, six-fold coordinated polyhedra for both the p and d sites. The restrictive nature of nitrogen, that prefers to be surrounded by six atoms, is also illustrated by the fact that none of the atoms in the coordination polyhedra may be nitrogen atoms. With increasing number of d electrons of the transition metal, the overall appearance of stable d-p compounds shifts from 1:1 composition (in general cF8-NaCl) to the transition metal-rich end. This is further accompanied by the tendency of d sites to resemble the global composition locally. For oxygen, the tendency of the d sites to resemble the global composition locally is shifted to the right of the transition metal block. Systems to the left tend to deviate stronger from the global composition, an exception being Cu-O and Ag-O.

The relationship between the global and local composition is different for the second row p-block elements. We will restrict the further discussion to the second row elements aluminum, silicon, phosphorus and sulfur, but the overall tendencies in the relationship between the global and local composition are also valid for the later p-block elements. We refer to Fig. 2.10, where we compiled the distribution of the coordination numbers for the p and d Wyckoff sites, respectively. In these histograms, very similar tendencies in the distribution have been observed for the second, third and fourth row elements. With regard to the relationship between the global and local composition, we find that compounds containing aluminum generally tend to mimic the global composition also locally. However, the d sites have usually a slightly larger local composition, while the p sites have a slightly smaller local composition. Sites with d and p elements, that are only surrounded by the other elements, are found for p sites at low p content and d sites for large p contents. Silicon shows the same tendency of the d sites to mimic the

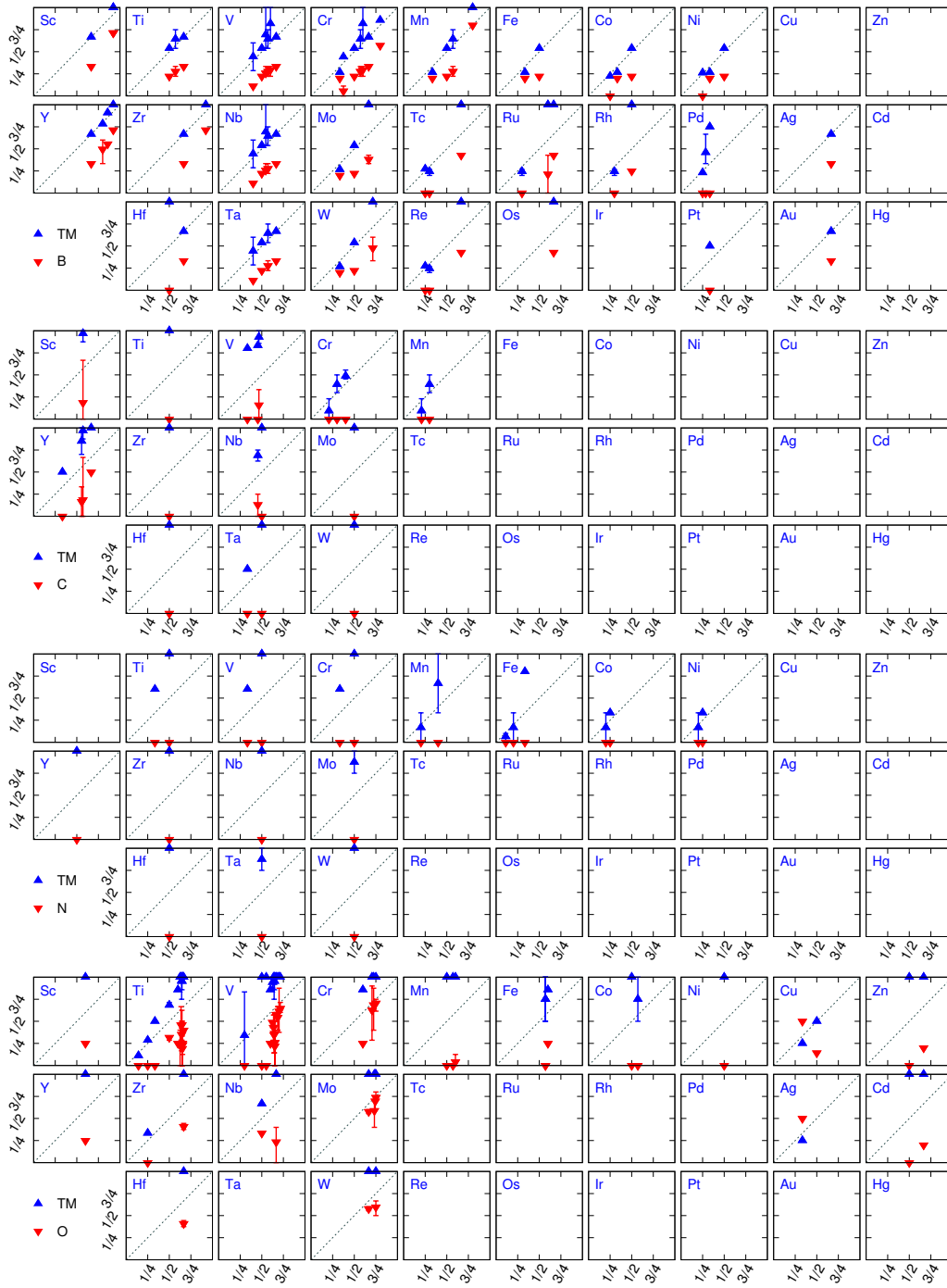


Figure 2.11.: Global versus local composition of binary d-p compounds with B/C/N/O. Error bars indicate the variation in the composition if several Wyckoff sites are occupied by d or p elements, respectively.

## 2. Structure Maps

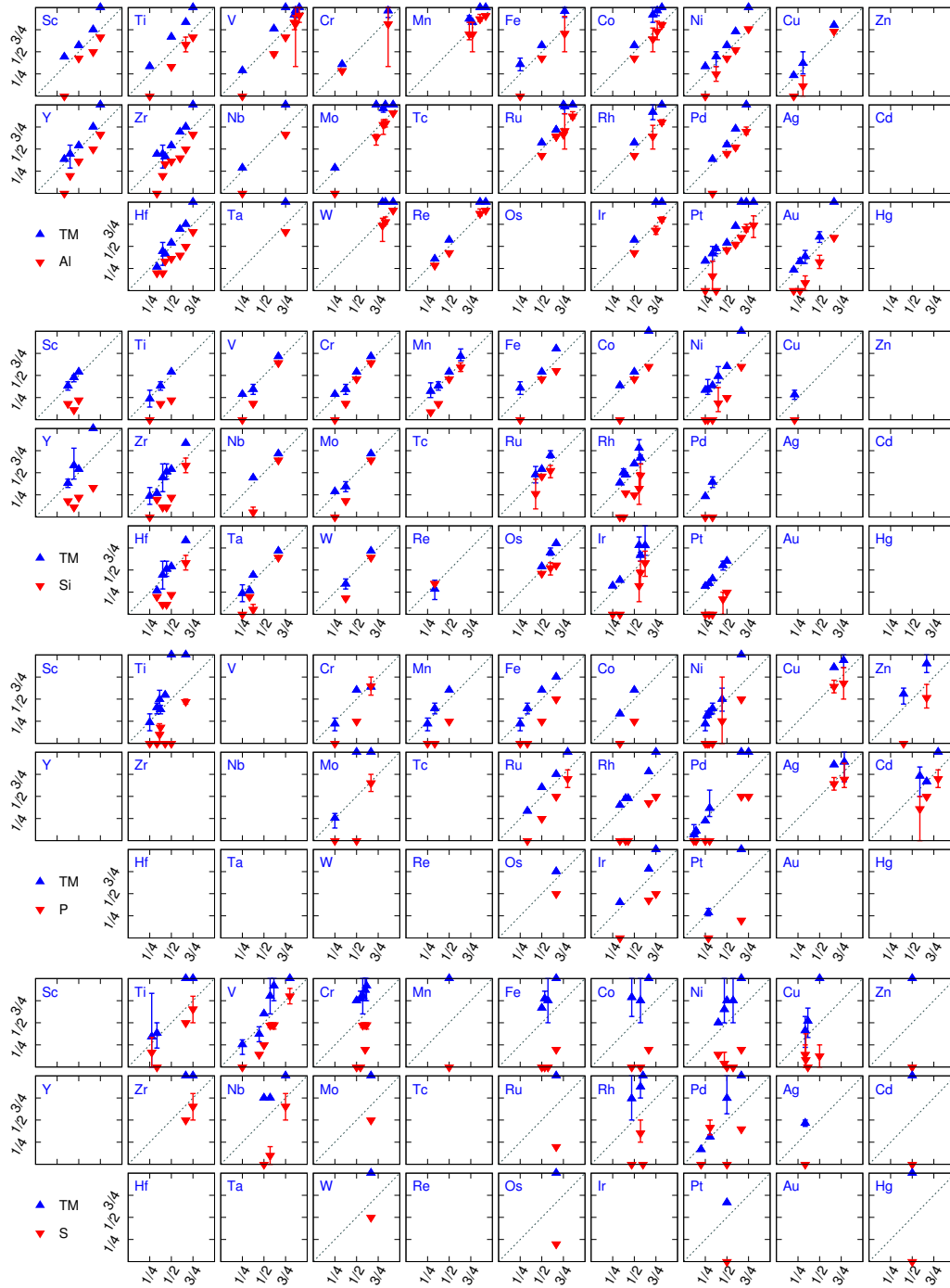


Figure 2.12.: Global versus local composition of binary d-p compounds with Al/Si/P/S. Error bars indicate the variation in the composition if several Wyckoff sites are occupied by d or p elements, respectively.

global composition locally, but the composition of the p sites is shifted downwards. Much of the overall tendencies are in line with boron. For phosphorus and sulfur, the appearance of p sites that are only surrounded by d elements are shifted to larger p contents. Similarly, the appearance of d sites being only surrounded by p elements are shifted to lower p contents. This effect is stronger for sulfur than for phosphorus. This is in line with the histogram of the distribution of coordination numbers (Fig. 2.10). Later p-block elements show the tendency to favor smaller coordination numbers, and it is more likely to have a polyhedron that comprises only the other element for lower coordination numbers. Phosphorus is more restrictive with regard to the d sites. Here, the global composition is often in line with the local composition. Sulfur is less restrictive in this case.

In summary, the analysis of the relationship between the global and local composition for both the p and d sites dependent on the p concentration reveals a few distinct features. First of all, the overall different chemical behavior of the first row p-block elements compared to the later ones becomes also apparent in the relationships between the global and local composition. Carbon and nitrogen usually prefer to have p and d sites that are surrounded only by the other element. Oxygen behaves similar to a certain degree. However, the tendencies are different in the oxygen-rich compounds in the Ti-O, V-O and Mo-O systems. Boron, on the other hand, shows a few features that are also observed for the second row p-block elements: the d sites tend to mimic the global composition, p sites have usually a smaller p content, and p (d) sites that are surrounded only by the other elements are for low (high) p contents. Aluminum is by far the most restrictive element that prefers to have the global composition locally. Silicon resembles boron with respect to the relationship between the global and local composition for the d and respective p sites. Phosphorus and sulfur shift the appearance of p (d) sites that are surrounded by the other elements to higher (lower) p contents. Many of the observed tendencies are in line with trends that have been observed and discussed with regard to the distribution of the coordination numbers for the p and d sites, respectively (Fig. 2.10).

#### 2.3.4. New Order Parameters

In the previous sections we discussed trends regarding the polyhedron volumes and the composition of the coordination polyhedra that were obtained with a polyhedron analysis. These results allowed also the introduction of new order parameters for our structure maps that explicitly take into account information of the local environment of each Wyckoff site, as provided by the polyhedron analysis. By taking into account both atomic and compound-related properties, our approach represents to some extent a link between previous approaches for structure maps that used solely atomic properties (c.f. Tab. 2.1 in Sec. 2.2.1) and the discussion of the crystal structures in terms of the coordination polyhedra by Daams, Villars and co-workers (c.f. Sec. 2.2.3). In our search for suitable order parameters that provide good structural separation in the structure maps, we tested a set of tabulated or derived atomic and compound-related properties, the latter obtained from the polyhedron analysis. As a result, we identified a volumetric factor and a factor dependent on the electronic configuration as suitable order parameters for the polyhedra-based structure maps. Both parameters depend

## 2. Structure Maps

---

on atomic and compound-related properties. The volumetric factor  $f_V$  is defined as

$$f_V = \frac{1}{2} \left( \frac{\bar{V}_p^{\text{ph}}}{V_p^{\text{gs}}} + \frac{\bar{V}_d^{\text{ph}}}{V_d^{\text{gs}}} \right) \quad (2.1)$$

with

$$\bar{V}_i^{\text{ph}} = \frac{1}{N_{\text{Wyckoff}}} \sum_{j=1}^{N_{\text{Wyckoff}}} V_{i,j}^{\text{ph}}, \quad i \in (p, d) \quad (2.2)$$

as averaged polyhedron (ph) volume of the coordination polyhedra of the Wyckoff sites occupied by p and d elements, respectively. We used the averaged polyhedron volume, as the compounds differ in the number of Wyckoff sites. Without averaging, by taking into account the number of different Wyckoff sites that are occupied by a p or d element, respectively, more complex compounds are expected to be automatically separated from the simpler compounds.  $V_i^{\text{gs}}$  is the atomic volume of the constituent p or d element in its respective ground state (gs), taken from Ref. [191]. Thus, the factor  $f_V$  represents a measurement for the deviation of the atomic volumes obtained in the respective crystal structures and the ground states. The factor 1/2 is introduced for normalization, so that perfect agreement between atomic and polyhedron volume for both p and d elements results in the identity. The second factor is dependent on the electronic configuration of the constituent elements. The electronegativity values of the p elements are generally larger than for the d elements, i.e. it is more likely that the p elements gain electrons from the d elements. Therefore, we choose a factor that depends on the number of valence electrons for the d elements, but on the number of holes in the sp-band for the p elements. This factor is defined as

$$f'_N = \frac{\bar{N}_d}{\bar{N}_p} \quad (2.3)$$

with

$$\bar{N}_i = \frac{1}{N_{\text{Wyckoff}}} \sum_{j=1}^{N_{\text{Wyckoff}}} n_{ij}^d N^d + n_{ij}^p (8 - N^p), \quad i \in (p, d). \quad (2.4)$$

$n_{ij}^{p/d}$  is the number of p or d elements, respectively, that are present in the coordination polyhedron.  $N^{p/d}$  is the number of valence electrons in the corresponding sd/sp-band of the d or p element, respectively. Thus, the factor  $f_N$  measures the difference in the electronic configurations, given by the number of d and p elements that form the coordination polyhedron and their respective number of valence electrons in the sp/sd-band, that are present at the d and p sites in the crystal structures. Again, we include the number of Wyckoff sites in  $\bar{N}_i$  to account for the complexity of each compound. We further reduce the range of the parameter  $f_N$  by defining

$$f_N = \min (f'_N, 1/f'_N) = \min \left( \frac{\bar{N}_d}{\bar{N}_p}, \frac{\bar{N}_p}{\bar{N}_d} \right). \quad (2.5)$$

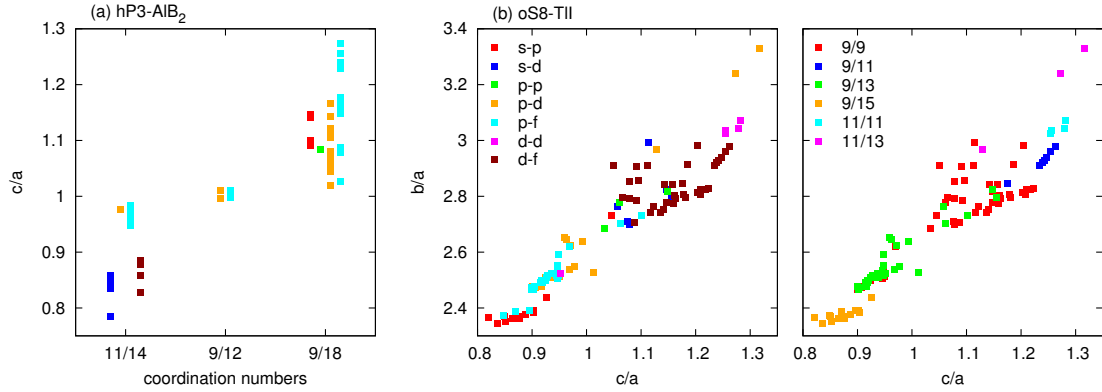


Figure 2.13.: Variation of the axis ratios of (a) hP3-AlB<sub>2</sub> and (b) oS8-TlI for different chemical systems and influence on the coordination number.

This restriction is not mandatory but is helpful to account for crystal structures where the p and d Wyckoff sites are swapped. Examples are the NiAs-type that crystallizes in the Rh-B system, which has swapped p and d Wyckoff sites compared to other systems, and the tI12-CuAl<sub>2</sub> prototype that appears for both 2:1 and 1:2 d:p ratios (c.f. Fig. 2.8).

The equations for the volumetric and electronic factor, as presented in Eqs. 2.1, 2.4 and 2.5, are valid for the binary case. However, the extension of these equations to ternary d-d-p or d-p-p systems that adopt binary crystal structures, the pseudobinaries, is straightforward. In the volumetric factor (Eq. 2.1), the ground state volumes  $V_{p/d}^{gs}$  are replaced by weighted volumes, calculated from the ground state volumes of the mixing d or p elements and their respective concentration in the pseudobinary. The mixing of two different d or p elements is already accounted for in the polyhedron volumes. In the electronic factor, the appearance of two different elements splits the factor  $n_{ij}^{p/d}$  into two contributions, and the magnitude of each contribution depends on the concentration of the mixing elements at each Wyckoff site that is part of the coordination polyhedron.

The order parameters introduced in this section depend explicitly on atomic and compound-related properties. Approaches with only atomic-dependent order parameters are briefly discussed in Sec. A.1 of the appendix.

### 2.3.5. Restriction to the d-p System

In our investigation, we only considered compounds that are observed in the d-p system. However, our approach of analyzing the local environment of each compound and using this information to calculate the order parameters we have introduced in Sec. 2.3.4 is not restricted to the d-p system only. In principle, this approach is applicable to any given chemical system, e.g. s-s or s-p.

## 2. Structure Maps

---

However, there are two reasons why we restrict the investigation to the d-p system. First, some crystal structures may only appear in a specific chemical system. If we consider all chemical systems, these crystal structures might appear in lesser number than other compounds that are observed in different chemical systems. In view of our approach of considering only these compounds whose number of appearance is above a certain limit, some compounds we considered in our investigation of the d-p system might not be considered if we take into account additional chemical systems. Second and far more important, crystal structures that appear in different chemical systems still maintain the Bravais lattice and symmetry group. However, the atomic positions and axis ratios of the lattice might be significantly altered in different chemical systems. Obviously, this will affect the coordination number and therefore the coordination polyhedron.

In order to investigate the variation of the coordination numbers dependent on chemical system and lattice parameters, we discuss two exemplary crystal structures that appear in various chemical systems: hP3-AlB<sub>2</sub> and oS8-TiI. Both crystal structures are relatively simple builds, with only two Wyckoff sites each. hP3-AlB<sub>2</sub> (Fig. 2.13(a)) is hexagonal, thus the  $c/a$  ratio is the only degree of freedom. The observe a strict dependence of the coordination number on the  $c/a$  ratio: 9/12 for both Wyckoff sites are observed in compounds with a  $c/a$  ratio close to one, 11/14 and 9/18 are only observed in compounds with a  $c/a$  ratio below and above one, respectively. The chemical systems s-p, s-d, p-p and d-f appear only with a specific  $c/a$  ratio: s-d and d-f are only observed for a  $c/a$  ratio below one, while s-p and p-p have a  $c/a$  ratio above one. p-f and p-d, in contrast, show  $c/a$  ratios above, below and close to one. Two entries for the p-d system, Fe-B and W-B, show a  $c/a$  ratio close to one. However, both entries are not considered in our investigation, as both compounds listed in [178] are not included in the experimental phase diagrams in [193]. The single p-d entry for a  $c/a$  ratio below one belongs to the Ga-Y system. Entries for a  $c/a$  ratio above one contain essentially boron. For oS8-TiI (Fig. 2.13(b)), the  $b/a$  ratio correlates well with the  $c/a$  ratio. The chemical systems s-p and p-f are concentrated at low axis ratios and have in general the coordination numbers 9/9,13,15. s-d, p-p and d-f and are mainly concentrated in the center of the diagram, while d-d is shifted to larger axis ratios. The chemical systems in the center of the diagram have the coordination numbers 9/9,13, a few of the d-f entries that are shifted to slightly larger axis ratios and contain mainly gold have the coordination numbers 9/11. The d-d entries, placed in a confined region close to the latter d-f entries, have only the coordination numbers 11/11. Entries for the p-d system are located in general close to the p-f system with the coordination numbers 9/13. However, the aluminum-containing compounds have significantly larger axis ratios, and the coordination numbers are changed to 11/13. We note that for oS8-TiI the coordination numbers correlate stronger with the axis ratios than the chemical system. Apart from 9/9 and 9/13 which usually mix, the specific coordination numbers are located in very confined domains.

In our discussion of two exemplary compounds, hP3-AlB<sub>2</sub> and oS8-TiI, that appear in various chemical systems we outlined the reasons why we restricted our investigation to one specific chemical system. The variation in the atomic positions and the lattice parameters dependent on chemical system influence the coordination numbers and therefore the coordination polyhedra. Thus, we expect an increased variation in the order parameters. Hence, the overlap between



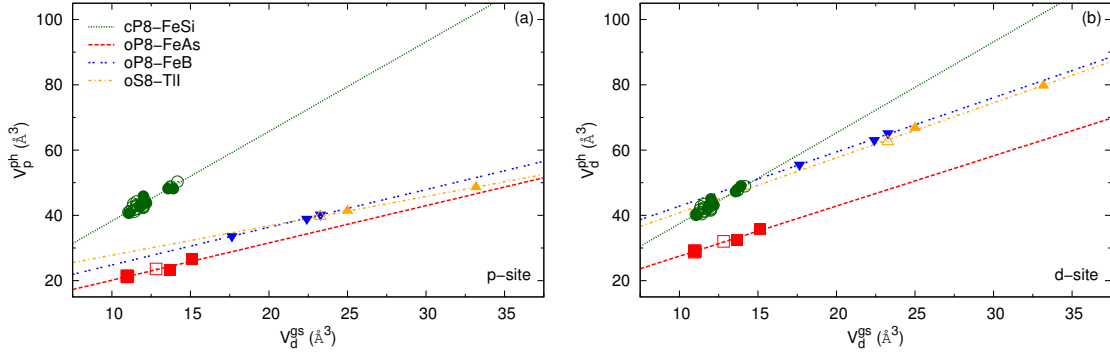


Figure 2.14.: Correlation between d ground state volume and polyhedron volumes for the (a) p- and (b) d-sites in the d-Si systems. Filled symbols represent binaries, open symbols represent pseudobinaries with mixed d sites.

different crystal structures is expected to increase when considering different chemical systems in the same structure map.

We further note that variation of the coordination numbers in the same chemical system, as observed for hP3-AlB<sub>2</sub> and oS8-TiI, appears in the clear minority of compounds we have considered in our investigation. For the majority of compounds, the coordination numbers are constant in the various d-p systems.

### 2.3.6. Estimation of Polyhedron Volumes

In Sec. 2.3.4 we introduced the order parameters that we used in the structure maps for d-p systems. However, the usage of compound-related properties in our definition of the order parameters, namely the polyhedron volume of the p- and d-sites that is required for  $f_V$  (Eq. 2.1), reduces the predictive ability of our structure maps, as the polyhedron volume of compounds in systems that do not adopt the crystal structure is unknown. We note that the electronic factor  $f_N$  (Eq. 2.5) can be calculated for these systems.

Here, we propose an approach to estimate the polyhedron volume of compounds for systems that do not adopt this crystal structure. As an example, we discuss the d-Si system at 1:1 composition that lists four compounds: cP8-FeSi, oP8-FeAs, oP8-FeB and oS8-TiI. Investigating the polyhedron volumes for the p- and d-sites of the binaries and pseudobinaries that have mixed d sites shows an approximately linear correlation between the ground state volume of the d element and the polyhedron volume. Thus, we are able to interpolate/extrapolate the polyhedron volumes for both the p- and d-site from the ground state volume of the d element that is listed in Ref. [191]. With the estimated value for the polyhedron volumes, we are able to calculate  $f_V$  and therefore the location of the compound in the structure map. We demonstrate this procedure in Sec. A.2.

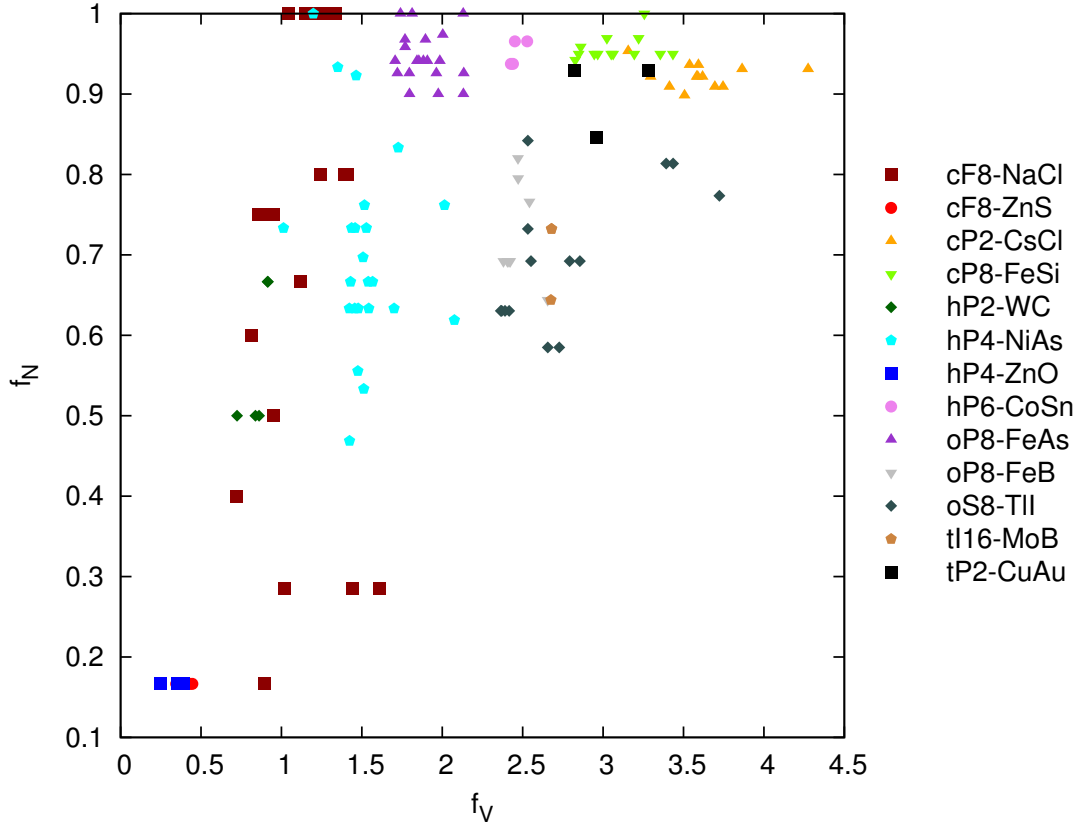


Figure 2.15.: Structure map for 1:1 composition.

### 2.3.7. Binary Structure Maps

**1:1 Composition** With the aforementioned order parameters we compiled the structure map for 1:1 composition given in Fig. 2.15. The accessible number of entries due to the separation of the data set according to the global composition allows the usage of Eq. 2.5 instead of Eq. 2.3 without sacrificing the overall good structural separation. Another advantage is the ability to account for compounds which may appear with swapped Wyckoff positions for the p and d elements, respectively. The most apparent feature of the structure map is the blank area for large values of  $f_V$  and small values of  $f_N$ , i.e. for large mismatches in the volumetric or electronic factor. This indicates that the compounds may allow either for large mismatches in the volumes for the Wyckoff positions with respect to the ground state volume or for large mismatches in the number of electrons and holes, respectively, between the d and p Wyckoff sites. Compounds consisting of polyhedra with low coordination numbers are located in the low  $f_V$  range, and the increase in  $f_V$  is accompanied by an increase in the coordination number of the corresponding polyhedra.

The two most important 1:1 compounds, cF8-NaCl and cP2-CsCl, are located in different regions of the structure map. cF8-NaCl is bounded by hP2-WC to the left and by hP4-NiAs to

the right. In both cases, the border between the structures is not a straight line, but shows an oscillatory dependence on the volumetric and electronic factor. oP8-FeAs to the top right of hP4-NiAs is located in a very confined region, with a small hP6-CoSn region to its right. Below is the oP8-FeB, oS8-TiI and tI16-MoB region. The Wyckoff sites of the three structure have polyhedra with the same coordination number and composition. oS8-TiI and tI16-MoB are also built of the same coordination polyhedra (c.f. Fig. 2.6). The close geometrical relationships of these structures were already described elsewhere [204]. This can account for the close alignment of the three structures in the structure map. However, for the identical electronic factor, oS8-TiI is shifted towards lower volumetric factors, while tI16-MoB is shifted to higher volumetric factors. The three deviating oS8-TiI are due to aluminum, that significantly alters the coordination number of the smaller polyhedron. To the right of hP6-CoSn is the also confined cP8-FeSi region. tP2-CuAu is represented by few data points that are distributed in the structure map with negligible overlap with other regions. hP4-ZnO and cF8-ZnS, on the contrary, are located in a very confined region and overlap significantly. This is attributed to the same coordination polyhedron both structures are built of (c.f. Fig. 2.6).

We further investigated the ability of the order parameters to account for defect structures. Focusing on crystal structures that appear at least twice in the different d-p systems as defect structures at ambient temperature, we checked cF8-NaCl, hP4-NiAs and tP2-CuAu. cF8-NaCl ( $\text{Pd}_{0.163}\text{B}_{0.88}\text{VC}_{0.33}\text{YC}_{0.33}$ ) and hP4-NiAs ( $\text{Co}_{0.88}\text{S}_{0.88}\text{CoSe}_{0.88}\text{Ta}_{0.45}\text{Hf}_{0.67}\text{Te}_{0.8}\text{Ni}_{0.8}\text{Te}_{0.67}\text{Zr}_{0.67}\text{Te}$ ) appear only as defect structures with imperfect occupation of one of the Wyckoff sites. On the contrary, defect structures of tP2-CuAu-type ( $\text{Hg}_{0.7}\text{Pb}_{1.3}\text{Mn}_{1.33}\text{Ga}_{0.67}\text{Zr}_{1.33}\text{In}_{0.67}$ ) contain Wyckoff sites that are occupied by both p and d elements, which results in the fractional occupancy of these Wyckoff sites. Defect structures that appear at high temperatures were excluded. Here, the appearance of defects is expected to be strongly influenced by the temperature. We do not expect the chosen order parameters to be able to account for these effects.

The structure map containing defect structures is shown in Fig. 2.16. Open symbols denote the position if perfect occupation is assumed. The shift in the position due to fractional occupancy is indicated by lines. Some of the aforementioned compounds are also listed with perfect occupation, thus we can account for changes in the volumetric factor due to introduction of defects. However, corresponding values are missing for the majority of the considered defect structures, but the structure map containing defect structures shows that the volumetric factor is only slightly affected. Thus, for defect structures without the volume for perfect occupation, we simply assume that the volumetric factor is not affected.

For cF8-NaCl, the point for  $\text{YC}_{0.33}$  that is located in the hP4-NiAs region, if perfect occupancy is assumed, is shifted to the lower boundary, just outside the region. The remaining two points are placed in the vicinity of other NaCl-type points, if perfect occupancy is assumed, but the shift places both again in the vicinity of other NaCl-type points. For hP4-NiAs, the two points in the top left corner ( $\text{Hf}_{0.67}\text{Te}_{0.67}\text{Zr}_{0.67}\text{Te}$ ) are shifted away from the cF8-NaCl region and closer to other NiAs-type points. The three points in the region below are shifted closer to the center of the hP4-NiAs region. The remaining point ( $\text{Ta}_{0.45}\text{N}$ ) that is placed between the hP2-WC and cF8-NaCl region, if perfect occupancy is assumed, is shifted downwards, away

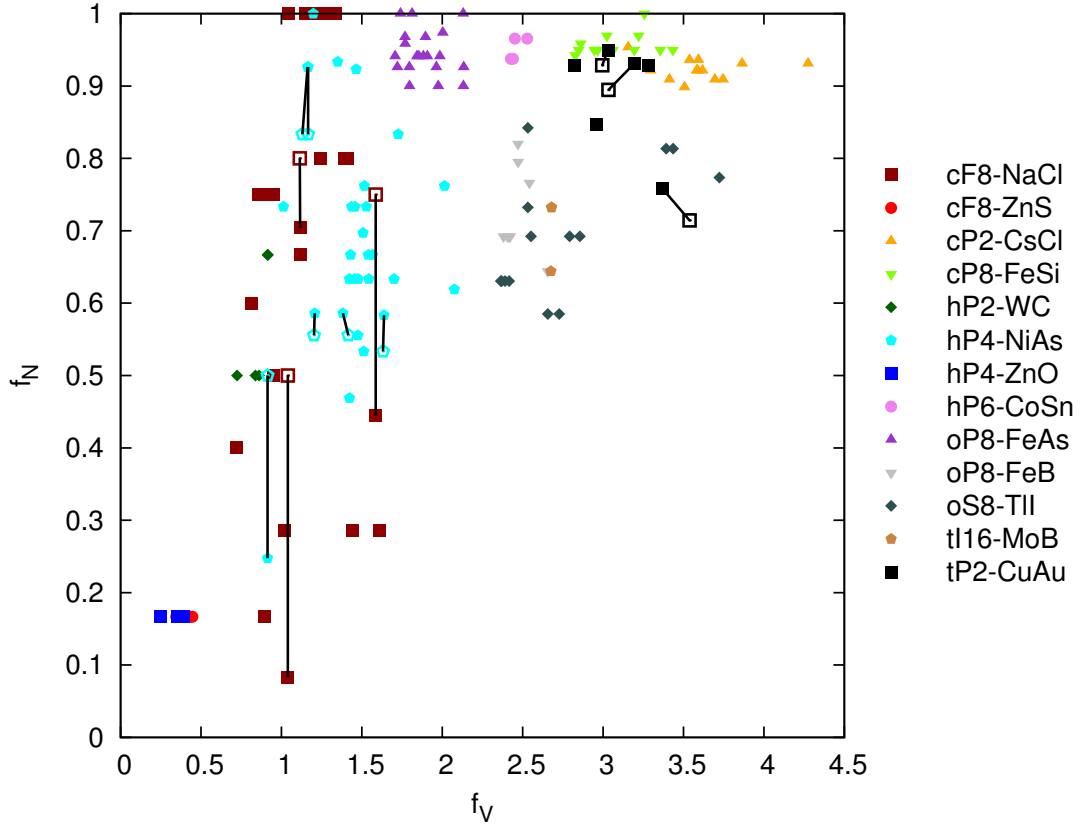


Figure 2.16.: Structure map for 1:1 composition explicitly including defect structures shown by filled symbols. Open symbols denote the position in the structure map if perfect occupation is assumed. The shift in position by taking into account the fractional occupancy is indicated by a line.

from the hP4-NiAs region. However, similar to Rh-B the occupation of the Wyckoff sites for Ta-N is swapped with respect to the majority of NiAs-type compounds. This may explain why this point is explicitly located in a different region. Furthermore, the placement at this point does not overlap with other regions. For tP2-CuAu, the inclusion of the fractional occupancy shifts the electronic parameter of the structures upwards. The volumetric parameter takes into account the modified ground state volume, that is weighted according to the fraction of p and d elements. This leads to the placement of one of the points in the cP2-CsCl region. However, given the number of considered defect structures and the overall success in placing these structures in the structure map suggests that the chosen order parameters are indeed suitable and well-chosen.

**2:1/1:2 Compositions** The order parameters Eq. 2.1 and 2.5 resulted in overlapping regions of appearance if d-rich and p-rich compounds are plotted in the same diagram. Therefore, we separated the structure maps, plotting each for a d:p ratio of 2:1 and 1:2.

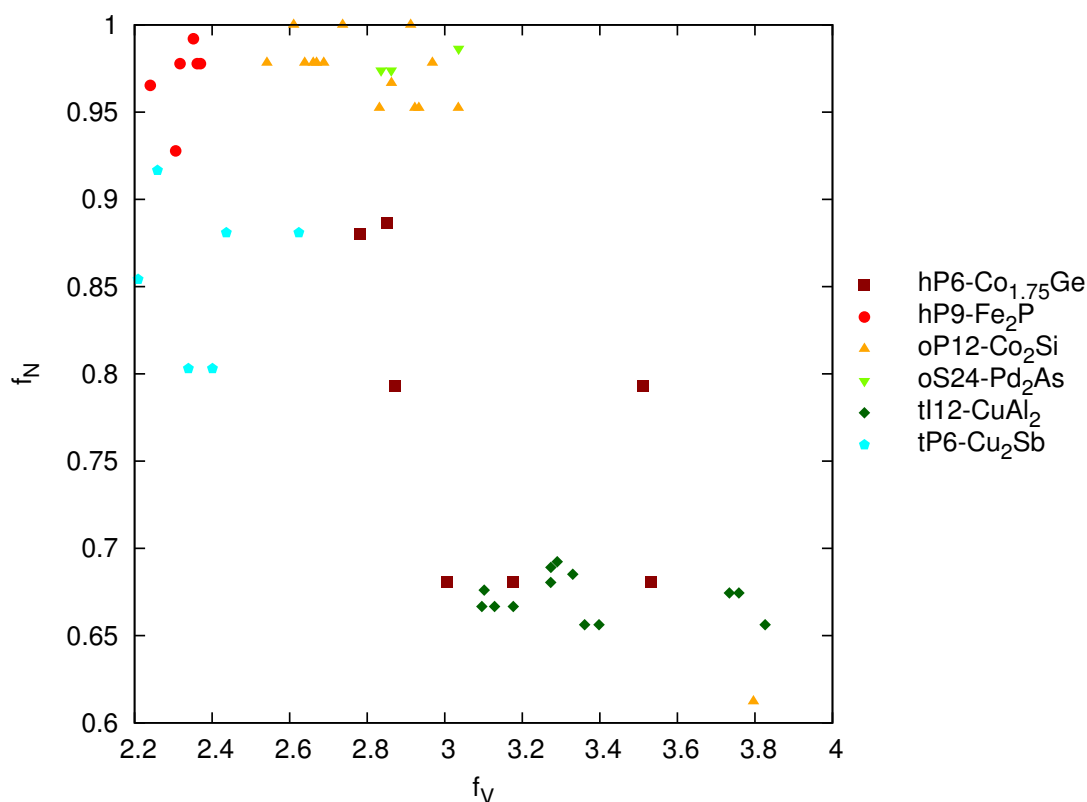


Figure 2.17.: Structure map for a d:p ratio of 2:1.

The discussion of the distribution of d-rich and p-rich 2:1 compounds in Fig. 2.8 revealed the preferred appearance of 2:1 compounds in the p-rich region. Thus, the structure map for d-rich compounds of 2:1 composition (Fig. 2.17) presents only a few entries. Note also the significantly reduced range for both the volumetric and electronic factor compared to the 1:1 structure map. Nevertheless, the overall structural separation is excellent. hP9-Fe<sub>2</sub>P, tP6-Cu<sub>2</sub>Sb and hP6-Co<sub>1.75</sub>Ge are located in well defined regions. The lower boundary of the hP6-Co<sub>1.75</sub>Ge region is close to the tl12-CuAl<sub>2</sub> region, but this is due to the appearance of both compounds for aluminum and gallium in combination with early transition metals (Fig. 2.8). oP12-Co<sub>2</sub>Si is intersected by oS24-Pd<sub>2</sub>As. The reason for that is not apparent from Fig. 2.8. The deviating oP12-Co<sub>2</sub>Si point is due to the appearance of this compound in the Y-Al system. Formation of this compound is predominantly observed for late transition metals.

The corresponding structure map for the p-rich compounds reveals overall good structural separation (Fig. 2.18). There are a few regions with some overlap, however this lack of separation is predominantly due to close geometric relationships between crystal structures that appear in the same region. Both FeS<sub>2</sub> compounds, cP12 and oP6, are built of the same coordination polyhedra (c.f. Fig. 2.6). The same holds for tl12-CuAl<sub>2</sub> and oF48-Mg<sub>2</sub>Cu. mS18-NbTe<sub>2</sub> has the same coordination numbers, but one of the polyhedra differs. Identical coordination polyhedra are also found for tl6-MoSi<sub>2</sub>, hP9-CrSi<sub>2</sub> and oF24-TiSi<sub>2</sub>. This accounts

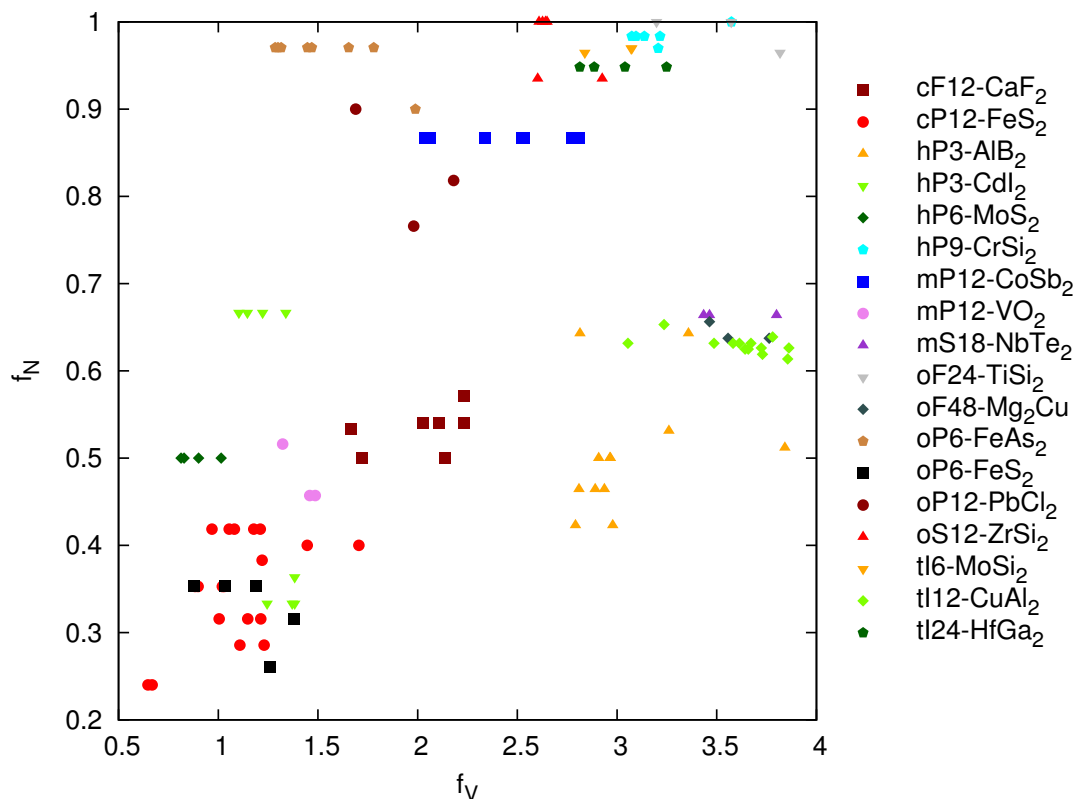


Figure 2.18.: Structure map for a d:p ratio of 1:2.

for the close appearance and minor overlap. The appearance of the two isolated hP3-AlB<sub>2</sub> is due to formation of these compounds for boron with late transition metals. Usually these compounds prefer early transition metals (Fig. 2.8). Separation of hP3-CdI<sub>2</sub> in two distinct regions, one encapsulated by the FeS<sub>2</sub> compounds, is due to formation of this compound for early and late transition metals with p elements from the oxygen column. For the late transition metals, hP3-CdI<sub>2</sub> is located adjacent to both FeS<sub>2</sub> compounds.

**3:1/1:3 Compositions** Following the approach in the previous section, we separated also the 3:1 composition into d-rich and p-rich compounds. Contrary to the 2:1 composition, more compounds with 3:1 composition appear in the d-rich region. In the corresponding structure map (Fig. 2.19(a)), hP8-Mg<sub>3</sub>Cd, oP8-Cu<sub>3</sub>Ti and cP4-Cu<sub>3</sub>Au appear nearly inseparable because of the same coordination number, and same compositions of the coordination polyhedra. hP8-Mg<sub>3</sub>Cd and oP8-Cu<sub>3</sub>Ti are also built of the same coordination polyhedra (c.f. Fig. 2.6). cP8-Cr<sub>3</sub>Si is intersected by the aforementioned compounds, but appears in a well defined region. tl32-Ni<sub>3</sub>P and tP32-Ti<sub>3</sub>P differ only in an additional Wyckoff site for tP32-Ti<sub>3</sub>P that is twelve-fold coordinated. oP16-Fe<sub>3</sub>C is not well localized.

Structural separation is much better in the p-rich 1:3 structure map (Fig. 2.19(b)). The three

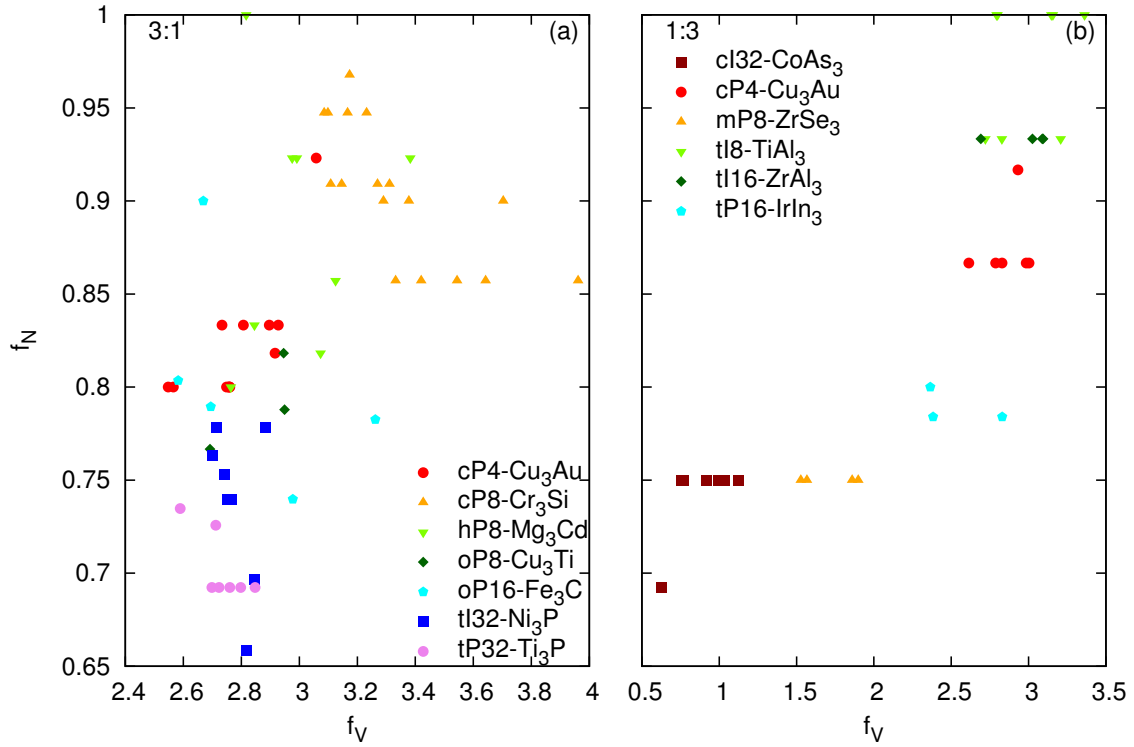


Figure 2.19.: Structure map for a d:p ratio of (a) 3:1 and (b) 1:3.

compounds cP4-Cu<sub>3</sub>Au, tI8-TiAl<sub>3</sub> and tI16-ZrAl<sub>3</sub> have the same coordination polyhedra (c.f. Fig. 2.6) and compositions of the corresponding polyhedra. We observe a mixed tI8-TiAl<sub>3</sub> and tI16-ZrAl<sub>3</sub> region with an identical electronic factor, but varying volumetric factor.

**3:2/2:3,3:4,5:3 Compositions** Due to the small number of entries for compounds with d:p ratios of 3:2 and 2:3, the corresponding structure map contains both ratios (Fig. 2.20(a)). Nevertheless, the compounds are localized in well-defined regions. The placement of hR30-Al<sub>2</sub>O<sub>3</sub> in the rather isolated region might be attributed to the relatively simple construction with only two distinct coordination polyhedra. The other compounds have either three or four distinct coordination polyhedra. The isolated point for hP5-Ni<sub>2</sub>Al<sub>3</sub> is due to the Rh-Si system, where the d and p elements swapped the Wyckoff sites. This comprises oP20-Ni<sub>3</sub>Sn<sub>2</sub> and oP40-Ru<sub>2</sub>Ge<sub>2</sub>. tP10-U<sub>3</sub>Si<sub>2</sub> is intersected by oF40-Zr<sub>2</sub>Al<sub>3</sub>. The isolated point of tP10-U<sub>3</sub>Si<sub>2</sub> does not result from swapped d and p Wyckoff sites.

We only show the structure map for a d:p ratio of 3:4 (Fig. 2.20(b)). The number of entries with a d:p ratio of 4:3 is negligible, and the majority of compounds appear only once in the d-p system. For the d:p ratio of 3:4, the four compounds that appear at least three times are placed in well-defined regions. Most of the compounds are built of three distinct coordination polyhedra, except oI14-Ta<sub>3</sub>B<sub>4</sub> that is built of four distinct ones.

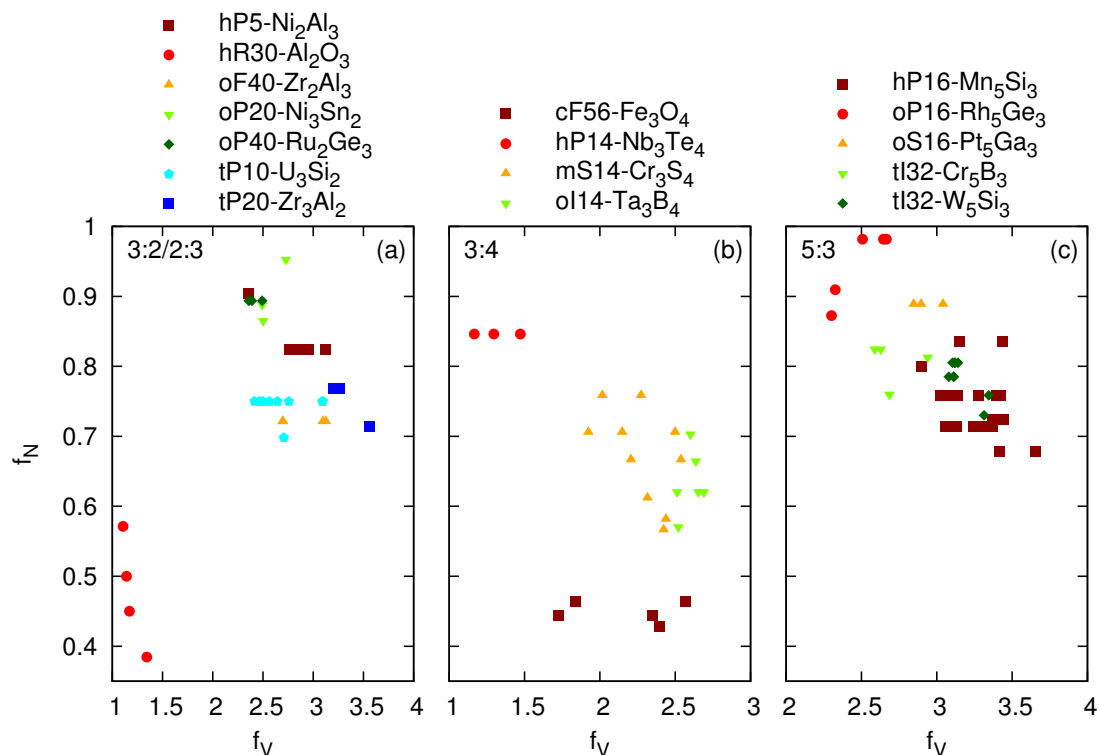


Figure 2.20.: Structure map for d:p ratio of (a) 3:2/2:3, (b) 3:4 and (c) 5:3.

The structure maps for a d:p ratio of 5:3 is shown in Fig. 2.20(c). The inverted 3:5 ratio shows a negligible number of entries, and the majority of compounds appear only once in the d-p system. For the d:p ratio of 5:3, the compounds are generally placed in well-defined regions (Fig. 2.20(c)). tl32-W<sub>5</sub>Si<sub>3</sub> is encapsulated by hP16-Mn<sub>5</sub>Si<sub>3</sub>. However, there is no noticeable similarity in their constituting coordination polyhedra. The regions for hP16-Mn<sub>5</sub>Si<sub>3</sub> and tl32-Cr<sub>5</sub>B<sub>3</sub> overlap slightly, leaving one hP16-Mn<sub>5</sub>Si<sub>3</sub> point in the tl32-Cr<sub>5</sub>B<sub>3</sub> region and vice versa.

**Other Compositions** We summarized compounds with compositions that appear less frequently in a single structure map (Fig. 2.21). In this structure map, the overall structural separation is excellent. Compounds with identical global compositions generally appear in adjacent regions.

### 2.3.8. Pseudobinary Structure Maps

In the pseudobinary structure maps, we highlight the regions that were defined by the binary compounds by plotting the boundary of the convex hull. For simplicity, we combine the datasets



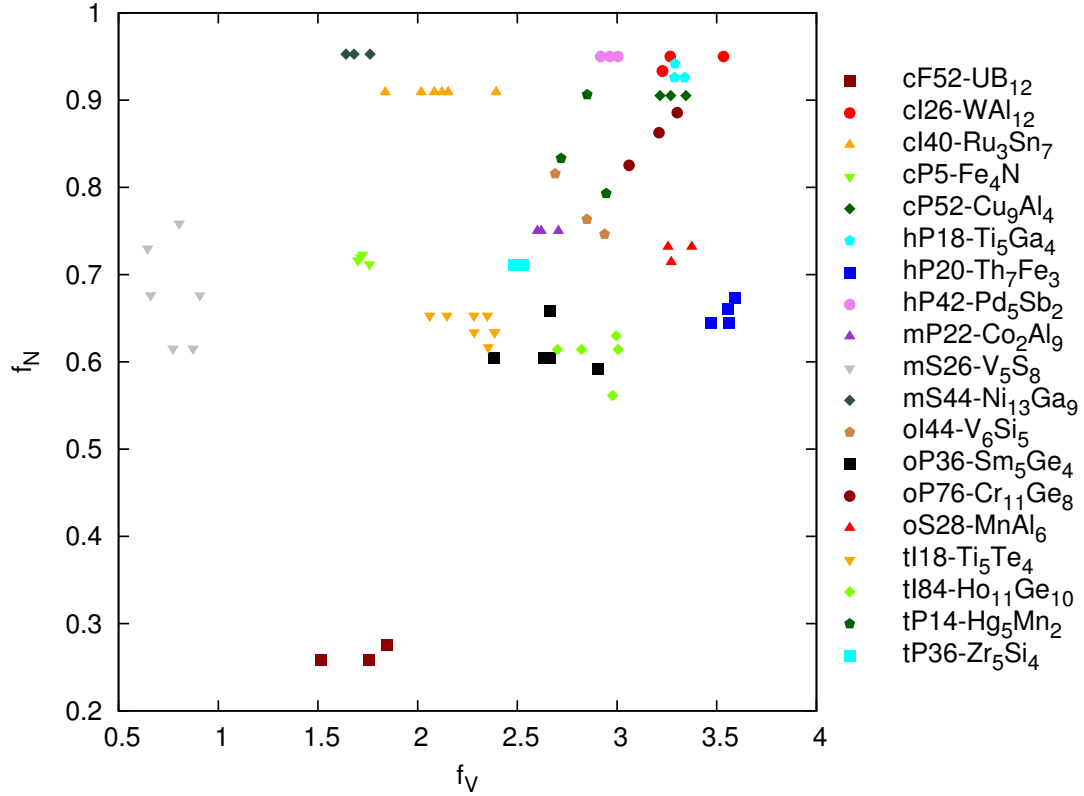


Figure 2.21.: Structure map for the less important compositions.

for compounds that are built of the same coordination polyhedra (Fig. 2.6) when calculating the boundary of the convex hull.

In the pseudobinary structure maps we differentiate between pseudobinaries with perfect composition and pseudobinaries containing defects. In the former case, two d or p elements mix at the same Wyckoff site, but in summary the composition is perfect, i.e. for a 1:1 compound with two d elements mixed at the same Wyckoff site, we have  $d_x d'_y p$  with  $x+y=1$ . In the latter case, either the mixed or the unmixed site deviates from perfect composition, i.e. for a 1:1 compound we observe  $d_x d'_y p_z$  with  $x+y < 1$  and/or  $z < 1$ . In our pseudobinary structure maps, we mark the pseudobinaries with perfect composition with filled symbols and the defect pseudobinaries with open symbols. We further include only the defect pseudobinaries where the composition deviates at most 10% from the perfect composition.

**1:1 Composition** In the pseudobinary structure map for 1:1 composition, we combine the datasets for cF8-ZnS and hP4-ZnO as well as oS8-TiI and tI16-MoB when calculating the boundary of the convex hull. For the latter compounds, we also added oP8-FeB due to the close geometrical relationship [204]. The majority of pseudobinaries, with perfect composition and defect-containing ones, are placed in the convex hull that is defined by the binary compounds.

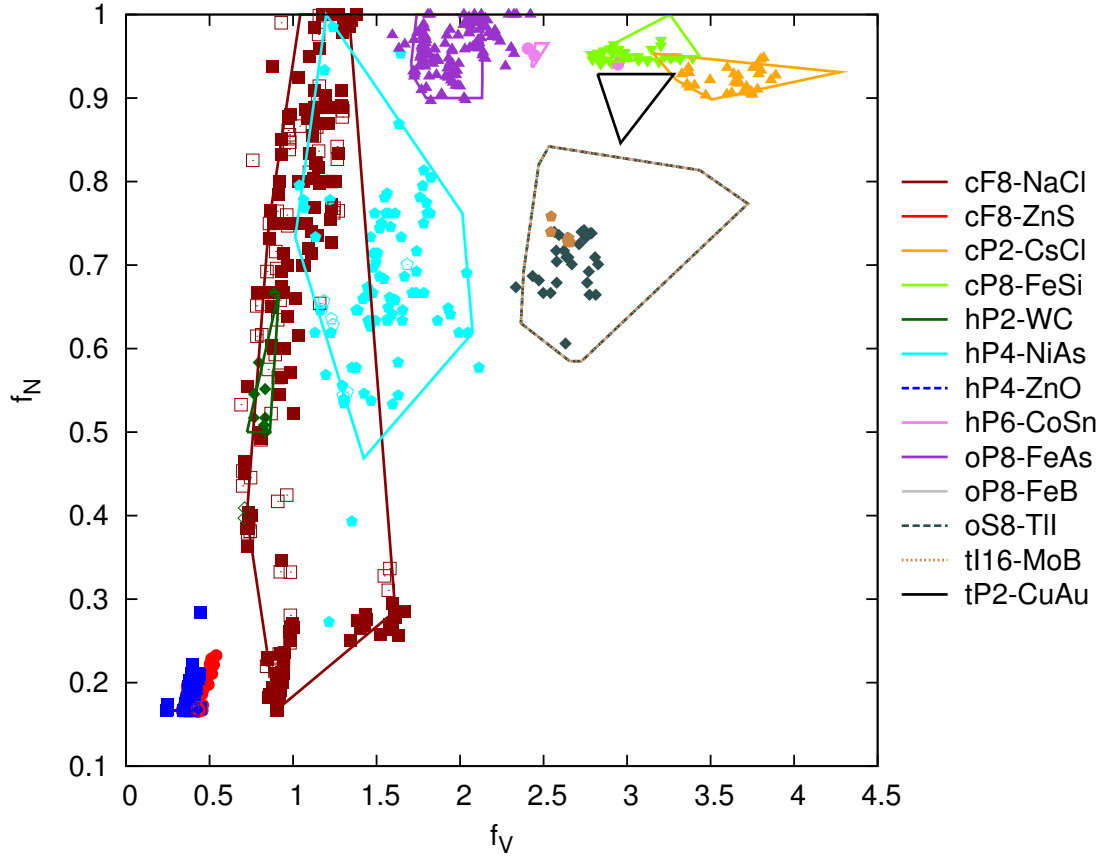


Figure 2.22.: Pseudobinary structure map for the 1:1 composition.

We observe some overlap between the hP2-WC/hP4-NiAs and cF8-NaCl regions. However, this is caused by the minority of the hP2-WC and hP4-NiAs entries. For hP2-WC, the majority of entries is placed in the lower region of the convex hull, where no cF8-NaCl entries appear. For hP4-NiAs, the majority of entries appear for larger  $f_V$ , where no overlap occurs with cF8-NaCl entries. Pseudobinaries of cF8-ZnS- and hP4-ZnO-type appear also for higher  $f_N$ . This is attributed to pseudobinaries with mixed d sites, where a late transition metal, as observed in the binary case (Fig. 2.7), mixes with an earlier, predominantly 3d transition metal. The p-block element belongs always to the oxygen column in the periodic table, and pseudobinaries with mixed p elements are an exception. Pseudobinaries for cP2-CsCl, cP8-FeSi, oS8-TiI and tI16-MoB are placed in their respective convex hulls. oP8-FeB-type pseudobinaries are not listed in [178]. For oP8-FeAs, a small number of entries is placed outside the convex hull. These ones contain predominantly d elements which in the binary case do not form this compound. However, some of these configurations are also placed within the convex hull. The single hP6-CoSn point shifted to the right is peculiar. However, all of the three elements forming this compound are also observed in the binary case. No pseudobinaries at ambient temperatures and pressures are listed in [178] for the compounds that have not been addressed

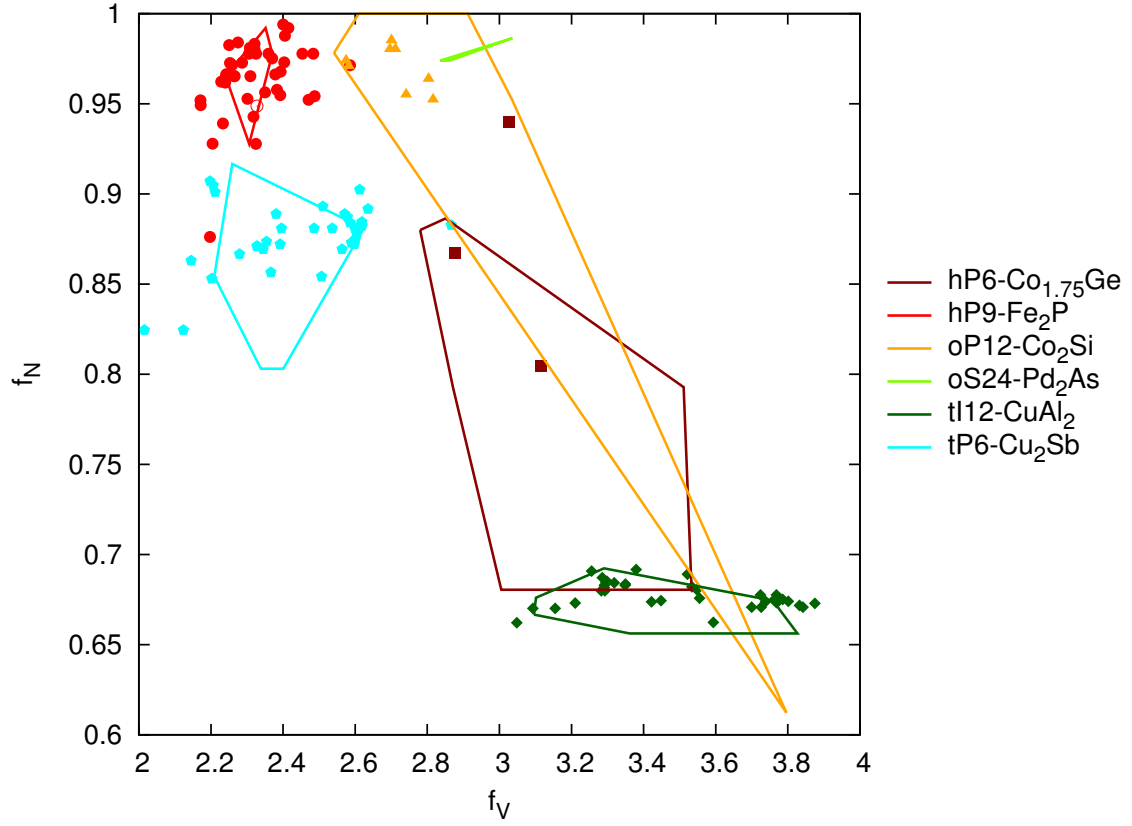


Figure 2.23.: Pseudobinary structure map for a d:p ratio of 2:1.

in this discussion.

**2:1/1:2 Compositions** The pseudobinary structure map for the d:p ratio of 2:1 is shown in Fig. 2.23. Pseudobinary entries for hP6-Co<sub>1.75</sub>Ge, hP9-Fe<sub>2</sub>P, oP12-Co<sub>2</sub>Si, tI12-CuAl<sub>2</sub> and tP6-Cu<sub>2</sub>Sb are in general placed in or close to the convex hull defined by the binary entries. The misplacement of some of the entries, like the single entry for hP6-Co<sub>1.75</sub>Ge that is placed outside the convex hull and the two entries for hP9-Fe<sub>2</sub>P that are shifted to the right and bottom of the structure map, is attributed to the appearance of elements in the pseudobinary that are not observed in the binary compounds. For hP9-Fe<sub>2</sub>P, the single defect pseudobinary is placed in the convex hull.

For the pseudobinary structure maps for a d:p ratio of 1:2 (Fig. 2.24), we combine the datasets for cP12- and oP6-FeS<sub>2</sub>, tI12-CuAl<sub>2</sub> and oF48-Mg<sub>2</sub>Cu as well as for hP9-CrSi<sub>2</sub>, oF24-TiSi<sub>2</sub> and tI6-MoSi<sub>2</sub> when calculating the convex hull. All pseudobinary entries for cP12-FeS<sub>2</sub> except one are placed in or very close to the convex hull. Entries for oP6-FeS<sub>2</sub> are placed outside the pseudobinary cP12-FeS<sub>2</sub> region. In this case, the pseudobinaries cP12-FeS<sub>2</sub>/oP6-FeS<sub>2</sub> show more ordering than the binaries, see the placement of the binaries in Fig. 2.18. For

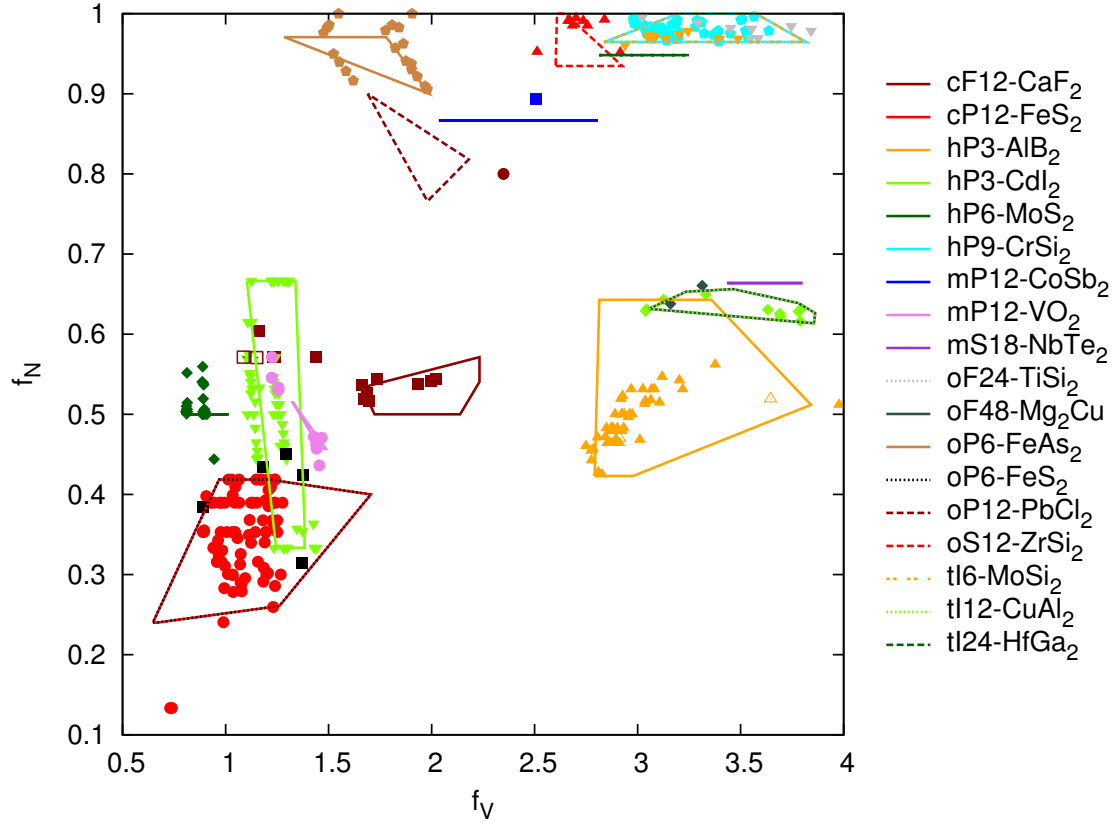


Figure 2.24.: Pseudobinary structure map for a d:p ratio of 1:2.

hP3-CdI<sub>2</sub>, the entries that are located close to the binary entries at the top/bottom represent pseudobinaries where predominantly the p elements mix. However, we also observe a few entries at the top of the convex hull where early transition metals mix at the d site. We do not observe the mixture of late transition metals. The entries that align in between represent pseudobinaries where an early transition metal mix with a late one at the d site. No mixing of p elements is observed here. For the cP12-FeS<sub>2</sub>, oP6-FeS<sub>2</sub> and hP3-CdI<sub>2</sub> pseudobinaries we note that there is only negligible overlap between these three structures: entries for hP3-CdI<sub>2</sub> with mixed early and late transition metals do not enter the cP12-FeS<sub>2</sub>/oP6-FeS<sub>2</sub> convex hull, and the hP3-CdI<sub>2</sub> entries in the cP12-FeS<sub>2</sub>/oP6-FeS<sub>2</sub> convex hull do not mix with the cP12-FeS<sub>2</sub>/oP6-FeS<sub>2</sub> entries. About half of the entries for mP12-VO<sub>2</sub> are placed in the convex hull, the rest is shifted to lower (higher)  $f_V$  ( $f_N$ ) and is placed in the hP3-CdI<sub>2</sub> region. This is attributed to the mixing of transition metals that do not crystallize in this compound in the binary case. The same argument, the observation of pseudobinaries with elements that do not appear in the binary case, also explains the few cF12-CaF<sub>2</sub> entries that are shifted into the hP3-CdI<sub>2</sub> region. All these pseudobinaries contain oxygen, while no stable oxygen-containing cF12-CaF<sub>2</sub> compound is listed in Fig. 2.18. hP6-MoS<sub>2</sub> pseudobinaries appear only with mixed d sites, that explains the shift along  $f_N$ . To the right in the structure map, the pseudobinary

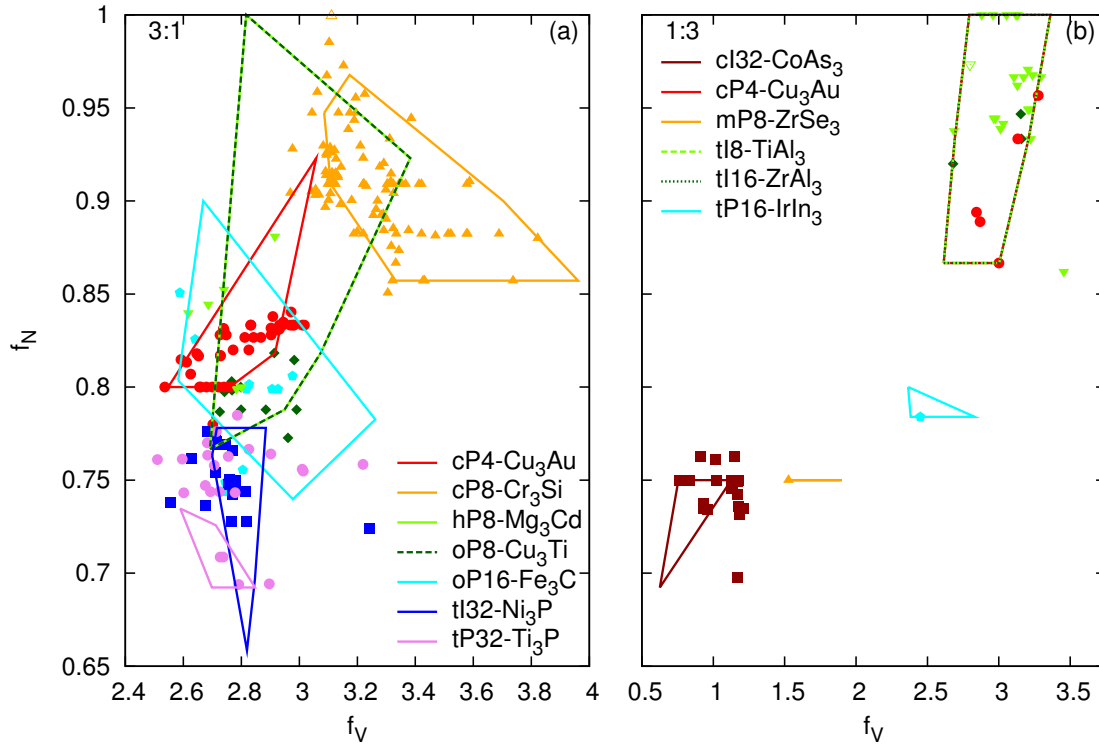


Figure 2.25.: Pseudobinary structure map for a d:p ratio of (a) 3:1 and (b) 1:3.

entries for hP3-AlB<sub>2</sub> are placed in or close to the convex hull. Pseudobinary entries for tI12-CuAl<sub>2</sub> and oF48-Mg<sub>2</sub>Cu are also placed in the convex hull. At the top of the structure map, pseudobinary entries for oP6-FeAs<sub>2</sub> are all placed outside the binary region. However, this behavior cannot be solely attributed to the appearance of elements in the pseudobinary which do not appear in the binary compound. Even mixtures with elements that are observed in the binary compound are placed outside the convex hull. For oS12-ZrSi<sub>2</sub>, all pseudobinary entries are placed in or close to the convex hull. The same holds for pseudobinary entries for hP9-CrSi<sub>2</sub>, oF24-TiSi<sub>2</sub> and tI6-MoSi<sub>2</sub>. The single pseudobinary entries for mP12-CoSb<sub>2</sub> and oP12-PbCl<sub>2</sub> are placed outside the convex hulls. Again, this is attributed to the appearance of elements in the pseudobinaries not observed in the binary.

**3:1/1:3 Compositions** In the pseudobinary structure maps for a d:p ratio of 3:1 (Fig. 2.25(a)), we combine the datasets for hP8-Mg<sub>3</sub>Cd and oP8-Cu<sub>3</sub>Ti for the calculation of the convex hull. Pseudobinary entries for cP4-Cu<sub>3</sub>Au, cP8-Cr<sub>3</sub>Si and oP16Fe<sub>3</sub>C are placed in or very close to the convex hull. For the structures that are built of the same coordination polyhedra, entries for hP8-Mg<sub>3</sub>Cd are placed either close to oP8-Cu<sub>3</sub>Ti or at higher  $f_N$ . Although the convex hulls of cP4-Cu<sub>3</sub>Au, oP16Fe<sub>3</sub>C and hP8-Mg<sub>3</sub>Cd/oP8-Cu<sub>3</sub>Ti overlap significantly, the pseudobinary entries are placed in well-defined regions with negligible overlap. Entries for tI32-Ni<sub>3</sub>P are also

## 2. Structure Maps

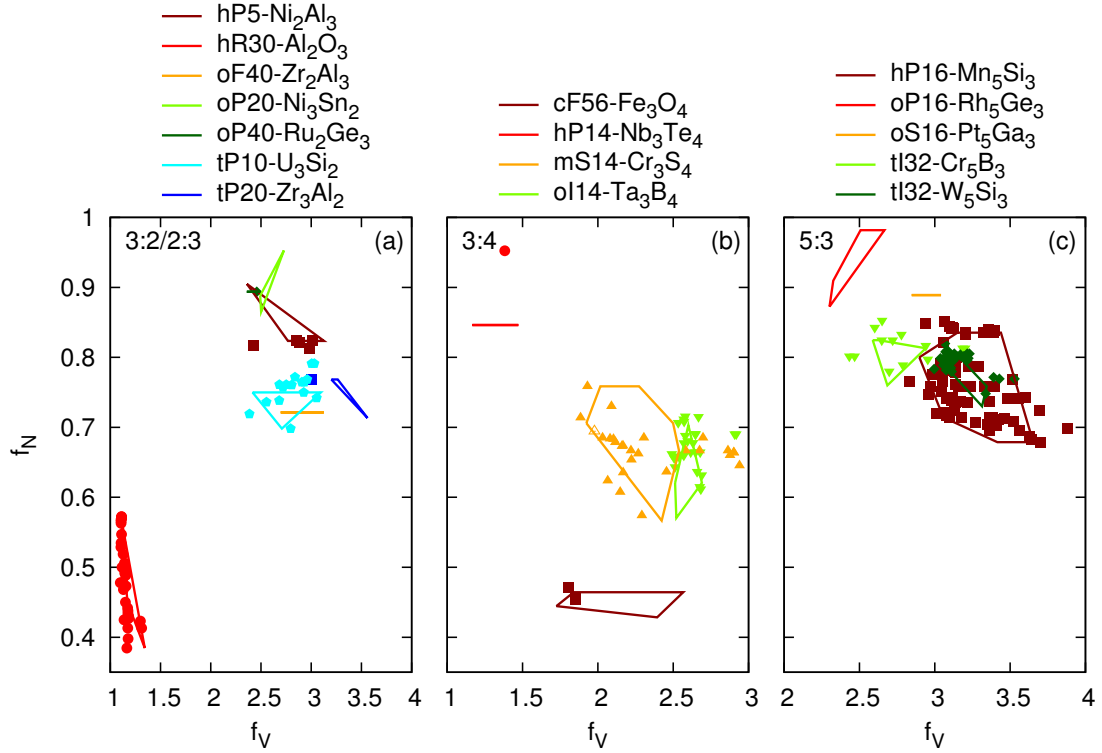


Figure 2.26.: Pseudobinary structure map for d:p ratio of (a) 3:2/2:3, (b) 3:4 and (c) 5:3.

placed in or close to the convex hull. The single entry that is shifted to the right contains boron with mixed transition metals. However, none of the binary compounds contains boron. The performance of the pseudobinary entries for tP32-Ti<sub>3</sub>P is relatively poor. Many of the entries are shifted to significantly higher  $f_N$  and lower/higher  $f_V$ . Again, this is attributed to the appearance of elements in the pseudobinaries not observed in the binary compounds. The majority of misplaced compounds contain boron, which is not observed in the binary compounds, and transition metals with more d electrons than in the binary compounds.

In the pseudobinary structure map for a d:p ratio of 1:3 (Fig. 2.25(b)), we combine the datasets of cP4-Cu<sub>3</sub>Au, tI8-TiAl<sub>3</sub> and tI16-ZrAl<sub>3</sub> for the calculation of the convex hull. For these compounds, all pseudobinary entries except one are placed in the convex hull. The single exception is due to the appearance of copper in the pseudobinary: tI8-TiAl<sub>3</sub> contains in general only early transition metals. The single pseudobinary entries for mP8-ZrSe<sub>3</sub> and tP16-IrIn<sub>3</sub> are placed in the respective convex hulls. Some pseudobinary entries for cI32-CoAs<sub>3</sub> are placed outside the convex hull. Again, this is attributed to the appearance of elements in the pseudobinary that are not observed in the binary case. The majority of these elements, both d and p elements, are located in the adjacent columns with respect to these elements that form this compound in the binary case.

**3:2/2:3,3:4,5:3 Compositions** In the combined pseudobinary structure map for the d:p ratio of 3:2 and 2:3 (Fig. 2.26(a)), the pseudobinary entries for hR30-Al<sub>2</sub>O<sub>3</sub> are placed in or close to the convex hull. The single pseudobinary entry for oP40-Ru<sub>2</sub>Ge<sub>3</sub> is also placed in the convex hull, while the single entry for tP20-Zr<sub>3</sub>Al<sub>2</sub> is shifted to the left: this pseudobinary contains gallium, which is not observed in the binary case. The majority of pseudobinary entries for hP5-Ni<sub>2</sub>Al<sub>3</sub> are placed close to the lower boundary of the convex hull, the single point shifted to the right contains silicon. This causes the shift in  $f_V$ . For tP10-U<sub>3</sub>Si<sub>2</sub>, most of the pseudobinary entries that are placed outside the convex hull contain later transition metals (region above the convex hull) than observed in the binary case or earlier p-block elements (single point outside the left border).

In the pseudobinary structure map for a d:p ratio of 3:4 (Fig. 2.26(b)), the single entry for hP14-Nb<sub>3</sub>Te<sub>4</sub> contains the transition metals hafnium and zirconium, which causes the shift compared to the binary case that contains only niobium. The single cF56-Fe<sub>3</sub>O<sub>4</sub> entry outside the convex hull contains titanium: usually this compound contains only late transition metals. For mS14-Cr<sub>3</sub>S<sub>4</sub> and ol14-Ta<sub>3</sub>B<sub>4</sub>, the majority of pseudobinary entries are placed either in or close to the convex hulls. However, a few entries are shifted to higher  $f_V$ , and some mS14-Cr<sub>3</sub>S<sub>4</sub> entries are placed in the ol14-Ta<sub>3</sub>B<sub>4</sub> region. Most of these mS14-Cr<sub>3</sub>S<sub>4</sub> entries contain tellurium in combination with chromium and a late transition metal. The misplaced ol14-Ta<sub>3</sub>B<sub>4</sub> entries contain predominantly iron. We note that the misplacement is only in the volumetric factor  $f_V$ , but not in the electronic factor  $f_N$ .

In the pseudobinary structure map for a d:p ratio of 5:3 (Fig. 2.26(c)), the majority of pseudobinary entries for hP16-Mn<sub>5</sub>Si<sub>3</sub> are placed in the convex hull. Entries for tI32-W<sub>5</sub>Si<sub>3</sub> are concentrated in the top left region of the convex hull, a few entries are shifted to the right and placed in the hP16-Mn<sub>5</sub>Si<sub>3</sub> region. This is due to the appearance of p elements that do not appear in the binary compounds. For tI32-Cr<sub>5</sub>B<sub>3</sub>, a few entries are shifted to the left and right of the convex hull. The ones to the left contain p elements not observed in the binary compounds, the ones shifted to the right contain some transition metals not observed in the binary compounds.

## 2.4. Summary

In this section we presented the decomposition of binary d-p compounds in their respective coordination polyhedra, and used the information to define new order parameters for structure maps. All compounds, binaries and pseudobinaries, that we considered in our investigation were extracted from the Pearson's Crystal Database [178]. For the binaries, we compared the listed compounds with experimental phase diagrams [193] in order to exclude metastable, high-temperature and high-pressure phases as well as phases observed in thin films and entries with the crystal geometry obtained from calculations. We only considered phases that are stable at ambient temperatures and pressures. Due to the reduced number of experimental phase diagrams for ternary systems, we simply checked the pseudobinary entries for keywords to identify the compounds that are stable at ambient temperature and pressure.

## 2. Structure Maps

---

The investigation of the coordination polyhedra, their respective coordination number and composition for the various p elements demonstrated that the chemically distinct behavior of the first row p-block elements boron, carbon, nitrogen and oxygen compared to the remaining elements is also present in trends regarding the favorite coordination number and the composition of the coordination polyhedron, i.e. the number of d and p elements that represent the coordination polyhedron. Carbon and nitrogen are the most restrictive elements with regard to the favored coordination number, favoring six-fold coordination, followed by boron, favoring nine-fold coordination, and oxygen. The trends regarding a favorite coordination number are less clear for the remaining elements, as these show a larger variety of different crystal structures. However, in general the coordination numbers decrease with increasing number of valence p electrons, as expected.

The analysis of the polyhedron composition allowed the introduction of two order parameters, one volumetric and one electronic factor, that depend explicitly on atomic and compound-related properties. The volumetric factor relates the polyhedron volumes of the d/p sites to the respective ground state volumes. The electronic factor compares the electronic configuration of the coordination polyhedra for the d/p sites, respectively, by counting the number of valence electrons in the sd-band for d elements and number of holes in the sp-band for p elements. Applied to binaries, the order parameters we introduced resulted in overall good structural separation in two-dimensional structure maps for the most common compositions in the d-p system. Pseudobinaries were in general placed within the domains that were defined by the binary entries. The appearance of pseudobinary entries that were placed outside the binary domains was attributed to the appearance of p or d elements that do not adopt this compound in the binary d-p system. The order parameters that we introduced were also able to account for defects in the crystal structures, represented by fractionally occupied Wyckoff sites. Although our order parameters depend explicitly on compound-related properties, we showed that the predictive ability of the structure maps is not limited, as we demonstrated that it is in principle possible to estimate the electronic and volumetric factor for hypothetical compounds.

So far, we focused on binary d-p and ternary d-d-p/d-p-p compounds that adopt binary crystal structures. The latter is realized by mixing of the d or p elements at the same Wyckoff site. In the next step we will extend the investigation to real ternary compounds. We note that we require only slight modifications of the order parameters to be able to account for the ternary compounds. Furthermore, the order parameters still require the explicit separation of the compounds with respect to their respective global composition. This disagrees with the concept of polyhedra-based structure maps, as the usage of the local composition for the order parameter should make the global composition obsolete. An improvement in structural separation is expected by identifying a suitable third axis.



### 3. Electronic Structure Calculations

*"I'm afraid we need to use...math!"  
Professor Hubert J. Farnsworth  
Futurama S06E10: The Prisoner of Benda*

In order to study, analyze and understand the physical and chemical properties of matter, the solution of the Schrödinger equation [205], the equation to describe a system consisting of electrons and nuclei, is required. Although the general form of the equation is known, the actual solution is complicated due to the nature of the electrons, which cannot be treated as classical point-like particles, but have to be described by wavefunctions that obey the rules of quantum mechanics. Furthermore, electrons interact with each other via the Coulomb force, thus the presence of an electron influences the behavior of other electrons. Therefore, the solution of the Schrödinger equation for systems of many nuclei and electrons is a many-body problem.

In the past, several approximate schemes have been proposed in order to solve the many-body problem. This section gives an overview of some of the well-established approximate schemes. The approach by Hartree [206] is based on the decomposition of the many-body wavefunction into single-electron wavefunctions, thus reducing the many-body Hamiltonian to a simpler single-electron Hamiltonian that can be solved more easily. However, the Hartree approximation neglects that electrons are fermions, i.e. indistinguishable spin-1/2 particles, and have to obey the Pauli principle. A modified Hartree approximation, referred to as Hartree-Fock approximation [207, 208], has been developed in order to account for the treatment of the electrons as fermions. A different approximate scheme was developed by Thomas [209], and independently by Fermi [210], who introduced the electronic density, derived from the many-body wavefunction, as basic variable of the many-body problem. However, the approximations used in this approach were too crude, leading to a very poor description of the electronic system. Nevertheless, the Thomas-Fermi theory provided the basis for the development of density functional theory. Hohenberg and Kohn [211] provided the mathematical proofs for the validity of the electron density as basic variable of the many-body system, manifested in two theorems, while in a subsequent study Kohn and Sham [212] provided a scheme for the calculation of properties of a many-body system from the electronic density. As the theoretical investigations in this study have been performed using the numerical implementation of density functional theory, we will discuss this topic in more detail, including the fundamental theorems, the corresponding equations provided by Kohn and Sham and the specific treatment of many-body effects within density functional theory. We further discuss some approaches regarding the numerical implementation of density functional theory and address the development of approximate schemes in order to describe the electron-nucleus interaction. In the end,

we provide an overview of some observations of density functional theory, but also focus on limitations which arise from the underlying approximations.

## 3.1. Schrödinger Equation

The fundamental equation of quantum mechanics describing particles is the Schrödinger equation [205], which in its time-independent form and implicitly using the Born-Oppenheimer approximation [213], thus separating the Hamiltonian and the wavefunction into an electronic and ionic part, is written as

$$\hat{H}\Psi = E\Psi, \quad (3.1)$$

where  $\hat{H}$  denotes the many-body electronic Hamiltonian for  $N$  electrons

$$\hat{H} = \underbrace{-\frac{\hbar^2}{2m} \sum_{i=1}^N \vec{\nabla}_i^2}_{\hat{T}} + \underbrace{\frac{1}{2} \frac{1}{4\pi\epsilon_0} \sum_{i=1}^N \sum_{\substack{j=1 \\ i \neq j}}^N \frac{e^2}{|\vec{r}_i - \vec{r}_j|}}_{\hat{V}_{ee}} + \underbrace{\frac{1}{4\pi\epsilon_0} \sum_{i=1}^N \sum_{J=1}^N \frac{Z_J e^2}{|\vec{r}_i - \vec{R}_J|}}_{\hat{V}_{ie}} \quad (3.2)$$

and  $\Psi = \Psi(\{\vec{r}_i, \sigma_i\})$  denotes the many-body electron wavefunction dependent on the spatial coordinates  $\vec{r}_i$  and the spin coordinate  $\sigma_i$ , and  $E$  denotes the energy of the system.

However, the non-linearity of the Schrödinger equation in view of the many-body Hamiltonian and the wavefunction leads to only a few systems with analytical and exact solutions, including hydrogen and the  $\text{H}_2^+$  molecule. Systems with more electrons have to be solved numerically, although numerically exact solutions are still limited to systems with only a few electrons. In the past, several approximations of the Schrödinger equation have been developed that enable the treatment of systems with several electrons, but sacrifice an exact formulation. Among the proposed methods, two approaches stand out due to their relevance and success in describing many-body systems: Hartree-Fock and density functional theory, the latter being used for all calculations throughout this study. In the following the history and fundamentals of this methods shall be shortly reviewed.

## 3.2. Hartree and Hartree-Fock Approximations

### 3.2.1. Hartree Approximation

The approach to solve the many-body problem in quantum mechanics proposed by Hartree [206] in 1928 is based on the assumption that the many-body wavefunction can be written as a product of single-electron wavefunctions and that the electrostatic field felt by an electron is due to the potential of the nuclei together with the field created by all the other electrons. Only a

few years later, Slater formulated the corresponding mathematical background of this theory, obtained from a variational principle.

The many-body wavefunction is written as a product of single-electron wavefunctions

$$\Phi(\vec{r}) = \prod_{i=1}^N \phi_i(\vec{r}_i), \quad (3.3)$$

and the single-electron wavefunctions are normalized to one. The Hamiltonian of the many-body system is then written as

$$\hat{H}(\vec{R}, \vec{r}) = \sum_{i=1}^N \left( -\frac{\hbar^2}{2m} \vec{\nabla}_i^2 + v_{\text{ext}}(\vec{R}, \vec{r}_i) \right) + \frac{1}{2} \sum_{i=1}^N \sum_{\substack{j=1 \\ i \neq j}}^N \frac{1}{4\pi\epsilon_0} \frac{e^2}{|\vec{r}_i - \vec{r}_j|}, \quad (3.4)$$

whereas the former part denotes the single-electron operator, consisting of the kinetic part and the interaction with the nuclei, and the latter describes the interaction with the other electrons, represented by the Coulomb electron-electron interaction. The factor 1/2 in the Coulomb interaction is due to double counting. With Eq. 3.4, the expectation values becomes

$$\begin{aligned} \langle \Phi | \hat{H} | \Phi \rangle &= \sum_{i=1}^N \overbrace{\int d^3r_i \phi_i^*(\vec{r}_i) \left( -\frac{\hbar^2}{2m} \vec{\nabla}_i^2 + v_{\text{ext}}(\vec{R}, \vec{r}_i) \right) \phi_i(\vec{r}_i)}^{E_{ii}} \\ &+ \frac{1}{2} \sum_{i=1}^N \sum_{\substack{j=1 \\ i \neq j}}^N \underbrace{\int \int d^3r_i d^3r_j \phi_i^*(\vec{r}_i) \phi_j^*(\vec{r}_j) \frac{1}{4\pi\epsilon_0} \frac{e^2}{|\vec{r}_i - \vec{r}_j|} \phi_i(\vec{r}_i) \phi_j(\vec{r}_j)}_{J_{ij}}. \end{aligned} \quad (3.5)$$

The  $J_{ij}$  are denoted as Coulomb integrals.

The variation of the energy with respect to the single-electron wavefunctions  $\phi_i^*(\vec{r}_i)$  leads to Lagrange equations that provide single-electron Schrödinger equations. The variational equation includes suitable boundary conditions to account for the normalization of the single-electron wavefunctions and  $\epsilon_i$  enter as Lagrange multiplier. The single-electron Schrödinger equation for electron  $i$  reads

$$\left( -\frac{\hbar^2}{2m} \vec{\nabla}_i^2 + v_{\text{ext}}(\vec{R}, \vec{r}_i) + \int d^3r' \frac{1}{4\pi\epsilon_0} \frac{\sum_{j \neq i}^N e^2 |\phi_j(\vec{r}')|^2}{|\vec{r} - \vec{r}'|} \right) \phi_i(\vec{r}) = \epsilon_i \phi_i(\vec{r}). \quad (3.6)$$

The last term on the left-hand side in Eq. 3.6 represents the classical electrostatic potential that is felt by electron  $i$  due to the charge distribution of the other electrons. The Lagrange multipliers  $\epsilon_i$  are identified as the energy of electrons  $i$ .

The total energy of the system is not simply the sum of the single-electron energies  $\epsilon_i$ . Owing to the electrostatic potential that enters in Eq. 3.6 these contributions are counted twice, so

that the total energy of a many-body system in the Hartree approximation is written as

$$\langle \Phi | \hat{H} | \Phi \rangle = E_{\text{Hartree}} = \sum_{i=1}^N \epsilon_i - \frac{1}{2} \sum_{i=1}^N \sum_{\substack{j=1 \\ i \neq j}}^N J_{ij}. \quad (3.7)$$

#### 3.2.2. Hartree-Fock Approximation

Electrons in the Hartree approximation are not treated as fermions, i.e. indistinguishable spin-1/2 particles, that obey the Pauli principle. Thus, in the Hartree approximation the description of the many-body system is not complete. In the Hartree-Fock approximation, however, the Pauli principle is accounted for by proposing an antisymmetrized many-body wavefunction in form of a Slater determinant

$$\Phi_{\text{HF}}(\vec{x}_1, \vec{x}_2, \dots, \vec{x}_N) = \frac{1}{\sqrt{N!}} \begin{vmatrix} \phi_1(\vec{x}_1) & \phi_2(\vec{x}_1) & \dots & \phi_N(\vec{x}_1) \\ \phi_1(\vec{x}_2) & \phi_2(\vec{x}_2) & \dots & \phi_N(\vec{x}_2) \\ \dots & \vdots & \ddots & \vdots \\ \phi_1(\vec{x}_N) & \phi_2(\vec{x}_N) & \dots & \phi_N(\vec{x}_N) \end{vmatrix}, \quad (3.8)$$

where the single variable  $\vec{x}_i = (\vec{r}_i, \sigma_i)$  comprises the spatial coordinates  $\vec{r}_i$  and spin coordinates  $\sigma_i$ . Expression 3.8 ensures that the sign of the wavefunction is changed when the coordinates of two electrons are exchanged, which is in line with the Pauli principle that states that the many-body wavefunction has to be antisymmetric upon particle exchange. The postulation of a wavefunction of the form 3.8 is referred to as Hartree-Fock approximation [207, 208].

The single-electron energy, the first term in Eq. 3.5, in the Hartree-Fock approximation that contributes to the total energy of the many-body system is the same as in the Hartree approximation. In the two-electron term, however, a second contribution arises apart from the Coulomb integrals that also appear in the Hartree approximation. This is due to the numbering of the indexes, and these additional terms are referred to as exchange integrals that read

$$K_{ij} = \int \int d^3x_i d^3x_j \phi_i^*(\vec{x}_i) \phi_j^*(\vec{x}_j) \frac{1}{4\pi\epsilon_0} \frac{e^2}{|\vec{r}_i - \vec{r}_j|} \phi_i(\vec{x}_j) \phi_j(\vec{x}_i). \quad (3.9)$$

The difference to  $J_{ij}$  is that the wavefunctions  $\phi$  and  $\phi^*$  appear with different electrons in the exchange integral  $K_{ij}$ .

The total energy of a many-body system in the Hartree-Fock approximation resembles the expression in the Hartree approximation. However, the exchange terms that were introduced in the Hartree-Fock approximation enter additionally in the expression for the total energy of the many-body system

$$\langle \Phi_{\text{HF}} | \hat{H} | \Phi_{\text{HF}} \rangle = E_{\text{Hartree-Fock}} = \sum_{i=1}^N \epsilon_i - \frac{1}{2} \sum_{i=1}^N \sum_{j=1}^N (J_{ij} - K_{ij}). \quad (3.10)$$

### 3.3. Density Functional Theory

Parallel to the development of the Hartree approximation that was discussed in the previous section, a different approach was proposed by Thomas [209] in 1927, and independently by Fermi [210] in 1928, which uses the full electronic density as the basic variable of the many-body system. Thomas [209] and Fermi [210] introduced a differential equation for the electronic density that, in contrast to the Hartree and Hartree-Fock approximation, prevented the usage of single-electron wavefunctions. However, the overall success of this approach was limited, mainly due to the poor description of the kinetic energy of the electrons that was unable to sustain bound states. Nevertheless, the approach by Thomas and Fermi provided the basis for the later development of density functional theory, based on the mathematical formulation postulated by Hohenberg and Kohn [211] and the development of suitable equations to determine the electronic density by Kohn and Sham [212].

#### 3.3.1. Thomas-Fermi Approximation

Thomas [209] in 1927, and independently Fermi [210] in 1928, presented a scheme to derive the energy of a many-body system solely using the electronic density as the fundamental variable. In this scheme, the energy contributions to the total energy of the many-body systems consist of a kinetic, correlation and exchange energy contribution. In order to construct these quantities for the many-body system that is treated as an inhomogeneous electron gas, the authors used expressions for the kinetic, correlation and exchange energy that were derived from the homogeneous gas. Thus, in the Thomas-Fermi theory the inhomogeneous system is assumed to be locally homogeneous, which allows the calculation of the kinetic, correlation and exchange contribution for the inhomogeneous system. With the expression for the kinetic energy density, the description of exchange according to Slater's expression for the homogeneous electron gas [214, 215], and the description of correlation according to, e.g., Wigner [216] the general expression for the energy of a many-body system within Thomas-Fermi theory is written as

$$E_{\text{TF}} = c_K \int d^3r \rho(\vec{r})^{\frac{5}{3}} + \int d^3r \rho(\vec{r}) v_{\text{ext}}(\vec{r}) + \frac{1}{2} \int \int d^3r d^3r' \frac{\rho(\vec{r}) \rho(\vec{r}')}{|\vec{r} - \vec{r}'|} - c_X \int d^3r \rho(\vec{r})^{\frac{4}{3}} + E_C[\rho]. \quad (3.11)$$

The usage of a variational scheme allows the search for the density  $\rho(\vec{r})$  that minimizes the energy  $E_{\text{TF}}$ , with the constraint that the integrated density is identical to the number of electrons, i.e.  $N = \int d^3r \rho(\vec{r})$ . The expression, where the constraint of fixed number of electrons enters as Lagrange multiplier,

$$\frac{\delta}{\delta \rho(\vec{r})} \left( E_{\text{TF}}[\rho] - \mu \int d^3r \rho(\vec{r}) \right) = 0, \quad (3.12)$$

leads to

$$\mu = \frac{5}{3} c_K \rho(\vec{r})^{\frac{2}{3}} + v_{\text{ext}}(\vec{r}) + \int d^3r' \frac{\rho(\vec{r}')}{|\vec{r} - \vec{r}'|} - \frac{4}{3} c_X \rho(\vec{r})^{\frac{1}{3}} + \frac{\delta E_C[\rho]}{\delta \rho(\vec{r})}. \quad (3.13)$$

$\mu$  represents the chemical potential. Inverting the equation leads to an expression of the density  $\rho(\vec{r})$  dependent on the external potential. However, due to the integral term and the non-integer powers of the density the equation is, in practice, solved using iterative methods.

The relative crude approximations in the Thomas-Fermi theory, especially the treatment of the kinetic energy, lead to relative poor results if applied to real many-body systems. However, the Thomas-Fermi theory provided the basis for the later development of the density functional theory. One of the main reasons for the success of the latter method is the improved treatment of the kinetic energy. However, this improvement requires the introduction of single-electron wavefunctions, that also occurred in the Hartree and Hartree-Fock approximation.

#### 3.3.2. Hohenberg-Kohn Theorem

The Thomas-Fermi theory introduced the electronic density as fundamental variable in the many-body system in order to determine the total energy of the many-body system. The mathematical proof of the validity of such a concept was provided in 1964 by Hohenberg and Kohn [211], who formulated the density functional theory as an exact theory for many-body systems, based on two theorems, and the corollary that follow directly.

Theorem I: The ground state density determines univocally the external potential, except for an additive constant, for any system of interacting particles.

Corollary I: Since the ground state density determines the external potential, it also determines the full Hamiltonian, and thus the many-body wavefunction  $\Phi$ . Therefore, all properties of the many-body system are completely determined by the ground state density.

Theorem II:  $E_{\text{HK}}[\rho]$  is defined as universal functional in terms of the density, valid for any external potential, in the form

$$E_{\text{HK}}[\rho] = F_{\text{HK}}[\rho] + \int d^3r \rho(\vec{r}) v_{\text{ext}}(\vec{r}) \quad (3.14)$$

with

$$F_{\text{HK}}[\rho] = T[\rho] + E_{\text{int}}[\rho]. \quad (3.15)$$

For any external potential, the ground state energy of the system is represented by the global minimum value of (3.14), and the density that minimizes the functional represents the exact ground state density.

Corollary II: The exact ground state energy and density are fully determined by the functional  $E_{\text{HK}}[\rho]$  alone.

### 3.3.3. Kohn-Sham Equations

In order to account for the kinetic term in Eq. 3.15 whose explicit expression in terms of the electronic density is unknown, Kohn and Sham [212] replaced the interacting many-body problem by an auxiliary non-interacting system, and it is assumed that the ground state density of the original, interacting many-body system is identical to the non-interacting system. In practice, the auxiliary non-interacting system is represented by an antisymmetric wavefunction of Slater determinant type, similar to the Hartree-Fock approximation, that allows the derivation of the kinetic energy in terms of the single-electron wavefunctions. With this assumption, Kohn and Sham derived single-electron equations can be considered exactly soluble with all terms describing the many-body system incorporated in an exchange-correlation functional. By solving the equations one finds the ground state density and energy of the original interacting many-body problem within the accuracy determined by the approximations used to describe the exchange and correlation.

The density of the auxiliary non-interacting system is derived from the single-electron wavefunctions  $\phi_i(\vec{r})$  for each spin  $\sigma$  as

$$\rho(\vec{r}) = \sum_{\sigma} \sum_{i=1}^{N_{\sigma}} |\phi_i^{\sigma}(\vec{r})|^2. \quad (3.16)$$

Thus the kinetic term for the independent-particle system is given by

$$T_{\phi}[\rho] = -\frac{\hbar^2}{2m} \sum_{\sigma} \sum_{i=1}^{N_{\sigma}} \langle \phi_i^{\sigma} | \vec{\nabla}^2 | \phi_i^{\sigma} \rangle = -\frac{\hbar^2}{2m} \sum_{\sigma} \sum_{i=1}^{N_{\sigma}} \int d^3r |\vec{\nabla} \phi_i^{\sigma}(\vec{r})|^2. \quad (3.17)$$

The single-electron wavefunctions  $\phi_i^{\sigma}(\vec{r})$  are the  $N_{\sigma}$  eigenfunctions with lowest energy of the Hamiltonian

$$\hat{H}_{\text{KS}} = -\frac{\hbar^2}{2m} \vec{\nabla}^2 + v_{\text{KS}}(\vec{r}) \quad (3.18)$$

and are obtained by solving the corresponding single-electron Schrödinger equation

$$\hat{H}_{\text{KS}} \phi_i^{\sigma} = \epsilon_i^{\sigma} \phi_i^{\sigma} \quad (3.19)$$

At this stage, the actual form of the potential  $v_{\text{KS}}(\vec{r})$  is unknown.

Kohn and Sham also decomposed the term  $E_{\text{int}}[\rho]$  in (3.15) describing the electron-electron interaction in several contributions. The largest contribution is represented by the Hartree term, which is simply the classical electrostatic energy, followed by an exchange term, that contributes to a lesser extent and is known from Hartree-Fock theory (3.9). Despite the knowledge of the exact form of the exchange energy, this term is usually approximated due to the relative costly calculation of the exchange integrals. The smallest contribution is the correlation energy, which comprises additional many-body interactions that have not been considered in the other two terms. The introduction of the kinetic term for the non-interacting system in exchange for the

### 3. Electronic Structure Calculations

---

kinetic term dependent on the electronic density in (3.15) leaves a kinetic correlation that is added to the exchange and correlation term.

With this in mind, the universal density functional is written in the form

$$F[\rho] = T_\phi[\rho] + \frac{1}{2} \int \int d^3r d^3r' \frac{\rho(\vec{r})\rho(\vec{r}')}{|\vec{r} - \vec{r}'|} + E_{\text{xc}}[\rho]. \quad (3.20)$$

Substituting the expression of  $F$  into the total energy functional (3.14) yields the Kohn-Sham functional

$$\begin{aligned} E_{\text{KS}}[\rho] &= T_\phi[\rho] + \int d^3r \rho(\vec{r}) v_{\text{ext}}(\vec{r}) + E_{\text{Hartree}}[\rho] + E_{\text{xc}}[\rho] \\ &= T_\phi[\rho] + \int d^3r \rho(\vec{r}) v_{\text{ext}}(\vec{r}) + \frac{1}{2} \int \int d^3r d^3r' \frac{\rho(\vec{r})\rho(\vec{r}')}{|\vec{r} - \vec{r}'|} + E_{\text{xc}}[\rho]. \end{aligned} \quad (3.21)$$

In order to determine the so far missing expression for the Kohn-Sham potential  $v_{\text{KS}}(\vec{r})$ , and therefore the determination of the single-electron wavefunction  $\phi_1^\sigma$ , the Kohn-Sham functional is minimized with respect to  $\phi_1^{\sigma*}$ . The variation principle yields

$$\frac{\delta}{\delta \phi_1^{\sigma*}} \left( E_{\text{KS}}[\rho] - \epsilon \int d^3r \rho(\vec{r}) \right) = 0. \quad (3.22)$$

Variation of the Kohn-Sham functional with respect to the single-particle wavefunction leads to

$$\frac{\delta E_{\text{KS}}}{\delta \phi_1^{\sigma*}} = \frac{\delta T_\phi}{\delta \phi_1^{\sigma*}} + \left[ v_{\text{ext}}(\vec{r}) + \frac{\delta E_{\text{Hartree}}}{\delta \rho} + \frac{\delta E_{\text{xc}}}{\delta \rho} \right] \frac{\delta \rho}{\delta \phi_1^{\sigma*}}. \quad (3.23)$$

Using the relations

$$\frac{\delta T_\phi}{\delta \phi_1^{\sigma*}} = -\frac{\hbar^2}{2m} \vec{\nabla}^2 \phi_1^\sigma(\vec{r}) \quad (3.24)$$

from (3.17) and

$$\frac{\delta \rho}{\delta \phi_1^{\sigma*}} = \phi_1^\sigma \quad (3.25)$$

we obtain a Schrödinger-like equation of the form (3.19) and identify the Lagrange parameter as energy  $\epsilon_1^\sigma$  of the single-electron wavefunction. With these results, the Kohn-Sham potential is identified as

$$\begin{aligned} v_{\text{KS}}(\vec{r}) &= v_{\text{ext}}(\vec{r}) + \frac{\delta E_{\text{Hartree}}}{\delta \rho} + \frac{\delta E_{\text{xc}}}{\delta \rho} \\ &= v_{\text{ext}}(\vec{r}) + v_{\text{Hartree}}(\vec{r}) + v_{\text{xc}}(\vec{r}). \end{aligned} \quad (3.26)$$

Equations (3.18), (3.19) and (3.26) are the well-known Kohn-Sham equations, with the resulting density given by (3.16) and the total energy given by (3.21). The equations have to



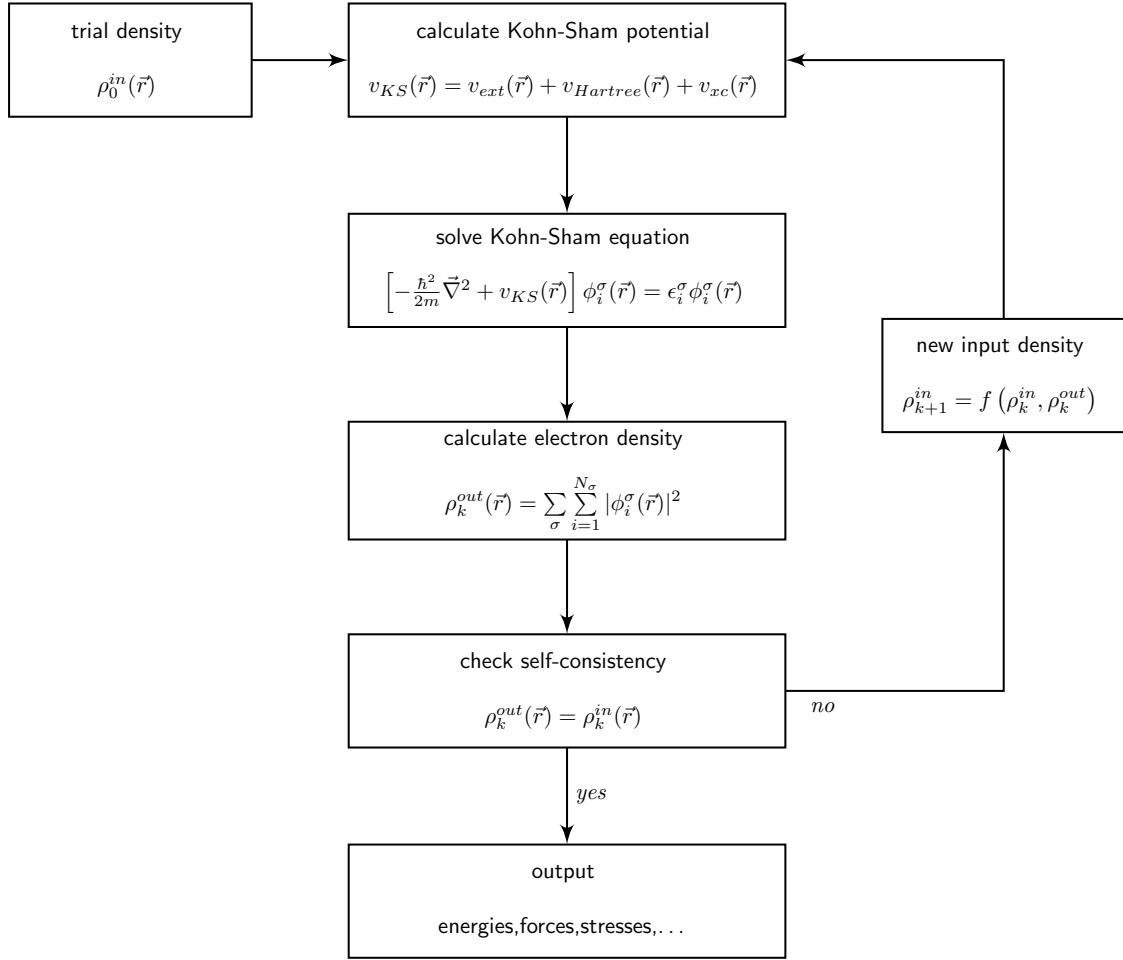


Figure 3.1.: Self-consistent loop for the solution of Kohn-Sham equations. Starting from a trial input density, the Kohn-Sham equations are solved in order to obtain the single-electron wavefunctions, and thus the output density. Self-consistency is achieved if the output density agrees with the input density within the specified limit. Otherwise a new input density for the next loop is calculated by mixing the input and output density.

be solved in a self-consistent approach, similar to the Hartree and Hartree-Fock equations, as the potential requires the input from the density, which is calculated from the single-electron wavefunctions  $\phi_1^\sigma$ , but which are unknown at the beginning. Therefore, in the self-consistent loop (Fig. 3.1) for the solution of the Kohn-Sham equations one starts from some trial density and calculates the Kohn-Sham potential (3.26). Solving the Kohn-Sham equations (3.18) yield the single-electron wavefunctions (3.19), from which the electron density (3.16) is obtained. Self-consistency is achieved if the output density agrees with the input density within the specified accuracy. Otherwise a new input density for the next loop is calculated by mixing of the input and output density.

### 3.4. Exchange and Correlation in DFT

The crucial point in solving the one-electron Kohn-Sham equations is the knowledge of the exchange and correlation energy expressed in the  $E_{xc}[\rho]$  term. However, the exact form of  $E_{xc}$  as functional of the density  $\rho$  is unknown. Usually, the exchange and correlation energy are written as stand-alone parameter, and the exchange-correlation energy is simply the sum of both quantities, i.e.  $E_{xc} = E_x + E_c$ . The exchange energy  $E_x$  is known in terms of the one-particle wavefunctions, although this involves solving the computationally expensive exchange integrals (3.9), but such a formulation for the correlation energy at the comparable level of approximation is not available. Treating the exchange energy exactly might not compensate for the errors introduced by approximating the correlation energy. Therefore, the exchange and correlation energy are usually treated as a sum and at the same level of approximation.

This section is devoted to the development of suitable approximations for the exchange and correlation energy, where both terms are treated in a similar manner. The local density approximation (LDA) has been proposed in the original work by Kohn and Sham, and worked remarkable well despite the relatively simple approximation. The generalized gradient approximations (GGA) have been developed later on and yield a notable improvement over LDA in many cases. Ongoing work is devoted to improvement of the treatment of the exchange and correlation energy, but as our investigation using DFT predominantly used an representative of the GGAs to describe  $E_{xc}$ , we restrict the discussion to only LDA and GGA.

#### 3.4.1. Local Density Approximation

The local density approximation (LDA) was initially proposed in the work by Kohn and Sham, as the authors argued that solids can be considered as being close to the limit of the homogeneous electron gas, where the exchange and correlation are local quantities. Within this approximation, the exchange-correlation energy is simply

$$E_{xc}^{\text{LDA}}[\rho] = \int d^3r \rho(\vec{r}) \epsilon_{xc}^{\text{hom}}[\rho(\vec{r})] \quad (3.27)$$

which represents an integral over all space with the exchange-correlation energy density  $\epsilon_{xc}^{\text{hom}}[\rho(\vec{r})]$  at each point assumed to be the same as in a homogeneous electron gas with that density.

Therefore, the only information required is the exchange-correlation energy of the homogeneous electron gas as function of the density. Indeed, analytical expressions for the exchange [214], given as a simple analytic form, and correlation energy [217], derived from Monte Carlo methods, in the homogeneous electron gas were already known.

#### 3.4.2. Generalized Gradient Approximation

Generalized gradient approximations have been developed in order to address inhomogeneities in the electronic density. The step beyond the local density approximation is due to considering

gradients of the electronic density. Within GGA, the exchange-correlation energy term is written as

$$\begin{aligned} E_{\text{xc}}^{\text{GGA}}[\rho] &= \int d^3r \rho(\vec{r}) \epsilon_{\text{xc}}[\rho(\vec{r}), |\vec{\nabla} \rho(\vec{r})|] \\ &= \int d^3r \rho(\vec{r}) \epsilon_{\text{xc}}^{\text{hom}}[\rho(\vec{r})] F_{\text{xc}}[\rho(\vec{r}), |\vec{\nabla} \rho(\vec{r})|], \end{aligned} \quad (3.28)$$

where  $\epsilon_{\text{xc}}^{\text{hom}}[\rho(\vec{r})]$  is the exchange-correlation energy density for the homogeneous electron gas and  $F_{\text{xc}}$  is a dimensionless quantity that can be properly chosen to modify the behavior at large gradients in order to preserve desired properties.

So far, a variety of different forms of  $F_{\text{xc}}$  have been proposed. Widely used forms are the so-called B88 by Becke [218], PW91 by Perdew and Wang [219], PBE by Perdew, Burke and Ernzerhof [220] and the newly proposed PBEsol [221]. Among the different proposed forms of  $F_{\text{xc}}$ , some were explicitly fitted to experimental values, e.g. the BLYP [222], which has been fitted to experimental molecular data, while other forms are simply chosen to satisfy as many properties and limits as possible, without using any experimental input as fitting parameter, e.g. PW91 [219] and PBE [220]. We tested our results with respect to different choices of the xc functional, c.f. Sec. 4.3 and A.4.

## 3.5. Basis Sets and *k*-point Sampling

### 3.5.1. Basis Sets

Solving the many-body problem via Hartree or Hartree-Fock approximation or DFT requires a mathematical representation of the corresponding single-electron wavefunctions. Using a proper basis set  $\phi_{\alpha}(\vec{r})$ , each single-electron wavefunction is represented as a linear combinations of the wavefunctions of the basis set

$$\Phi_i(\vec{r}) = \sum_{\alpha=1}^N c_{i\alpha} \phi_{\alpha}(\vec{r}). \quad (3.29)$$

with  $\Phi_i$  as single-electron wavefunction,  $\phi_{\alpha}$  are wavefunctions of the basis set of size or dimension  $N$ , respectively, and  $c_{i\alpha}$  are expansion coefficients of the wavefunction  $i$ .

The usage of a specific basis set often depends on the investigated atomic system, in order to solve the electronic problem with minimum effort, i.e. the number of wavefunctions in the basis set should be as small as possible. For molecular systems, the most common approach is the expansion of the single-electron wavefunction, or molecular orbitals, in terms of atomic orbitals, which are centered on the atomic nuclei. Examples for these atom-centered atomic orbitals are Slater-type [223, 224] or Gaussian-type [225] orbitals. A common approach for periodic systems (often used in materials science) are plane wave basis sets. The advantage is that plane waves naturally fulfill the periodic boundary conditions. This is in line with the

Bloch theorem [226], stating that for a periodic system the wavefunctions must be composed of a phase factor and a periodic part that captures the translational periodicity of the unit cell. Plane waves are also the natural solution of the Schrödinger equation for a constant potential, e.g. for a free electron.

#### 3.5.2. k-point Sampling

Owing to the Bloch theorem, the electronic wavefunction must fulfill the same periodicity as the unit cell, apart from a phase factor that is related to the wave vector  $\vec{k}$ . The electronic charge density is then calculated from the wavefunction, and as the system is periodic, the electronic charge density is repeated in all periodic images of the unit cell. Therefore, using the Bloch theorem reduces the problem of calculating an infinite number of electronic wavefunctions to a problem of calculating a finite number of electronic wavefunctions at an infinite number of points in the unit cell determined by the wave vector  $\vec{k}$ , denoted as k-points. However, as the wavefunctions at k-points that are very close together will be almost identical, one can approximate the infinite number of k-points by interpolating between a finite number of k-points which are uniformly distributed in the unit cell. This is referred to as k-point mesh. Here, one k-point of the finite set is representative for a region of k-points of the infinite set. In practice, the number of required k-points is dependent on the system. Metallic systems, for example, require finer k-point meshes as insulators or semiconductors because the Fermi surface needs to be sampled precisely in a metal [227]. The number of required k-points can be further reduced by taking into account the symmetry of the unit cell. k-points that sample the same region in the unit cell will give identical results, thus it is sufficient to solve for one k-point and introduce weight factors that account for the number of k-points that sample the same region in the unit cell. The part of the Brillouin zone which contains all required information in order to describe the whole zone is referred to as the irreducible wedge or irreducible part of the Brillouin zone.

#### 3.6. Pseudopotentials

According to the Bloch theorem the electronic wavefunction can be expanded using a discrete set of plane waves. However, an extremely large plane wave basis set would be necessary to describe the core electron wavefunction and the rapid oscillations of the valence electron wavefunction in the core region. With the help of the pseudopotential approximation a much smaller plane wave basis set is sufficient to describe the electronic system properly.

The basic idea of the pseudopotential approximation makes use of the fact that most of the properties of solids are predominantly determined by the valence electrons, as these participate in chemical bonding, and to a much lesser extent by the core electrons. Instead of treating the core electrons explicitly in the calculation, in the pseudopotential approximation the potential arising from the nucleus is replaced by a pseudopotential that contains both the strong Coulomb potential of the nucleus and the effects of the core electrons on the valence

electrons. Thus, the true wavefunctions of the valence electrons are replaced by new pseudo wavefunctions. However, the pseudopotential has to be constructed in a way that the phase shifts, or scattering properties, are identical to the original all-electron potential, although the radial pseudo wavefunction has no nodes in the core region. Outside the core region the pseudo wavefunction has to be identical to the true wavefunction of the valence electrons (Fig. 3.2).

The origin of modern pseudopotentials can be attributed to the pioneering work by Phillips and Kleinmann [228], who showed that one can construct a smooth valence wavefunction by a suitable combination of the core and true valence wavefunction, an approach inspired by the orthogonalized plane wave (OPW) method of Herring [229], whereas the new smooth valence wavefunction is not orthogonalized to the core wavefunctions. The pseudo wavefunction satisfies a modified Schrödinger equation, whereas a new pseudo-Hamiltonian can be identified which still reproduces the same eigenvalues as the original Hamiltonian, and comprises a modified potential, referred to as pseudopotential.

However, in this approach the normalized pseudo wavefunction had a different amplitude compared to the true wavefunction, although the shape of both wavefunctions was identical. The mismatch in the amplitudes lead to incorrect charge distributions of the valence electrons in the case of the pseudo wavefunctions, leading to an incorrect description of the bonding properties. A suggested approach was to renormalize the pseudo wavefunction in order to ensure the identity of the pseudo and true wavefunction outside the core region, referred to as norm-conserving pseudopotentials [230,231]. In addition, the norm-conservation condition also yields pseudopotentials that are accurate and transferable, i.e. pseudopotentials constructed for a specific environment, e.g. a single atom, can also describe the properties of the pseudo wavefunctions, and therefore the charge distribution of the valence electrons, in different environments, e.g. molecules or solids.

One of the disadvantages of norm-conserving pseudopotentials is that they are still relatively hard, i.e. the usage is computationally expensive as a relative large plane wave basis set is required for computation. In order to construct smoother pseudopotentials, Vanderbilt [232] proposed to decompose the pseudopotential into a sum of a smooth part and a rapidly varying function that is localized on each ion, a procedure that is formally related to the OPW method by Herring. These pseudopotentials result not only in less demanding calculations, but also

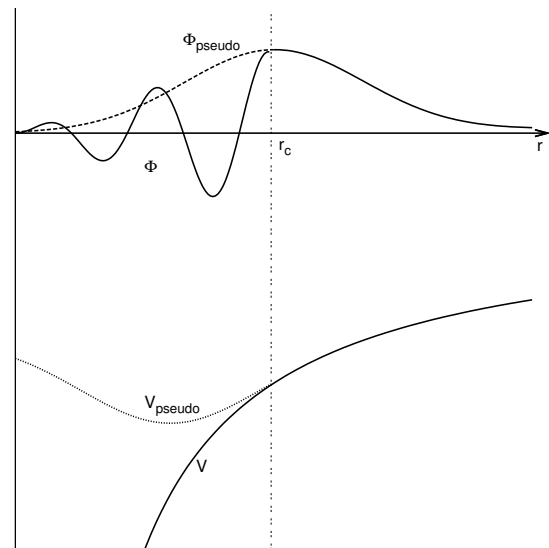


Figure 3.2.: Schematic illustration of the all-electron and pseudoelectron potentials and the corresponding wavefunctions (after Ref. [227]).

improve the accuracy compared to the norm-conserving pseudopotentials, and are referred to as ultrasoft pseudopotentials.

Also related to the OPW method is the approach by Blöchl [233] referred to as projected augmented wave (PAW) formulation. In this approach, the valence wavefunctions are expressed as the sum of smooth pseudo wavefunctions and rapidly varying terms localized in the core region. The main difference of the PAW formulation with respect to the concept of a pseudopotential is that the PAW method keeps the all-electron wavefunction, including also the core wavefunctions. In our investigation we used PAW potentials throughout.

## 3.7. Limitations of DFT

Although the physics and chemistry community accepted density functional theory as a versatile tool to calculate the properties of molecules and solids, such as binding energies, activation barriers or vibrational properties [234], there are a number of features that are not well reproduced in DFT. The origin of this failure is predominantly due to the approximations that have been introduced in the derivation of the Kohn-Sham single-electron equations. A few well-known failures and limitations will be summarized in here, as well as developed methods and approaches in order to provide a better and more accurate description of the system.

Density functional theory has been developed as a ground state theory. Therefore, physical quantities which require a proper treatment of the excited states are often poorly described and deviate from experimental results. A well-known failure of DFT is the tendency to underestimate the band gaps compared to the experimental values [235, 236]. Methods like the GW approximation [237] or time-dependent DFT [238] can be used to calculate reliable excitation energies, although the increased computational cost of these methods usually limits their application.

Kohn and Hohenberg formulated density functional theory as an exact theory for many-body systems, yielding the exact ground state energy if the exact form of the functional is known. However, the exact form of the exchange and correlation energy is not known, and the contribution to the total energy of a many-body system is represented by an approximation. Obviously, the agreement of the obtained ground state properties of the considered system with experimental values is highly dependent on the quality of the approximations. Although LDA represents the simplest approximation of the exchange and correlation energy, it yields remarkably accurate values for a variety of physical properties of solids, while it fails for others. While the geometry of molecules and solids are usually accurate, LDA tends to overbind, yielding consistently shorter equilibrium distances and overestimates the binding energy compared to experimental values [239]. The binding trends, however, are usually well described [240]. Furthermore, LDA predicts the wrong ground state for some elements. An example is iron [241]. On the contrary, the GGAs provide a better description of binding and atomic energies [242], among more accurate equilibrium distances. However, some properties of semiconductors and noble metals are better described by LDA compared to GGA.

Van der Waals interactions, arising from fluctuations in the dipole fields, represent a dynamical correlation effect, that is not captured in either LDA or GGA [242]. Methods developed to account for the van der Waals interaction enter as long-range part in the electron-electron interaction [243].

Systems with strong correlation effects, usually transition metal oxides or rare-earth metal compounds with localized and strongly interacting electrons, are also not well described within standard DFT. A well-known approach in order to account for the strong correlation effects is LDA+U [244], where an additional orbital-dependent interaction is taken into account for the highly localized electrons.

### 3.8. Computational Details

All density functional theory calculations presented in the sections 4 and 5 use the projector augmented waves method [233, 245] as implemented in VASP [246–249] and the Perdew-Burke-Ernzerhof (PBE) functional [220] within the generalized gradient approximation (GGA) for the exchange-correlation functional. As the ground state of iron is ferromagnetic, all calculations have been performed spin-polarized, unless stated otherwise. For every element we performed extensive convergence tests with respect to plane wave cutoff and k-point density in order to assure the formation energy differences to be converged within less than typically 1-2 meV/atom, see section A.4 in the appendix.

In section 4 we investigate the phase stability in the binary Fe-B system. The convergence tests yield a plane wave cutoff of  $E_{\text{cut}} = 450 \text{ eV}$  and a k-point density of  $\Delta k = 0.022 \text{ \AA}^{-1}$ , and are primarily required for the suitable description of iron. Throughout the study, we use k-point meshes of Monkhorst-Pack type [250, 251]. We use the first-order Methfessel-Paxton scheme for smearing with 0.1 eV and the conjugate-gradient algorithm implemented in VASP to optimize each structure with respect to atomic coordinates, cell volume and shape. After optimization, the volume of the cell has been varied in the range of -5%:5% in 1% steps and the total energy for each cell has been calculated using the tetrahedron method with Blöchl corrections. The equilibrium volume and total energy have been estimated by fitting the resulting  $E(V)$  curve to the Murnaghan equation of state [252]. All calculations were performed with the high-throughput environment `strucscan` (Sec. A.3).

In section 5 we investigate the behavior of boron point defects in  $\alpha$ -iron. Apart from the behavior of single boron point defects, we further investigated the interaction of boron with other point defects. In particular, we considered hydrogen and elements from the first and second row of the p-block in the periodic table that are important in steel manufacturing: carbon, nitrogen, oxygen and aluminum, silicon, phosphorus, sulfur. In order to discuss trends in the interaction associated with the number of valence electrons, we further considered fluorine, neon, chlorine and argon. The convergence tests showed that the plane wave cutoff and k-point density of the binary Fe-B system we used in section 4 is sufficient to describe hydrogen, aluminum, silicon, phosphorus and sulfur, but carbon, nitrogen and oxygen require an increase of the plane wave cutoff to  $E_{\text{cut}} = 525 \text{ eV}$ . In diagrams comparing the trends across

### *3. Electronic Structure Calculations*

---

the first p-block row, the corresponding configurations for the binary Fe-B system have been recalculated using the higher plane wave cutoff. Additional calculations for the validation of trends with the number of valence electrons have been performed with the same plane wave cutoff as corresponding elements in the p-block row.

All convergence tests regarding the plane wave cutoff and the number of k-points for the considered elements in this investigation are summarized in section A.4.



## 4. Iron-Boron Binary Compounds

*"A man can't tamper with nature beyond certain limits."*

*Howard Phillips Lovecraft*

*The Case of Charles Dexter Ward*

### 4.1. Introduction

Among the binary systems that consist of a transition metal (TM) and a p-block element that were investigated with the structure maps approach in chapter 2, the transition metal borides stand out due to their considerable practical importance and fundamental interest for science, technology and industrial applications. Examples for important properties are high melting temperatures, high hardness, good creep resistance, high electrical and thermal conductivity as well as chemical stability and inertness, which makes the transition metal borides ideal materials to provide oxidation resistance at high temperatures [253–262]. Recently, the interest in these materials has been renewed due to the discovery of superhard  $\text{ReB}_2$  [263]. Its synthesis followed a new design principle for new ultra-hard materials by combining small, strong covalent bonding elements with large, electron-rich transition metals [264–266].

Iron borides in particular are widely used as hard and protective coatings on steel surfaces for improved wear and corrosion resistance of the material [86–92]. The coating is produced via the process of boriding (or boronizing) which includes the deposition of boron and an additional heat treatment, e.g. in the form of laser irradiation [90] or a thermochemical process [91] to form the borides.

Iron borides formed in the microstructure of high-boron steels improve the tensile strength [93] of the steels, while boride formation reduces the hardenability of steels, as the hardenability is related to the amount of solute boron located at grain boundaries. Heat treatment during fabrication above certain temperatures leads to the formation of borides, which reduces the amount of solute boron, thus reducing the impact on the hardenability of steels [267, 268].

The experimental phase diagram [269–272] (Fig. 4.1(a)) from Ref. [272]) lists two compounds in the Fe-B system, the first at a Fe-B composition of 2:1 and the second at a composition of 1:1. The  $\text{Fe}_2\text{B}$  phase (Fig. 4.1(b)) corresponds to the *Strukturbericht* designation C16, the  $\text{CuAl}_2$  prototype with a tetragonal unit cell with 12 atoms, having the space group  $I4/mcm$  (space group # 140) and the Pearson symbol  $tI12$  [273, 274]. The FeB phase (Fig. 4.1(c)) corresponds to the *Strukturbericht* designation B27, the FeB prototype with an orthorhombic

#### 4. Iron-Boron Binary Compounds

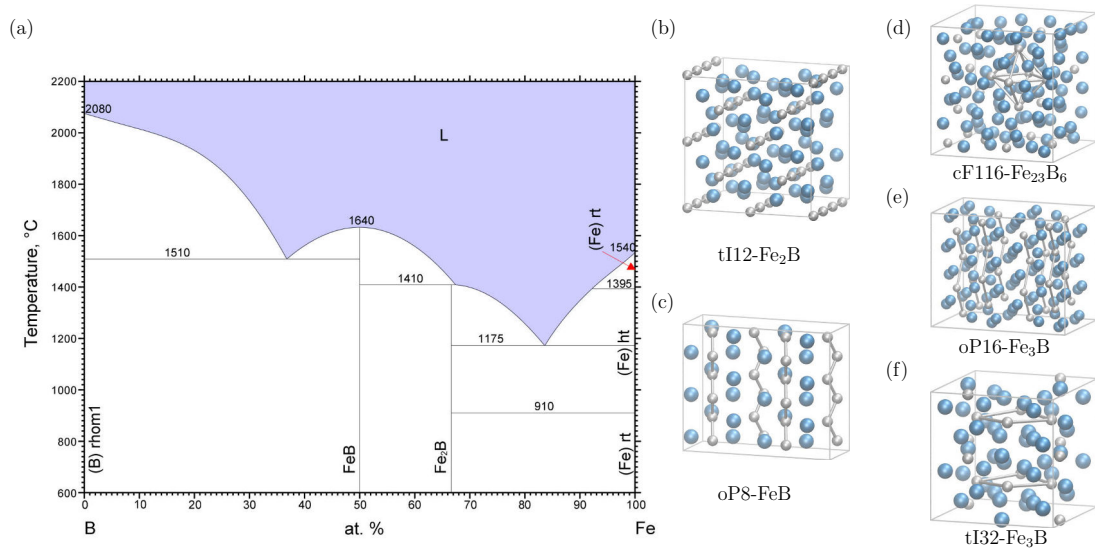


Figure 4.1.: (a) Fe-B phase diagram after Ref. [272] from [193]. Crystal structures of stable compounds in Fe-B system: (b) tI12-Fe<sub>2</sub>B and (c) oP8-FeB. Crystal structures of metastable compounds: (d) cF116-Fe<sub>23</sub>B<sub>6</sub>, (e) oP16-Fe<sub>3</sub>B and (f) tI32-Fe<sub>3</sub>B.

unit cell with 8 atoms having the space group Pnma (# 62) and the Pearson symbol oP8 [273, 274].

Experiments have also revealed the existence of two metastable compounds in the iron-rich region, with the Fe:B composition 23:6 and 3:1. The Fe<sub>23</sub>B<sub>6</sub> phase (Fig. 4.1(d)) is based on the *Strukturbericht* designation D8<sub>4</sub>, the Cr<sub>23</sub>C<sub>6</sub> prototype with a 116-atom cubic unit cell, space group Fm $\bar{3}$ m (# 225) and Pearson symbol cF116 [275]. The Fe<sub>3</sub>B compound is known to crystallize in two different crystal structures. The first one (Fig. 4.1(e)) is based on cementite (*Strukturbericht* designation D0<sub>11</sub>), the Fe<sub>3</sub>C prototype with space group Pnma (# 62) and Pearson symbol oP16 [276, 277]. The second one (Fig. 4.1(f)) is based on the Ni<sub>3</sub>P prototype with space group  $\bar{1}4$  (# 82) and Pearson symbol tI32 [277].

The electronic and structural properties as well as the stability of selected iron borides have been addressed in previous theoretical studies [278–286]. A recent theoretical study scanned the iron-rich domain up to 1:1 composition as well as the domain of dilute iron in boron, calculating the stability of known stable and metastable compounds as well as a selection of compounds from chemically similar binary systems [287]. However, the boron-rich domain in the Fe-B system has not yet been addressed.

An experimental study by Voroshnin *et al.* [288] found evidence of a FeB<sub>2</sub> phase with a crystal structure identical to AlB<sub>2</sub>. However, this compound was not detected in subsequent studies, and a FeB<sub>2</sub> phase is not listed in the latest experimental phase diagrams. The existence of a FeB<sub>2</sub> phase of AlB<sub>2</sub> type was discussed in literature and is still a controversial issue [289, 290]. Transition metal borides of AlB<sub>2</sub> type exist for the early transition metals. Reference [291] lists

manganese, to the left of iron in the periodic table, as 3d element with the largest number of valence electrons having a diboride phase of  $\text{AlB}_2$  type. However, the latest experimental phase diagram of the Mn-B system lists the diboride of  $\text{AlB}_2$  type as high-temperature phase [292]. We also do not list this phase in the Mn-B system (c.f. Fig. 2.8). It has been argued that the governing factor determining the existence of a diboride of  $\text{AlB}_2$  type is the size of the transition metal, with the atomic size of iron being too small for the formation of this phase [289]. Further, Duhaj and Hanic report the existence of a metastable  $\text{Fe}_4\text{B}$  phase [293, 294] which transforms into the tetragonal  $\text{Fe}_3\text{B}$  phase after ageing. Hohnke and Parthe [204] investigated the crystal structures of known monosilicides and monogermanides and suggest that compounds which crystallize within the FeB structure in general have a low-temperature modification, being isostructural to CrB. Experimental results also suggest that the Fe-B system possesses a low-temperature modification at 1:1 composition. In their phase diagram, Portnoi *et al.* [295] separated the 1:1 FeB phase into the low-temperature (designated as  $\alpha$ -FeB) and high-temperature (designated as  $\beta$ -FeB) modification. However, the crystal structure of the low-temperature modification is not resolved in the literature: Barinov *et al.* [296] found the crystal structure of CrB as low-temperature modification while according to Kanaizuka [94,95] a crystal intergrowth of both CrB and FeB represents the low-temperature modification. Portnoi *et al.* [295] also list a boron-rich alloy in the phase diagram, referred to as  $\text{FeB}_{19}$ . The authors assume this phase to be a distortion of one of the polymorphs of boron, namely  $\beta$ -rhombohedral boron. In addition, Balani *et al.* [297] report the existence of a phase with even higher boron content: a rhombohedral structure designated as  $\text{FeB}_{49}$  that is metastable.

In this section we will investigate the stability of compounds in the Fe-B system, with special emphasis on the possible existence of boron-rich compounds. For the newly identified possible ground states, we further discuss proper synthesis routes. Boron-rich TM-B have recently attracted a lot of attention due to the discovery of the remarkable  $\text{ReB}_2$  compound, which exhibits superior hardness and is the first TM boride which can scratch diamond, the hardest material known [263]. Due to the usage of iron borides, in general t12- $\text{Fe}_2\text{B}$  and oP8-FeB, in industry as hard and protective coatings on the steel surfaces [86–92], we briefly discuss the expected mechanical properties of the newly identified possible ground states and compare with the known Fe-B compounds and  $\text{ReB}_2$ .

## 4.2. Heat of Formation

In order to determine the stability of a compound, we calculate the heat of formation  $E_f$ , defined as the energy difference between a compound and the corresponding ground states of the elements of the compound, normalized to the energy per atom

$$E_f = E_{\text{Fe}_{1-x}\text{B}_x} - (1-x)E_{\text{gs,Fe}} - xE_{\text{gs,B}} \quad (4.1)$$

$E_{\text{Fe}_{1-x}\text{B}_x}$  denotes the energy of a compound per atom while  $E_{\text{gs,Fe}}$  and  $E_{\text{gs,B}}$  are the energies of the ground states of iron and boron per atom.  $x$  represents the boron content in the  $\text{Fe}_{1-x}\text{B}_x$  compounds. A negative value of  $E_f$  implies the stability of a compound against decomposition into the basic constituents while a positive value means that decomposition will occur.

The knowledge of the ground state is required for the correct reference energy  $E_{\text{gs},i}$  and therefore the correct estimation of phase stability. Iron is known to have a bcc structure below 912 °C and to be ferromagnetic below the Curie temperature.

For boron the picture is more complicated: At ambient pressure, boron has two polymorphs designated as  $\alpha$ -rhombohedral ( $\alpha$ -B) and  $\beta$ -rhombohedral ( $\beta$ -B) boron. At high temperatures,  $\beta$ -B is referred to as the most stable polymorph [298]. However, theoretical investigations show consistently  $\alpha$ -B (hR12) being more stable than  $\beta$ -B (hR105) at zero temperature [299–303]. The inclusion of vibrational contributions stabilizes  $\beta$ -B with respect to  $\alpha$ -B at elevated temperature [300, 301]. Furthermore, Widom *et al.* [302] showed that inclusion of fractional occupations of some of the Wyckoff positions of  $\beta$ -B leads to the stabilization of  $\beta$ -B over  $\alpha$ -B. However, the altered occupation of the Wyckoff sites breaks the symmetry of the rhombohedral unit cell. Recently, van Stetten *et al.* [303] modeled  $\beta$ -B using a 106-atom cell including fractional occupations and interstitial atoms, with a difference in the total energy of less than 1 meV/atom with respect to  $\alpha$ -B. By inclusion of the zero point energy the 106-atom  $\beta$ -B structure is stabilized over  $\alpha$ -B. Here, we will use  $\alpha$ -B as boron ground state throughout this study for the following reasons: First, the marginal total energy difference between  $\alpha$ -B and  $\beta$ -B of 1 meV/atom [303] is beyond the accuracy of standard DFT. Second, we do not include the vibrational contributions.

### 4.3. Phase Stability

Input files for the crystal structures have been obtained from the Pearson's Crystal Database (PCD) [178] and the database provided by the Naval Research Laboratory - Center for Computational Materials Science [304]. We focused on known prototypical crystal structures adopted in transition metal - boron systems. Furthermore, we also considered additional crystal structures that are adopted by TMs and other light p-block elements as well as common TM-TM compounds. A compilation of the calculated crystal structures with additional information is given in Sec. A.5.

The heat of formation versus the boron content in  $\text{Fe}_{1-x}\text{B}_x$  compounds is shown in Fig. 4.2. Connecting the crystal structures with the lowest  $E_f$  represents the boundary of the convex hull, defining the region of stable phases. Crystal structures above the convex hull are not expected to exist, at least not at zero Kelvin, and to decompose into stable compounds and/or the constituent elements in their ground state. Metastable phases which have been observed in experiment are expected to have a heat of formation very close to the boundary of the convex hull.

In agreement with the experimental phase diagram we observe a stable tI12- $\text{Fe}_2\text{B}$  compound (Fig. 4.3(a)). The known metastable phases cF116- $\text{Fe}_{23}\text{B}_6$  and both  $\text{Fe}_3\text{B}$  compounds are very close to the boundary of the convex hull, with an energy difference of 19 meV/atom for cF116- $\text{Fe}_{23}\text{B}_6$ , and 17 meV/atom and 22 meV/atom for  $\text{Fe}_3\text{B}$  in the oP16- $\text{Fe}_3\text{C}$  and tI32- $\text{Ni}_3\text{P}$  crystal structure, respectively. On the iron-rich side, we further observe additional crystal

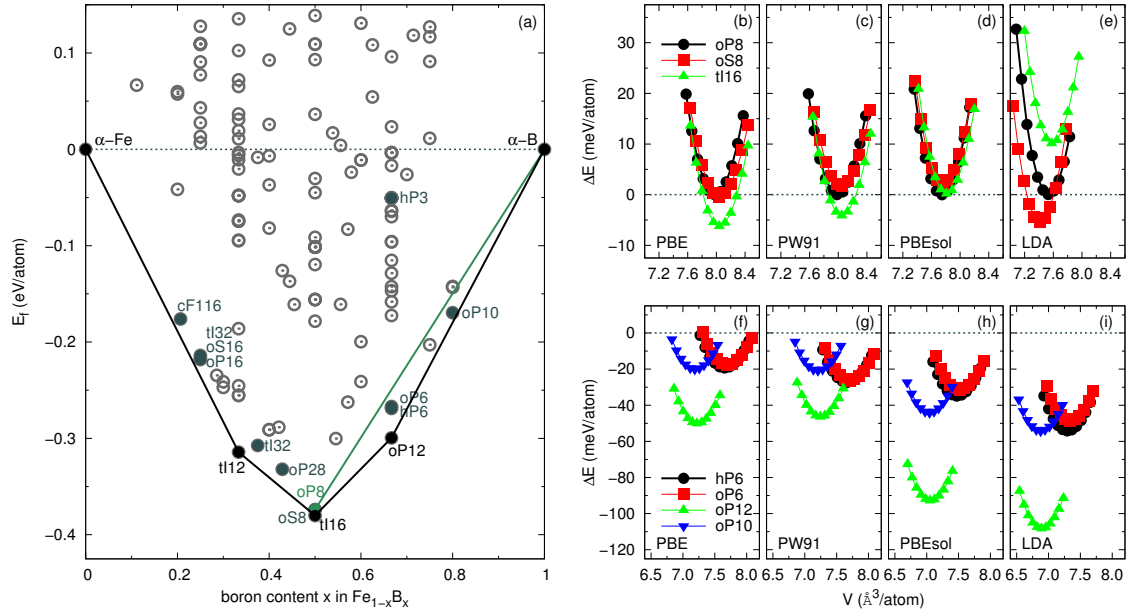


Figure 4.2.: (a) Heat of formation  $E_f$  for the considered crystal structures. (b-f) Relative stability of the competing 1:1 crystal structures, oP8-FeB, oS8-FeB, tI16-FeB, dependent on xc functional. (g-j) Relative stability of the boron-rich phases, oP6-FeB<sub>2</sub>, hP6-FeB<sub>2</sub>, oP12-FeB<sub>2</sub>, oP10-FeB<sub>4</sub> for various xc functionals.

structures with an energy difference in the range of 20 meV/atom towards the tie-line. oS16-Re<sub>3</sub>B, tI32-Cr<sub>5</sub>B<sub>3</sub> and oP28-Ni<sub>4</sub>B<sub>3</sub> are 19, 23 and 20 meV/atom above the tie-line, respectively. Due to the small energy difference, these structures represent viable candidates for metastable phases, although none of them were so far observed in experiment. At 1:1 composition, we find three different crystal structures close in energy, namely oP8-FeB, oS8-FeB and tI16-FeB. The latter one has the lowest  $E_f$ , although the energy difference with the other two phases, which are nearly degenerate, is very small, around 6 meV/atom. This finding disagrees with the experimental phase diagram, that lists oP8-FeB as stable phase at 1:1 composition.

Because of the disagreement with respect to the most stable experimental 1:1 phase and the very similar energies of the three crystal structures, we investigated the influence of the xc functional on the stability sequence. The choice of the xc functional represents one of the largest uncertainties in every DFT calculation. Thus, the most stable tI16-FeB might be solely an artifact of the PBE functional [220]. In addition, we checked the relative stability of oP8-, oS8- and tI16-FeB with PW91 [219], the new PBEsol [221] and LDA [217,305] (Fig. 4.2(b-e)). Despite the usage of different functionals, all three crystal structures are very close in energy, although we find a difference in the stability sequence. LDA is the only functional to favor oS8-FeB, while all three GGAs consistently favor tI16-FeB instead. Thus, the results are not solely an artifact of the PBE functional, as other GGAs yield the same stability sequence. However, the investigation of the vibrational properties of the three 1:1 compounds revealed that tI16-

FeB, at zero Kelvin marginally the most stable 1:1 compound, is destabilized at elevated temperature as we could show in a collaboration with the group of AN Kolmogorov [306]. This may explain why tI16-FeB has never been observed in experiment.

The reason for the very close energies independent of the xc functional might be the close geometrical relationship between the three crystal structures [204]. The close similarity in the three compounds was already discussed in Sec. 2.3.7. While the type of coordination polyhedra is not consistent among the three crystal structures, the coordination number and composition of the coordination polyhedra for the iron and boron Wyckoff sites are identical. This similarity becomes obvious in the nearest neighbor histograms (Fig. 4.3(b-d)). The boron atoms in oP8 and oS8 form infinite zigzag chains running along one of the crystallographic axes of the crystal structure. The main difference between oP8 and oS8 is how the boron chains are arranged with respect to each other. In oP8 the neighboring chains are tilted with respect to each other, while the second nearest neighbor chains have the same arrangement. In oS8, all boron chains have the same, parallel arrangement. tI16 has the same infinite zigzag boron chains, but in this crystal structure the chains run along two different crystallographic axis. Despite the differences in the alignment of the boron chains, the nearest neighbor histograms of the three crystal structures highlight their similarities. Two histograms are shown for each structure, taking into account the two non-equivalent sites of the three crystal structures, one occupied by iron and the other by boron. The iron atoms are consistently surrounded by seven boron and six iron atoms. The bond distances are virtually identical among the three crystal structures, only the Fe-B distance in oS8 differs slightly and splits into two distinct distances. The boron atoms have consistently two boron and seven iron atoms as neighbors. The distances between the boron atoms are also virtually identical. In fact, the differences in the crystal structures only become obvious at distances above 3 Å, where slight variations in number of nearest neighbors and distances appear.

On the boron-rich side, the suggested FeB<sub>2</sub> phase of hP3-AlB<sub>2</sub> type is found to be unstable, with an energy that is around 203 meV/atom above the tI16-FeB ↔  $\alpha$ -B tie-line. Taking the experimentally accepted oP8-FeB as reference state, the FeB<sub>2</sub> of hP3-AlB<sub>2</sub> type is still 199 meV/atom above the tie-line. Thus, the existence of this phase can be ruled out. However, two prototypes at 1:2 composition in the considered dataset, namely hP6-ReB<sub>2</sub> and oP6-RuB<sub>2</sub>, are found below the tI16-FeB (oP8-FeB) ↔  $\alpha$ -B tie-line by 15 (20) meV/atom and 14 (18) meV/atom, respectively. While the former prototype is somewhat surprising, the latter prototype is known to appear in the Ru-B and Os-B system, with the two transition metals located in the same column as iron in the periodic table. The boron atoms form 2D layers in both phases, but have a different alignment (Fig. 4.3(e,f)). In oP6, the boron atoms align in an armchair configuration, while zigzag chains are found in hP6. However, the polyhedron analysis revealed that both phases are built of the same coordination polyhedra. Also the nearest neighbor histograms reveal similarities in the number and distance of neighbors, at least at short distances. The iron atoms are surrounded by eight boron atoms and six iron atoms. The distances vary slightly in oP6, but remain unchanged in hP6. The boron atoms have three boron and four iron atoms as nearest neighbors.

In a subsequent step and in close collaboration with AN Kolmogorov, ER Margine and S Shah

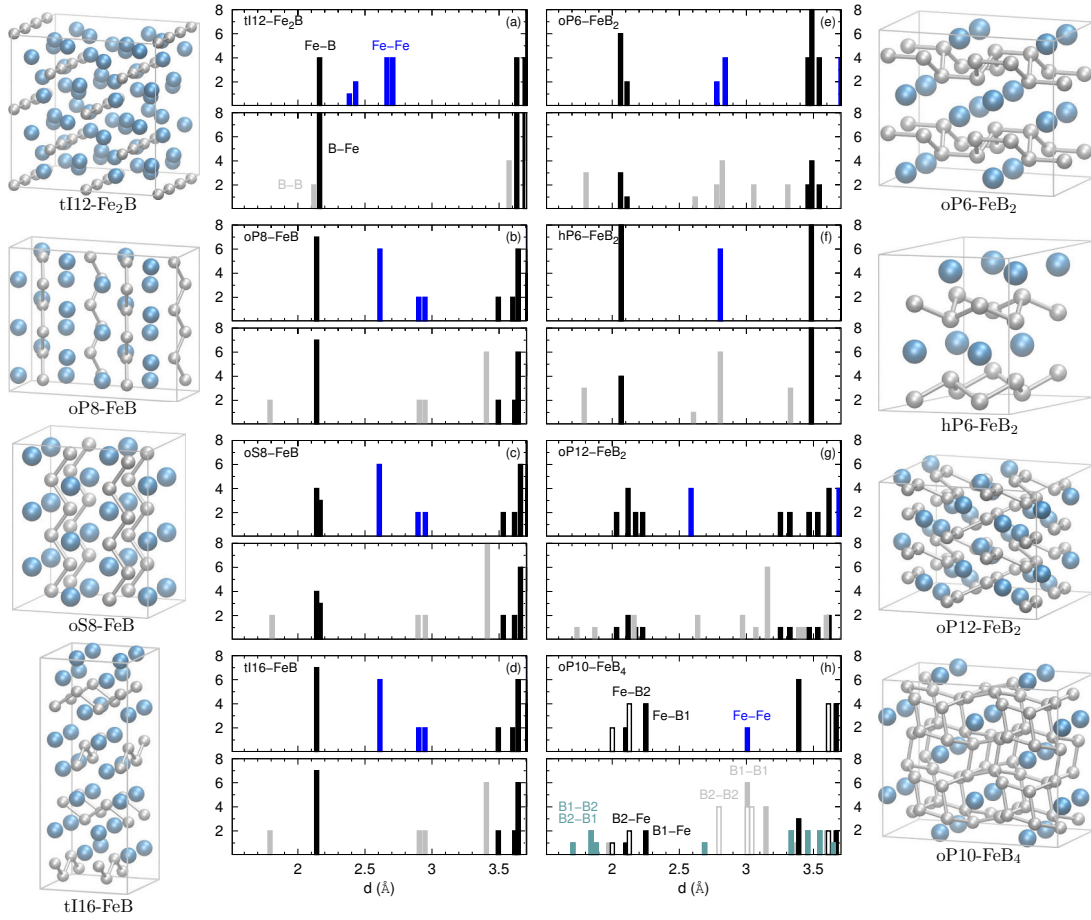


Figure 4.3.: The crystal structures and nearest neighbor histograms for (a) tI12-Fe<sub>2</sub>B, (b-d) oP8-,oS8-,tI16-FeB, (e-g) oP6-,hP6-,oP12-FeB<sub>2</sub> and (h) oP10-FeB<sub>4</sub>.

(University of Oxford), the boron-rich region of the Fe-B system has been investigated with the Module for *Ab Initio* Structure Evolution (MAISE) [307], that is linked with VASP and enables an evolutionary algorithm search for lowest  $E_f$  crystal structures [306]. The search has been constrained to 1:2, 1:3, 1:4 and 1:6 compositions that are most likely to occur. The evolutionary algorithm search at 1:2 composition identified a new viable ground state with simple orthorhombic Bravais lattice and 12 atoms in the unit cell, thus designated as oP12-FeB<sub>2</sub>, below the tI16-FeB (oP8-FeB)  $\leftrightarrow$   $\alpha$ -B tie-line by 46 (50) meV/atom. Unlike the oP6 and hP6 structures, the boron atoms form infinite chains instead of 2D layers (Fig. 4.3(g)). The nearest neighbor histogram for iron shows ten neighboring boron atoms instead of eight, found in oP6 and hP6. Furthermore, the distances vary more drastically than in oP6 and hP6. The polyhedron analysis includes the four iron atoms as nearest-neighbors, thus the coordination number of the iron site is fourteen. The boron atoms have four boron and five iron atoms as neighbors, again exceeding the number of neighbors in oP6 and hP6. However, the alignment

in the boron chains leads to a wide scattering of the B-B distances for the closest neighbors, a feature that has not been observed in the other crystal structures. Nevertheless, the nine-fold coordination of the boron site is in line with trends regarding the coordination number of boron (c.f. Fig. 2.10). At 1:4 composition, the evolutionary algorithm search identified a new crystal structure with simple orthorhombic Bravais lattice and ten atoms in the unit cell, thus designated as oP10-FeB<sub>4</sub>, that lies 18 (20) meV/atom below the tI16-FeB (oP8-FeB)  $\leftrightarrow$   $\alpha$ -B tie-line, but 10 meV/atom above the oP12-FeB<sub>2</sub>  $\leftrightarrow$   $\alpha$ -B tie-line. This crystal structure is geometrically closely related to the oI10-CrB<sub>4</sub> prototype, the main difference is the alignment of the boron atoms, having a rectangular shape in oI10-CrB<sub>4</sub>, but forming parallelograms in oP10-FeB<sub>4</sub> (Fig. 4.3(h)). The newly identified crystal structure has three non-equivalent sites, one occupied by iron and two by boron atoms. The nearest neighbor histograms show iron to be surrounded by twelve boron atoms, the two different boron non-equivalent sites only slightly varying in distance, and having no other iron atoms in the near vicinity. The polyhedron analysis reveals the two boron sites to be eight-fold and nine-fold coordinated, respectively, with five or six boron atoms, and three iron atoms. Again the boron-boron distances show a scattering, but weaker than in oP12-FeB<sub>2</sub>. The different alignment of the boron network in oP10-FeB<sub>4</sub> compared to oI10-CrB<sub>4</sub> substantially changes the coordination numbers. In oI10-CrB<sub>4</sub>, the transition metal site is fourteen-fold coordinated while the single boron site is only seven-fold coordinated. Thus, the new arrangement of the boron network in oP10-FeB<sub>4</sub> reduces the coordination number of the transition metal site, but increases the coordination number for the boron sites. With inclusion of vibrational contributions both crystal structures remain stable at elevated temperatures [306].

Again we investigated the influence of the xc functional on the relative stability of the boron-rich compounds of interest (Fig. 4.3(f-i)). Independent of the xc functional, all considered crystal structures lie below the oP8-FeB  $\leftrightarrow$   $\alpha$ -B tie-line. Furthermore, the near degeneracy of the energies of oP6-FeB<sub>2</sub> and hP6-FeB<sub>2</sub> is consistently found in GGAs, while a larger difference can be observed in the case of LDA.

	Fe	B	$E_f$ (meV/atom)	method	
Fe <sub>2</sub> B	$\alpha$	$\alpha$	-314	PAW-PBE	this work
	$\alpha$	$\alpha$	-330	USPP-PBE	[283]
	$\alpha$	$\beta$	-308	PAW-PW91	[287]
	$\alpha$	$\beta$	-231	expt.	[308]
	$\gamma$	$\beta$	-234	expt.	[309]
FeB	$\alpha$	$\alpha$	-374	PAW-PBE	this work
	$\alpha$	$\beta$	-368	PAW-PW91	[287]
	$\alpha$	$\beta$	-369	expt.	[308]
	$\alpha$	$\beta$	-335	expt.	[309]

Table 4.1.: Comparison of the calculated  $E_f$ , given in meV/atom along with the used reference states for iron and boron, for tI12-Fe<sub>2</sub>B and oP8-FeB with experimental and other theoretical values.



The calculated  $E_f$  values of the compounds in the experimental phase diagram,  $\text{tl12-Fe}_2\text{B}$  and  $\text{oP8-FeB}$ , are summarized in Tab. 4.1 along with other values from theory and experiment for comparison as well as the reference state for iron and boron. Our calculated value for  $\text{tl12-Fe}_2\text{B}$  is in very good agreement with previous studies, but deviates from experiment. However, the experimental measurements have been performed at elevated temperature, while the results obtained from theoretical investigations represent the total energy at zero Kelvin. Better agreement with experiment might be achieved by taking into account further contributions, e.g. the vibrational contribution to the total energy. For  $\text{oP8-FeB}$ , our calculated value agrees well with both previous theoretical investigations and experimental measurements.

#### 4.4. Possible Routes for Synthesis

Applied to the Cr-B system, the  $\text{ol10-CrB}_4$  compound listed in experimental phase diagrams [310] was found to be unstable with respect to the newly identified  $\text{oP10-FeB}_4$  prototype. In addition, our investigation of the vibrational properties by Kolmogorov *et al.* [306] showed the dynamical instability of the  $\text{ol10-CrB}_4$  compound, resulting in imaginary frequencies. Although the boron network is substantially distorted when going from  $\text{ol10}$  to  $\text{oP10}$ , the lattice parameters and simulated powder diffraction patterns are very similar, which may be the reason why the crystal structure of  $\text{CrB}_4$  was originally identified as  $\text{ol10}$ . A recent experimental investigation confirmed the theoretical prediction, and found  $\text{CrB}_4$  to adopt the  $\text{oP10}$  structure [311]. With Fe-B and Cr-B both adopting the  $\text{oP10}$  structure, one may assume that the pseudobinary  $\text{Fe}_x\text{Cr}_{1-x}\text{B}_4$  will also adopt the  $\text{oP10}$  structure under standard synthesis conditions. Indeed, for the past synthesis of ternary Fe-Cr-B compounds, no special requirements regarding the heat treatment or starting materials were mentioned, apart from cold compacting of the metal boron powders [312, 313]. Examples for such compounds are the metal-rich  $\text{MnB}_4$ -type compound [314], that due to the metal site occupation by iron and chromium is a  $(\text{Fe,Cr})_2\text{B}$  compound, or the  $\text{oP8-FeB}$ - and  $\text{oS8-CrB}$ -type compounds with partial substitution of the host metal atom with chromium and iron, respectively [312, 313].

The stability and geometrical as well as electronic properties of the pseudobinary  $\text{oP10-Fe}_x\text{Cr}_{1-x}\text{B}_4$  compound are investigated via the supercell approach. The supercells were created by up to three repetitions of the  $\text{oP10}$  unit cell along the three crystallographic axis, with the largest considered supercell containing 180 atoms. Up to two defect iron (chromium) atoms were introduced in the  $\text{oP10-CrB}_4$  ( $\text{oP10-FeB}_4$ ) supercell. In configurations with two defects, we also considered variations in the distance between the iron and chromium defects, respectively.

Stabilization of the pseudobinary  $\text{oP10-Fe}_x\text{Cr}_{1-x}\text{B}_4$  compound with respect to  $\text{oP10-CrB}_4$  and  $\text{oP10-FeB}_4$  is dependent on the occupation pattern of the metal atoms (Fig. 4.4(a)). Several configurations lie below the  $\text{CrB}_4\text{-FeB}_4$  tie-line. The largest stabilization is observed at  $x=0.5$  with 28 meV/f.u. below the tie-line. This value is comparable to the contribution from configurational entropy, arising from the disorder in the population of the metal sites. At 1000 K and  $x=0.5$  the configurational entropy  $\Delta G_{conf}(T) = -k_B T [x \ln x + (1-x) \ln(1-x)]$  is in the

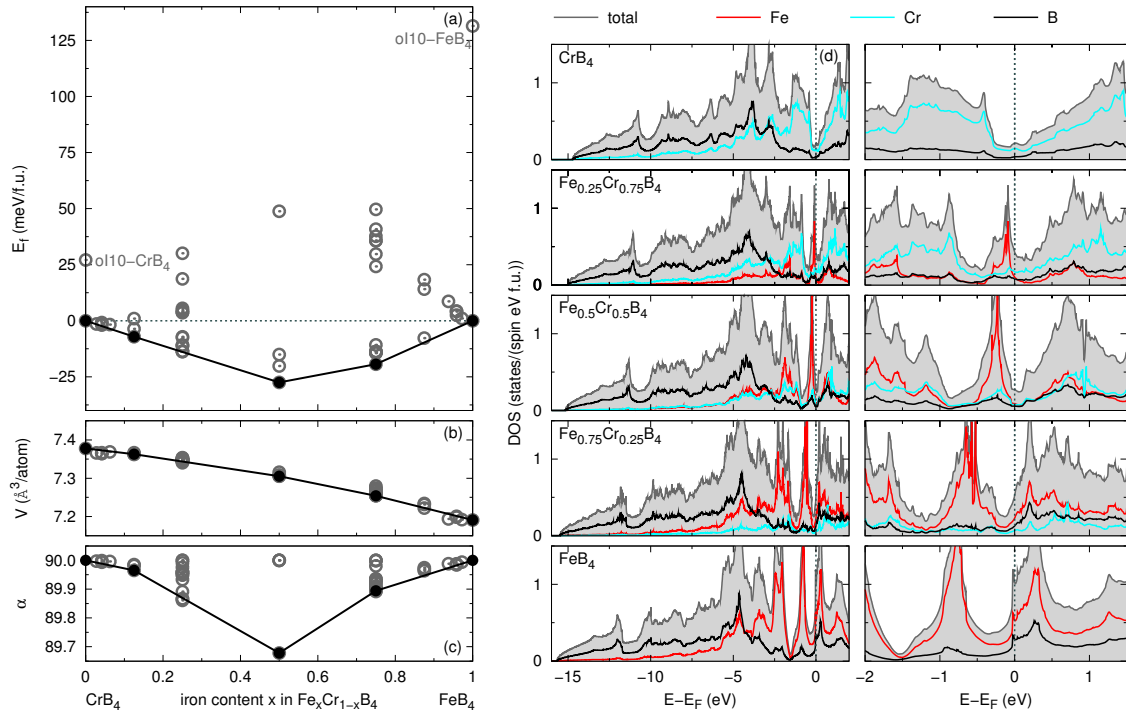


Figure 4.4.: (a) Relative stability, (b) volume per atom and (c) monoclinic distortion of pseudobinary oP10- $\text{Fe}_x\text{Cr}_{1-x}\text{B}_4$  compound. (d) Total and projected density of states for lowest energy compounds at  $x=0, 0.25, 0.5, 0.75, 1$ .

range of 60 meV/f.u. if all occupations are degenerate in energy. At  $x=0.5$  the iron-chromium mixture has the same number of valence electrons as manganese, and the Mn-B phase diagram [292] lists a compound at a TM:B composition of 1:4, namely mS10-MnB<sub>4</sub> [315]. Following the example of  $\text{Os}_{0.5}\text{W}_{0.5}\text{B}_2$  that is known to crystallize in the ReB<sub>2</sub> prototype [261], we investigated the relative stability of the pseudobinary  $\text{Fe}_{0.5}\text{Cr}_{0.5}\text{B}_4$  adopting the mS10-MnB<sub>4</sub> structure. However, the lowest energy configuration of mS10-MnB<sub>4</sub> type is above the  $\text{FeB}_4 \leftrightarrow \text{CrB}_4$  tie-line by 22 meV/f.u. Owing to the larger atomic size of chromium compared to iron, the volume per atom in the pseudobinary oP10- $\text{Fe}_x\text{Cr}_{1-x}\text{B}_4$  decreases with increasing iron content (Fig. 4.4(b)). The relationship is not exactly linear, and leaves a small excess volume of the oP10- $\text{Fe}_x\text{Cr}_{1-x}\text{B}_4$  compound. For some decorations of the metal atoms the orthorhombic unit cell is distorted into a monoclinic one (Fig. 4.4(c)). The compounds forming the boundary of the convex hull have the largest distortion of the unit cell, represented by the angle  $\alpha$  between two crystallographic axes, although the overall magnitude in the distortion is relatively small. The total and projected density of states (Fig. 4.4(d)) of the oP10- $\text{Fe}_x\text{Cr}_{1-x}\text{B}_4$  compounds drops rapidly at the Fermi level when going from oP10- $\text{FeB}_4$  to oP10- $\text{CrB}_4$  and is sensitive to the occupation pattern of the metal atoms at the iron-rich end.

Promotion of compound formation can also be achieved via application of medium pressures in the range of a few GPa in multianvil or diamond anvil cells. Pressure might improve the

thermodynamic stability or the reaction kinetics. Boron-rich  $\text{CdB}_4$  [316] and  $\text{NdB}_6$  [317] and metal-rich  $\text{Fe}_2\text{B}$  [318] materials represent examples for this synthesis route. In close collaboration with AN Kolmogorov we examined the response of the lowest energy compounds listed in Sec. A.5 of the appendix to hydrostatic pressure [319]. For both oP12- $\text{FeB}_2$  and oP10- $\text{FeB}_4$  the application of pressures lowers the corresponding formation energy. Thus the application of pressure might be the key for successful synthesis of these compounds.

## 4.5. Mechanical Properties

Owing to the usage of the tI12- $\text{Fe}_2\text{B}$  and oP8- $\text{FeB}$  phase as hard and protective coatings on steel surfaces, we investigated the newly identified boron-rich borides with respect to their mechanical properties, including also the expected hardness of the phases. This is of particular interest, as generally the hardness tends to increase with boron content [261]. However, due to the limitations of DFT with respect to the number of atoms in the considered systems, we are only able to make a statement on the intrinsic or microscopic hardness, which is in principle determined by the crystal geometry and the bond strength between adjacent atoms. The macroscopic hardness, in contrast, of the material also depends on the grain size, grain boundary orientation and the influence of defects.

In order to estimate the expected hardness, we follow two approaches. First, we determine the shear modulus  $G$  by calculation of the elastic constants for a given set of borides, as  $G$

	$\text{Fe}_2\text{B}$		$\text{FeB}$		$\text{FeB}_2$	$\text{FeB}_4$	$\text{ReB}_2$
	tI12	oP8	oS8	tI16	oP12	oP10	hP6
$C_{11}(\text{GPa})$	413	371	363	421	589	406	632
$C_{12}(\text{GPa})$	154	250	139	220	180	156	154
$C_{13}(\text{GPa})$	132	188	217	197	154	158	131
$C_{22}(\text{GPa})$		431	416		714	756	
$C_{23}(\text{GPa})$		209	197		133	150	
$C_{33}(\text{GPa})$	389	505	457	513	574	452	1005
$C_{44}(\text{GPa})$	148	207	189	184	274	217	248
$C_{55}(\text{GPa})$		118	202		201	143	
$C_{66}(\text{GPa})$	157	194	178	195	220	224	
$B(\text{GPa})$	228	287	257	286	311	274	339
$G(\text{GPa})$	143	138	153	157	231	187	266
$Y(\text{GPa})$	355	358	383	399	556	457	632
$\nu$	0.24	0.29	0.25	0.27	0.20	0.22	0.19

Table 4.2.: Calculated single-crystal elastic constants  $C_{ij}$ , the bulk ( $B$ ), shear ( $G$ ), and Young's ( $Y$ ) moduli and Poisson ratio ( $\nu$ ) for known and predicted Fe-B phases. Values for hP6- $\text{ReB}_2$  are added for comparison.

often correlates with the hardness [265, 266, 320–322], although a quantitative prediction of the materials' hardness based on the elastic properties alone is not possible [323]. Second, we follow the scheme described by Simunek and Vackar [324] and Simunek [325, 326], that allows to calculate the directionally dependent hardness based on the geometry of the crystal structure.

In order to determine the mechanical properties of the borides, we calculated the elastic constants by the application of a set of given strains on the crystal structure, leading to a deformation and therefore a change in the total energy of the system. The number of strain operations is equal to the number of independent elastic constants for the structure, i.e. 3 for cubic cells, 4 for hexagonal ones, 6 for tetragonal and 9 for orthorhombic ones, leading to a system of linear equations allowing to solve for the elastic constants  $C_{ij}$  dependent on the energy-strain relationship (Sec. A.7). Using then the Voigt-Reuss-Hill theorem [327] allows to determine the polycrystalline elastic (Young's) modulus  $Y$  and the shear modulus  $G$  for the considered phases, as summarized in Tab. 4.2. The bulk modulus  $B$  and the Poisson's ratio  $\nu$  are derived from the Young's and shear modulus.

The calculated single-crystal elastic constants fulfill the corresponding stability criteria [328] for cubic, tetragonal, orthorhombic and hexagonal cells, thus the crystal structures are mechanically stable. The elastic constants of the crystal structures listed in the experimental phase diagram, tI12-Fe<sub>2</sub>B and oP8-FeB, vary but lead to very similar polycrystalline Young's and shear modulus. The calculated single-crystal elastic constants for the competing crystal structures at 1:1 composition, oS8 and tI16, result in a larger Young's and shear modulus. The slightly larger elastic moduli for tI16 might be attributed to the boron chains running in two directions instead of one, as found in oP8 and oS8. The calculated elastic constants for tI12-Fe<sub>2</sub>B are generally in good agreement with a previous DFT calculation [284]. We note that the disagreements in some  $C_{ij}$  result in a very similar bulk modulus, but a significantly increased shear (compared to 60.2 GPa) and Young's modulus (compared to 184.4 GPa) in our case. However, our results for the shear and Young's modulus are in good agreement with DFT results from Ref. [283]. Our calculated bulk modulus is close to the experimental value of  $B = 164$  GPa [329] while our Young's modulus is in excellent agreement with experimental values of  $Y = 290$ – $343$  GPa [330–333]. For oP8-FeB our calculated Young's modulus agrees well with experimental values of  $Y = 284$ – $350$  GPa [332, 333]. In the case of the newly identified possible ground state oP12-FeB<sub>2</sub> the polycrystalline Young's and shear modulus calculated from the single-crystal elastic constants exceed the elastic moduli of the crystal structures with less boron content. Values for hP6-ReB<sub>2</sub> have been added for comparison. None of the elastic constants or elastic moduli of oP12-FeB<sub>2</sub> surpass the corresponding values for hP6-ReB<sub>2</sub>, which are in good agreement with previous DFT [334–336] and experimental studies [263, 266, 337]. However, oP12-FeB<sub>2</sub> still represents an interesting candidate for further experimental investigation due to its promising mechanical properties. The single-crystal elastic constants and polycrystalline elastic moduli for the crystal structure with the largest boron content, oP10-FeB<sub>4</sub>, are generally in the range or slightly larger than the corresponding values for tI12-Fe<sub>2</sub>B and the three crystal structures at 1:1 composition. The reason for the superior single-crystal elastic constants and polycrystalline elastic moduli of oP12-FeB<sub>2</sub> might be attributed to the

peculiar geometry of the crystal structure, especially the disintegration of the typical 2D boron layers found in other transition metal diborides into boron chains.

The original scheme proposed by Simunek and Vackar [324] provides a semi-empirical estimation of the materials' hardness based on the concept of bond strength. This parameter takes the hardness proportional to an energy value for the corresponding elements divided by the distance between the atoms and the number of nearest neighbors. Subsequent modifications of this approach included using tabulated values for the energy scale, instead of first-principles calculations [325], and the anisotropy of the hardness related to crystal orientation [326]. Using the tabulated values, Simunek estimated the hardness for hP6-ReB<sub>2</sub> to  $H(\mathbf{c}) = 46.7$  GPa,  $H(\mathbf{a}) = 39.7$  GPa and  $H(\mathbf{x}) = 38.1$  GPa, where  $\mathbf{x}$  is perpendicular to  $\mathbf{a}$  and  $\mathbf{c}$ . The mean value is  $H = 41.1$  GPa, and falls in the middle within the range of experimentally measured hardness of  $H = 30.1$ -55.5 GPa [263]. In the case of oP12-FeB<sub>2</sub> the hardness is calculated to  $H(\mathbf{x})=45$  GPa,  $H(\mathbf{y})=31$  GPa and  $H(\mathbf{z})=30$  GPa, with a mean value of about  $H=35$  GPa. For oP10-FeB<sub>4</sub>, the hardness is calculated to  $H(\mathbf{x})=35$  GPa,  $H(\mathbf{y})=28$  GPa and  $H(\mathbf{z})=35$  GPa, with a mean value of about  $H=33$  GPa. Thus, the calculated values are consistent with the previous approach: none of the calculated values of the iron borides for the hardness surpasses the hardness for hP6-ReB<sub>2</sub>, and according to the calculated values oP12-FeB<sub>2</sub> would have an improved hardness over oP10-FeB<sub>4</sub>.

## 4.6. Summary

The investigation of the phase stability in the binary Fe-B system with DFT revealed an excellent agreement with the experimental phase diagram on the iron-rich side, regarding the known stable and metastable compounds. We obtain a stable tI12-Fe<sub>2</sub>B phase, and the known metastable phases oP16-Fe<sub>3</sub>B, tI32-Fe<sub>3</sub>B and cF116-Fe<sub>23</sub>B<sub>6</sub> are close to the tie-line. At 1:1 composition we identified three crystal structures, oP8-FeB, oS8-FeB and tI16-FeB, that are very close in energy. This is independent of the xc functional and is primarily attributed to close geometrical relationships between the three crystal structures, also apparent in the discussion of the coordination polyhedra of these crystal structures in Sec. 2.3.7. oP8-FeB is listed in the experimental phase diagram, and oS8-FeB is assumed to represent the crystal structure of the low-temperature modification in the Fe-B system. tI16-FeB is the most stable crystal structure at zero Kelvin, but is expected to be destabilized at elevated temperature. On the boron-rich side, the existence of a FeB<sub>2</sub> phase of AlB<sub>2</sub>-type, that has been observed in one experimental study and whose existence has been a controversial issue, can be ruled out due to the large energy difference towards the tie-line. In close collaboration with the group of AN Kolmogorov, the application of an evolutionary algorithm for crystal structure prediction on the boron-rich side of the experimental phase diagram revealed two viable ground states with the crystal structures oP12-FeB<sub>2</sub> and oP10-FeB<sub>4</sub>, that have not yet been observed experimentally.

We further investigated possible synthesis routes for the newly identified viable ground states. We showed that the oP10 compound may be realized as pseudobinary Fe<sub>x</sub>Cr<sub>1-x</sub>B<sub>4</sub> compound. However, the stability of the pseudobinary with respect to oP10-Fe/CrB<sub>4</sub> is highly dependent

#### 4. Iron-Boron Binary Compounds

---

on the occupation pattern of the metal atoms. The application of pressure may also be the key for synthesis of both oP12-FeB<sub>2</sub> and oP10-FeB<sub>4</sub>, as pressure lowers the corresponding formation energies.

As iron borides are used in industrial applications as hard and protective coatings, we investigated the newly identified compounds with respect to their elastic properties and their potential to serve as hard material. Both new crystal structures are predicted to possess superior elastic properties compared to the known iron borides, and yield promising values for the hardness. However, none of the newly identified compounds are expected to surpass the mechanical properties of hP6-ReB<sub>2</sub>.

In this section we investigated ordered boron-containing compounds. We focused on the binary Fe-B system and the ternary Fe-Cr-B system. As a step towards steel, we will focus in the next section on boron point defects in  $\alpha$ -iron. Since contemporary steels are multicomponent alloys, we will further extend the investigation to other light elements that are important in steel production.

## 5. Boron Point Defects in $\alpha$ -Iron

*"Not what I came looking for, but treasures  
often turn up when you're not looking."*

*Kevin Killiany*

*MechWarrior Dark Age # 30: To Ride the Chimera*

### 5.1. Introduction

#### 5.1.1. Impact on Mechanical Properties

Modern steels are multicomponent alloys that combine the main ingredients iron and carbon with a set of additional elements to achieve specific properties. Boron is a common additive element, and is usually added in very small quantities, in the range of a few parts per million (ppm). Nevertheless, even at these small concentrations, it is found to have a significant impact on the mechanical properties [338].

The addition of boron leads to improved hardenability of low-carbon and low-alloy steels [82,94–108], ductility at room [109] and high temperature [110–115], ultimate tensile strength [93], (fracture) toughness [116,117] and creep rupture properties of both ferritic [118–124] and austenitic stainless steels [125–131]. Boron additives also improve the corrosion resistance [132–134] and strongly affect the final microstructure of the steel [339–341], by e.g. affecting the austenitic [135] and ferritic [136–138] grain size.

The variety of beneficial impacts on steel properties due to boron addition stem from several mechanisms, which require boron to be present as a solute element or bound in precipitates and located appropriately in the microstructure. The solution type and location of boron results from a complex interplay between the fabrication process (e.g. temperature and cooling rate) and the chemical composition of the base material (type and amount of additive elements or already present impurities). This determines the distribution and solution type of boron, and therefore the impact on the mechanical properties [342]. Experimental studies revealed a strong tendency of boron to segregate to grain boundaries [139–141], although the amount of boron at grain boundaries depends strongly on the applied temperature and holding time [142–144] as well as the cooling rate [144,145]. Boron can also be present as solute atom, or bound in boron-containing precipitates or borides [343,344], where the formation of the phases depends also on temperature and holding time [345]. In precipitates of  $\text{Fe}_{23}(\text{B,C})_6$  type, boron may be present in the precipitates or enrich the austenitic matrix-precipitate interface [346]. Furthermore, boron may still be present in precipitates or inclusions in the austenitic matrix. Experimental

studies of ferritic steels found in general the same tendencies. Boron can segregate to the ferritic grain boundaries [347], either as solute element or bound in precipitates [137, 344], or be present in precipitates or inclusions in the ferritic matrix [348–350]. The effect of the solution type and distribution on boron on some mechanical properties is discussed below.

**Hardenability** The improvement in the hardenability of low-carbon and low-alloy steels by boron addition is primarily attributed to boron located at austenite grain boundaries [101]. This delays the ferritic/pearlitic transformation, thus increasing the time range for the bainitic and martensitic transformation [102, 103]. The improvement of the hardenability is by far the most common application of boron addition. However, the beneficial impact of boron requires its existence in solid solution, and its position at the grain boundaries. Because of varying processing parameters and chemical compositions of the base material, it is therefore not surprising to find different optimum boron contents providing the maximum hardenability [82, 104–106]. Excess boron and/or excessive fabrication temperatures can lead to the formation of borides or boron-containing phases at the grain boundaries [94, 95, 107], and are reported to have either no effect [106] or to effectively decrease the hardenability of the steel [108] by reduction of boron in solid solution. Furthermore, the impact of boron is also dependent on the carbon content, leading to a decreasing impact on the hardenability by boron with increasing carbon content [103, 107].

**Ductility** Steels subject to mechanical working, e.g. hot/cold rolling, in the fabrication process require a high ductility in order to prevent the formation of cracks, leading to failure of the material. In general, the steels show a reduced ductility in the temperature range associated with the austenite-ferrite transformation. This is referred to as ductility trough. The suggested underlying mechanism [111] is crack formation in the thin ferrite layers along austenite grain boundaries, thus promoting intergranular fracture, as ferrite is softer than austenite. With decreasing temperature the ductility recovers, as the volume fraction of ferrite increases [351]. However, precipitates may also influence the ductility of the material, depending on their location and size [352]. The addition of boron generally improves the so-called hot ductility by reducing the ductility trough. However, the suggested mechanisms vary with chemical composition of the steel as well as the fabrication temperature. Below the austenite-ferrite transformation temperature, the beneficial impact of boron is attributed to intragranular formation of  $\text{Fe}_{23}(\text{B,C})_6$  particles, acting as nucleation sites for ferrite [111] or other carbides that influence the microstructure [112]. In the austenite single-phase region, the beneficial impact of boron is attributed to enhanced grain boundary cohesion by segregation to the grain boundaries [113]. In the case of niobium-containing steels, boron enhances the segregation and diffusion of niobium, and thereby promotes the precipitation of coarse  $\text{Nb}(\text{C,N})$  particles at grain boundaries [114]. Chown *et al.* [115] investigated the influence of the B:N ratio on the hot ductility. A B:N ratio of 0.75 was found to entirely suppress the ductility trough, and the impact was attributed to the formation of hexagonal BN, thus reducing the amount of nitrogen in solid solution. Furthermore, the precipitation of other boron-containing phases including carbon and nitrogen, that reduce the amount of carbon and nitrogen in solid solu-



tion, are also expected to play an important role [114, 353]. However, in the case of ferritic steels with high chromium content boron was found to have a detrimental effect due to the precipitation of iron- and chromium-containing borides [354]. Furthermore, a study by Li *et al.* [355] attributed the beneficial impact of boron in preventing the segregation of sulfur to the grain boundaries, which is known to reduce the ductility, while boron itself has no influence on the ductility.

**Tensile Strength** An improvement in the ultimate tensile strength was found in alloys with an unusually high boron content of 2.2 wt % and a carbon content of 0.1 wt % at low and intermediate temperatures [93]. This improvement is mainly attributed to the microstructure, consisting of ferrite and homogeneously distributed borides of Fe<sub>2</sub>B type. However, in Mn-C duplex steels (coexisting ferrite and austenite) with boron additions in the range of a few ppm the ultimate tensile strength decreased with increasing boron content, although the effect was negligible compared to the influence of the annealing temperature during fabrication [356].

**Toughness** The improvement of the toughness is attributed to microstructure evolution, where additions of boron in the ppm range result in a finer martensitic substructure after quenching and a more dispersed substructure of martensite and carbides during tempering [116]. However, the influence of the fracture toughness is dependent on boron content [117], and concentrations above a critical limit result in boride precipitation, which reduces the fracture toughness [83, 357]. Furthermore, segregation of boron to grain boundaries is reported to cause a reduction of fracture toughness [358].

**Creep Properties** The effect of boron on the creep properties, in particular the creep strength, is attributed to its impact on the microstructure [119]. In Cr-W-Co-V-Nb ferritic/martensitic stainless steel with 9 wt % chromium the addition of boron prevents the long-term degradation of creep strength and improves the time to rupture at low stresses, but scarcely affects the time to rupture at high stresses. This is attributed to the enrichment of M<sub>23</sub>C<sub>6</sub> carbides near prior austenite grain boundaries with boron, thus suppressing the coarsening of the carbides during creep and maintaining a homogeneous distribution of fine M<sub>23</sub>C<sub>6</sub> carbides [120–123]. The addition of excess nitrogen results in formation of boronitride, that reduce the amount of dissolved boron and the enrichment of boron in M<sub>23</sub>C<sub>6</sub> carbides, which leads to the promotion of accelerated creep [124]. In Cr-Ni-Mn-Si austenitic stainless steels (type 304), in contrast, the formation of boronitride at the cavity surface increases the creep rupture strength and ductility, particularly for longer rupture time, although simultaneously the segregation of sulfur has to be prevented by addition of titanium or cerium [125, 126]. In type 347 stainless steels, both the formation of boronitride and segregation of boron to grain boundaries are attributed to improve the creep strength and ductility [146]. Furthermore, the beneficial impact of boron on the creep properties in Cr-Ni-Mo-Mn-Si austenitic stainless steels is related to the behavior of carbide precipitation [127]. Austenitic steels with additive boron subject to irradiation exhibit less reduction of the creep strength than the steel containing an extremely low boron content. The authors suggested that boron prevents the responsible

impurities from segregating to grain boundaries [128]. A subsequent study of the same steel showed the effect of boron to be highly dependent on the heat treatment, effectively influencing the boron distribution. Boron at grain boundaries improves the creep strength, while a homogeneous distribution has the opposite effect, and the distribution itself has no effect on the creep ductility [129].

### 5.1.2. Solution Character of Boron in Ferrite

As outlined, the impact of boron on the mechanical properties of the steels is primarily determined by the concentration, the distribution and whether it is present as solute element or bound in boron-containing precipitates. The factors that may influence the distribution and form of boron are the diffusion and the interaction with point defects, and depend also on the solution behavior of boron in  $\alpha$ -iron. Although several experimental studies have addressed the nature of boron in  $\alpha$ -iron, predominantly focusing on the solution behavior, whether it enters as substitutional or interstitial point defect, and the activation energies required for diffusion, the picture is somewhat controversial.

A substitutional solution of boron has been proposed by Busby *et al.* [359] from diffusion experiments using a spectroscopic analysis, yielding activation energies usually corresponding to a substitutional migration mechanism, and by Strocchi *et al.* [360] and Ray *et al.* [361] using a X-ray diffraction method to measure the variation of the lattice parameter of  $\alpha$ -Fe dependent on boron content. The decrease of the lattice parameter in samples including boron was attributed to a substitutional solution of boron in  $\alpha$ -iron. The substitutional solution of boron has also been highlighted in the review article by Bobkova *et al.* [338]. On the contrary, internal friction measurement by Thomas *et al.* [362] suggested an interstitial solution of boron. Measurements using the particle tracking autoradiography, which make use of the  $^{10}\text{B}(n,\alpha)\text{Li}$  fission reaction, by Wang *et al.* [363] for bcc-based Fe-3%Si-B (in wt%) alloys yield activation energies for diffusion which also suggest an interstitial solution of boron. Other studies suggested an influence of alloying elements on the solution behavior of boron. Alloying elements with an atomic diameter larger than iron expand the host lattice, thus expanding the interstitial site and allowing boron to occupy these sites [364, 365]. Indeed, this mechanism has been experimentally verified in Fe-Cr-B alloys [365]. Additionally, apart from an increased lattice parameter of ferrite due to boron addition, thus indicating an interstitial solution, an increased solubility of boron has been measured due to copper addition [366]. Hayashi *et al.* [367] suggested that boron is able to occupy both the substitutional and interstitial sites, with the larger amount of boron occupying the substitutional sites, and proposed a dissociative (or Frank-Turnbull [368]) mechanism for boron diffusion, predominantly to explain the deviating experimental data regarding boron diffusion. In this mechanism, a point defect in a substitutional site dissociates into a vacancy and the point defect in an interstitial site or vice versa.

Several experimental studies addressed the solution behavior of boron in  $\alpha$ -iron. However, the discrepancies in the results regarding the solution behavior may be attributed, at least to some extent, to the varying temperature range at which the experiments have been performed

and also to the chemical composition of the material. Impurities in the base material are expected to influence and alter the experimental results, predominantly by stronger response in the measurement and substantial interaction with boron.

From experimental studies, the interaction of boron with other point defects are only known for a few elements. An attractive interaction is generally assumed between boron and carbon, nitrogen and oxygen, due to the tendency to form precipitates, thus removing these elements from solid solution [115, 344, 350, 369]. An example is the addition of boron in order to bind solute nitrogen in boronitride, that prevents solute nitrogen from exhibiting a detrimental impact on the ductility [115]. An experimental probe analysis by Dubben *et al.* [370] on welds revealed the existence of boron-carbon pairs and borons' tendency to form small clusters with carbon and oxygen.

Density functional theory studies of various light element in  $\alpha$ -iron addressed their solubility and migration [371–374], point defect interactions [374–379] and elastic properties [380], but such studies are rather sparse for boron, despite its usage in steel production. In a recent theoretical study, Fors *et al.* [155] addressed the solution and migration of a single boron point defect in  $\alpha$ -iron using DFT. Their calculations supported the substitutional solution of boron in  $\alpha$ -iron, but a small formation energy difference with respect to boron in an interstitial site, namely the octahedral one, indicates that a certain amount might still reside in interstitial sites. Regarding the migration of boron, the calculated activation energies for substitutional and interstitial mechanisms via first nearest-neighbor migration showed the interstitial mechanism having a smaller activation energy than the substitutional one. A significant contribution to the latter mechanism stems from the necessity of an adjacent vacancy, thus the vacancy formation energy has to be interpreted as additional barrier. A subsequent theoretical study by Baik *et al.* [156] supported the substitutional solution of boron in  $\alpha$ -iron.

In this section we will investigate the interaction of boron point defects in  $\alpha$ -iron using DFT. Starting with one point defect in the host matrix, we first address the solution behavior of boron and compare to experiment and recently published theoretical results [155]. Addressing the migration of boron in  $\alpha$ -iron, we further investigate the activation energies required for migration using the nudged elastic band method for pathways based on the results for the solution behavior. We also investigate the impact of substitutional point defects on the elastic properties of  $\alpha$ -iron, comparing the impact of boron, a vacancy, aluminum, silicon, phosphorus and sulfur on the elastic constants and the directional dependence of the Young's modulus. As a step towards multicomponent systems, we further investigate the interaction of a boron point defect with a second one in the ferritic host matrix. Apart from a second boron and a vacancy, we also consider hydrogen as well as important elements in steel production in the first and second row of the p-block in the periodic table, namely carbon, nitrogen and oxygen as well as aluminum, silicon, phosphorus and sulfur. The latter elements, including boron, are also nearest neighbors in the periodic table, thus allowing us to study tendencies of the interaction associated with the number of valence electrons as well as atomic size.

## 5.2. Single Boron Point Defect

### 5.2.1. Supercell Construction

The solution behavior, the migration barriers, the influence on the elastic properties and the interaction between point defects are investigated via a supercell approach. Using repetitions of one cubic bcc unit cell along the three axis, large supercells are constructed, and the point defects are introduced at specific position in the supercell. Defects enter either as substitutional (*SB*) or interstitial atom in the tetrahedral (*TH*) or octahedral (*OH*) site (Fig. 5.1(a-c)). The tetrahedral defect is positioned in the center of a distorted tetrahedron formed by four iron host atoms, with distances of either  $\sqrt{3}a/2$  or  $a$  between the host atoms, where  $a$  represents the lattice constant. The point defect has the same distance of  $\sqrt{5}a/4$  to the four host atoms. The octahedral defect is in the center of a distorted octahedron formed by six iron host atoms, with distances of  $\sqrt{3}a/2$  between the corner and top/bottom host atoms and a distance of  $a$  between the corner host atoms, respectively. The distance between a top/bottom atom and a point defect is  $a/2$ , thereby smaller than the distance of  $a/\sqrt{2}$  between the point defect and a corner host atom. Two point defects or one point defect and a host atom, respectively, can form dumbbells in the  $\langle 100 \rangle$ ,  $\langle 110 \rangle$  or  $\langle 111 \rangle$  direction (Fig. 5.1(d-f)). In supercells containing two point defects, both may align along high-symmetry axes, and we refer to these directions of defect alignment for the analysis of defect-defect interactions.

The introduction of a point defect influences the volume of the supercell. Therefore, calculations have been performed using two conditions regarding the optimization of the atomic coordinates, cell shape and volume, unless stated otherwise. In the first set of calculations, we fix the volume and shape and allow only atomic relaxation, whereas in the second set we allow full relaxation including changes of supercell volume and shape. In calculations with atomic relaxation we use our calculated lattice constant of  $\alpha$ -Fe of 2.842 Å that is in very good agreement with experimental [381] and other theoretical values [155].

The migration barriers are determined using the nudged elastic band (NEB) method [382,383] as implemented in VASP, and refined with the climbing-image nudged elastic band (CI-NEB) method if required [384]. Due to the computational effort we used a  $3 \times 3 \times 3$  supercell and only allowed atomic relaxation. A description of the method is given in Sec. A.6 following the discussion in Refs. [382–384].

The scheme for the calculation of elastic constants is given in Sec. A.7 of the appendix. For  $\alpha$ -iron, we used a  $1 \times 1 \times 1$  bcc cell to determine the elastic constants. Introducing one point defect in the host matrix, we used different supercell sizes (between  $2 \times 2 \times 2$  and  $3 \times 3 \times 4$ ) in order to investigate varying point defect concentrations. In all calculations, only the ions and the supercell volume were optimized, before the strain tensor for the calculation of elastic constants was applied. The supercell was fixed to be cubic, as we implicitly assumed that the defect atoms are randomly distributed, thus leaving the number of independent elastic constants unchanged:  $C_{11}$ ,  $C_{12}$  and  $C_{44}$ .

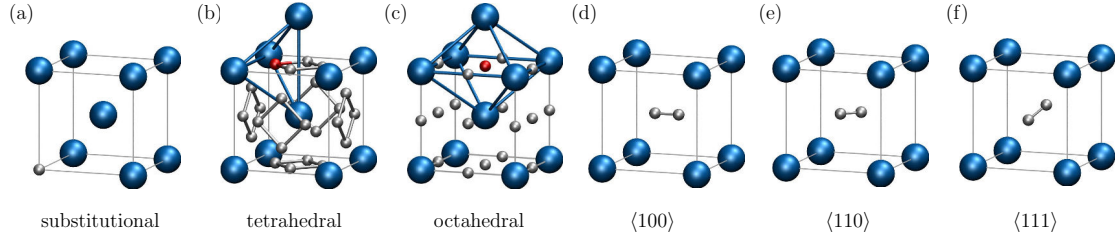


Figure 5.1.: Point defect in the (a) substitutional, (b) tetrahedral and (c) octahedral site of bcc. The tetrahedron and octahedron encapsulating the point defect marked in red are highlighted, respectively. Point defects forming dumbbells with (d)  $\langle 100 \rangle$ , (e)  $\langle 110 \rangle$  and (f)  $\langle 111 \rangle$  alignment. Dumbbells can be formed by two point defects of the same or different kind, or by one point defect with a host atom.

### 5.2.2. Solution Behavior

We first address the solution behavior of boron in  $\alpha$ -iron, thus identifying the preferred boron site occupancies in the host matrix. The identification is crucial for the next steps in our investigation. In the case of boron migration, the stable sites represent the initial and final states of the migration process. Regarding the influence on the mechanical properties, e.g. the elastic constants, this will be heavily affected by the solution behavior of boron.

In order to determine the stable solution sites, we calculated the corresponding formation energy  $E_f$  that is given by

$$E_f = E_{\text{Fe}+X} - E_{\text{Fe}} - E_X. \quad (5.1)$$

Here,  $E_{\text{Fe}+X}$  is the total energy of a ferritic host matrix containing a single point defect  $X$ ,  $E_{\text{Fe}}$  is the energy of the pure ferritic host matrix and  $E_X$  is the total energy of point defect  $X$  in its corresponding ground state. In the case of boron, it is the  $\alpha$ -B structure.

The calculated formation energies for a fully relaxed  $4 \times 4 \times 4$  supercell are summarized in Tab. 5.1, along with corresponding formation energies for borons' neighbors in the periodic table: carbon, nitrogen and oxygen. The substitutional site of boron yields the lowest formation energy, thus boron favors the replacement of an iron host atom instead of occupying an interstitial position [385]. This is in agreement with Refs. [155] and [156], but these works used an isolated boron atom as reference state for the calculation of the defect formation energy. Therefore, we also give the difference in the formation energies which are independent of the reference ground state. These formation energy differences indicate consistently that at elevated temperature boron can also occupy the  $OH$  site, while the  $TH$  site is ruled out by the large energy difference [155].

The substitutional solution of boron is different from its neighbors in the periodic table: carbon, [372] nitrogen [375] and oxygen [386] occupy the octahedral site, also apparent in the

formation energies summarized in Tab. 5.1. The corresponding ground state energies were calculated with carbon in diamond structure and nitrogen and oxygen as dimers. Baik *et al.* [156] attributed the solution behavior of boron to its atomic radius that is too large to occupy interstitial positions in  $\alpha$ -iron [387]. Indeed, within the sequence  $B \rightarrow C \rightarrow N \rightarrow O$  the covalent radius decreases as  $0.88 \text{ \AA} \rightarrow 0.76 \text{ \AA} \rightarrow 0.71 \text{ \AA} \rightarrow 0.66 \text{ \AA}$  [388]. This leads to considerable geometric modifications for point defects in the  $OH$  site. Compared to the unperturbed state, the 1NN Fe-X ( $X=B,C,N,O$ ) distances are elongated about 28% for boron, 25% for carbon, in agreement with Ref. [155], and 24% for nitrogen and 26-27% for oxygen. The 2NN Fe-X distances are nearly unaffected in the boron case, but contracted by 2% for carbon and nitrogen, and elongated by 1% for oxygen. Weaker geometrical modifications occur for substitutional point defects. The smaller radii of these elements compared to the iron radius result in contraction of the 1NN Fe-X distances: 3-4% for boron, 5% for carbon, 4% for nitrogen, and 3% for oxygen.

Given the listed atomic radii of the four p-block elements, for boron, carbon and nitrogen the atomic size is clearly reflected in the magnitude of the distortion of the nearest-neighbor distance, while the effect of substitutional and interstitial oxygen is quite peculiar. Despite the lowest radii among the four elements, only about 75% of the radii of boron, oxygen is found to have a nearly similar impact on the distortions of the nearest-neighbor distance as boron.

### 5.2.3. Migration Barriers

According to the formation energies of a single boron point defect, the  $SB$  or  $OH$  sites are the most likely point defect sites in the ferritic matrix, thus representing viable initial and final states for boron migration. In the calculation of the migration barriers of the solely substitutional and interstitial mechanisms, we consider migration processes to the first (1NN) and second (2NN) nearest-neighbor position. As a dissociative (or Frank-Turnbull [368]) mechanism was proposed for analysis of available diffusion data [367], we also investigated a

	B	C	N	O	
$E_{SB}$	0.73	2.96	3.06	1.17	this work
$E_{OH}$	0.80	0.60	0.05	-0.45	this work
$E_{TH}$	1.54	1.54	0.85	0.12	this work
$E_{SB} - E_{OH}$	-0.07	2.36	3.01	1.62	this work
	-0.06	2.34			Ref. [155] <sup>a</sup>
	-0.17	2.09			Ref. [156] <sup>b</sup>
$E_{SB} - E_{TH}$	-0.81	1.42	2.21	1.05	this work
	-0.75	1.49			Ref. [155] <sup>a</sup>

Table 5.1.: Formation energy and differences of the formation energies (in eV) for substitutional ( $SB$ ), octahedral ( $OH$ ) and tetrahedral ( $TH$ ) sites. <sup>a</sup>PAW, 128-atom cell, fully relaxed, PW91; <sup>b</sup>FLAPW, 48-atom cell, ionic relaxation.

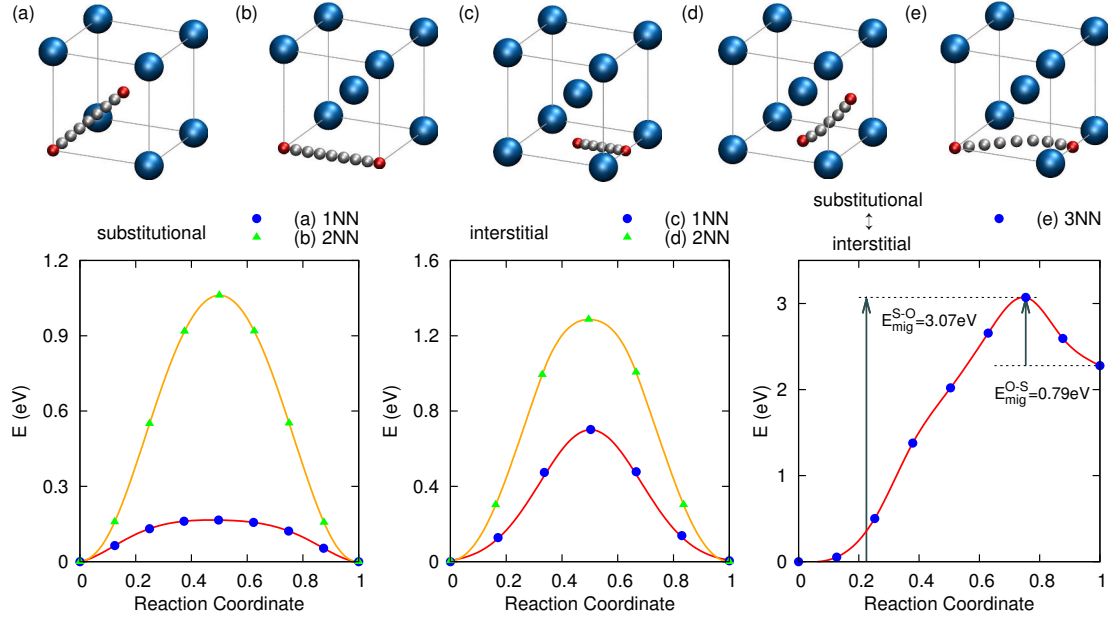


Figure 5.2.: Migration path of boron for the (a,b) substitutional and (c,d) interstitial (octahedral) configurations with final states in (a,c) first and (b,d) second nearest-neighbor position and (e) the dissociative mechanism (upper panel) and calculated migration barriers (lower panel).

migration path with substitutional and interstitial sites as initial and final states, respectively. From the possible migration paths, the  $SB \rightarrow OH_{1NN}$  and  $SB \rightarrow OH_{2NN}$  paths have been omitted as boron is mechanically unstable in the  $OH$  site next to the vacancy, relaxing towards the vacant site. We only considered boron in the 3NN  $OH$  site, as in this configuration boron remains in the  $OH$  site.

The atomic geometries for the five migration paths are sketched in the upper panel of Fig. 5.2. Configuration (a) and (b) show the migration of a point defect from the  $SB$  site to a 1NN vacancy along  $\langle 111 \rangle$  and a 2NN vacancy along  $\langle 100 \rangle$ , respectively. Configuration (c) and (d) show the migration of a point defect from the  $OH$  site to a 1NN  $OH$  site along  $\langle 100 \rangle$  and a 2NN  $OH$  site along  $\langle 101 \rangle$ , respectively. The dissociative mechanism is shown in configuration (e), where boron in the  $SB$  site dissolves into boron in the 3NN  $OH$  site and a vacancy. The paths of substitutional and dissociative (interstitial) migration were sampled with 7 (5) images, respectively. The energy differences to the initial state with respect to the normalized reaction coordinate for the different configurations are shown in the lower panel of Fig. 5.2. For the substitutional and interstitial mechanisms (Fig. 5.2(a-d)), the energy difference is symmetric with respect to the migration barrier, as the initial and final state are represented by a boron point defect in the identical defect site. The calculated migration barriers are summarized in Tab. 5.2, along with experimental and other theoretical values for boron and its

## 5. Boron Point Defects in $\alpha$ -Iron

closest neighbors in the periodic table, carbon, nitrogen and oxygen. For the latter elements, the migration barriers have been calculated from the energy difference  $E_{\text{TH}} - E_{\text{OH}}$ , using a  $3 \times 3 \times 3$  supercell with fixed lattice parameter, the same setup that was used for the NEB calculations. Values in brackets have been calculated with a  $4 \times 4 \times 4$  supercell for comparison, in order to quantify finite size effects.

For boron, the calculated migration barrier for 1NN hops is in good agreement with Ref. [155] and consistently lower than the barriers for 2NN hops, i.e. 0.17 eV versus 1.06 eV for the substitutional mechanism and 0.70 eV versus 1.26 eV for the interstitial one. The  $SB \rightarrow SB_{1\text{NN}}$  hop has the lowest migration barrier, but requires an adjacent vacancy ( $\square$ ), thus the vacancy formation energy adds to the migration barrier for the substitutional mechanism [155]. Our calculated vacancy formation energy of 2.19 eV is close to the vacancy formation energy in Ref. [155]. However, we observe that an adjacent boron in the 1NN (2NN) site with respect to

atom	migration path	$E_{\text{mig}}$ (eV)	method	
B	$SB \rightarrow SB_{1\text{NN}}$	0.17 / 2.26 <sup>a</sup>	PAW-PBE	this work
	$SB \rightarrow SB_{1\text{NN}}$	0.15 / 2.31 <sup>a</sup>	PAW-PW91	[155]
	$SB \rightarrow SB_{2\text{NN}}$	1.06 / 2.98 <sup>a</sup>	PAW-PBE	this work
	$OH \rightarrow OH_{1\text{NN}}$	0.70 (0.73)	PAW-PBE	this work
	$OH \rightarrow OH_{1\text{NN}}$	0.67	PAW-PW91	[155]
		0.65	expt.	[362]
		0.92	expt.	[363]
	$OH \rightarrow OH_{2\text{NN}}$	1.26	PAW-PBE	this work
	$SB \rightarrow OH_{3\text{NN}}$	3.07	PAW-PBE	this work
	$OH \rightarrow SB_{3\text{NN}}$	0.79	PAW-PBE	this work
C	$OH \rightarrow OH_{1\text{NN}}$	0.89 (0.95)	PAW-PBE	this work
	$OH \rightarrow OH_{1\text{NN}}$	0.86	PAW-PW91	[372]
	$OH \rightarrow OH_{1\text{NN}}$	0.92	USPP-PW91	[375]
	$OH \rightarrow OH_{1\text{NN}}$	0.75	PAW-PBE	[389]
		0.81-0.87	expt.	[390–393]
N	$OH \rightarrow OH_{1\text{NN}}$	0.72 (0.80)	PAW-PBE	this work
	$OH \rightarrow OH_{1\text{NN}}$	0.79	USPP-PW91	[375]
		0.76-0.80	expt.	[390–392]
O	$OH \rightarrow OH_{1\text{NN}}$	0.47 (0.57)	PAW-PBE	this work
		0.93	expt.	[394]

Table 5.2.: Calculated migration barriers for boron in a  $3 \times 3 \times 3$  supercell using the NEB method. Values from Ref. [155] are listed for comparison, as well as  $E_{\text{TH}} - E_{\text{OH}}$  for a  $3 \times 3 \times 3$  supercell with fixed lattice constant for carbon, nitrogen and oxygen among experimental and other theoretical migration barriers. Values in brackets are calculated for a fully relaxed  $4 \times 4 \times 4$  supercell, in order to quantify finite size effects (<sup>a</sup>vacancy formation energy included).



the vacant site reduces the vacancy formation energy to 2.09 eV (1.92 eV). The reduction in the vacancy formation energy can be attributed to B-□ interactions, see Sec. 5.3.3. Inclusion of the distance-dependent vacancy formation energy increases the 1NN (2NN) migration barrier to 2.26 eV (2.98 eV). The migration of boron via the substitutional mechanism is further hindered by the high barrier for vacancy migration of  $E_{\square}^m = 0.55$  eV [393], the experimental value being close to the theoretical value of 0.65 eV [395]. The relatively high migration barrier for vacancy diffusion compared to the migration barrier for the substitutional 1NN hop implies that boron would only jump back and forth to the vacant site, without actually migrating through the crystal. In contrast, the formation of a vacancy is not required for the migration of interstitial boron, and the calculated lowest migration barrier for the 1NN hop of 0.7 eV falls in between experimental values of 0.65 eV by Thomas *et al.* [362] and 0.92 eV by Wang *et al.* for Fe-3%Si-B alloys [363]. In the dissociative mechanism the migration barrier depends on the initial state. The dissociation of boron in the *SB* site into a boron atom in the 3NN *OH* site and a vacancy requires a comparably large energy of 3.07 eV. This value exceeds the vacancy formation energy in  $\alpha$ -iron. The opposite mechanism of a boron in the *OH* site annihilating a vacancy requires a significantly lower migration barrier of 0.79 eV. The sketched migration path (Fig. 5.2(e)) indicates that this value arises from the required  $OH_{3NN} \rightarrow OH_{2NN}$  hop, before boron is dragged towards the vacancy. The deviation from the calculated  $OH \rightarrow OH_{1NN}$  migration barrier can be attributed to the geometric influence of the vacancy on the host iron atoms, resulting in a slightly bent  $OH_{3NN} \rightarrow OH_{2NN}$  path that circumvents the *TH* site. Given the relatively low migration barriers for both interstitial boron and a vacancy, compared to the vacancy formation energy and the energy required to release a substitutional boron, the tendency of interstitial boron to annihilate adjacent vacancies implies a reduction of the vacancy concentration and the vacancy mobility, at the expense of the mobility of boron.

In order to quantify finite size effects, we performed additional calculations for fully relaxed  $4 \times 4 \times 4$  supercells. The  $OH \rightarrow OH_{1NN}$  migration barrier for boron yields 0.73 eV that is close to the value obtained with NEB in a  $3 \times 3 \times 3$  bcc supercell with fixed lattice constant and only ionic relaxation. Similar calculations for carbon, nitrogen and oxygen showed that finite size effects influence the results by less than about 0.1 eV. The calculated values for carbon and nitrogen are in good agreement with previous theoretical and experimental results. For oxygen, the calculated value agrees with a previous calculation [386], but deviates from the experimental value, an indication that oxygen might diffuse by a different mechanism. This has not yet been considered in a theoretical investigation.

#### 5.2.4. Influence on Elastic Properties

The influence of boron content on the mechanical properties of  $\alpha$ -iron was determined by calculation of the elastic constants of a iron supercell containing a single boron point defects. In order to model different boron content, we varied the size of the iron supercell containing the boron atom. In this investigation, we considered boron only in the energetically favorable *SB* site. For comparison, we also determined the influence of a vacancy on the elastic constants, as a vacancy exerts almost the same strain on the 1NN host iron atoms (3%-4%

contraction) as boron in the  $SB$  site, and the influence of aluminum, silicon, phosphorus and sulfur on the elastic constants. The latter elements are common additives or impurities in steel manufacturing. Similar to boron the elements occupy substitutional sites in  $\alpha$ -iron, which is confirmed due to experimentally observed bcc-based Fe-Al [396, 397] and Fe-Si [398] alloys and DFT calculations for silicon [374] and phosphorus [376] in  $\alpha$ -iron. Sulfur is also referred to occupy substitutional sites in  $\alpha$ -iron [378]. This is in line with the calculated formation energy differences of  $E_{SB} - E_{OH} = -2.18$  eV and  $E_{SB} - E_{TH} = -2.25$  eV. These values were calculated for a  $3 \times 3 \times 3$  supercell with a fixed lattice constant. The set of considered point defects (except for the vacancy) allows us to study the influence of atomic size and electronic configuration of the point defects on the elastic constants of  $\alpha$ -iron. The directional-dependence of Young's modulus  $Y$  of the Fe-X ( $X=B, \square, Al, Si, P, S$ ) alloys is then calculated from the elastic constants.

The applied scheme for the determination of the elastic constants is given in Sec. A.7 of the appendix. Throughout this investigation we kept the supercell shape cubic and optimized only the atomic positions and the supercell size, before applying the strain tensors for calculation of the elastic constants. This is motivated by the assumption that the defect atoms are randomly distributed in the alloy and leave the number of independent elastic constants unchanged. Usually, the optimization of the supercell shape would lead to a tetragonal distortion of the supercell, if the number of repetitions of the basis bcc cell along the crystallographic axis is not identical, thus leading to unequal distances between the point defects and its periodic image. For tetragonal unit cells, the number of independent elastic constants increases to six. For a  $2 \times 2 \times 4$  supercell, one of the considered supercells with largest discrepancy between the number of repetitions, we therefore checked the tetragonal distortion evoked by substitutional boron and a vacancy. The deviation of the  $c/a$  ratio is small, in the range of 0.4% for a vacancy, and 0.1% for substitutional boron. We further calculated the elastic constants for the  $2 \times 2 \times 4$  supercell with a tetragonal distortion containing substitutional boron and a vacancy, and compared with the elastic constants of a  $2 \times 2 \times 4$  supercell with cubic shape. In the former case the corresponding elastic constants were averaged in order to compare with the elastic constants for a cubic cell. However, the influence of the supercell shape on the elastic constants was found to be negligible, thus validating our approach of assuming a random distribution of the defect atoms and leaving the supercell shape cubic.

Elastic constants for  $\alpha$ -iron yield  $C_{11} = 274$  GPa,  $C_{12} = 149$  GPa and  $C_{44} = 97$  GPa, in very good agreement to other theoretical values, and with similar overestimation (underestimation) of the experimentally determined  $C_{11}$  and  $C_{12}$  ( $C_{44}$ ) (see Ref. [380] and references therein). The error bars for the calculated elastic constants of the Fe-X alloys (Fig. 5.3(a-c,g-i)) are estimated from polynomials of different orders for the fit, along with a linear fit for the calculated elastic constants as function of point defect concentration. Below a boron concentration of approximately 3%, the influence of boron on the elastic constants is very similar to that of a vacancy. The linear fit exhibits nearly the same slope for both boron and a vacancy (Tab. 5.3). However, above a boron concentration of 3% the tendencies change substantially for the three elastic constants  $C_{11}$ ,  $C_{12}$  and  $C_{44}$ :  $C_{11}$  is only weakly dependent on the boron concentration, while  $C_{12}$  and  $C_{44}$  increase with boron concentration. In the considered defect concentration, the increase in boron content nearly mitigates the effect of boron addition for  $C_{12}$ , while in

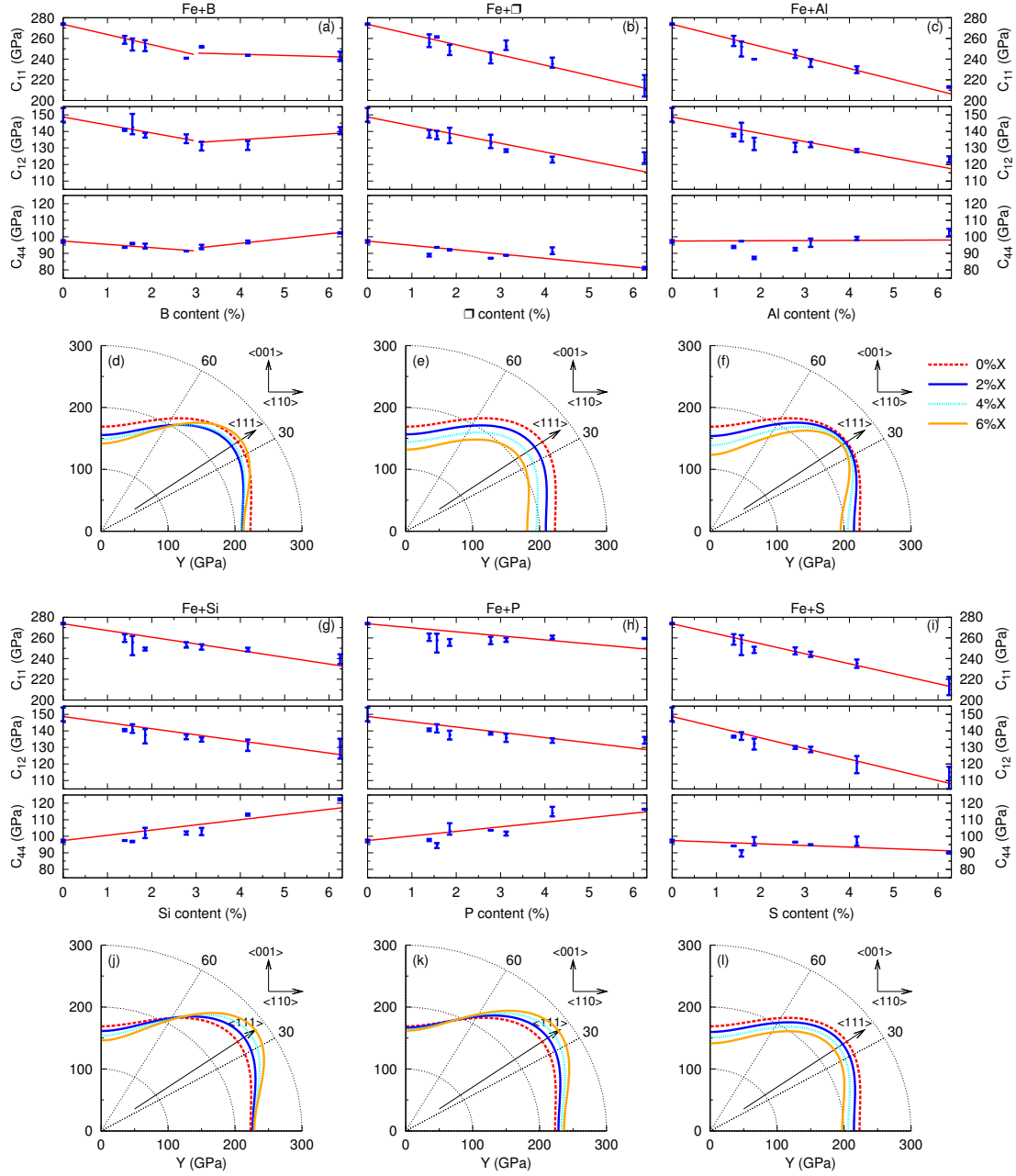


Figure 5.3.: Calculated elastic constants  $C_{11}$ ,  $C_{12}$  and  $C_{44}$  of ferritic Fe-X ( $X=B, \square, Al, Si, P, S$ ) alloys as function of defect concentration. Error bars are estimated from second-, third- and fourth-order polynomials for the fit. The directional-dependence of Young's modulus  $Y$  is shown for varying defect concentrations, calculated from values of  $C_{ij}$  taken from the fit. Lines are only a guide to the eye.

the case of  $C_{44}$  the addition of boron increases the elastic constant above the value for  $\alpha$ -iron. The increase of the aluminum content decreases both  $C_{11}$  and  $C_{12}$ , with slopes very similar to boron below 3% and a vacancy, but has only a weak effect on  $C_{44}$ . An increase of both silicon and phosphorus content decreases  $C_{11}$  and  $C_{12}$ , but simultaneously increases  $C_{44}$ . Except  $C_{11}$ , which shows a larger slope in the case of silicon compared to phosphorus,  $C_{12}$  and  $C_{44}$  have a very similar dependence on the defect concentration. Trends in the elastic constants for Fe-Al and Fe-Si are in line with a previous theoretical study [399]. Increasing the sulfur content leads to reduction of both  $C_{11}$  and  $C_{12}$  with a larger slope when compared to silicon and phosphorus.  $C_{44}$  is also reduced with increasing sulfur content, with a slope that is in between aluminum and a vacancy.

From the linear fit of the calculated elastic constants, we determined the directional dependence of the Young's modulus [400] for different defect concentrations of the Fe-X alloys (Fig. 5.3(d-f,j-l)). The Young's modulus for  $\alpha$ -iron has the lowest magnitude along  $\langle 100 \rangle$  with a value of  $Y_{\langle 100 \rangle} = 169$  GPa, while the largest value is found along  $\langle 111 \rangle$  with  $Y_{\langle 111 \rangle} = 250$  GPa, which is a common feature of metals with cubic cells [401]. The calculated results agree well with experimental values [401,402] of  $Y_{\langle 100 \rangle} = 132$ -141 GPa and  $Y_{\langle 111 \rangle} = 277$ -293 GPa. Below a concentration of 3%, boron reduces the Young's modulus uniformly. The change in the tendencies above a boron concentration of 3% is reflected in a further reduction of the Young's modulus along the elastically soft  $\langle 100 \rangle$  axis, while the elastically hard  $\langle 111 \rangle$  axis shows strengthening with increasing boron concentration. An increasing vacancy concentration leads to uniform reduction of the Young's modulus. With increasing aluminum content, the Young's modulus is reduced along the elastically soft  $\langle 100 \rangle$  axis and to a lesser extent along the  $\langle 110 \rangle$  axis, while the elastically hard  $\langle 111 \rangle$  receives marginal softening with increasing aluminum content. An increase in the silicon content softens the Young's modulus along the  $\langle 100 \rangle$  axis, leaves the Young's modulus virtually unchanged along  $\langle 110 \rangle$  and hardens the Young's modulus along  $\langle 111 \rangle$ . For phosphorus, an increasing content leaves the Young's modulus virtually unchanged along the  $\langle 100 \rangle$  axis, and strengthens both the  $\langle 110 \rangle$  and  $\langle 111 \rangle$  axis. Given the very similar slopes in the dependence of  $C_{12}$  and  $C_{44}$  on the silicon and phosphorus content, we observe a very similar strengthening effect along the  $\langle 111 \rangle$  axis, while the other two crystallographic axes show phosphorus to be a more effective strengthener than silicon. An increase in the sulfur content leads to uniform reduction of the Young's modulus, similar to a vacancy, although sulfur reduces the Young's modulus to a lesser extent.

Kinks in the dependence of elastic constants with respect to defect concentration, that have been observed at a boron content of approximately 3%, were also observed in Fe-Si alloys, but affected only  $C_{11}$  with a minimum in  $C_{11}$  at approximately 11 at% Si [403]. However, neither volumetric nor magnetic effects (Fig. 5.4(a,b)) can be held responsible for the observed kink in Fe-B alloys. The relationship between defect concentration and the modification of the lattice constant and magnetic moment of the supercell is approximately linear for all point defects we considered in our investigation. Boron and a vacancy reduce the supercell volume with increasing defect concentration, whereas the reduction is more pronounced in the case of boron. However, the slope is steeper compared to the experimental value from Ref. [360]. The influence of aluminum, silicon and phosphorus on the supercell volume clearly reflects the larger size of aluminum compared to iron and the decreasing atomic size when going from aluminum

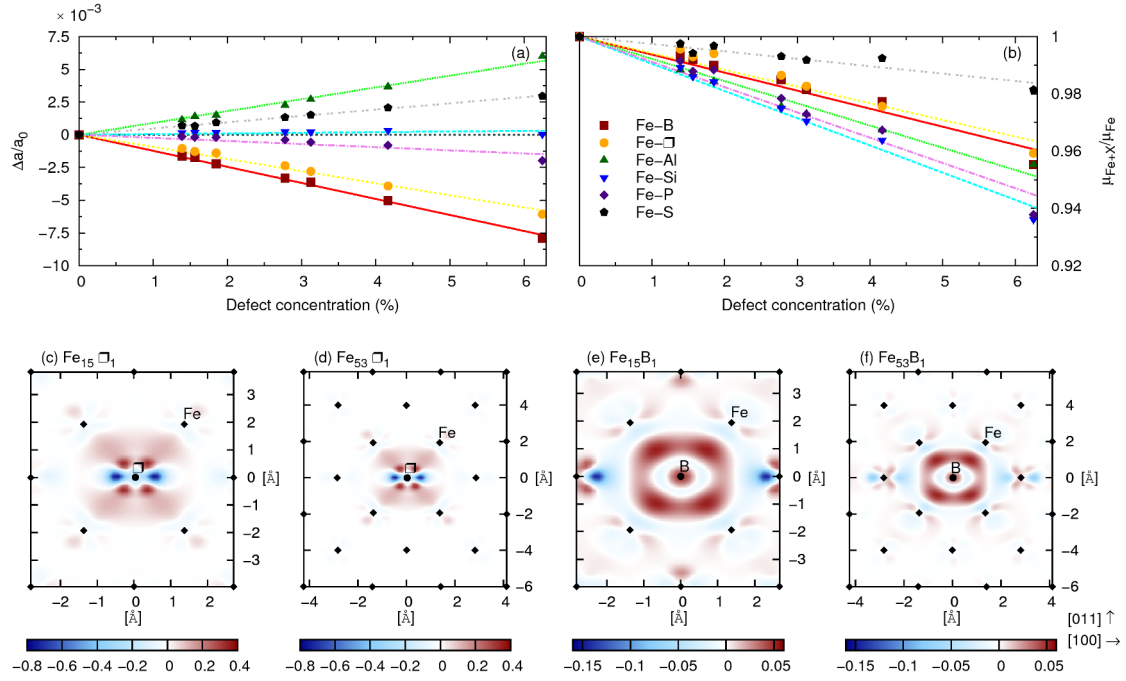


Figure 5.4.: (a) Relative lattice parameter modification and (b) reduction of normalized total magnetic moment of ferritic Fe-X (X=B, □, Al, Si, P, S) alloys as function of defect concentration. Charge density difference of (c,e)  $2 \times 2 \times 2$  and (d,f)  $3 \times 3 \times 3$  supercells containing (c,d) a vacancy or (e,f) substitutional boron.

to silicon and phosphorus. The calculated parameter for the lattice constant modification due to aluminum addition is larger than the experimental value in Ref. [396]. In our calculations,

	$C_{11}$	$C_{12}$	$C_{44}$	$\Delta a / a_0$	$\Delta a / a_0  _{\text{expt}}$	$\mu_{\text{Fe}+X} / \mu_{\text{Fe}}$
< 3% B	274-987 $x$	149-481 $x$	97-199 $x$	-0.122 $x$	-0.081 $x^a$	1-0.63 $x$
> 3% B	249-115 $x$	128+175 $x$	85+289 $x$	-0.122 $x$	-0.081 $x^a$	1-0.63 $x$
□	274-988 $x$	149-529 $x$	97-261 $x$	-0.092 $x$		1-0.58 $x$
Al	274-1068 $x$	149-496 $x$	97-10 $x$	0.090 $x$	0.057 $x^b$	1-0.78 $x$
Si	274-648 $x$	149-369 $x$	97+315 $x$	0.005 $x$	-0.024 $x^c$	1-0.95 $x$
P	274-389 $x$	149-318 $x$	97+276 $x$	-0.024 $x$		1-0.88 $x$
S	274-966 $x$	149-645 $x$	97-99 $x$	0.048 $x$		1-0.26 $x$

Table 5.3.: Fit for the elastic constants, relative volume modification and reduction of magnetic moment of ferritic Fe-X (X=B, □, Al, Si, P, S) alloys as a function of defect concentration for small defect contents. Experimental data for the lattice parameter modification from <sup>a</sup>Ref. [360], <sup>b</sup>Ref. [396] and <sup>c</sup>Ref. [398].

silicon has a negligible effect on the lattice constant. However, Ref. [398] measured a more pronounced and negative modification of the lattice parameter. The increasing lattice constant with increasing sulfur content is not intuitive, as sulfur has a smaller tabulated atomic size than phosphorus [388], thus a reduction of the lattice constant with increasing sulfur content would be expected. We observed a similar effect with oxygen as a point defect in  $\alpha$ -iron, that has the smallest tabulated atomic size compared to boron, carbon and nitrogen, but exerts virtually the same strain on the host iron lattice as boron, the element with the largest tabulated atomic size among the four elements. This indicates that the effect might be attributed to the electronic configuration, as oxygen and sulfur are in the same column of the periodic table. All considered point defects reduce the magnetic moment with increasing defect concentration. The magnitude of reduction decreases with the sequence  $\text{Si} \rightarrow \text{P} \rightarrow \text{Al} \rightarrow \text{B} \rightarrow \square \rightarrow \text{S}$ . Again the influence of boron and a vacancy is very similar, and again the impact is more pronounced for boron.

In order to understand the change of the influence that boron has on the elastic constants above a boron content of approximately 3%, we analyzed the distribution of the charge density in the  $2 \times 2 \times 2$  and  $3 \times 3 \times 3$  supercell with a vacancy or a substitutional boron. These supercells represent a point defect concentration of 6.25% and 1.85%, respectively. For a vacancy, the difference in the charge density distribution is calculated according to

$$\Delta\rho = \rho_{\text{Fe}+\square_{\text{Fe}}} - (\rho_{\text{Fe}+\square} + \rho_{\square_{\text{Fe}}}), \quad (5.2)$$

whereas  $\rho_{\text{Fe}+\square}$  is the charge density of a supercell with a vacancy,  $\rho_{\square_{\text{Fe}}}$  is the charge density of a single iron atom at the position of the vacancy, and  $\rho_{\text{Fe}+\square_{\text{Fe}}}$  is the charge density of the supercell with an iron atom at the position of the vacancy at fixed geometry. A similar equation is used in the case of substitutional boron

$$\Delta\rho = \rho_{\text{Fe}+\text{B}} - (\rho_{\text{Fe}} + \rho_{\text{B}}), \quad (5.3)$$

with  $\rho_{\text{Fe}+\text{B}}$  as the charge density of an iron supercell with a substitutional boron,  $\rho_{\text{Fe}}$  as charge density of the same supercell without boron and fixed geometry, and  $\rho_{\text{B}}$  as charge density of a single boron atom in the supercell. The charge density difference plots (Fig. 5.4(c-f)) are plotted in the  $[0\bar{1}1]$  plane in order to discuss the modification of the charge density distribution in between the 1NN and 2NN host Fe atoms with respect to the point defect. In the case of a vacancy, both supercells (Fig. 5.4(c,d)) yield a virtually identical distribution of the charge density. We find a gain in charge density towards the 1NN host iron atoms, along  $\langle 111 \rangle$ , and a depletion in  $\langle 100 \rangle$ , without altering the charge density close to the 2NN host iron atoms. The charge density difference plots for substitutional boron (Fig. 5.4(e,f)) are very similar in both supercells. However, an exception is the charge density difference in the proximity of the 2NN host iron atoms, and to a lesser extent, the charge density difference in the proximity of the 3NN host iron atoms. The depletion of the charge density close to the 2NN host iron atoms, pointing towards boron, is stronger in the  $2 \times 2 \times 2$  supercell, while in the  $3 \times 3 \times 3$  supercell the depletion is only half as strong. Additionally we observe a depletion on the opposite side, pointing away from boron, with a similar magnitude. Towards the 3NN host iron atom, we observe a small charge density gain in the  $2 \times 2 \times 2$  supercell, which cannot be observed in

the  $3 \times 3 \times 3$  supercell. However, the magnitude is relatively small. In summary, the different impact of boron on the elastic properties of  $\alpha$ -iron above a boron content of approximately 3% can be attributed to the formation of regular Fe-B (Fe-Fe-B) chains along the  $\langle 100 \rangle$  axis in the  $2 \times 2 \times 2$  ( $3 \times 3 \times 3$ ) supercell which influence the distribution of the charge density significantly. The formation of regular Fe-□ or Fe-Fe-□ chains, in contrast, does not have a notable impact on the elastic properties in the investigated concentration range and no observable influence on the charge density distribution.

## 5.3. Point Defect Interaction

### 5.3.1. Supercell Construction

In order to investigate the interaction between two point defects we constructed supercells that include two point defects at different positions that vary in the distance. In some cases, the two point defects may align along a high-symmetry crystallographic axis in the ferritic matrix. We will highlight the axis in the corresponding diagrams in order to identify crystallographic axes with pronounced interaction. Regarding the size of the supercell, we used a  $4 \times 4 \times 4$  supercell throughout the investigation of point defect interaction. Tests with smaller unit cells showed significant finite size effects in the  $2 \times 2 \times 2$  supercell, while tests with a  $3 \times 3 \times 3$  supercell for boron-boron interaction showed good agreement with the larger  $4 \times 4 \times 4$  supercell. However, for the smaller  $3 \times 3 \times 3$  supercell, we find larger discrepancies between the two relaxation conditions, which will be discussed below.

The calculations were performed with two relaxation conditions regarding the atomic positions and the supercell shape and volume. In the first set of calculations we only allowed relaxation of the atoms, while the cell shape was kept cubic and the lattice constant was identical to our calculated lattice constant of  $\alpha$ -iron. In the second set of calculations we also allowed the optimization of the supercell shape and volume. Calculations with these two conditions will help to clarify whether volume effects play an important role in the interaction of boron with other point defects.

In order to quantify the interaction between two point defects  $X$  and  $Y$ , we define the interaction energy  $E_{\text{int},X+Y}$  as

$$E_{\text{int},X+Y} = (E_{\text{Fe}+X+Y} + E_{\text{Fe}}) - (E_{\text{Fe}+X} + E_{\text{Fe}+Y}). \quad (5.4)$$

$E_{\text{Fe}+X+Y}$  is the total energy of a supercell containing two point defects,  $E_{\text{Fe}}$  is the reference energy of an  $\alpha$ -iron cell, and  $E_{\text{Fe}+X}$  and  $E_{\text{Fe}+Y}$  are reference energies of a supercell containing one point defect  $X$  or  $Y$ , respectively. According to this definition, a negative (positive) interaction energy denotes attractive (repulsive) interaction.

### 5.3.2. Boron - Boron

The calculated formation energies identified boron in  $\alpha$ -iron as occupying the *SB* site with a small formation energy difference to the *OH* site. Therefore, in the investigation of point defect interactions we considered boron in both the *SB* and *OH* site. This leads to three configurations: two boron atoms located at substitutional sites (*SB-SB*), one boron at a substitutional and the other one at the octahedral interstitial site (*SB-OH*), and two boron atoms located at the octahedral interstitial sites (*OH-OH*). We considered all possible configurations of two point defects for both relaxation conditions, unless stated otherwise, which leads to 13 supercells for the *SB-SB* case, 18 for the *SB-OH* case, and 31 for the *OH-OH* case in the  $4 \times 4 \times 4$  bcc supercell with varying initial point defect separation.

For the *SB-SB* configurations (Fig. 5.5(a)) the 2NN arrangement along  $\langle 100 \rangle$  (the elastically soft axis in ferrite) is significantly more attractive than the 1NN arrangement along  $\langle 111 \rangle$  (the elastically hard axis in ferrite). This behavior is virtually independent on the relaxation condition and quite different from, e.g. solely repulsive P-P [376] and attractive Cu-Cu [395] interactions in  $\alpha$ -iron that show a monotonic decay in the magnitude of the interaction energy with increasing point defect separation, regardless of the corresponding crystallographic directions. The borons' differing tendency may be due to the elastic properties of  $\alpha$ -iron: the strong response in the interaction energy for the 2NN configuration may be evoked by the elastic softness along the  $\langle 100 \rangle$  axis, while the elastically hard  $\langle 111 \rangle$  axis may prevent a pronounced response in the interaction energy. For the 3NN arrangement along  $\langle 110 \rangle$  and larger point defect separations, the interaction energies are much weaker. Due to the finite size of the considered supercell the interaction energy does not vanish at large separations. The origin of the more pronounced interaction energy for the supercell with maximum point defect separation is attributed to geometric effects in a highly symmetric network of boron atoms. We confirm this by breaking the  $4 \times 4 \times 4$  symmetry with a  $4 \times 4 \times 5$  supercell which reduces the interaction energy significantly (marked as  $\times$  in Fig. 5.5(a)). In order to maintain consistency, the reference energies, i.e. the values for the  $\alpha$ -iron cell and a iron cell containing one substitutional boron, were also calculated with the same  $4 \times 4 \times 5$  supercell.

The initial 1NN, 2NN and 4NN of the *SB-OH* configurations (Fig. 5.5(c)) stand out due to large attractive interaction energies, which are virtually independent of the relaxation condition and arise from considerable atomic relaxation of one or both of the boron point defects. Supercells representing the 1NN (2NN) configuration relax to two boron atoms surrounding a vacancy and form a  $\langle 100 \rangle$  ( $\langle 110 \rangle$ ) dumbbell with a B-B distance of 1.71 Å (1.66 Å). The third possible alignment along  $\langle 111 \rangle$  is energetically between the  $\langle 110 \rangle$  and  $\langle 100 \rangle$  dumbbell, with a shorter B-B distance of 1.63 Å. Hence, the observed sequence  $E_{\langle 110 \rangle} < E_{\langle 111 \rangle} < E_{\langle 100 \rangle}$  of the B-B dumbbells is identical to the sequence of Fe-Fe dumbbells in  $\alpha$ -iron [404]. The B-B distances in the dumbbells are similar to the typical B-B distances of the intericosahedra bonds which link the icosahedra units of the polymorphs  $\alpha$ -boron and  $\beta$ -boron. These intericosahedra distances are shorter than the usual bond length within the icosahedra units [300]. Reported values for the intericosahedra distances are 1.67 Å for  $\alpha$ -boron [302], and 1.624 Å and 1.71 Å for  $\beta$ -boron [298], which agree well with the B-B distances observed in our calculations. The 3NN configuration yields a weak repulsion, while the large attractive interaction energy of the 4NN



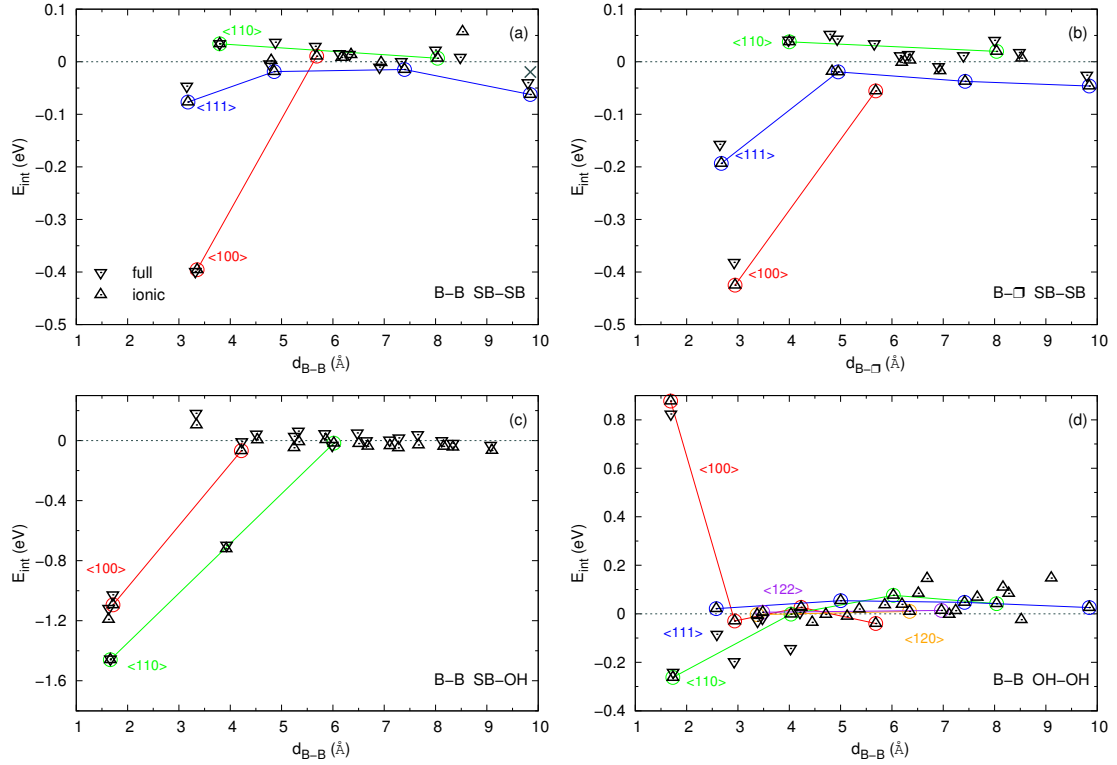


Figure 5.5.: Interaction energy versus point defect separation for (a) B-B and (b) B-□ *SB-SB*, (c) B-B *SB-OH* and (d) *OH-OH* with the high-symmetry crystallographic axis indicated.

configuration is due to considerable atomic rearrangement: Boron in the *OH* site has been dragged out from its initial position and aligned itself along the  $\langle 111 \rangle$  axis. In this configuration, the boron atom has one iron atom between itself and the second boron, i.e. it forms a B-Fe-B complex. The remaining configurations yield very weak interaction energies, which are virtually independent of the relaxation condition, with similar finite size effects as mentioned above.

For the *OH-OH* configurations (Fig. 5.5(d)), we used a full relaxation only for the 8 smallest point defect separations. A notable effect of the relaxation condition is only observed for the 4NN and 7NN configuration where the octahedra surrounding both point defects have parallel alignment with an unperturbed volume expansion along one crystallographic axis. The 1NN configuration along the  $\langle 100 \rangle$  axis yields strong repulsion, while weak attraction is found for the 2NN configuration aligned along the  $\langle 110 \rangle$  axis. This behavior is qualitatively different to the purely repulsive interaction of C-C, C-N and N-N in  $\alpha$ -iron [375, 379]. The repulsive 1NN B-B configuration, obtained with ionic and full relaxation of the supercells, disagrees with a previous work that uses unrelaxed DFT calculations in combination with microscopic elasticity theory [405]. For the 4NN configuration, aligned along  $\langle 100 \rangle$ , the interaction energy

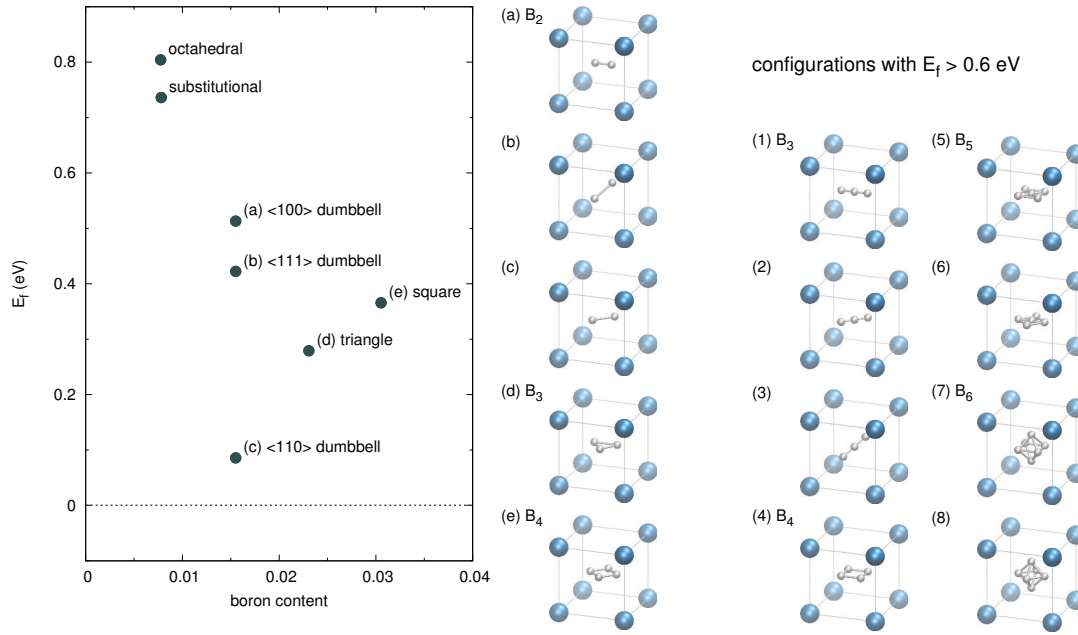


Figure 5.6.: Formation energy of boron complexes with up to six atoms incorporated into a vacant site in  $\alpha$ -iron.

depends on the initial boron positions. The data point shown in Fig. 5.5(d) corresponds to two common corner host atoms (2NN) of the octahedron that are shared by the boron atoms. The alternative configuration with common top/bottom host atom (1NN) is energetically unfavorable with  $E_{\text{int}} = 1.63 \text{ eV}$  ( $1.95 \text{ eV}$ ) for calculations with full (ionic) relaxation. Simple geometry might explain this large value by realizing that a single boron in the  $OH$  site elongates the 1NN Fe-B distance by about 25%. This elongation is suppressed in the case of opposing boron atoms that share one of the 1NN host iron atoms which increases the total energy of the system. The remaining configurations show generally weak interaction energies, also along the  $\langle 111 \rangle$ ,  $\langle 120 \rangle$  and  $\langle 122 \rangle$  axes.

Due to the relatively large gain in the total energy from the formation of dumbbells in some configurations of the  $SB-OH$  case, we investigated these configurations with respect to the formation energy. Given the solution behavior of boron in ferrite (whether it enters in substitutional or interstitial sites) one might argue that boron tends to be present in another configuration, that has not yet been observed experimentally, but still bears enough resemblance to a substitutional or interstitial solution to account for the different results regarding the favorite defect site of boron in  $\alpha$ -iron. A possible configuration is a B-B dumbbell, although this would imply that boron tends to appear in pairs and less as pure point defects in  $\alpha$ -iron. Indeed, the calculation of the formation energy (Fig. 5.6) shows that the lowest energy  $\langle 110 \rangle$  dumbbell has a lower formation energy than the substitutional and interstitial sites, although the formation energy is still positive. Nevertheless, the significantly reduced formation energy of the B-B dumbbell indicates that boron as impurity might not be present as

a single point defect, but rather binds to other boron atoms and forms dumbbells instead. This idea is further supported by the synthesis of metastable, bcc-based Fe-B alloys with up to 12% boron content, where, on average, two iron atoms were replaced by three boron atoms [361]. Following the idea of boron in a bound configuration instead of an isolated point defect, we investigated the impact of further boron incorporation into the cavity on the formation energy, by testing several alignments with boron complexes built of up to six atoms. The lowest energy configuration for three boron atoms is a triangle formed by boron. In the case of four boron atoms the lowest energy configuration is represented by the boron atoms forming a square aligned along  $\langle 100 \rangle$ , thus increasing the distance towards the 1NN host iron atoms. However, these configurations yield larger formation energies than the  $\langle 110 \rangle$  dumbbell, but are smaller than the configurations containing only one point defect. Other configurations with up to six boron atoms and formation energies above 0.6 eV are shown for completeness in the right panel of Fig. 5.6. In recent DFT studies, the trapping of defect atoms by single vacancies was also observed for other light elements apart from boron. In  $\alpha$ -iron, single vacancies can bind up to two carbon and nitrogen atoms [375] and up to three hydrogen atoms [406]. For comparison, in  $\gamma$ -iron a single vacancy can trap up to six hydrogen atoms [407].

### 5.3.3. Boron - Vacancy

The B- $\square$  interaction is important due to the influence of the boron mobility in  $\alpha$ -iron [155]. The setup of the calculations was similar to B-B, except that we restricted boron occupation to the *SB* site, as boron in the 1NN and 2NN *OH* site relative to the vacancy was found to be unstable. In order to calculate the B- $\square$  distance, we determined the vacancy position as the geometric center of the relaxed position of the eight 1NN host iron atoms. Comparing the B- $\square$  case (Fig. 5.5(b)) with the B-B *SB-SB* case (Fig. 5.5(a)) reveals a similar qualitative tendency with an attractive interaction energy for the 1NN and 2NN configuration. While the interaction energy for the 1NN configuration is about three times larger than the corresponding interaction energy in the B-B case, we find a nearly identical value for the 2NN configurations. Our calculated values for the interaction energy are in between previous theoretical estimates of 0.091 eV [408] and 0.47 eV [409].

This attractive interaction might affect the mobility of substitutional boron in two ways: First, the attraction between boron and a vacancy increases the barrier for the vacancy migration and thereby reduces the mobility of boron. Second, the attractive interaction introduces the possibility of the migration of bound B- $\square$  complexes. However, although this migration process dominates in austenitic steels [141, 143], predominantly due to a large binding energy of B- $\square$  complexes of 0.5 eV [410], no evidence of the migration of bound B- $\square$  complexes was observed in bcc-based Fe-3%Si alloys [347]. This supports the idea that substitutional boron is immobile and the interstitial migration mechanism is the governing one.

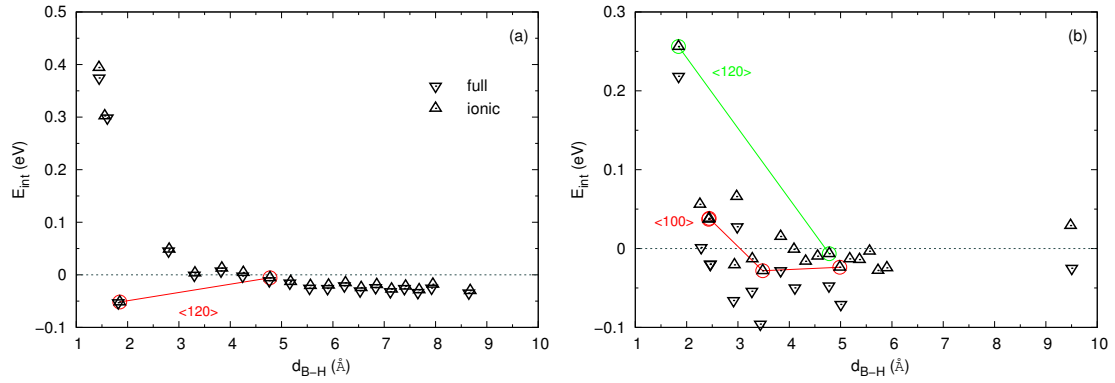


Figure 5.7.: Interaction energy versus point defect separation for (a) B-H *SB-TH* and (b) *OH-TH* with high-symmetry crystallographic axis indicated.

### 5.3.4. Boron - Hydrogen

Hydrogen is a common but unwanted impurity in steels, as it is known to cause embrittlement. In  $\alpha$ -iron, hydrogen occupies the *TH* site [371]. Therefore, we considered the *SB-TH* and *OH-TH* defect configurations with 17 and 37 different configurations, respectively, in order to characterize the B-H interactions. Following our results for the B-B and B- $\square$  interaction, we considered only closer distances of the *OH-TH* configurations, and the largest point defect separation in the  $4 \times 4 \times 4$  supercell. In the *SB-TH* case, we considered all 17 configurations.

For the *SB-TH* configurations (Fig. 5.7(a)) the largest interaction energies are again found for the smallest point defect separations. The closest possible arrangement of a boron in the *SB* site and hydrogen in the *TH*, initially aligned along  $\langle 120 \rangle$ , is attractive and relaxed to a B-H dumbbell aligned along  $\langle 100 \rangle$ , a tendency already observed in the *SB-OH* configurations for the B-B case. Additional calculations for dumbbells aligned along  $\langle 111 \rangle$  ( $\langle 110 \rangle$ ) yield repulsive interaction energies with a B-H distance of 1.44 Å (1.55 Å) and  $E_{\text{int}} = 0.39$  eV (0.30 eV). The initially 2NN configuration (at 2.8 Å in Fig. 5.7(a)) is repulsive, most likely due to distorted local environments of both point defects that share two host iron atoms as 1NN neighbors. The remaining configurations yield weak interaction energies with small deviations from the zero-line due to the finite size of our supercell.

For the *OH-TH* configurations (Fig. 5.7(b)) the initially closest arrangement along  $\langle 100 \rangle$  is mechanically unstable and hydrogen is pushed to the nearest *TH* along  $\langle 100 \rangle$  with a weak attractive (repulsive) interaction for full (ionic) relaxation. Thus, the initially second-closest arrangement along  $\langle 120 \rangle$  becomes the mechanically stable 1NN arrangement, which yields a strong repulsive interaction energy. The calculated interaction energies for larger point defect separations are weakly attractive.

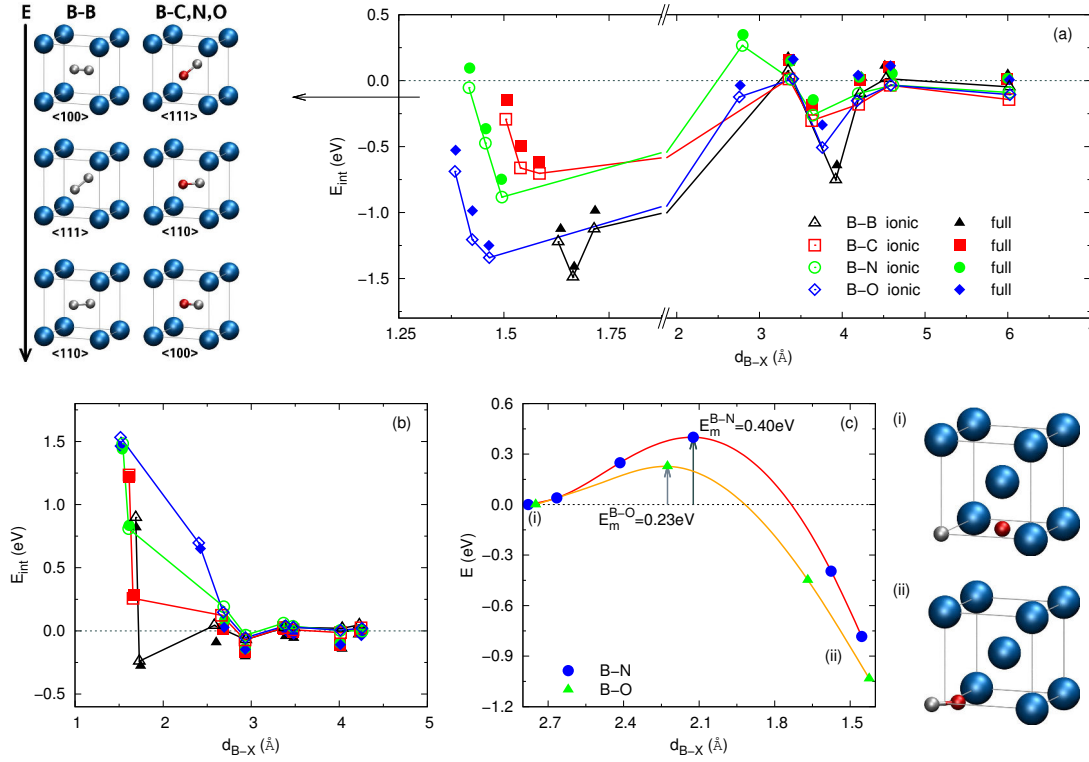


Figure 5.8.: Interaction energy versus point defect separation for (a) B-B/C/N/O  $SB-OH$  and (b)  $OH-OH$ .  $SB-OH$  configurations with small point defect separation form B-B/C/N/O dumbbells with different alignment and varying stability sequence. (c) Energy barrier for the formation of  $\langle 110 \rangle$  dumbbells in B-N and B-O.

### 5.3.5. Boron - Carbon, Nitrogen, Oxygen

In contrast to the substitutional solution of boron in  $\alpha$ -iron, carbon [372], nitrogen [375] and oxygen [386] occupy the  $OH$  site. Therefore, we only considered the  $SB-OH$  and  $OH-OH$  configurations. We further considered only configurations with a distance of up to 7 Å ( $SB-OH$ ) and 5 Å ( $OH-OH$ ), respectively, that we identified as interaction range in the calculations of B-B interactions above.

Interaction energies for the  $SB-OH$  and  $OH-OH$  B-B configurations in this investigation have been recalculated with the same plane wave cutoff used for B-C/N/O and are added for comparison. For the  $SB-OH$  configurations (Fig. 5.8(a)) we observe the same tendency of interaction energies for all types of second defect with the largest magnitude for B-B, followed by B-O, and weaker magnitude for B-C and B-N. Similar to the B-B case, the 1NN (2NN) configuration in the B-C case forms a  $\langle 100 \rangle$  ( $\langle 110 \rangle$ ) dumbbell. However, in the B-N and B-O case only the 1NN configuration formed a  $\langle 100 \rangle$  dumbbell, while the 2NN configuration is repulsive. Additional calculations of the  $\langle 111 \rangle$  dumbbell for all cases and the  $\langle 110 \rangle$  dumb-

bells for B-N and B-O showed that B-C, B-N and B-O favor the  $\langle 100 \rangle$  dumbbell, followed by the  $\langle 110 \rangle$  and  $\langle 111 \rangle$  dumbbell. This is in contrast to B-B where we observe the stability sequence  $\langle 110 \rangle$ ,  $\langle 111 \rangle$  and  $\langle 100 \rangle$ . The distance between both point defects within the dumbbells generally match typical bond lengths in bulk phases: distances for the B-C dumbbells in the range of 1.50-1.58 Å are typical B-C bond lengths found in the only carbide listed in the experimental phase diagram [411], hR45-B<sub>13</sub>C<sub>2</sub> [412], and agree well with tabulated B-C bond lengths in organic compounds [413, 414]. The only boronitride listed in the experimental phase diagram [415], hR6-BN [416], with a B-N bond length of 1.446 Å and the tabulated values in Ref. [414] are close to our calculated B-N distances of 1.42-1.50 Å in the dumbbells. The B-O distances of 1.38-1.47 Å for the dumbbells are longer than the bond length reported in Ref. [413], but matches the tabulated values in Ref. [414]. In the 4NN configuration of *SB-OH* B-B, the two boron atoms formed a B-Fe-B complex along  $\langle 111 \rangle$  with an attractive interaction energy. In the B-C, B-N and B-O cases, however, the atoms in the *OH* site remain in this position, but we observe relative large interaction energies. This effect might be attributed to favorable geometric alignment with one of the host iron atoms as 1NN to both point defects: boron in the *SB* and carbon, nitrogen and oxygen in the *OH* site. The tendency of substitutional boron to contract 1NN Fe-B distances seems to match the tendency of octahedral carbon, nitrogen and oxygen to elongate the 1NN Fe-X distance, and give rise to the attractive interaction energy. The strongest geometric modifications are observed for B-O, which is consistent with the largest influence on the interaction energy. A recent atom probe analysis on welds by Dubben *et al.* [370] identified the existence of B-C pairs and suggested that boron forms small clusters with carbon and oxygen. Thus, the tendency of substitutional boron to bind to these point defects is consistent with experimental results.

We further investigated the B-N and B-O case with respect to the repulsion which occurred in the 2NN configuration (along  $\langle 110 \rangle$ ), which did not appear in the B-B and B-C case. This indicates the existence of an additional barrier which hinders the formation of the  $\langle 110 \rangle$  dumbbell, which does not exist in the B-B and B-C case. We performed a CI-NEB calculation in order to estimate the height of the barrier. For both the B-N and B-O case we used the distant alignment, where boron (nitrogen and oxygen) remains in the *SB* (*OH*) site, as initial and the forced, close alignment, i.e. the  $\langle 110 \rangle$  dumbbell, as final state with 7 NEB images along the path between them. The energy versus the point defect separation is shown in Fig. 5.8(c). Here, we refrained from using the reaction coordinate as abscissas, as some NEB images represented virtually identical energies and point defect separation, but differing reaction coordinates. Thus, less than 7 points appear in Fig. 5.8(c), despite the usage of 7 NEB images. The plot shows clearly the existence of a migration barrier for both cases. We find a higher barrier for B-N with a value of  $E_{\text{mig}}^{\text{B-N}} = 0.40$  eV compared to B-O with a barrier of  $E_{\text{mig}}^{\text{B-O}} = 0.23$  eV.

The B-C/N/O dumbbells we investigated showed the stability sequence  $E_{\langle 100 \rangle} < E_{\langle 110 \rangle} < E_{\langle 111 \rangle}$  which is different from the stability sequence we observed for the B-B dumbbells. Here, the sequence  $E_{\langle 110 \rangle} < E_{\langle 111 \rangle} < E_{\langle 100 \rangle}$  is unique among the boron-containing dumbbells we have investigated, but the stability sequence is identical to the sequence of Fe-Fe dumbbells in  $\alpha$ -iron [404]. However, calculations for other single-type dumbbells containing carbon, nitrogen

and oxygen show that the stability sequence of B-B and Fe-Fe dumbbells is not solely related to the formation of dumbbells by atoms of the same type. The C-C and N-N dumbbells show the same stability sequence that was observed for the B-C/N/O dumbbells (Tab. 5.4). For these systems, we added the interaction energies if both point defects form a  $OH-\square-OH$  complex instead of a dumbbell. In this configuration, the interstitial point defects remain in the  $OH$  site. Such complexes containing interstitial carbon and nitrogen have been addressed in previous DFT studies [375, 378, 379]. However, these studies did not compare the stability of the complexes with the stability of the dumbbells. For B-B, we note that the  $\langle 100 \rangle$  and  $\langle 110 \rangle$   $OH-\square-OH$  complexes are not stable, and the boron atoms form a dumbbell instead. In bcc, a  $OH-\square-OH$  complex with  $\langle 111 \rangle$  alignment is not possible: this configuration represents a dumbbell. For carbon, we find that dumbbell formation is favored over the  $OH-\square-OH$  complex. This is inverted for nitrogen. For oxygen, the only mechanically stable configuration along  $\langle 100 \rangle$  is the  $OH-\square-OH$  complex. Along  $\langle 110 \rangle$  we observed a configuration that is neither a dumbbell nor a  $OH-\square-OH$  complex, with an interaction energy of  $E_{\text{int}} = -2.07$  eV that is in between the  $\langle 100 \rangle$   $OH-\square-OH$  complex and the  $\langle 111 \rangle$  dumbbell.

In the  $OH-OH$  configurations (Fig. 5.8(b)) all 1NN configurations exhibit a repulsive behavior where the magnitude in the interaction energy increases with the number of valence electrons from boron over carbon and nitrogen to oxygen. The same tendency of increasing interaction energy is observed for the 2NN configurations, with a transition of attractive to repulsive interaction energy when going from boron to carbon, and a different point defect separation for B-O compared to the other three cases. We note that the trend of increasing interaction energy with the number of valence electrons of the point defects was also observed in Refs. [379, 405]. For the blocked 4NN configuration we find 1.55 eV (1.95 eV) with full (ionic) relaxation for carbon, 1.50 eV (1.90 eV) for nitrogen and 1.46 eV (1.85 eV) for oxygen. As in the case of B-B (see Sec. IV.A), the lower interaction energies calculated with fully relaxed supercells can be attributed to the volume expansion of the supercells that increases the distance between point defects and common 1NN iron atom.

The attractive interaction for the 2NN B-B arrangement is not reproduced for B-C, B-N and B-O. The investigation of the local magnetic moments for boron and the six host iron atoms that form the octahedron surrounding the boron atoms reveals that the 2NN arrangement differs substantially in the magnetic moment of the host iron atoms (Fig. 5.9(a)). For the

	dumbbell			$OH-\square-OH$	
	$\langle 100 \rangle$	$\langle 110 \rangle$	$\langle 111 \rangle$	$\langle 100 \rangle$	$\langle 110 \rangle$
B-B	-1.12	-1.49	-1.22	...	...
C-C	-1.66	-1.65	-1.19	-1.32	-0.36
N-N	-0.22	0.34	1.29	-1.96	-0.74
O-O	...	...	-0.89	-3.54	...

Table 5.4.: Interaction energies (in eV) for single-type dumbbells and  $OH-\square-OH$  complexes. All results are calculated with ionic relaxation only.

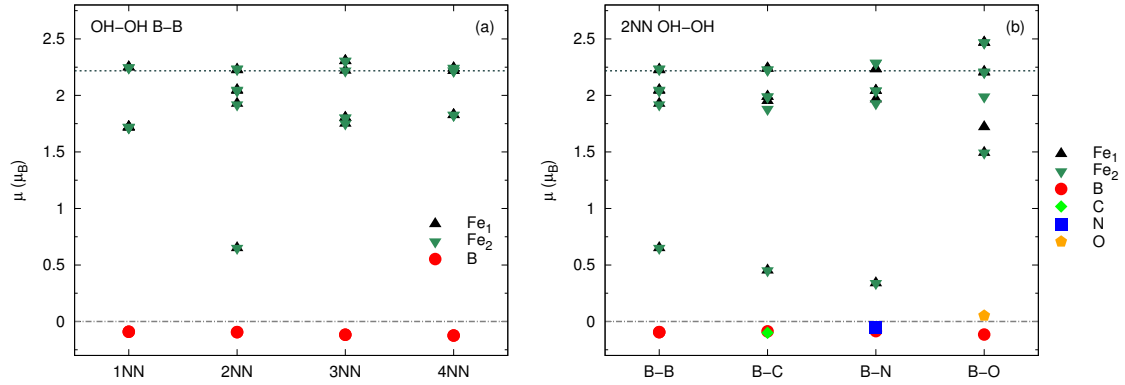


Figure 5.9.: Local magnetic moments of point defects and the six nearest-neighbor host iron atoms for (a) the four closest *OH-OH* B-B arrangements and (b) the 2NN *OH-OH* B-X arrangement (X=B,C,N,O). The six nearest-neighbor host iron atoms form the octahedron that encapsulates the boron atoms. The local magnetic moment of iron in a pure bcc structure is indicated by the dashed line.

1NN, 3NN and 4NN arrangements the local magnetic moments are either slightly increased compared to the magnetic moment of iron in pure bcc or reduced to a value of approximately  $1.8 \mu_B$ , independent on the number of host iron atoms that both boron atoms share as nearest neighbors. In the 2NN arrangement, both boron atoms share one of the top/bottom host iron atoms, which forms the octahedron surrounding the boron atom. These host iron atoms have a smaller distance to the boron atoms compared to the corner atoms of the octahedron. The local magnetic moment of the shared host iron atom is significantly reduced compared to the other cases. The remaining host iron atoms have local magnetic moments very similar to the pure bulk value, or are reduced to a value of approximately  $2 \mu_B$ . The boron atoms align antiparallel to the iron atoms, with local magnetic moments in the range of  $-0.1 \mu_B$  which is similar to the local magnetic moment of a single boron point defect in the *OH* site, and independent of the B-B distance. However, the change in the local magnetic moment of the iron atoms for the 2NN arrangement is not restricted to the B-B case. A similar behavior is observed for the corresponding B-C and B-N configurations. Despite carbon and nitrogen having the same tendency of their local magnetic moments to align antiparallel to the iron atoms, with a similar magnitude compared to boron, the local magnetic moment of the shared iron atom is reduced when going from boron to carbon and nitrogen. To some extent the decrease in the local magnetic moment of the shared host iron atom coincides with the corresponding interaction energy. However, this can not fully account for these tendencies, as the 2NN B-O arrangement is also repulsive, but due to the larger point defect separation the impact on the local magnetic moments of the host Fe atoms is less pronounced. Furthermore, oxygen is the only considered point defect in this row of the periodic table which aligns its local magnetic moment parallel to the host atoms.



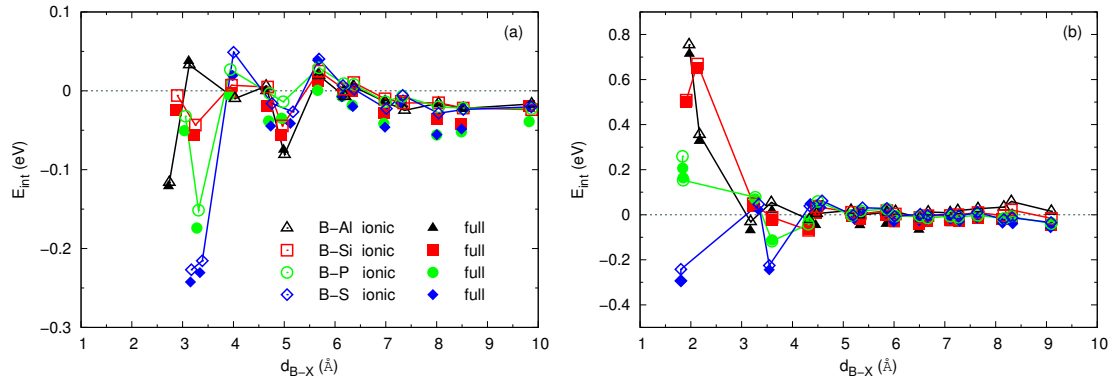


Figure 5.10.: Interaction energy versus point defect separation for (a) B-Al/Si/P/S *SB-SB* and (b) *OH-SB*.

### 5.3.6. Boron - Aluminum, Silicon, Phosphorus, Sulfur

The elements aluminum, silicon, phosphorus and sulfur in the second row of the p-block in the periodic table are substitutional elements in  $\alpha$ -iron. The investigation of point defect interactions between boron and aluminum, silicon, phosphorus and sulfur is performed with boron in either the *SB* and *OH* site. The interaction of boron in the *SB* site (Fig. 5.10(a)) with silicon and phosphorus resembles the previously discussed *SB-SB* B-B and B-□ case. In particular, we find a larger magnitude of the interaction energy for the 2NN configuration with both point defect aligned along  $\langle 100 \rangle$  as compared to the 1NN configuration with both point defects aligned along  $\langle 111 \rangle$ . However, the interaction energy is very small in the case of silicon. The interaction is different for aluminum, with an attractive interaction for the 1NN configuration and a weaker repulsive interaction for the 2NN configuration. For sulfur both the 1NN and 2NN arrangement yield an attractive interaction of similar strength. The overall attractive interaction of substitutional boron with aluminum, silicon, phosphorus and sulfur is in line with tendencies that we could identify for boron and a vacancy. Similar to these previous cases, the relaxation condition has a very small effect on the interaction energy. Configurations with larger point defect separation show small interaction energies. An exception is the 5NN configuration with a dip in the interaction energy. This may be attributed to matching strain effects, as in this configuration both point defects align along the  $\langle 111 \rangle$  axis, with a host iron atom in between, and the second row p-block element (boron) tends to increase (decrease) the distance towards the shared host iron atom. The strongest effect is found for aluminum, the largest considered second row p-block element, and decreases with atomic size: the effect is weaker for silicon, which has a smaller atomic size compared to aluminum, and again weaker for phosphorus and sulfur, which have a smaller atomic size compared to silicon.

With boron in the *OH* site (Fig. 5.10(b)), the 1NN and 2NN arrangements yield repulsive interactions for aluminum, silicon and phosphorus. The interaction energies for 1NN and 2NN B-S for only ionic and fully relaxed supercells are similar and overlap in Fig. 5.10(b). For aluminum and silicon in the 1NN and 2NN arrangement both point defects remain in

their initial *SB* and *OH* position, respectively, but for both phosphorus and sulfur the two point defects form dumbbells, a tendency that has been previously observed for close *SB-OH* configurations of B-B/C/N/O and close *SB-TH* configurations of B-H. However, the solely repulsive interaction for B-P deviates from these tendencies, where in general the most favorable dumbbell was always attractive, while the behavior of B-S matches the tendency. Similar to B-C/N/O the most favorite alignment is the  $\langle 100 \rangle$  dumbbell for B-P and B-S, followed by the  $\langle 110 \rangle$  dumbbell. For completeness we also calculated the alignment along  $\langle 111 \rangle$  for all four configurations, but obtained consistently larger interaction energies compared to the other two alignments. For aluminum, we obtain  $E_{\text{int}} = 1.77 \text{ eV}$  (1.89 eV) for full (ionic) relaxation, for silicon  $E_{\text{int}} = 1.21 \text{ eV}$  (1.30 eV), for phosphorus  $E_{\text{int}} = 0.60 \text{ eV}$  (0.67 eV) and for sulfur  $E_{\text{int}} = 0.30 \text{ eV}$  (0.37 eV) (not included in Fig. 5.10(b)). Thus, the stability sequence of B-P and B-S dumbbells matches the sequence of B-C/N/O dumbbells with  $E_{\langle 100 \rangle} < E_{\langle 110 \rangle} < E_{\langle 111 \rangle}$ . The dip in the interaction energy for the 4NN arrangement has also been observed in *SB-OH* configurations for B-B/C/N/O (Fig. 5.8(a)) and was related to matching strain effects. Here, the interaction energy varies with atomic size of the second row p-block element, and is weakest for aluminum, the largest element. It increases from silicon to phosphorus and sulfur with decreasing atomic size. For the remaining configurations the interaction energies are weak but never vanish due to the finite size of the supercell. Furthermore, the relaxation condition has a negligible effect on the magnitude of the interaction energy.

## 5.4. Trends in Point Defect Interaction

In the investigation of the point defect interaction of boron located in either the *SB* or *OH* site, we took into account a considerable number of elements that are important in steel manufacturing. In particular, we considered hydrogen and the elements of interest in the first (B,C,N,O) and second (Al,Si,P,S) row of the p-block of the periodic table. Furthermore, we investigated the interaction between boron and a vacancy. However, despite the variety of considered elements and configurations dependent on the favored defect site of the element, certain trends in the interaction became apparent that were predominantly determined by the defect site of boron and to a lesser extent by the type of the second point defect. Substitutional boron tends to bind the second point defect, while interstitial boron located in the *OH* site tends to repel it. The type of second point defect usually determines the magnitude in the interaction.

The interaction energies are summarized in Fig. 5.11. The relaxation condition has an influence on the magnitude of the interaction energy, but not on the overall attractive/repulsive tendency. Therefore, we show only results that were calculated with ionic relaxation. The largest magnitudes of the interaction are obtained for the smallest point defect separations. Thus, we summarize only the interaction energies for the 1NN and 2NN configuration if the point defects remained in the defect site, or the three dumbbell alignments if a dumbbell is formed. In order to discuss trends in the interaction energy associated with band-filling, i.e. the number of valence electrons, we add results for the elements fluorine, neon, chlorine and argon, that are substitutional elements in  $\alpha$ -iron (Tab. 5.5). For chlorine and argon this is in

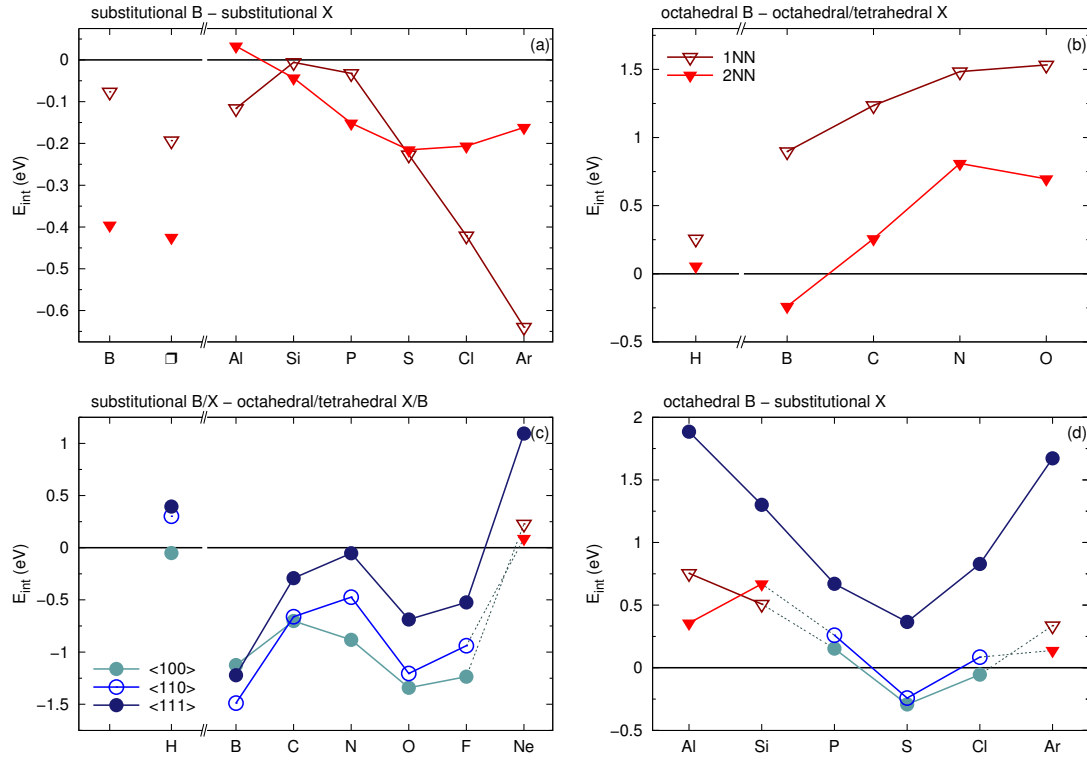


Figure 5.11.: Interaction energies of boron with a second point defect for the closest arrangements as obtained from ionic relaxation.

line with the other second row p-block elements. Fluorine and neon, in contrast, deviate from their direct neighbors in the first row of the p-block. However, their substitutional solution in  $\alpha$ -iron is in line with boron. Furthermore, the addition of the remaining first and second row p-block elements in general does not alter the observed trends that the attractive/repulsive tendency is predominantly determined by the defect site of boron.

In order to understand the tendencies of the interaction between boron and other point defects, that are dependent on the arrangement between both point defects and the type of second point defect, we analyze the configurations with respect to volumetric effects and by decomposing the interaction energies into the individual contributions. In the former case, we investigate whether the attraction/repulsion and the magnitude of the interaction energy can be related to the distortions of the host lattice, that are required for incorporation of the point defects. In the latter case, we decompose the interaction energy into a mechanical and chemical contribution. This approach was used to understand trends related to single point defects at grain boundaries [147, 152, 154] or in the bulk material [155], but the extension to systems containing two or more point defects is straightforward. We will briefly introduce the concepts in the following sections.

### 5.4.1. Geometric Factor

In the first step we investigated whether the changes and calculated magnitudes of the interaction energies might be related to the distortions of the host matrix that arise due to the incorporation of substitutional and interstitial point defects. These distortions are reflected in modified atomic positions of the host atoms that are shifted in order to accommodate the point defect. This is stronger for the closest host atoms, and we refer to these atoms as the local environment of a point defect. In Sec. 5.2.2, we already discussed the impact of single substitutional and interstitial boron, carbon, nitrogen and oxygen atoms on the position of the host iron atoms, reflected in the modified distances towards the 1NN and 2NN host iron atoms.

Incorporation of a second point defect in close vicinity to an already present point defect in the host matrix will additionally alter the atomic positions of the host atoms, as the host matrix is distorted in order to accommodate the second point defect. With increasing distance between the first and second point defect, the mutual distortion of the local environment should decrease, and above a certain distance incorporation of a second point defect should not alter the local environment of the first point defect. In order to quantify the distortion of the local environment of a point defect due to presence of a second one, we first introduce a volumetric measure for a single point defect  $i$

$$\Delta V_i = \frac{V_i - V_{i0}}{V_{i0}}, \quad i \in \{1, 2\}. \quad (5.5)$$

$V_i$  represents the volume of the local environment of point defect  $i$  in a supercell containing two point defects and  $V_{i0}$  as reference volume of the local environment in a supercell with only one point defect  $i$ , c.f. Sec. 5.2.2. For substitutional point defects and dumbbells, the local environment is given by the eight 1NN host atoms. The local environment volume corresponds to the volume of the cube that is spanned by the eight 1NN host atoms. Presence of a second point defect in the near vicinity will distort the cube. For the tetrahedral and octahedral sites, the local environment volume corresponds to the volume of the tetrahedron and octahedron, respectively, that is formed by four and six host atoms around the point defect, c.f. Fig. 5.1(a-c). For all systems except the dumbbell-forming ones the volumes  $V_i$  and  $V_{i0}$  for each point defect correspond to the same point defect site, i.e. located either in the *SB*, *OH* or *TH* site. In dumbbell-forming systems, in contrast, we used the *SB* site for single point defects in order to calculate the reference volume  $V_{i0}$ , although this site is not the favored one for hydrogen and

	F	Ne	Cl	Ar
$E_{SB} - E_{OH}$	-0.77	-3.41	-2.29	-3.78
$E_{SB} - E_{TH}$	-1.03	-3.31	-2.30	-3.64

Table 5.5.: Formation energy difference in eV between substitutional and interstitial point defects fluorine, neon, chlorine and argon in  $\alpha$ -iron calculated with a  $3 \times 3 \times 3$  supercell and ionic relaxation.

some of the first row p-block elements. The calculation of the local environment volume was carried out with qhull-2011.1 [203]. In order to define one parameter for each configuration containing two point defects, we set the mean value as geometric factor

$$\overline{\Delta V} = \frac{1}{2} (\Delta V_1 + \Delta V_2). \quad (5.6)$$

According to the definition of Eq. 5.5 and 5.6, the geometric factor  $\overline{\Delta V}$  will be close to zero above a certain distance between both point defects. This is in line with the distance-dependent interaction energy that is close to zero for the configurations above a certain point defect separation.

We further note that  $\overline{\Delta V}$  takes only into account the distortions of the host lattice that are required for the incorporation of the point defects. However, this factor is not expected to be able to account for the chemical interaction, e.g. bond formation, between the two point defects at small separations.

#### 5.4.2. Mechanical and Chemical Contribution

For a better understanding of the trends in the interaction energy, it is helpful to decompose the interaction energy into a mechanical and chemical contribution. This approach was used to understand trends of single point defects by decomposing the formation energies into a mechanical and chemical contribution. We show that this concept can be easily extended to configurations containing two or more point defects. The mechanical contribution is associated with the energy that is required to distort the host lattice in order to accommodate the point defect. In the case of the formation energy, this contribution is defined as the difference in the energy of a relaxed host matrix containing a point defect, but the point defect removed and the lattice geometry frozen, and the energy of an undisturbed host matrix without point defect. For substitutional point defects, one can add and subtract the energy of a host matrix containing a vacancy, so that after rearrangement of terms one obtains the sum of the mechanical energy (with respect to the matrix containing a vacancy) and the vacancy formation energy. The chemical contribution comprises the remaining energy, and is associated with the bond formation of the incorporated point defect with the nearest host atoms.

As the interaction energy (Eq. 5.4) can be rewritten in terms of formation energies of the contributing supercells, the concept of the decomposition into a mechanical and chemical contribution can be extended to configurations containing two or more point defects. This yields

$$\begin{aligned} E_{\text{int},X+Y} &= E_{f,X+Y} - (E_{f,X} + E_{f,Y}) \\ &= E_{\text{mech},X+Y} + E_{\text{chem},X+Y} - (E_{\text{mech},X} + E_{\text{chem},X} + E_{\text{mech},Y} + E_{\text{chem},Y}) \\ &= (E_{\text{mech},X+Y} - E_{\text{mech},X} - E_{\text{mech},Y}) + (E_{\text{chem},X+Y} - E_{\text{chem},X} - E_{\text{chem},Y}) \\ &= \Delta E_{\text{mech}} + \Delta E_{\text{chem}}. \end{aligned} \quad (5.7)$$

Thus, the interaction energy comprises a relative mechanical and chemical contribution, that is calculated from the mechanical and chemical contributions between the supercell containing two point defects and the two supercells containing one of the point defects. In this form, Eq. 5.7 is valid for all solely interstitial and *SB-OH/TH* configurations, if in the latter case the reference states are also one substitutional and one interstitial element. The vacancy formation energy does not enter in Eq. 5.7 for *SB-OH/TH* configurations. Here, the parameter is canceled as it enters in both  $E_{f,X+Y}$  and  $E_{f,X}$  or  $E_{f,Y}$ . In the case of two substitutional elements, we obtain an additional term in Eq. 5.7 that represents the interaction energy between two vacancies. Thus, Eq. 5.7 is modified to

$$E_{\text{int},X+Y} = \Delta E_{\text{mech}} + E_{\text{int},\square-\square} + \Delta E_{\text{chem}}. \quad (5.8)$$

We note that  $E_{\text{int},\square-\square}$  is not a constant value, like the vacancy formation energy itself, but depends of the alignment and distance between the two vacancies that are introduced in the iron host matrix.

For simplicity, we will hereafter drop the term relative when referring to the mechanical and chemical contribution. When we refer to these two contributions, it corresponds to the difference in these contributions from the three supercells that contain the point defects.

### 5.4.3. Point Defects in Similar Sites

In the first step, we focus on the configurations with the point defects in similar sites, i.e. both point defects in the *SB* site or both in one of the interstitial sites.

In configurations with both point defect in *SB* sites, we investigated the interaction among boron and a second boron, a vacancy, and the second row p-block elements aluminum, silicon, phosphorus and sulfur. We further added results for the remaining elements of the second row in the p-block, chlorine and argon. For the 1NN and 2NN B-B and B- $\square$  arrangements (Fig. 5.11(a)), the interaction is attractive and more pronounced for the 2NN arrangement, with both point defects aligned along  $\langle 100 \rangle$ , the elastically soft axis in  $\alpha$ -iron. B-Al has the same number of valence electrons as B-B, but the interaction is different, as for B-Al the 1NN arrangement is attractive, and repulsive for the 2NN arrangement. The interaction for B-Si and B-P is attractive and more pronounced for the 2NN arrangement than for the 1NN arrangement, similar to B-B and B- $\square$ . For B-S, both arrangements are attractive with a similar magnitude in the interaction energy. Similar to B-Al, B-Cl and B-Ar have a more pronounced interaction energy for the 1NN arrangement compared to the 2NN arrangement. In contrast to B-Al, both arrangements are attractive.

The tendencies in the interaction and the influence on the elastic constants and directional-dependence of Young's modulus (see Fig. 5.3) are similar for boron and a vacancy in the point defect concentration we have considered. Therefore, we investigated the observed tendencies in the point defect interactions with respect to the influence of the corresponding point defect on the directional-dependence of Young's modulus. The advantage is that the closest arrangement aligns along the axis of  $\alpha$ -iron with the most pronounced Young's modulus. The 1NN (2NN)

arrangement aligns along  $\langle 111 \rangle$  ( $\langle 100 \rangle$ ), the elastically hard (soft) axis in  $\alpha$ -iron. However, while we observe similarities in the interaction and the influence on the elastic properties for the configuration of boron and a vacancy, and silicon and phosphorus, it fails for sulfur. This element exerts a slightly weaker reduction of the elastic properties as a vacancy, but the tendency in the interaction differs significantly. The influence of aluminum on the elastic properties, on the contrary, is unique among the considered point defects, as is the tendency in the interaction.

With regard to the interaction to other point defects, substitutional boron resembles a vacancy. This has already been observed in the impact of substitutional boron and a vacancy on the elastic properties of  $\alpha$ -iron, if the boron content is below 3% (see Fig. 5.3). Regarding point defect interaction,  $SB-SB$  B-B and B- $\square$  show the same attractive behavior for the 1NN and 2NN configuration, with the larger magnitude for the 2NN configuration, that is virtually identical for both B-B and B- $\square$ . The 1NN interaction is more pronounced for B- $\square$ . The trends observed for the 1NN and 2NN arrangements for the B-Al/Si/P/S configurations on band-filling, i.e. the number of valence electrons, are in line with trends for  $\square$ -Al/Si/P/S interactions [417], that are parabolic-like for the 1NN and monotonically decreasing for the 2NN arrangements. In this study, the interaction between a vacancy and chlorine or argon, respectively, was not addressed.

Regarding configurations with both point defects in interstitial sites, we investigated the interaction between boron and hydrogen and the first row p-block elements boron, carbon, nitrogen and oxygen. For all considered configurations the interaction is more pronounced for the 1NN arrangement compared to the 2NN arrangement (Fig. 5.11(b)) and is repulsive, except 2NN B-B which shows attractive interaction.

For the first row p-block the interaction energy of the 1NN arrangement increases with band-filling from boron to nitrogen, with a maximum in the interaction energy for nitrogen and oxygen. The same holds for the 2NN arrangement, if oxygen is omitted due to the larger point defect separation when compared to the other three elements (c.f. Fig. 5.8(b)). The approximately linear dependence in the interaction energy from boron to nitrogen, omitting oxygen, correlates with the decrease of the local magnetic moment of the 1NN host iron atom that is shared by both point defects (c.f. Fig. 5.9(b)). The overall repulsive behavior of interstitial boron resembles carbon and nitrogen. Previous DFT studies [375,379] showed that C-C, C-N and N-N repel each other which suggests that carbon and nitrogen point defects in  $\alpha$ -iron will lie as far away from another as possible.

**Geometric factor** The calculation of the geometric factor  $\overline{\Delta V}$  was performed for all configurations with two point defects in similar sites. We considered the 1NN and 2NN arrangements because the largest magnitudes in the interaction energy were observed for these arrangements. The 3NN arrangement is taken into account as verification. Here the interaction energies were small and the point defect separation is significantly larger. Hence, we expect less distortion of the local environment due to the presence of a second point defect. Indeed, for the majority of considered configurations, the geometric factor scales with the interaction energy. For the

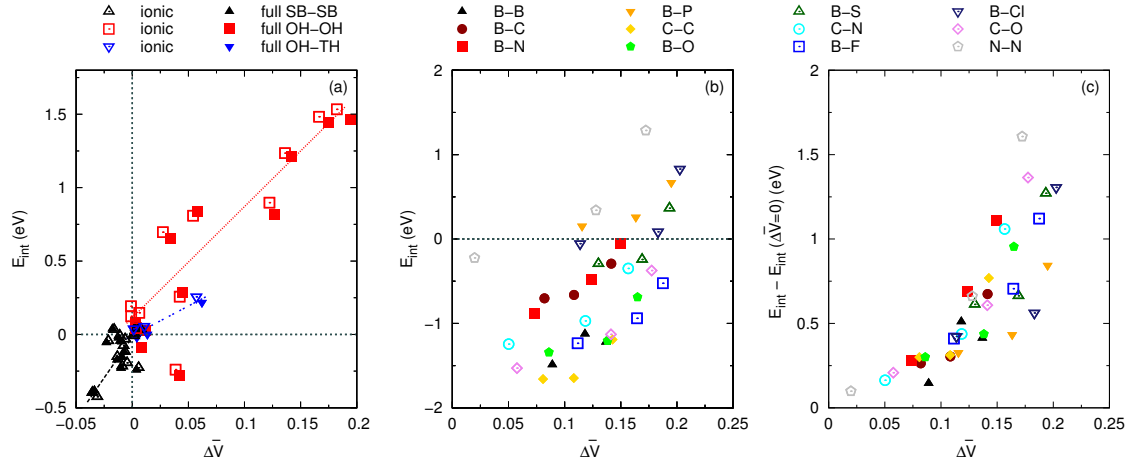


Figure 5.12.: Geometric factor  $\overline{\Delta V}$  versus interaction energy for configurations with point defects in (a) similar sites and (b) with dumbbell formation. (c) Shifted interaction energies with respect to  $E_{\text{int}}(\overline{\Delta V} = 0)$  for the dumbbell configurations. The lines in (a) are only a guide for the eye.

interstitial configurations  $\overline{\Delta V}$  is predominantly positive, indicating an expansion of the local environment volume at small point defect separations. However, this simple approach fails to account for the attractive 2NN B-B configuration. For the configurations with both point defects in *SB* sites, the magnitudes in  $\overline{\Delta V}$  and the interaction energy are much weaker. The geometric factor is predominantly negative which indicates a compression of the local environment volume at small point defect separations. However, the scatter in the data points is much stronger, which means that this simple approach is not sufficient to explain the observed values for the interaction energy. Furthermore, this approach relies on the local environment formed by the neighboring host iron atoms. In the 1NN arrangement of two substitutional point defects, however, one of the host iron atoms of the local environment is replaced by the other point defect. Here, the corresponding local environment volume is calculated with a virtual eight host iron atom with its position extrapolated from the other seven host iron atoms.

**Mechanical and chemical contribution** The decomposition of the interaction energy into the mechanical, chemical and  $\square$ - $\square$  interaction energies is shown in Fig. 5.13. The  $\square$ - $\square$  interactions are attractive with an interaction energy of  $E_{\text{int},\square-\square} = -0.17$  eV ( $-0.26$  eV) for the 1NN (2NN) arrangement. These values agree well with other calculations [378] and the larger magnitude for the 2NN arrangement is in line with B-B/ $\square$ /Si/P interactions (Fig. 5.13(a,b)). For B-B and B- $\square$ , the attractive interaction for the 1NN (2NN) arrangement can be mainly attributed to the  $\square$ - $\square$  interaction energy ( $\square$ - $\square$  interaction and chemical energy). The mechanical contribution has a positive value, thus the lattice distortions in order to accommodate both point defects in close vicinity are more expensive than the incorporation of two single point defects in separate supercells. The larger magnitude for the 1NN arrangement (along



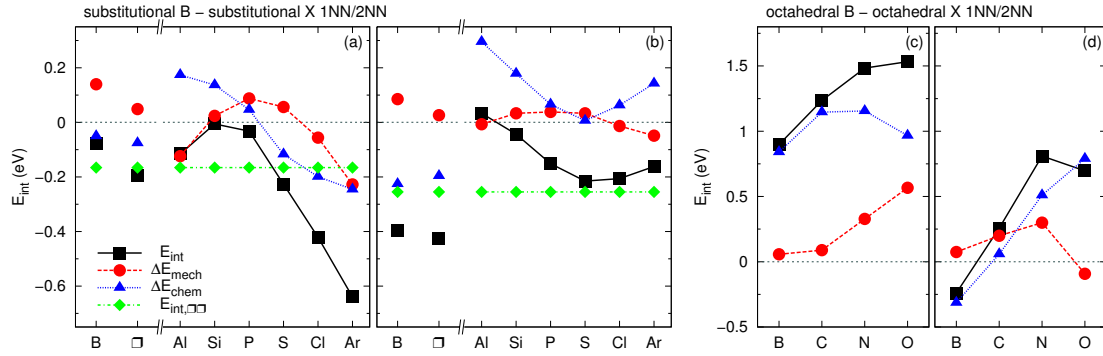


Figure 5.13.: Decomposition of the interaction energy into mechanical and chemical contribution and  $\square$ - $\square$  interaction energy for (a,b) 1NN and 2NN  $SB$ - $SB$  and (c,d)  $OH$ - $OH$  configurations.

$\langle 111 \rangle$ ) can be attributed to increased asymmetry in the host lattice distortion when compared to the 2NN arrangement (along  $\langle 100 \rangle$ ). For the second row p-block elements, the trends in the interaction energy for the 1NN arrangement can be decomposed into a monotonically decreasing chemical and parabolic-like mechanical contribution, excepting the constant  $\square$ - $\square$  term. We note that the trend in the mechanical energy correlates inversely with the size of the point defects in  $\alpha$ -iron (c.f. Fig. 5.14). A larger size mismatch between boron and the second-row p-block elements results in a more attractive mechanical contribution. For the 2NN arrangement, in contrast, the overall attractive interaction can be solely attributed to the  $\square$ - $\square$  term. The chemical contribution is consistently repulsive, in contrast to B-B/ $\square$ , while the mechanical contribution is relatively weak and negligible. The interaction energy decreases when going from aluminum to sulfur and increases again for chlorine and argon: this change in the trend can be attributed to the chemical contribution.

For the 1NN  $OH$ - $OH$  configurations (Fig. 5.13(c)), the trends in the interaction energy are determined by an increasing mechanical and parabolic-like chemical contribution with band-filling. We note that the trend in the mechanical contribution does not correlate with the required distortion of the host lattice in order to incorporate a single interstitial point defect. The largest distortions were observed for boron and oxygen, and weaker distortions for carbon and nitrogen, c.f. Sec. 5.2.2. This trend is not reflected in the mechanical contribution. For the 2NN arrangement (Fig. 5.13(d)), the deviation of B-O from the monotonically increasing interaction energy can be solely attributed to the deviating mechanical contribution. This is in line with the significantly larger point defect separation that we observed for the B-O case compared to B-B/C/N (c.f. Fig. 5.8(b)).

This analysis also reveals why the geometric factor  $\overline{\Delta V}$  is able to account for the trends in the interaction energy for the interstitial configurations, but fails for the substitutional ones. Similar to the mechanical contribution this factor represents distortions of the host lattice. For the interstitial configurations, the mechanical contribution shows the same trend as the interaction energy dependent on band-filling. This is not observed for the substitutional configurations.

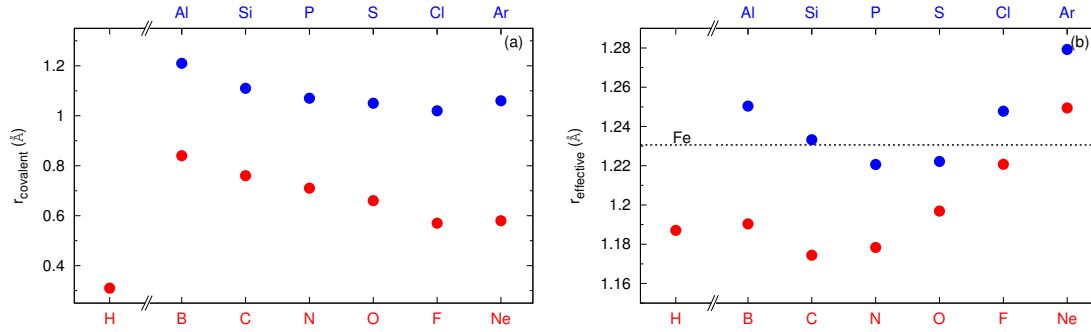


Figure 5.14.: (a) Tabulated covalent and (b) effective radii for s-block and p-block elements in  $\alpha$ -iron.

#### 5.4.4. Point Defects in Different Sites

In all configurations with boron in the *SB* site and one of the first row p-block elements B/C/N/O (H) in the *OH* (*TH*) site the closest arrangements always lead to dumbbell formation with a predominantly attractive interaction. We further observed dumbbell formation in combination with fluorine, but not with neon. Again, substitutional boron resembles a vacancy, as a binding tendency has been observed for  $\square$ -C and  $\square$ -N pairs [375, 378, 379]. For interstitial boron, our investigations of  $\square$ -B pairs also revealed an attractive interaction, which actually drags the interstitial boron towards the vacancy, thus annihilating the vacant site. In configurations with one of the second row p-block elements Al/Si/P/S/Cl/Ar in the *SB* site and boron in the *OH* site, the formation of the aforementioned dumbbells was only observed in the case of B-P, B-S and B-Cl, while for B-Al, B-Si and B-Ar both point defects remained in their respective defect site. In terms of band-filling, the interaction shows a parabolic dependence for the first row p-block elements B/C/N/O (Fig. 5.11(c)) that is centered on carbon and nitrogen. The kink in the interaction for B-F and B-Ne is due to the switched point defect sites as reference values, as fluorine and neon are substitutional elements in  $\alpha$ -iron. Therefore, boron in the *OH* site was used as reference. Trends in the interaction energy for the dumbbells for B-P/S/Cl (Fig. 5.11(d)) are similar to the isovalent systems B-N/O/F, while the energies are shifted upwards for the second row p-block elements. For early p-block elements, we observe the same energy shift upwards for the second row p-block elements. However, for these elements we do not observe the same trends among isovalent systems.

**Role of atomic size** The finding of dumbbell formation for phosphorus and sulfur was somewhat unexpected, given the relatively large atomic radius of the second row p-block elements compared to hydrogen and the first row p-block elements. Tabulated covalent radii [388] for the selected elements (Fig. 5.14(a)) show hydrogen to have the lowest covalent radius, which is much smaller than the value for the other elements. For the first row p-block elements, the covalent radius decreases with increasing number of valence electrons, except for the noble gas neon. Second row p-block elements have larger radii, but the decay of covalent radius with

increasing number of valence electrons follows a very similar shape. This indicates that the tendency to form dumbbells might be related to the atomic size of the constituent elements, with dumbbell formation only below a certain threshold.

The incorporation of point defects into a host matrix alters the atomic positions of the nearest host atoms, leading to a specific distance dependent on the element and its atomic size. In order to quantify the atomic size of a given point defect in an  $\alpha$ -iron host matrix and to be able to compare the size with the tabulated radii, we define an effective radii of a point defect as half of the distance between the 1NN host atoms and the point defect in the *SB* site. We calculated the effective radii for all elements we considered in our investigation (Fig. 5.14(b)), independent of whether or not the element favors the *SB* site. These effective radii will differ from the tabulated values of atomic radii, as the size of an atom depends on its chemical environment.

In contrast to the tabulated covalent radii, the effective radii for the first and second row p-block elements show a parabolic-like dependence on the number of valence electrons, with the center slightly shifted to lower number of valence electrons for the first row. A decreasing effective radii, a trend that resembles the covalent radii, is only observed for the early p-block elements. For the first row p-block elements, the effective radii are much larger compared to the tabulated covalent radii. This is also true for hydrogen. Given the effective radius of iron in the ferritic host matrix, all elements that formed a dumbbell, independent of favored alignment, have a smaller effective radius. The elements, that did not form a dumbbell, in particular neon, aluminum, silicon and argon, have an effective radius that is similar to or larger than the effective radius of iron. Chlorine is the only exception from this general trend that shows weakly bound dumbbells for an effective radius that is slightly larger than iron. This finding indicates that the arrangement of two point defects as dumbbell might be determined by the atomic size of the point defects in  $\alpha$ -iron. We note that for the isovalent systems which show the same trend in the interaction energy (B-N/P, B-O/S, B-F/Cl), a decrease of effective radii leads to more stable dumbbells. This dependence is inverted for comparisons of the interstitial elements boron, carbon, nitrogen and oxygen in the first p-block row.

**Geometric factor** Next, we investigated the relationship of the abovementioned geometric factor with the interaction energy. As the two point defects forming a dumbbell surround a vacancy, this represents a substitutional defect. Therefore, the local environment volume for the dumbbells is given by the eight 1NN host iron atoms, thus  $V_1 = V_2$ , and the corresponding reference volume  $V_{i0}$  represents the local environment volume obtained from a supercell with one point defect at the *SB* site, despite the fact that this is not the favored site for hydrogen, carbon, nitrogen and oxygen. The geometric parameter (Fig. 5.12(b)) is able to account for the most stable alignment for boron-containing dumbbells. The favored alignment induces throughout the weakest distortion of the local environment volume. For comparison, we further calculated the corresponding dumbbells for the C-C, C-N, C-O and N-N configuration. We restricted the calculation to the ionic relaxation, as the relaxation condition only affects the magnitude in the interaction energy, but never the overall attractive/repulsive interaction. The interaction energy for these configurations has been calculated using carbon, nitrogen

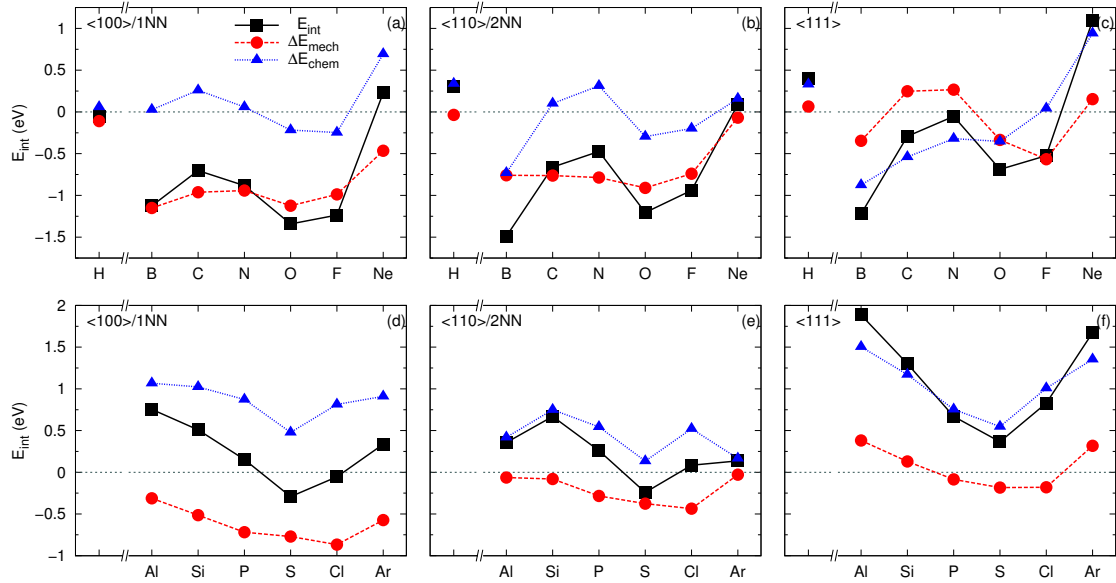


Figure 5.15.: Decomposition of interaction energy into mechanical and chemical contribution for (a,b,c) first and (d,e,f) second row *SB-OH/TH* configurations, separated according to point defect orientation: (a,d)  $\langle 100 \rangle / 1\text{NN}$ , (b,e)  $\langle 110 \rangle / 2\text{NN}$  and (c,f)  $\langle 111 \rangle$ . We do not explicitly separate between the dumbbell-forming systems and systems where no dumbbell was formed.

and oxygen in the *OH* site as reference state. All configurations favor the same stability sequence as found in the B-C, B-N and B-O configuration, and the smallest geometric factor is consistently associated with the largest interaction energy. This finding excludes that the origin of the deviating sequence for B-B dumbbells is simply the formation of a dumbbell by two point defects of the same type. However, our simple approach is not sufficient to explain the whole stability sequence in terms of local environment distortions. For example, in the case of B-B dumbbells the  $\langle 111 \rangle$  has a larger interaction energy than the  $\langle 100 \rangle$ , but induces a larger local environment distortion. As the relationship between the geometric factor  $\overline{\Delta V}$  and the interaction energy  $E_{\text{int}}$  resembles a parabola, we used a fit of the form  $a + b \cdot x^2$  in order to determine the value  $E_{\text{int}}(\overline{\Delta V} = 0)$ , the interaction energy associated with zero distortion of the local environment. This represents purely an energy contribution due to the different point defects forming the dumbbell. Shifting  $E_{\text{int}}$  (Fig. 5.12(c)) with respect to  $E_{\text{int}}(\overline{\Delta V} = 0)$  places the data points for the different configurations onto one parabola with a certain width which increases with increasing geometric parameter, as dumbbells with boron and a first or second row p-block elements follow slightly different trends.

**Mechanical and chemical contribution** For all *SB-OH/TH* configurations the mechanical contribution is always lowest for configurations with both point defects aligned along  $\langle 100 \rangle$ , followed by the  $\langle 110 \rangle$  and  $\langle 111 \rangle$  alignment (Fig. 5.15). We note that this is valid

for both dumbbell-forming systems and systems that do not form dumbbells with  $\langle 100 \rangle$  and  $\langle 110 \rangle$  orientation. This sequence of the mechanical contribution is in line with the overall dumbbell stability sequence for the majority of dumbbell-forming systems, except B-B. For dumbbell-forming systems, this sequence in the mechanical contribution can be attributed to an increasing asymmetry in the host lattice distortions that are required to incorporate the dumbbell. For the  $\langle 100 \rangle$  dumbbell, the distortions are symmetric, because both dumbbell atoms have a similar distance to four of the eight host iron atoms. This is reduced to two host atoms in the  $\langle 110 \rangle$  dumbbells and effectively to one host atom in the  $\langle 111 \rangle$  dumbbells. We further note that the mechanical contributions in the majority of configurations, except for a few  $\langle 111 \rangle$  dumbbells, contribute to attraction between both point defects. Furthermore, the mechanical contribution is shifted upwards for the larger second row p-block elements compared to the first row. The chemical contribution, in contrast, does not show an universal stability sequence, as observed for the mechanical contribution, but is rather determined by the combination of point defects. No clear trend is observed among isovalent systems: in some cases the trends in the chemical contributions dependent on point defect alignment are identical, e.g. B-Ne and B-Ar, while in other cases the trends differ substantially, e.g. B-N and B-P. We further note that the trends in the interaction energy usually correlate well with the chemical contributions, except for the  $\langle 111 \rangle$  dumbbells with first row p-block elements. The deviating dumbbell sequence for B-B can be attributed to the negligible chemical contribution of the  $\langle 100 \rangle$  alignment, compared to the attractive chemical contributions for the  $\langle 110 \rangle$  and  $\langle 111 \rangle$  dumbbell, that shift the  $\langle 100 \rangle$  dumbbell to higher interaction energies. This makes the  $\langle 110 \rangle$  the favorite dumbbell.

**Trends in charge density difference** The charge density difference that arises from incorporating the two point defects allows us to study trends of atomic position and the distribution of the charge density with respect to atomic size and the number of valence electrons (Fig. 5.16). We focus on the  $\langle 100 \rangle$  alignment because it represents the most favorable alignment for the majority of the considered configurations, except B-B which favors the  $\langle 110 \rangle$  alignment. The difference in the charge density is calculated according to

$$\Delta\rho = \rho_{\text{Fe+B+X}} - \frac{1}{2}(\rho_{\text{Fe+B}} + \rho_{\text{X}} + \rho_{\text{Fe+X}} + \rho_{\text{B}}) \quad (5.9)$$

with  $X \in (\text{B,C,N,O,Al,Si,P,S})$ . Here,  $\rho_{\text{Fe+B+X}}$  represents the charge density of the reference system,  $\rho_{\text{Fe+B}}$  and  $\rho_{\text{Fe+X}}$  is the charge density of a supercell where X and B has been removed, respectively, and  $\rho_{\text{B}}$  and  $\rho_{\text{X}}$  is the charge density of a supercell containing only B and X, respectively. The factor 1/2 is due to double-counting. The charge density of supercells with some of the atoms removed have been calculated with fixed atomic positions and supercell shape and volume. This approach allows the identification of the change in charge distribution solely due to the close arrangement of both point defects.

For the first row p-block elements (Fig. 5.16(a-d)), the alignment for B-B is symmetric with respect to the vacant iron site. For the remaining dumbbells the larger element boron is closer to the vacant iron site than the second element carbon, nitrogen and oxygen. The difference in the charge density indicates an interaction between both point defects. The variation in the

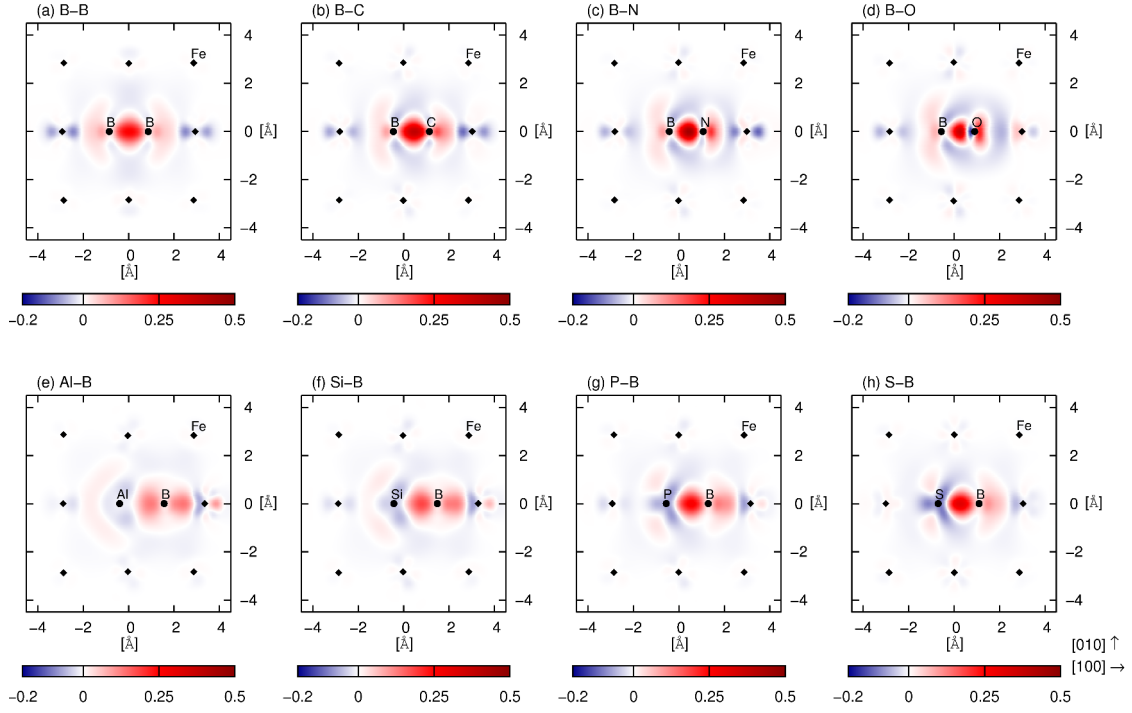


Figure 5.16.: Variation in the charge density evoked by incorporation of point defects aligned along  $\langle 100 \rangle$ .

charge density with an increasing number of valence electrons becomes noticeable with the charge density depletion at the second point defect directed towards boron and an increase in the charge density directed to the opposite site, towards the 2NN host iron atom.

For the second row p-block elements (Fig. 5.16(e-h)), the larger element is dragged away from the vacant iron site with increasing number of valence electrons, while boron is dragged closer to the vacant site. This becomes obvious due to the decreasing charge density between boron and the 2NN host iron atom with increasing number of valence electrons of the second point defect, while simultaneously the magnitude in the charge density between both point defects increases. The latter scales with the value of the interaction energy: the larger the magnitude in the charge density, the smaller the interaction energy (c.f. Fig. 5.11(d)).

### 5.5. Summary

In this section we investigated the behavior of boron point defects in  $\alpha$ -iron. We addressed the solution behavior and the migration barriers of single boron atoms and investigated the influence of boron on the elastic properties of  $\alpha$ -iron. As a step towards multicomponent alloys and steels, we further investigated the interaction of boron atoms with other point defects.

Apart from hydrogen and a vacancy, we predominantly focused on important elements in the steel production that are located in the first and second row of the p-block in the periodic table. In particular, we considered boron, carbon, nitrogen and oxygen from the first and aluminum, silicon, phosphorus and sulfur from the second row. In order to study trends with band-filling we added results for the remaining first and second row p-block elements fluorine, neon, chlorine and argon.

Regarding the solution behavior, the calculated formation energies indicate boron to be present as substitutional element in  $\alpha$ -iron. However, the formation energy of the octahedral site is only marginally higher, in the range of 70 meV. This is in agreement with previous theoretical investigations [155, 156] and supports the controversial findings of experimental studies. The calculated migration barriers for the substitutional and interstitial mechanism show consistently smaller migration barriers for 1NN hops compared to 2NN hops. In total, the 1NN substitutional mechanism yields the lowest migration barrier, but requires an adjacent vacancy. Thus, the vacancy formation energy enters in the energy barrier for migration. Therefore, the mechanism with lowest migration barrier is the 1NN interstitial mechanism. We further investigated the dissociative mechanism, with a substitutional boron dissolving into an interstitial boron and a vacancy. Here, the migration barrier depends on the initial state, whether boron occupies the substitutional or interstitial site. The energy that is required to release a substitutional boron atom is relatively large and exceeds the vacancy formation energy in  $\alpha$ -iron. Boron migrating via the interstitial mechanism is likely to be trapped by vacancies. Investigation of the influence of boron on the elastic properties of  $\alpha$ -iron showed that boron has a virtually identical effect on the elastic properties as a vacancy, if the boron content is below 3%. In this range, the elastic constants and Young's modulus are decreased. Above 3% boron content, the effect on the elastic constants and Young's modulus is qualitatively altered. This may be attributed to a difference in the charge distribution associated with the formation of regular Fe-B chains in the  $\langle 100 \rangle$  or equivalent  $\langle 010 \rangle$  and  $\langle 001 \rangle$  directions.

The investigation of point defect interactions revealed that the attractive/repulsive interaction is primarily determined by the position of boron in  $\alpha$ -iron. Substitutional boron tends to bind the second point defect, while interstitial boron tends to repel other point defects. We find that these trends are independent of the position of the second point defect. The magnitude in the interaction is primarily determined by the type of point defect. In order to understand the trends and magnitudes of the interaction we decomposed the interaction energies into a mechanical and chemical contribution, and further analyzed the magnitude of the host matrix distortions that arise from the incorporation of the point defects in the host matrix. This approach allowed us to identify the dominant contributions that determine the interactions. This includes the attractive/repulsive interactions, the magnitude in the interaction energy and the trend with band-filling. For 1NN/2NN *OH-OH* configurations, we find that the mechanical contributions correlates well with the interaction energy. The general attractive interaction in 1NN/2NN *SB-SB* configurations can be attributed to the contribution that represents the attractive  $\square$ - $\square$  interaction. The majority of configurations with small point defect separation of substitutional first and interstitial second point defects resulted in the formation of dumbbells. All systems we considered favor the  $\langle 100 \rangle$  alignment, except B-B which favors  $\langle 110 \rangle$ . The preference of the  $\langle 100 \rangle$  alignment is attributed to the weakest required distortion of the host

iron atoms to incorporate the dumbbell. The asymmetry in the host matrix distortion increases for the  $\langle 110 \rangle$  and  $\langle 111 \rangle$  dumbbell, reflected in an increase of the mechanical contribution. The deviation of the B-B dumbbells is attributed to the negligible chemical contribution for the  $\langle 100 \rangle$  dumbbell, in contrast to the attractive contributions for  $\langle 110 \rangle$  and  $\langle 111 \rangle$  dumbbells, which shifts the interaction energy of the  $\langle 100 \rangle$  dumbbell upwards. This makes the  $\langle 110 \rangle$  dumbbell the preferred dumbbell. The formation of B-B dumbbells significantly reduces the total energy of the system that results in significantly lower formation energies compared to systems containing a single boron point defect. This raises the question whether boron point defects are always present in bound configurations in the ferritic host matrix. In principle, this finding would make the discussion whether boron enters as substitutional or interstitial point defect obsolete.

To a certain degree, substitutional boron resembles a vacancy considering its impact on elastic properties and its interactions with other point defects. For boron content below 3%, the impact on the elastic constants  $C_{11}$ ,  $C_{12}$  and  $C_{44}$  is virtually identical to the impact exerted by vacancies. With respect to point defect interactions,  $SB-SB$  B-B and B- $\square$  show the same attractive interactions, with the larger magnitude for the 2NN arrangement. For  $\square$ -Al/Si/P/S interactions [417], the 1NN (2NN) interaction yields the same parabolic-like (monotonically decreasing) dependence on the number of valence electrons as observed in our study for boron. The attractive interaction of  $SB-OH$  B-C and B-N pairs resemble the binding tendency for  $\square$ -C and  $\square$ -N pairs [375, 378, 379]. Interstitial boron, in contrast, resembles carbon and nitrogen point defects in  $\alpha$ -iron. The overall repulsive interactions for the point defect pairs we have investigated match the behavior of interstitial C-C, C-N and N-N pairs [375, 379].

The present investigation revealed interesting properties of boron point defects in  $\alpha$ -iron. However, some of the results open up new questions. The investigated dissociative mechanism revealed a strong affinity of interstitial boron to move towards vacancies, resulting in boron being trapped in the vacancy, thus becoming a substitutional point defect. Given the usual concentrations of temperature-induced vacancies and the relative small boron contents in the range of a few ppm one may ask to which extent this affects the boron diffusivity in  $\alpha$ -iron. The observed formation of B-B dumbbells raises questions regarding the mobility of these complexes. However, the vast number of possible migration paths of such complexes are far too expensive to be addressed via DFT. The configurations that need to be accounted for include the migration of the dumbbell itself, the migration of single boron atoms which leads to a mechanism governed by dissociation and subsequent formation of dumbbells, and the identification of possible intermediate states, like modification of the dumbbell alignment.

In this investigation we concentrated primarily on boron in bulk  $\alpha$ -iron. We did not address the behavior of boron at grain boundaries, although experiments revealed a strong tendency of boron to segregate to grain boundaries and to contribute to grain boundary strengthening. A number of theoretical studies already investigated boron point defects at grain boundaries, but given the number of elements currently used in steel production, little attention was paid on the influence of other point defects on the behavior of boron at grain boundaries. Furthermore, we did not address the behavior of boron in bulk  $\gamma$ -Fe.



## 6. Impact on Steel Design

*"When all the profits and losses of victory ...  
come to be weighed up there is one item which  
will deny an estimate. That is knowledge."*

*Sean Longden  
T-Force*

**Structure maps** We presented new structure maps for d-p compounds that use order parameters which explicitly take into account both atomic and compound-related properties. The latter properties were obtained from a polyhedron analysis of the various crystal structures that appear in the d-p system. We defined two quantities that represent a volumetric and electron-count factor which provide overall good structural separation in the structure maps and are therefore able to account for the factors that drive the formation of a specific compound. In our structure maps, we considered binary d-p compounds, but we also checked the applicability of the order parameters on ternary d-d-p or d-p-p systems that crystallize in pseudobinaries, i.e. the ternary system adopts a compound observed in a binary system by mixing d or p elements at the same Wyckoff site. In general, the pseudobinary entries are located within the domains defined by the binary entries. Pseudobinary entries that were placed outside the domains in general contained d or p elements that do not form this compound in a binary system. Furthermore, the order parameters were able to account for defects in the crystal structures, represented by a fractional occupation of a Wyckoff site, that are observed at ambient temperatures and pressures. These structure maps are expected to provide support in steel design. Although the order parameters depend explicitly on atomic and compound-related properties, the latter being unknown for chemical systems that do not form the compound, the predictive ability of our structure maps is not limited. The electronic factor can be calculated because the coordination number is a constant among the same crystal structure observed in various d-p elements, except for very few crystal structures. For the volumetric factor the polyhedron volume for the d and p elements can be estimated, as this value scales with the ground state volumes of the d and p elements. This can be done with experimental entries, or in the case of a lack of experimental data the information can be extracted from DFT calculations. Nevertheless, further investigations are required with regard to the order parameters. The next step is the application of the order parameter to ternary compounds that adopt ternary prototypes, and comparing the location of these ternary compounds in the structure maps with the domains of the pseudobinaries. Ideally, these ternary compounds should be placed in regions with zero or negligible overlap with the binary/pseudobinary domains, unless the ternary crystal structure possesses a close geometrical relationship with a binary crystal structure, reflected in identical or very similar coordination polyhedra.

**Fe-B binaries** The investigation of ordered structures in the Fe-B system revealed two new viable ground states in the boron-rich region that have not yet been observed in experiment. The polyhedron analysis revealed that the geometric properties are in line with other compounds that are observed in transition metal - boron systems. Although the usual boron content in steel production rarely exceeds a few ppm, local enrichment of boron atoms can occur due to borons' tendency to segregate to grain boundaries. Thus, in these sites the formation of the new boron-rich phases might be promoted. This should result in a measurable effect on the mechanical properties of the steel.

Fe-B compounds are also used as hard and protective coatings on steel surfaces. The boron content is much higher in this case compared to the usual content added in steel production as the formation of the borides has to be promoted. Compared to the known iron borides that are listed in the experimental phase diagram, the newly identified boron-rich compounds yield superior elastic properties. Also the hardness of the boron-rich compounds is expected to exceed the hardness of the known borides, making them ideal candidates for hard and protective coatings. However, in order to form the newly identified borides, the identification of adequate fabrication parameters is necessary. Our investigation showed that pressure might promote the formation of the two newly identified iron borides, while the boron-rich oP10-FeB<sub>4</sub> compound might be realized as oP10-Fe<sub>x</sub>Cr<sub>1-x</sub>B<sub>4</sub> pseudobinary. However, at this stage the experimental verification and successful synthesis of these compounds has not yet been achieved.

**Point defects** The findings regarding the behavior of boron point defects in  $\alpha$ -iron show that boron differs greatly from its closest neighbors in the periodic table, carbon, nitrogen, and oxygen, which are also present in steels as additive or impurity. The complexity is reflected in experimental studies, which identified boron to be an effective but hard to control alloying element, with a significant impact on the mechanical properties, if the fabrication process and the chemical composition are able to ensure that boron is present in the proper form and location in the microstructure.

Experimental studies on the solution behavior of boron in  $\alpha$ -iron suggested different solution types: boron occupies either substitutional or interstitial sites, or is even able to occupy both sites, with the boron atoms distributed between the substitutional and interstitial sites. We find in that boron prefers the substitutional site, in agreement with previous DFT studies. We also find that the calculated formation energy difference between the substitutional and one of the interstitial sites, namely the octahedral site, is in the range of 70 meV, which is small compared to the formation energy differences of the closest neighbors, carbon, nitrogen and oxygen. However, the investigation of point defect interactions in  $\alpha$ -iron showed that boron tends to bind to a second one via the formation of a dumbbell. This leads to a considerable reduction in the formation energy, lower than for boron either in the substitutional or octahedral site. This raises the question whether boron point defects are always present in bound configurations, and are never present as single point defects occupying either the substitutional or interstitial sites in the ferritic host matrix. In principle, this finding would be able to account for the controversial experimental findings regarding the solution behavior of boron.

---

Our investigation of the interaction of boron atoms with other point defects, namely a vacancy, hydrogen and elements of interest in the first and second row of the p-block in the periodic table, showed that the attractive/repulsive trend in the interaction is primarily determined by the position of the boron atom. Substitutional boron binds other point defects, while interstitial boron tends to repel them. The magnitude in the interaction depends on the type of point defect. For some interactions, we observed a non-monotonic decay of the magnitude in the interaction energy with point defect interaction. Here, the most attractive configurations were observed in the 2NN arrangement. Examples are the interaction between two substitutional boron atoms, and one substitutional boron atom and a vacancy or phosphorus. It is therefore interesting how the observed behavior in the interaction will affect the distribution of point defects in the host material and to which extent this can be influenced or even controlled by the fabrication parameters.

In the majority of configurations with substitutional boron and an interstitial point defect we observed an attractive interaction between both point defects and the formation of a dumbbell. This attractive interaction is in line with experimental findings for some of the elements we considered in our investigations, e.g. carbon, nitrogen and oxygen, as an attractive interaction between boron and these elements is generally assumed due to the formation of precipitates, that remove these elements from solid solution. Other experiments revealed also the existence of boron-carbon pairs in the ferritic host matrix. However, with respect to the usual boron concentrations used in the steel production, it is questionable whether the tendency of boron to bind other point defects would have a measurable effect on e.g. the diffusivity of any of the elements which boron tend to bind to. On the contrary, the usually low boron contents compared to other additives mean that the diffusion of boron is expected to be heavily affected by the presence of other elements. This also includes vacancies which are important for the mobility of boron in the substitutional sites, as in this mechanism an adjacent vacant site is required for the migration.



## 7. Conclusion

*"... but soon you shall see that every move,  
every strike was meant to bring us to this."*

*Vladimir Makarov*

*Call of Duty: Modern Warfare 3 (Redemption Trailer)*

In this study we addressed the compound formation of binary d-p and ternary d-d-p/d-p-p systems via a structure map approach by analyzing the local environment of each atomic site and linking it to suitable atomic and compound-related properties. We further investigated the Fe-B system due to its relevance in steel fabrication with respect to compound formation as well as the behavior of boron point defects in a ferritic host matrix using DFT.

Using a built-in polyhedron analysis in BOPfox, we decomposed the compounds that appear in binary d-p and pseudobinary d-d-p/d-p-p systems in their respective coordination numbers, which serve as the basis for the order parameters for the structure maps. We only considered compounds that are stable at ambient temperature and pressure. For that purpose, we compared the entries for binary compounds in the Pearson's Crystal Database with experimental phase diagrams in order to exclude metastable, high-temperature and high-pressure phases as well as phases that appear in thin films and entries that list the geometry obtained from calculations. Due to the significantly reduced number of experimental phase diagrams for ternary systems, we simply checked the pseudobinary entries for keywords to exclude the abovementioned phases. For the binary d-p compounds, the investigation of the coordination polyhedra, their respective coordination number and the composition, i.e. the numbers of d and p elements in the coordination polyhedra, for the various p elements revealed that the chemically distinct behavior of the first row p-block elements boron, carbon, nitrogen and oxygen compared to the remaining elements is also represented in trends regarding the favorite coordination number and the composition of the coordination polyhedron. Nitrogen, and to a lesser extent carbon, are the most restrictive elements with regard to favored coordination number, favoring six-fold coordination, followed by boron, favoring nine-fold coordination, and oxygen. The trends regarding a favorite coordination number are less clear for the remaining elements, as these tend to crystallize in a larger variety of different crystal structures. As expected, the coordination numbers in general decrease with increasing number of valence p electrons. Analysis of the coordination polyhedron volumes revealed relatively strict relationships for the ratios between the volumes of the polyhedra that surround the d and p Wyckoff sites, respectively. As expected, the ratios between the d and p site polyhedron volumes are approximately constant among identical crystal structures that crystallize in the d-p systems. We further observed that even different crystal structures can yield virtually identical ratios between d and p site polyhedron volumes. Thus, we obtained only a limited number of branches that represent the

## 7. Conclusion

---

allowed polyhedron volume ratios. The analysis of the coordination polyhedra for each crystal structure allowed the introduction of two order parameters, one volumetric and one electronic factor, that in general result in overall good structural separation in two-dimensional structure maps. Both order parameters depend explicitly on atomic and compound-related properties. We presented structure maps for binary compounds for the most important compositions in the d-p system. The extension to ternary phases that adopt binary crystal structures showed that these pseudobinary entries were in general placed within the domains that were determined by the binary entries. Pseudobinaries that were placed outside the binary domains contained in general d or p elements that do not adopt this crystal structure in the binary d-p system. The order parameters we introduced were also able to account for defects in the crystal structures. Although our order parameters depend explicitly on atomic and compound-related properties, the predictive ability of our structure maps is not limited. We showed that it is possible to estimate the electronic and volumetric factor for d-p systems that do not adopt this crystal structure. For the electronic factor, the coordination numbers are constant among identical compounds, except for very few cases. For the volumetric factor, we showed that the polyhedron volumes for elements, which do not adopt the compound of interest, can be estimated due to an approximately linear relationship between the polyhedron and ground state volume. Thus, we were able to determine the location of these hypothetical compounds in our structure maps. In our investigation, we did not introduce a third axis that depends explicitly on the electronegativity. However, the electronegativity scale enters indirectly in the electronic factor.

The investigation of the binary Fe-B system via DFT with respect to compound formation reproduced the known stable phases, that are shown in the experimental phase diagram, as well as the known metastable phases or low-temperature modifications described in literature. In close collaboration with the group of AN Kolmogorov, University of Oxford, the application of an evolutionary algorithm search identified a set of new viable ground states in the boron-rich region, which so far have not been observed in experiment, namely a stable phase at 1:2 composition designated as oP12-FeB<sub>2</sub> and a phase at 1:4 composition designated as oP10-FeB<sub>4</sub> close to the boundary of the convex hull. The investigation of the newly identified compounds with respect to trends regarding the coordination polyhedra revealed that both compounds are in line with identified trends observed for the known compounds in the transition metal - boron systems. We investigated the newly identified compounds with respect to suitable synthesis routes. The formation of both compounds might be promoted by application of pressure during fabrication, while the more boron-rich oP10-FeB<sub>4</sub> might be realized as oP10-Fe<sub>x</sub>Cr<sub>1-x</sub>B<sub>4</sub> pseudobinary. Due to the usage of iron borides as hard and protective coatings on steel surfaces, we investigated the known stable compounds and newly predicted ground states with respect to their mechanical properties, and found superior mechanical properties for both predicted ground states with respect to the iron-rich iron borides that are used as coatings. We observed that the compound at 1:2 composition exhibits superior mechanical properties compared to the more boron-rich compound at 1:4 composition. This may be attributed to the geometry of oP12-FeB<sub>2</sub> which combines a relatively low volume per atom ratio and the boron atoms aligned in chains, in contrast to the alignment in boron nets like in hP6-ReB<sub>2</sub>, which so far is the transition metal boride that exhibits the highest hardness in experimental

---

measurements.

The investigation of boron point defects in a ferritic matrix focused on the solution behavior, the migration, the impact on the elastic properties, and the interaction between a boron point defect and a vacancy, hydrogen and elements of the first and second p-block row, that are important in steel fabrication: in particular, we considered a second boron, carbon, nitrogen and oxygen as well as aluminum, silicon, phosphorus and sulfur. In order to discuss trends of the interaction with band-filling, we extended the investigation of point defect interaction with the remaining elements of the first and second p-block row: fluorine, neon, chlorine and argon. Owing to the controversial solution behavior of boron in  $\alpha$ -iron - whether it occupies substitutional or any of the interstitial sites - we calculated the corresponding formation energies that in agreement with prior theoretical investigations showed boron to favor the substitutional site. However, the formation energy of boron in one of the interstitial sites, namely the octahedral site, is only marginally higher, in the range of 70 meV. This indicates that boron may occupy this site at elevated temperature. Thus, the possibility of boron to occupy both sites is in agreement with the different experimental findings of borons' favored site in  $\alpha$ -iron. Owing to the possibility of boron to occupy different point defect sites, our investigation regarding the migration included both substitutional and interstitial mechanisms as well as a dissociative mechanism that has been put forward in order to interpret experimental diffusion data. For the solely substitutional and interstitial mechanisms we considered 1NN and 2NN hops, and found consistently the 1NN hops preferred over the 2NN hops. The lowest migration barrier is found for the 1NN substitutional mechanism, but as this mechanism requires an adjacent vacancy, the vacancy formation energy enters in the barrier. Therefore, the dominant process is represented by the interstitial mechanism. Regarding the dissociative mechanism, we identified a strong affinity of interstitial boron to move towards vacancies, as these configurations with boron in 1NN or 2NN position with respect to the vacancy are mechanically unstable, and the interstitial boron relaxes towards the vacancy. Boron is mechanically stable in the 3NN interstitial position, and the corresponding migration barriers in the dissociative mechanism depend on the initial state. First, the release of substitutional boron requires a large energy which exceeds the vacancy formation energy in  $\alpha$ -iron. Second, boron migrating via an interstitial mechanism is likely to be trapped if it approaches vacancies in the host matrix. As a consequence, the tendency of interstitial boron to annihilate adjacent vacancies may cause a reduction of the boron mobility. We further investigated the impact of substitutional boron on the elastic properties of  $\alpha$ -iron, and compared the impact to a vacancy, that has been found to exert a similar strain on the 1NN host iron atoms as boron, and the substitutional elements aluminum, silicon, phosphorus and sulfur. The impact of boron is very similar to the impact of vacancies, reducing both the elastic constants and the Young's modulus. However, above a boron content of 3% the impact on the elastic constants and the Young's modulus is substantially altered, leading to increasing elastic constants with boron content and, with respect to the Young's modulus, hardening (softening) of the elastically hard  $\langle 111 \rangle$  (soft  $\langle 100 \rangle$ ) axis in  $\alpha$ -iron. This change is attributed to the formation of regular Fe-B chains in the unit cells. We did not observe a similar behavior for Fe-Al/Si/P/S alloys in the point defect concentration we considered. The attractive/repulsive interaction between boron and a second point defect is predominantly determined by the boron position in the ferritic matrix and to a lesser extent determined by the

type of second point defect. We find a general trend that substitutional boron binds a second point defect, while interstitial boron tends to repel the point defect. In order to understand the trends and magnitudes of the interaction we decomposed the interaction energies into a mechanical and chemical contribution, and further analyzed the magnitude of the host matrix distortions that arise from the incorporation of the point defects in the host matrix. This approach allowed us to identify and discuss the dominant contributions that determine the interactions. For two interstitial point defects, the trend in the interaction with band-filling is primarily attributed to the mechanical contribution. For two substitutional point defects, the overall attractive interaction can be attributed to the contribution that represents the attractive  $\square$ - $\square$  interactions. Trends in the interaction of substitutional boron resemble interactions of vacancies with point defects. Interstitial boron, in contrast, behaves similar to carbon and nitrogen which are interstitial point defects in  $\alpha$ -iron. In the majority of configurations with a substitutional and interstitial point defect we observed dumbbell formation for close point defect separations. The appearance of dumbbell formation may be determined by the atomic size of the point defects, as we predominantly observed dumbbell formation for elements that have a smaller atomic size in  $\alpha$ -iron compared to the atomic size of iron. The majority of configurations favor the  $\langle 100 \rangle$  dumbbell over the  $\langle 110 \rangle$  and  $\langle 111 \rangle$  dumbbells. This stability sequence is attributed to the required host matrix distortions in order to incorporate the dumbbell. The  $\langle 100 \rangle$  dumbbell requires the weakest host matrix distortion. The asymmetry in the host matrix distortion increases for the  $\langle 110 \rangle$  and  $\langle 111 \rangle$  dumbbells, reflected in an increase of the mechanical contribution. The B-B dumbbell is the only exception, where the  $\langle 100 \rangle$  dumbbell is significantly shifted to higher interaction energies. The deviation of B-B is attributed to a negligible chemical contribution for the  $\langle 100 \rangle$  dumbbell which shifts the energy of the configuration upwards. This makes the  $\langle 110 \rangle$  dumbbell the preferred dumbbell.



# A. Appendix

## A.1. Atomic Properties-Based Structure Maps

Following prior approaches for structure maps, we first tried to identify order parameters which are solely based on tabulated or derived atomic properties. In particular, we considered values that represent the electronic configuration, the atomic size and the electronegativity of the element. For the electronic configuration, we took into account the number of valence electrons as well as the number of holes in the corresponding sd- or sp-band, respectively. For the atomic size we considered the tabulated covalent and metallic radii, Zunger's pseudopotential radii [163] and the atomic volumes by Villars *et al.* [191]. Furthermore, we considered the Pauling [418, 419], Mulliken [420, 421], Allred-Rochow [422] and Martynov-Batsanov electronegativity scales [165]. We further considered the multiplicity  $2S+1$  as well as the quantities  $L$  and  $J$  for each element, but after first tests rejected these quantities.

For each quantity we introduced a set of functions that combine the corresponding values for the d and p element. We tested the sorting of the data set according to the prototype, the environmental type as well as the coordination number of the p-block element. In view of the large number of possible combinations of order parameters for the two-dimensional structure maps, we used the following approach: For every combination, we calculated the corresponding position of each data point in the structure map, calculated the boundary of the convex hull for the data points for the same prototype, environmental type or coordination number, and estimated the success of the tested order parameters by an error  $\Delta$  that is calculated from the overlap between the regions

$$\Delta = \frac{2}{N(N-1)} \sum_{i=1}^{N-1} \sum_{j=i+1}^N \frac{A_{ij}^o}{\min(A_i^c, A_j^c)} \quad (\text{A.1})$$

with  $A_{ij}^o$  as overlap between the two regions  $A_i^c$  and  $A_j^c$ . Taking the minimum of  $A_i^c$  and  $A_j^c$  and the pre-factor ensures that  $0 \leq \Delta \leq 1$ . In an ideal structure map, the overlap between the regions assigned to a different prototype etc. is zero. However, none of the tested parameters provided overall good structural separation. Furthermore, order parameters that provided comparatively good results for a specific composition, were unable to maintain their utility if tested for other compositions, even if the composition was explicitly included in the order parameters. Exemplary structure maps are shown in Fig. A.1 separated according to prototype and the coordination number of the p-block element, which provided relatively low overlap errors compared to other order parameters. Nevertheless, the overlap is significant, therefore one would reject such order parameters. Note that different quantities are used for

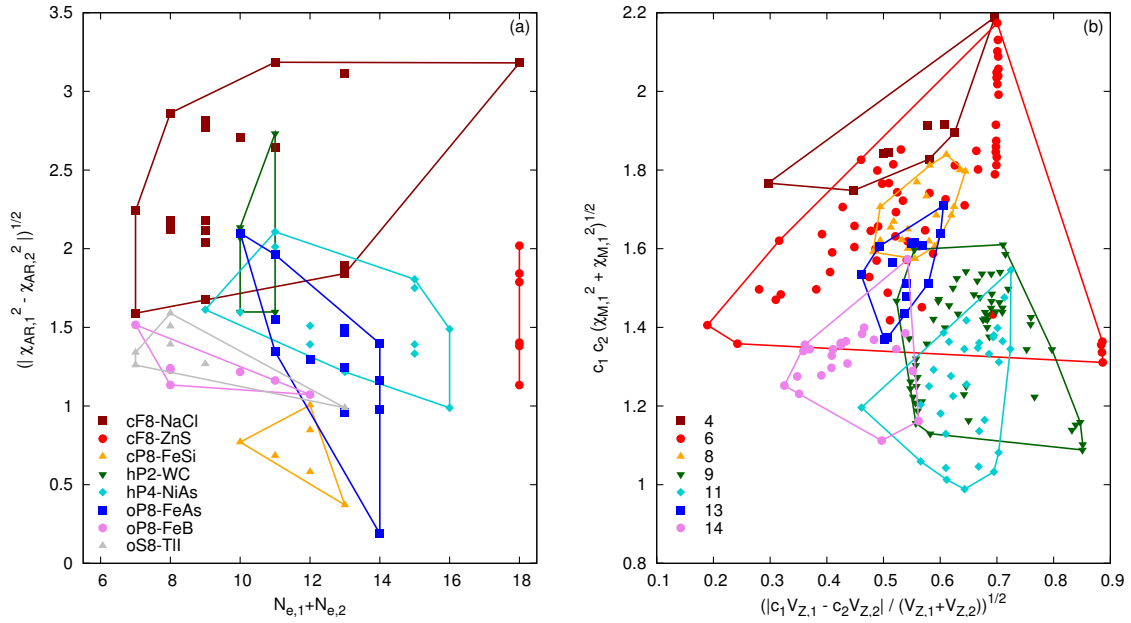


Figure A.1.: Order parameters based solely on atomic properties. We separated according to (a) prototype and (b) coordination number of the p-block element. For the latter we only considered crystal structures that have only one Wyckoff site occupied by a p-block element.

the order parameters. Separation according to prototype yields best results with the number of valence electrons and the Allred-Rochow electronegativity scale, while separation according to coordination number works best with the volume according to Zunger's pseudopotential radii and the Mulliken electronegativity scale.

Going a step further, we tested the approach using the maximal information coefficient [423], that allows a measurement of the strength of the linear or non-linear relationship between two variables. Due to the limitation of the provided executable [424] to be able to compare only two variables at the same time, we followed the approach by Villars [159] who identified the set of three order parameters by comparing which of them alone is able to provide good structural separation. However, the approach with the maximal information coefficient identified in principle the same quantities (but usually not the same combinations of quantities) that were already identified with the overlap approach. Nevertheless, the overall agreement in the identified quantities is encouraging, and proves that the approach by simply calculating the overlap is at least to some extent useful compared to well-developed statistical approaches.

## A.2. Predictive Ability of Structure Maps

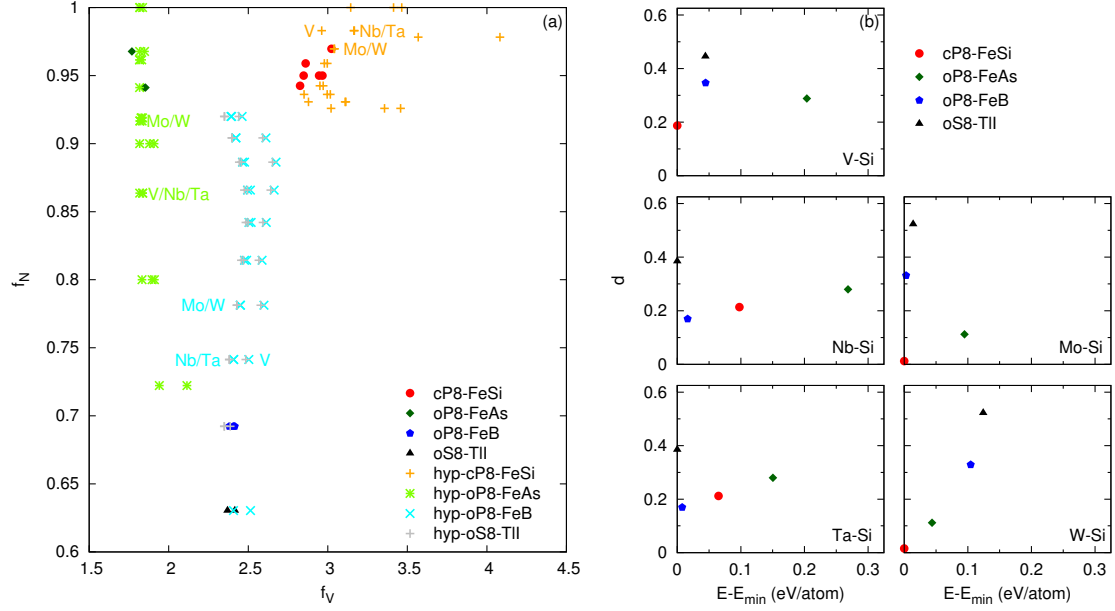


Figure A.2.: (a) Location of hypothetical d-Si 1:1 compounds in the structure map. (b) Distance between hypothetical and existing compounds versus total energy, shifted with respect to  $E_{\min}$ .

In this section, we will briefly discuss a possible approach to use the predictive ability of our structure maps in combination with the search for new viable ground states in chemical systems using DFT calculations. For the demonstration we choose silicon-containing transition metals alloys with 1:1 composition. First, in this system only four different crystal structures are observed: cP8-FeSi, oP8-FeAs, oP8-FeB and oS8-TiI (c.f. Fig. 2.7). The structures appear in sufficient numbers, including also the pseudobinaries that contain silicon among two transition metals, so that we can estimate the polyhedron volume for transition metals that do not form this compound, see Sec. 2.3.6 and Fig. 2.14. Second, we observe a gap between the oS8-TiI/oP8-FeB and cP8-FeSi/oP8-FeAs regions where no stable 1:1 compounds are listed. In addition, neither the entries in the PCD [178] nor the experimental phase diagrams in [193] list any metastable, high-temperature or high-pressure phases at 1:1 composition for vanadium, niobium, tantalum, molybdenum and tungsten. Thus, in an investigation addressing the lowest-energy compound at 1:1 composition with DFT we do not have an indication what this compound might be. For clarification, we skipped rhenium and technetium as entries in the PCD show both elements to form the cP8-FeSi compound in combination with silicon at 1:1 composition.

We now discuss an approach to combine our structure maps with the selection of compounds that are investigated with DFT. The aim is to use the information of the structure maps to reduce the number of compounds that need to be investigated with DFT. From the binary

1:1 structure map (Fig. 2.15) we already know the location of the stable silicon-containing compounds. By estimating the polyhedron volume for transition metals that do not adopt the crystal structures we are able to include the location for these hypothetical compounds in our structure map. In Fig. A.2(a) we show both the known and hypothetical compounds. Some of the hypothetical compounds are placed closer to the existing compounds than other. With regard to our predictive ability of the structure map, a smaller distance of a hypothetical compound with respect to an existing compound should increase the probability that the hypothetical compound represents the lowest-energy crystal structure in the chemical system. In order to investigate this relationship, we performed DFT calculations for the five aforementioned transition metals in combination with silicon for the four crystal structures cP8-FeSi, oP8-FeAs, oP8-FeB and oS8-TiI. All calculations were performed with a plane wave cutoff of  $E_{\text{cut}} = 500 \text{ eV}$  and a k-point density of  $\Delta k = 0.02 \text{ \AA}^{-1}$ . Fig. A.2(b) shows the total energy of each compound for the five systems, shifted with respect to  $E_{\text{min}}$ , i.e. the lowest energy among the four crystal structures, with respect to the distance of the hypothetical compound compared to the existing compounds in the d-Si system. We observe that in the systems V/Mo/W-Si the hypothetical compound that has the smallest distance to the existing compounds represents also the lowest-energy phase according to the DFT calculations: cF8-FeSi. For Nb/Ta-Si we observe that according to the distance oP8-FeB should represent the lowest-energy phase. However, DFT calculations show that this compound is only the second-lowest phase in energy: oS8-TiI is slightly lower in energy, but has a significantly increased distance to the existing oS8-TiI. We note that the large distance is mainly due to the variation of the electronic factor  $f_N$ . In contrast, the volumetric factor  $f_V$  of the hypothetical Nb/Ta-Si compounds agrees well with the existing compounds in the d-Si system. This disagreement might be due to the close geometrical relationship between oP8-FeB and oS8-TiI [204] that results in very similar total energies in the DFT calculation, with oS8-TiI preferred over oP8-FeB. This is not represented in the distance, as the neighbors of niobium and tantalum to the left adopt oP8-FeB.

In this section, we discussed the usage of our structure maps, in particular the predictive ability, in combination with DFT calculations for the search of lowest-energy phases. Information from existing compounds may be used to estimate values for elements that do not adopt the crystal structure. That allows to determine the location of these hypothetical compounds in our structure maps, and therefore the distance of these hypothetical compounds with respect to the existing ones. A test for the d-Si system showed that in general the compounds with smallest distance represent also the lowest-energy phase. However, compounds with close geometrical relationships might have similar total energies, and the sequence is not well represented in the distance value. Nonetheless, checking the location of hypothetical compounds in the structure maps might significantly reduce the number of compounds that are investigated with DFT calculations.

## A.3. High-Throughput Environment

*"Effective soldiers require effective tools."*

*Geoffrey Tolwyn*

*Wing Commander IV: The Price of Freedom*

The availability of high-performance computer clusters require a well-defined and appropriate high-throughput environment, that can also be adjusted easily, in order take full advantage of the existing computational capabilities. This includes not only the subroutines for job submission, but also subroutines for job control as well as the ability to restart from a given point if the calculation was interrupted. Further requirements for such a high-throughput environment include the existence of a well-defined database of structure files and initial magnetic configurations, if the calculation has to be performed spin-polarized, as input, as well as the ability to choose the properties of interest, e.g. equilibrium volume, total energy, elastic constants etc., that need to be calculated and summarized in a compact way. Additionally required parameter control the input parameter of the density functional theory package used for the calculations. In the case of VASP, the parameter consist of the plane wave cutoff and the k-point density, used as input for a built-in subroutine in order to compute the k-point mesh.

The high-throughput environment used at AMS is called `strucscan` and has been developed by Prof. Ralf Drautz and Dr. Thomas Hammerschmidt. A schematic representation is given in Fig. A.3. It comprises a database of structure files and corresponding initial magnetic configurations, the required potentials for the different elements in the periodic table, a set of `csh/tcsh` scripts and `fortran` code for job submission, control and evaluation, and a specific machine file consisting of information for the job submission, e.g. queue, number of cores, runtime, which are ordered by keyword. The scripts and `fortran` programs are kept as compact as possible which has the advantage of easier modification and extension with additional tasks and features.

The job creation is controlled by input files, which consist of information about the considered chemical system, the required task, i.e. the properties of interest that need to be calculated, and a list of structure files and corresponding initial magnetic configurations, if the calculations have to be performed spin-polarized. Further entries control the VASP input parameter plane wave cutoff and k-point density, as well as the xc functional that will be used for the specific calculations, and a keyword controlling the submission parameter, i.e. name of the queue and number of cores.

The information listed in the input file are passed to `strucscan`. In the first step, the required subfolders are generated, using the information of the chemical system and the required task, as well as by looping over the listed structure files, the plane wave cutoffs, the k-point densities and the xc functionals. The subfolders will contain the job control files for VASP, including also the potential and the structure file. In the next step, the corresponding submission script is generated, consisting of all required steps in order to calculate the required properties, as determined by the task in the input file. After submission, the steps listed in the submission script are evaluated, including copying the required files in the subfolder, adjusting the job

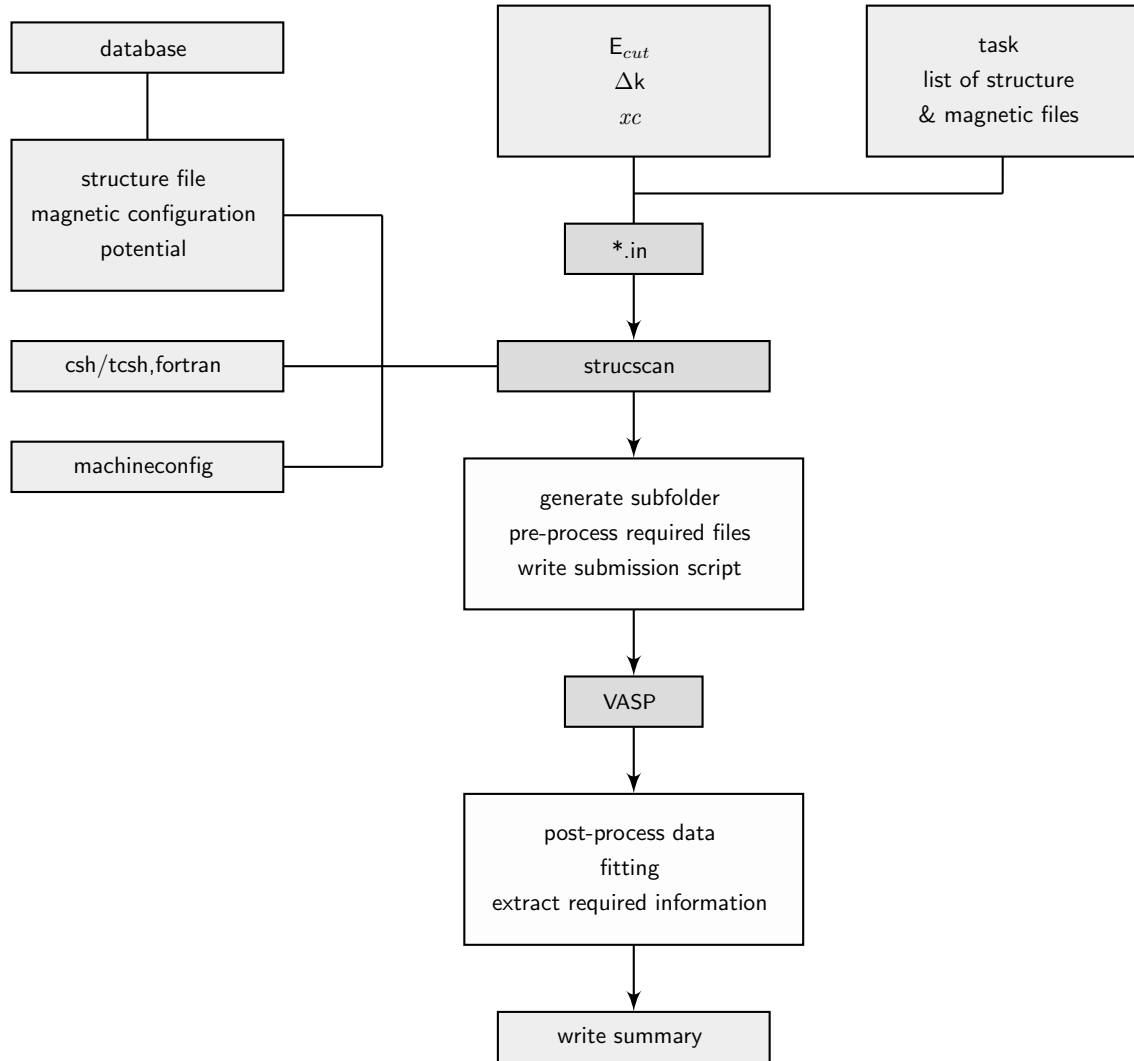


Figure A.3.: Schematic representation of the high-throughput environment strucscan. The environment comprises a database of structure files, initial magnetic configurations and potentials, as provided by VASP, a set of csh/tcsh scripts and fortran programs for job preparation, submission and evaluation, and a machine configuration file required for job start parameter. Input files for strucscan pass the chemical system, the task, a list of structure files and initial magnetic configurations, if spin-polarized calculations are required, and a set of required parameter for VASP. Determined by the task, the sequence of required calculations is listed in the submission script, and the required input files for VASP are copied into the corresponding subfolders. After successful completion of the calculations performed by VASP, the results are evaluated and summarized.

control parameters, starting the calculation, checking for successful completion of the calculation, post-processing the data, i.e. zipping required files while deleting unnecessary ones, listing achieved steps in a separate file which is used as restart point if the calculation has been interrupted or exceeded the allowed runtime, usage of fitting subroutines if necessary, and summarizing the final results in separate files.

Already built-in tasks for ordered structures include the calculation of the equilibrium volume, total energies and the bulk modulus of given structures via the calculation of the  $E(V)$  curve and corresponding fits to second- and fourth order polynomials, as well as the Rose-Vinet and Birch-Murnaghan equation of state. The author of this thesis included subroutines to calculate the elastic constants and extended `strucscan` with the defect and transformation task. Elastic constants for given structures are calculated either from stress-strain or energy-strain relationships, with or without additional ionic relaxation after application of the strain tensor. For defect structures, the input task controls predominantly the relaxation condition, including a fixed calculation, ionic, volume and full relaxation, respectively. Additional parameter control the determination of the local magnetic moment for magnetic systems. Furthermore, the transformation task uses an input structures together with a range for the variation of two axis of the structure, allowing to determine the energy surface associated with the deformation of a given structure, e.g. the Bain path.

## A.4. Convergence Tests & Exchange Correlation Functional

The first task before starting a serious investigation of a system comprises convergence tests for the constituent elements, finding parameter for both the plane wave cutoff and the resolution of the k-point mesh that yield converged total energies below a certain threshold, usually 1-2 meV/atom. For the considered elements in the investigation, we calculated the total energies for bcc, fcc, sc and the diamond structure and used the energy differences between two different structures at the same plane wave cutoff and k-point density, thus constructing the mesh, as convergence criterion. The four structures represent different bonding situations: bcc and fcc are closely packed and important for transition metals, the diamond structure is usually found in the p-block of the periodic table, e.g. carbon or silicon, and sc is added because it is the simplest possible unit cell. All four structures have also the advantage of being cubic, thus e.g. the c/a ratio does not enter as additional degree of freedom.

For all considered elements, we first started the convergence test for the k-point density while keeping the plane wave cutoff fixed, and use approximately double the suggested value for the plane wave cutoff as listed in the corresponding pseudopotential provided by VASP. We then check the convergence of the energy differences with respect to k-point density, and the final k-point density leading to converged values is defined by the worst case, i.e. the energy difference between two structures that require the finest mesh. Using the observed k-point density as input, we repeat the test for varying plane wave cutoffs, and the final value is again determined by the worst case, i.e. the largest plane wave cutoffs needed to yield converged energy differences for all combinations.

The convergence tests for iron, boron, carbon, nitrogen, oxygen and hydrogen are shown in Fig. A.4 for the PBE and in Fig. A.5 for LDA. The right panel shows the results for varying k-point densities at fixed plane wave cutoff, as described previously, and the left panel shows the results for varying plane wave cutoffs with the k-point density that yields converged total energy differences. In general, the different xc functionals have a negligible impact on the values for the plane wave cutoff and the k-point density that yield converged total energies. The convergence test of iron is presented for the nonmagnetic case. As the calculations for iron have been performed spin-polarized throughout the study, we also checked the influence of magnetism on the convergence test. We noticed larger variations in the total energies at very low k-point densities and plane wave cutoffs due to oscillations between low-spin and high-spin states, especially for fcc. Regarding the values that yield converged total energies, the additional inclusion of magnetism showed no influence of the plane wave cutoff, but required a small increment of the k-point density to  $0.022 \text{ \AA}^{-1}$ .

Additional convergence tests for the elements aluminum, silicon, phosphorus and sulfur are shown in Fig. A.6 only for PBE. The left panel shows again the variation of the k-point density at fixed plane wave cutoff, and the right panel shows the result for varying plane wave cutoffs at the k-point density that yield converged total energies.

In all cases, the found values for the plane wave cutoffs were smaller than the double of the suggested value as listed in the pseudopotential, which were used as input for the first part of



#### A.4. Convergence Tests & Exchange Correlation Functional

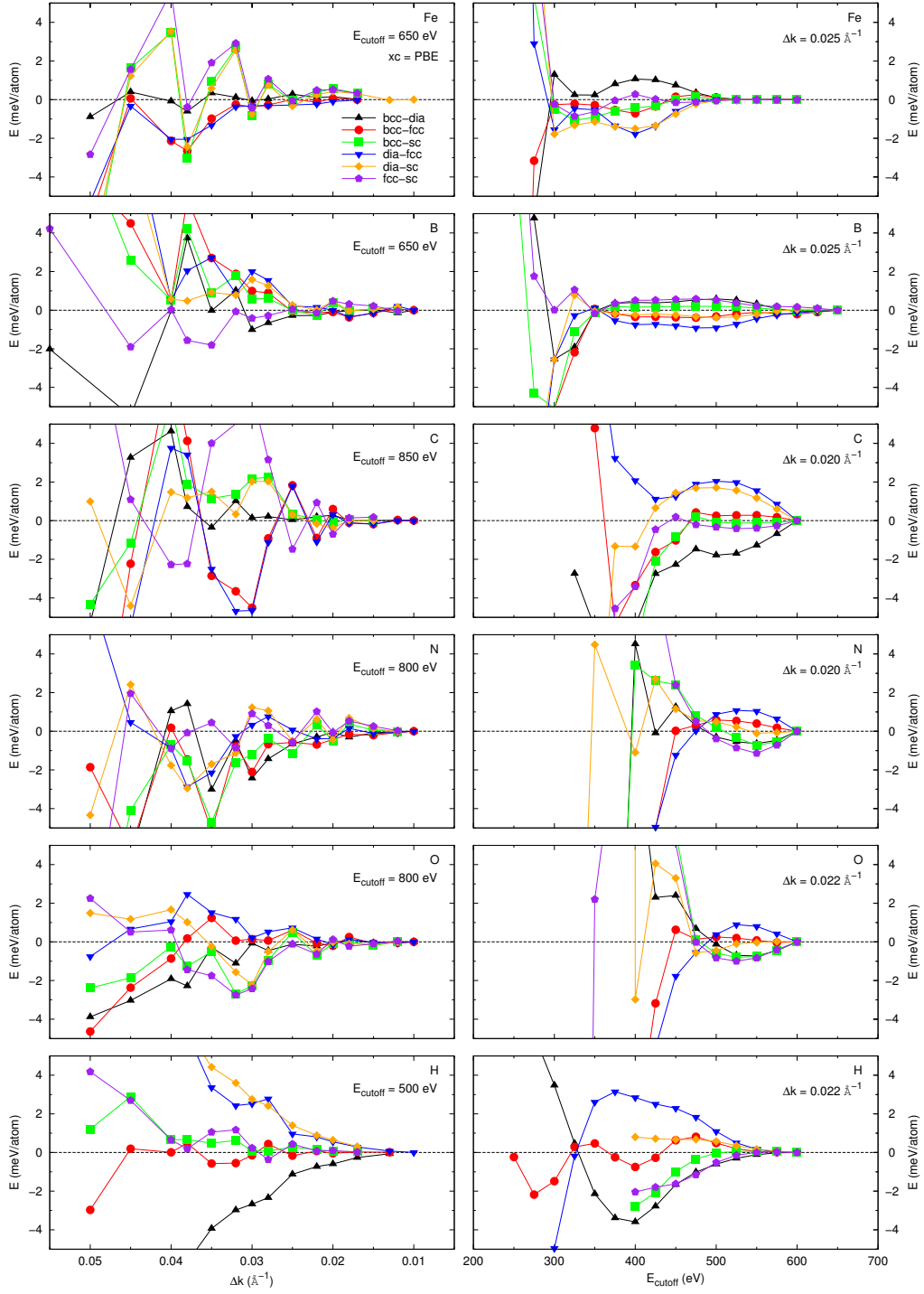


Figure A.4.: Convergence tests of k-point density (left panel) and plane wave cutoff (right panel) for Fe/B/C/N/O/H for PBE.

## A. Appendix

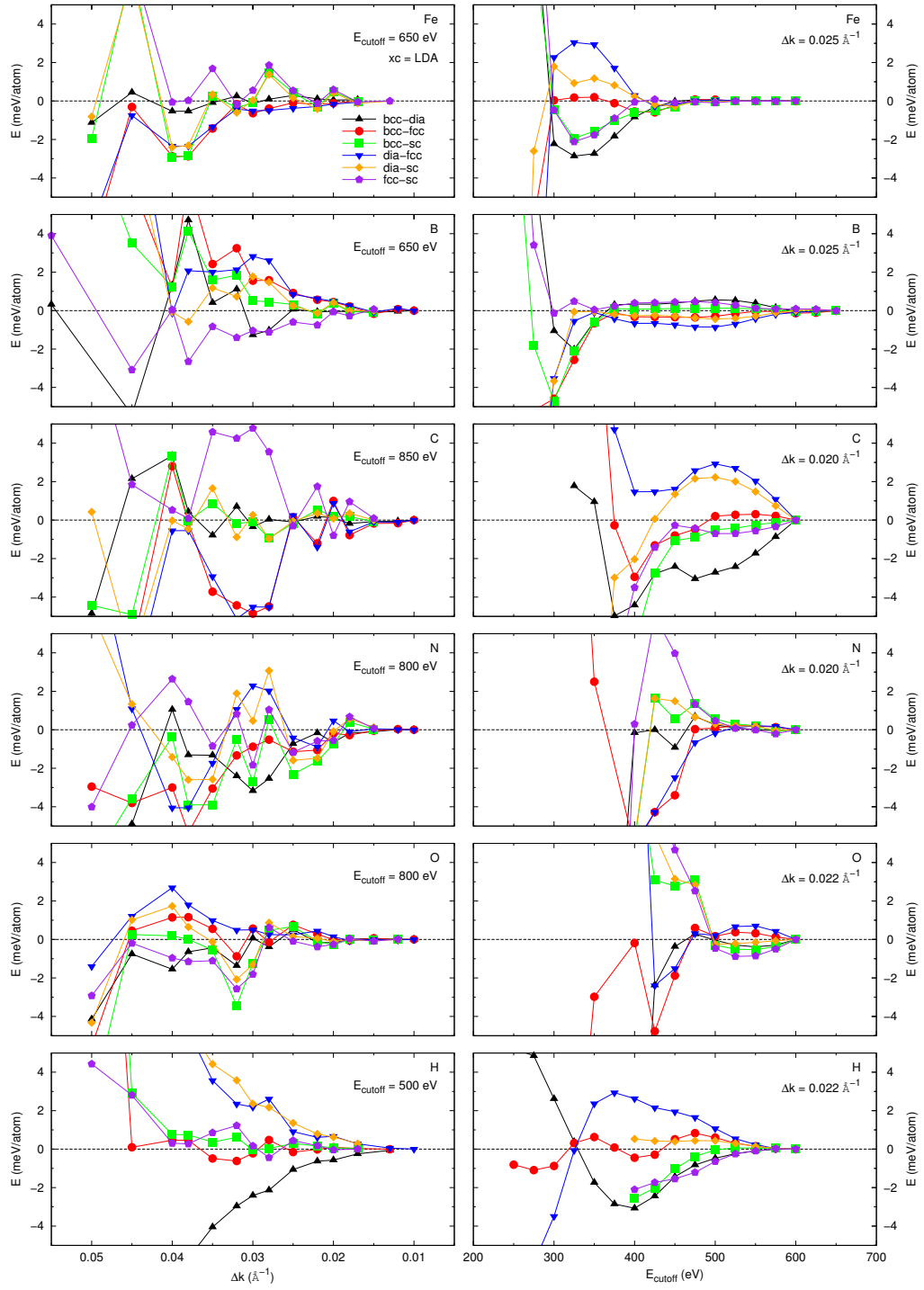


Figure A.5.: Convergence tests of k-point density (left panel) and plane wave cutoff (right panel) for Fe/B/C/N/O/H for LDA.

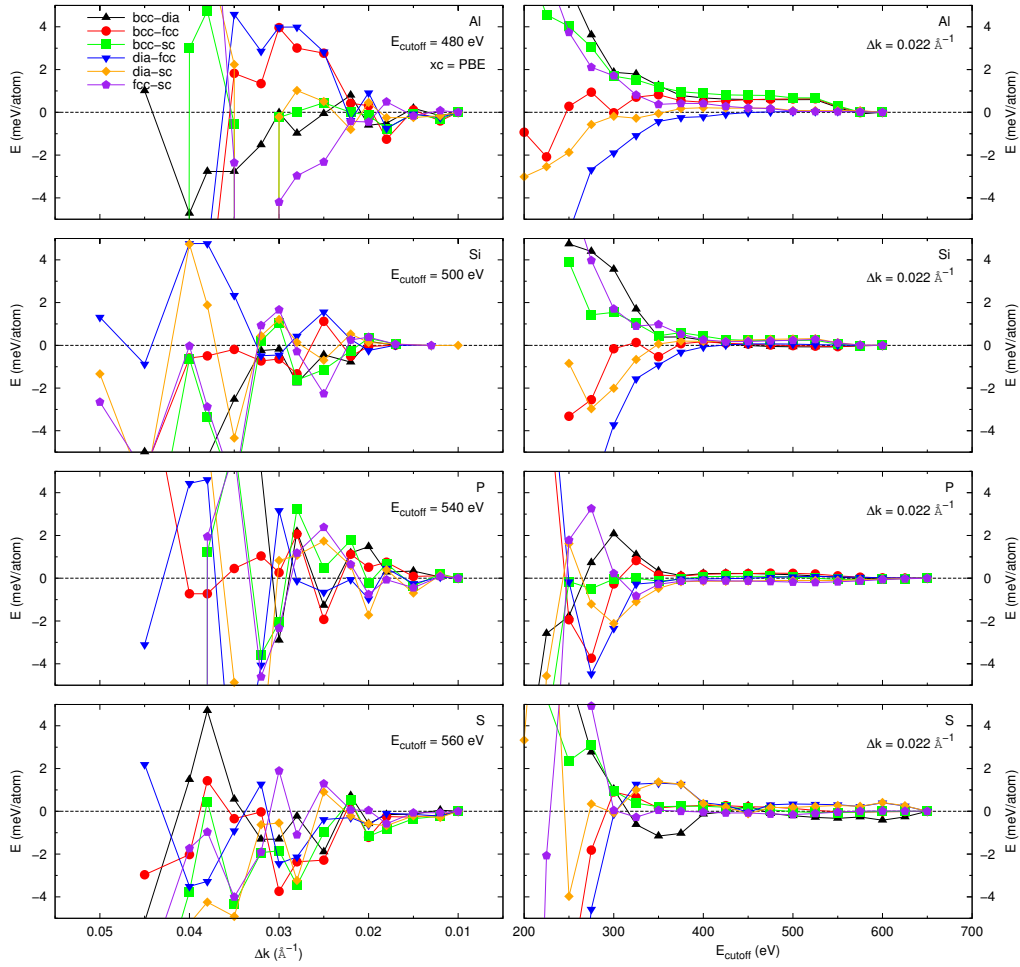


Figure A.6.: Convergence tests of k-point density (left panel) and plane wave cutoff (right panel) for Al/Si/P/S for PBE.

the convergence test, in order to find the k-point density that yields converged results.

Regarding the xc functional describing the exchange and correlation, we used throughout the study the formulation by Perdew, Burke and Ernzerhof [220]. This functional belongs to the family of GGAs that usually exhibit a better description of bulk properties compared to LDA. In the case of iron, the usage of the PBE functional also ensures that the ground state of iron is represented by ferromagnetic bcc, while LDA fails and predicts nonmagnetic hcp as ground state of iron [241], see Fig. A.7.

In the case of iron, LDA predicts nonmagnetic hcp as ground state structure. Additional spin-polarized calculations of hcp with initially ferromagnetic and anti-ferromagnetic configurations yield negligible magnetic moments, thus these energy-volume curves lie on top of each other. The same behavior is found for fcc. All spin-polarized calculations with initially non-zero magnetic moments yield negligible magnetic moments after convergence of the electron density.

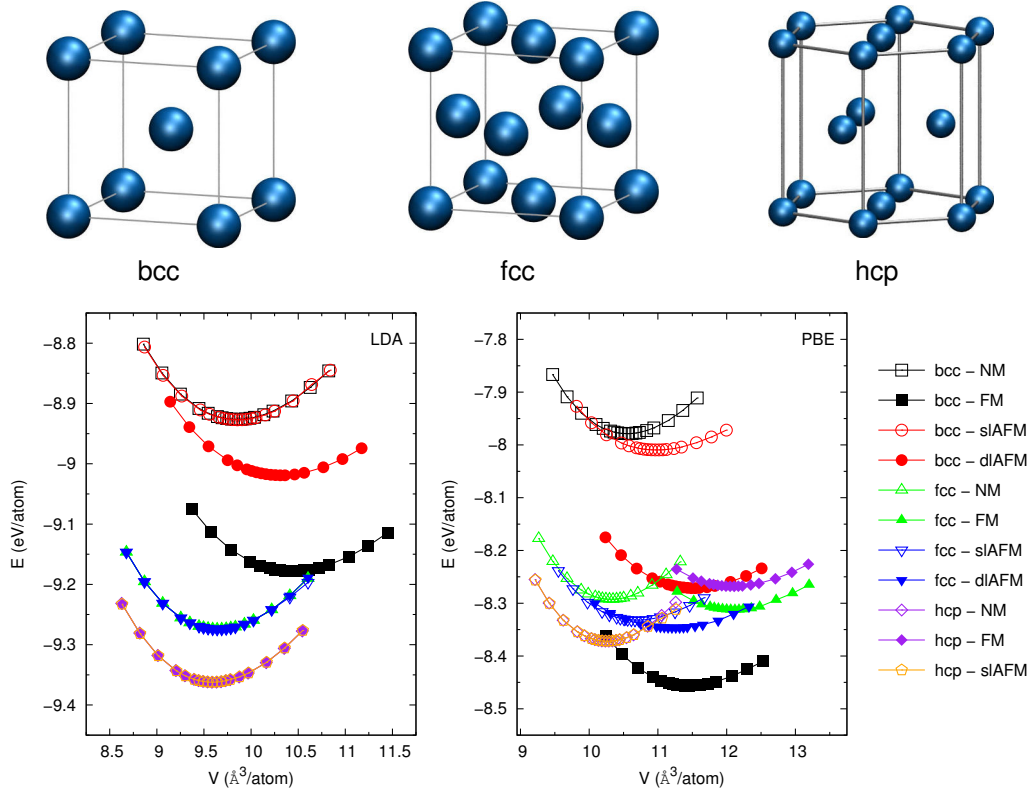


Figure A.7.: Crystal structures of bcc, fcc and hcp (upper panel). Total energies for the crystal structures with varying initial magnetic configurations for LDA and PBE.

In the case of bcc, the favored magnetic alignment is represented by the ferromagnetic case, with the other configurations having a higher total energy. For PBE, the ground state of iron is represented by bcc with a ferromagnetic configuration, in agreement with experiment. hcp, the phase of iron appearing at high pressures and ambient temperatures, is energetically above ferromagnetic bcc. The high-temperature phase fcc is energetically above the hcp phase, with the double-layer anti-ferromagnetic configuration being the favorite configuration. In the case of PBE, the different initial magnetic moments yield usually results with non-zero magnetic moments, unlike LDA. However, this behavior is not expected to be solely determined by the xc functional, as in the case of the PBE functional VASP employs the interpolation by Vosko *et al.* [425] for the correlation part of the xc functional. This usually results in larger magnetic moments.

## A.5. List of Binary Compounds

Table A.1 summarizes the results of the investigation of phase stability in the Fe-B system. The considered crystal structures are listed with Pearson symbol, the name of the prototype, the *Strukturbericht* designation if known, and the composition. The volume and energy per atom and the bulk modulus have been calculated with DFT. Some crystal structures have different prototypes, but virtually identical values for the volume, energy and bulk modulus. This is due to close geometrical relationships between some crystal structures, which relax towards the same structure if calculated in the Fe-B system. Structures denoted with an asterisk have been identified by the MAISE module [307].

Pearson Symbol	Prototype	Strukturbericht	Fe:B	V ( $\text{\AA}^3/\text{atom}$ )	E (eV/atom)	B (GPa)
tI18	NbNi <sub>8</sub>	-	8:1	10.856	-8.1923	154.81
hP6	CaCu <sub>5</sub>	D2 <sub>d</sub>	5:1	11.831	-7.3405	168.72
oS20	PtSn <sub>4</sub>	D1 <sub>c</sub>	5:1	10.714	-8.0429	168.32
cP5	Fe <sub>4</sub> C	-	4:1	11.815	-7.5375	136.01
hP20	WB <sub>4</sub>	-	4:1	11.926	-7.2515	132.37
mS10	MnB <sub>4</sub>	-	4:1	10.523	-7.6325	217.04
oI10	CrB <sub>4</sub>	-	4:1	11.164	-7.3281	172.33
oP10	FeB <sub>4</sub> *	-	4:1	11.167	-7.5405	177.38
oP20	MgB <sub>4</sub>	-	4:1	10.863	-8.0408	174.86
tI10	MoNi <sub>4</sub>	D1 <sub>a</sub>	4:1	9.288	-8.1421	290.22
cF116	Cr <sub>23</sub> C <sub>6</sub>	D8 <sub>4</sub>	23:6	10.344	-8.2643	214.91
cP4	$\alpha$ ReO <sub>3</sub>	D0 <sub>9</sub>	3:1	14.320	-7.3313	124.95
cP4	AuCu <sub>3</sub>	L1 <sub>2</sub>	3:1	10.054	-7.9019	199.46
hP8	Na <sub>3</sub> As	D0 <sub>18</sub>	3:1	10.190	-8.0048	211.18
hP8	Ni <sub>3</sub> Sn	D0 <sub>19</sub>	3:1	9.600	-7.9209	192.24
hP8	Fe <sub>3</sub> N	-	3:1	10.557	-7.9840	184.05
hP8	ReB <sub>3</sub>	-	3:1	10.352	-7.5535	216.96
hR8	BiI <sub>3</sub>	D0 <sub>5</sub>	3:1	10.369	-7.9683	180.68
mP8	FeB <sub>3</sub> *	-	3:1	10.555	-7.9983	175.07
oP8	$\beta$ Cu <sub>3</sub> Ti	D0 <sub>a</sub>	3:1	9.409	-7.9018	198.23
oP16	Fe <sub>3</sub> C	D0 <sub>11</sub>	3:1	9.861	-8.2298	194.21
oS16	Re <sub>3</sub> B	-	3:1	9.798	-8.2284	196.89
t16	Al <sub>3</sub> Zr	D0 <sub>23</sub>	3:1	9.828	-7.8842	170.38
tI16	SiU <sub>3</sub>	D0 <sub>c</sub>	3:1	9.533	-7.9343	193.22
tI16	Ir <sub>3</sub> Si	D0' <sub>c</sub>	3:1	10.062	-7.9027	202.54
tI32	Ni <sub>3</sub> P	-	3:1	9.654	-8.2254	221.73
tP4	CuTi <sub>3</sub>	L6 <sub>0</sub>	3:1	10.052	-7.9025	203.52
mS28	Mn <sub>5</sub> C <sub>2</sub>	-	5:2	9.680	-8.1825	216.66
hP20	Th <sub>7</sub> Fe <sub>3</sub>	-	7:3	9.453	-8.1640	217.64
oP40	Cr <sub>7</sub> C <sub>3</sub>	D10 <sub>1</sub>	7:3	9.526	-8.1697	226.76
cF12	CaF <sub>2</sub>	C1	2:1	10.137	-7.9379	202.86

# A. Appendix

cF24	Cu <sub>2</sub> Mg	C15	2:1	11.075	-6.7783	151.00
cP6	Ag <sub>2</sub> O	C3	2:1	13.013	-6.8186	114.86
hP3	AlB <sub>2</sub>	C32	2:1	9.537	-7.2950	347.40
hP6	InNi <sub>2</sub>	B8 <sub>2</sub>	2:1	9.091	-7.8694	164.89
hP6	ReB <sub>2</sub>	-	2:1	10.373	-7.5380	211.82
hP9	$\eta$ AgZn	B <sub>b</sub>	2:1	9.343	-8.0496	201.34
hP9	Fe <sub>2</sub> P	C22	2:1	9.208	-8.1088	244.15
hP9	CrSi <sub>2</sub>	C40	2:1	9.510	-7.7277	181.33
hP12	MgZn <sub>2</sub>	C14	2:1	12.085	-7.0106	85.19
hP18	Mg <sub>2</sub> Ni	C <sub>a</sub>	2:1	10.429	-7.5957	194.82
hP24	MgNi <sub>2</sub>	C36	2:1	12.153	-7.0126	84.01
mS6	AuTe <sub>2</sub>	C34	2:1	9.992	-7.8741	179.23
oF24	TiSi <sub>2</sub>	C54	2:1	9.529	-7.7612	167.96
ol6	ReSi <sub>2</sub>	-	2:1	8.569	-7.9578	297.09
oP6	FeS <sub>2</sub>	C18	2:1	10.099	-7.9115	187.37
oP6	CaCl <sub>2</sub>	C35	2:1	10.100	-7.9112	186.39
oP6	RuB <sub>2</sub>	-	2:1	10.141	-7.9367	190.60
oP12	PbCl <sub>2</sub>	C23	2:1	9.296	-8.1187	221.24
oP12	HgCl <sub>2</sub>	C25	2:1	10.014	-7.8837	181.23
oP12	Co <sub>2</sub> Si	C37	2:1	9.296	-8.1187	221.42
oP12	FeB <sub>2</sub> *	-	2:1	9.832	-7.8264	158.01
oP24	TiO <sub>2</sub>	C21	2:1	10.141	-7.8525	170.33
oP24	AuTe <sub>2</sub>	C46	2:1	10.004	-7.8442	168.40
oS12	Au <sub>2</sub> V	-	2:1	8.579	-7.9581	297.88
oS12	HgBr <sub>2</sub>	C24	2:1	9.954	-7.8669	178.36
tl6	ThH <sub>2</sub>	L'2	2:1	10.137	-7.9379	202.93
tl12	TiO <sub>2</sub>	C5	2:1	10.008	-7.7981	136.06
tl12	CuAl <sub>2</sub>	C16	2:1	9.039	-8.1775	219.16
tl12	Fe <sub>2</sub> B	-	2:1	10.166	-7.7910	189.08
tl24	Ga <sub>2</sub> Hf	-	2:1	9.621	-7.7057	114.97
tP6	TiO <sub>2</sub>	C4	2:1	10.543	-7.8322	176.48
tl32	Cr <sub>5</sub> B <sub>3</sub>	-	5:3	8.907	-8.0965	233.87
oS16	Pt <sub>5</sub> Ga <sub>3</sub>	-	5:3	8.717	-7.7976	240.85
cl80	Mn <sub>2</sub> O <sub>3</sub>	D5 <sub>3</sub>	3:2	9.970	-7.7520	185.48
hP10	Ru <sub>2</sub> B <sub>3</sub>	-	3:2	8.681	-7.8267	275.66
hR5	Bi <sub>2</sub> Te <sub>3</sub>	C33	3:2	9.602	-7.7188	183.18
hR5	Ni <sub>3</sub> S <sub>2</sub>	D5 <sub>e</sub>	3:2	9.429	-7.6523	183.26
tP10	Si <sub>2</sub> U <sub>3</sub>	D5 <sub>a</sub>	3:2	8.762	-8.0358	213.66
oS20	V <sub>2</sub> B <sub>3</sub>	-	3:2	9.033	-7.7816	200.26
oP38	Ru <sub>11</sub> B <sub>8</sub>	-	11:8	8.711	-7.9956	220.82
tl28	Mn <sub>3</sub> O <sub>4</sub>	-	4:3	9.979	-7.5345	197.41
ol14	Ta <sub>3</sub> B <sub>4</sub>	-	4:3	8.669	-7.8197	231.79
oP28	Ni <sub>4</sub> B <sub>3</sub>	-	4:3	8.602	-8.0259	261.10
hP18	Rh <sub>5</sub> B <sub>4</sub>	-	5:4	8.930	-7.8026	245.05

# A.5. List of Binary Compounds

tl18	Ti <sub>5</sub> Te <sub>4</sub>	-	5:4	9.371	-7.5408	157.05
oS22	V <sub>5</sub> B <sub>6</sub>	-	6:5	8.566	-7.8090	219.99
hR13	Fe <sub>7</sub> W <sub>6</sub>	D8 <sub>5</sub>	7:6	9.716	-7.0692	136.38
cF8	NaCl	B1	1:1	8.595	-7.4578	248.75
cF8	ZnS	B3	1:1	10.352	-7.5535	216.96
cF16	NaTl	B32	1:1	8.395	-7.0311	263.09
cl16	CoU	B <sub>a</sub>	1:1	7.698	-7.6679	303.07
cP2	CsCl	B2	1:1	9.680	-8.1825	216.66
cP6	NbO	-	1:1	9.702	-7.1355	207.20
cP8	FeSi	B20	1:1	8.081	-7.6583	275.67
hP2	WC	B <sub>h</sub>	1:1	8.209	-7.7452	291.76
hP4	ZnS	B4	1:1	10.863	-8.0408	174.86
hP4	NiAs	B8 <sub>1</sub>	1:1	8.246	-7.7228	297.78
hP4	BN	B12	1:1	8.247	-7.7227	297.06
hP8	AsTi	B <sub>i</sub>	1:1	8.567	-7.6865	236.95
hR32	CuPt	L1 <sub>1</sub>	1:1	8.278	-7.4734	354.07
mP4	NiTi	-	1:1	7.698	-7.6684	307.75
oF8	TlF	B24	1:1	8.594	-7.4577	248.37
oP4	CuTe	-	1:1	8.422	-7.5306	223.44
oP8	CoAs	-	1:1	8.249	-7.7228	292.74
oP8	FeB	B27	1:1	7.979	-7.9408	281.88
oP8	MnP	B31	1:1	8.329	-7.6119	262.52
oS8	TlI	B33	1:1	8.042	-7.9411	247.96
oS8	IrV	-	1:1	7.695	-7.6685	309.65
tl8	NbP	-	1:1	8.329	-7.4280	198.26
tl16	SeTl	B37	1:1	7.698	-7.6680	299.50
tl16	MoB	B <sub>g</sub>	1:1	8.043	-7.9470	282.31
tP2	AuCu	L1 <sub>0</sub>	1:1	7.696	-7.6682	310.00
tP4	PbO	B10	1:1	7.694	-7.6685	308.52
tP4	γCuTi	B11	1:1	7.915	-7.5972	283.66
hR13	Fe <sub>7</sub> W <sub>6</sub>	D8 <sub>5</sub>	6:7	7.715	-7.4820	285.26
oS22	V <sub>5</sub> B <sub>6</sub>	-	5:6	7.885	-7.7862	258.18
tl18	Ti <sub>5</sub> Te <sub>4</sub>	-	4:5	8.120	-7.4640	213.75
hP18	Rh <sub>5</sub> B <sub>4</sub>	-	4:5	8.112	-7.6289	271.66
oP28	Ni <sub>4</sub> B <sub>3</sub>	-	3:4	7.998	-7.5304	240.13
ol14	Ta <sub>3</sub> B <sub>4</sub>	-	3:4	7.772	-7.7022	262.90
tl28	Mn <sub>3</sub> O <sub>4</sub>	-	3:4	10.127	-6.6265	181.03
oP38	Ru <sub>11</sub> B <sub>8</sub>	-	8:11	8.458	-7.4515	215.42
oS20	V <sub>2</sub> B <sub>3</sub>	-	2:3	7.659	-7.5886	252.50
tP10	Si <sub>2</sub> U <sub>3</sub>	D5 <sub>a</sub>	2:3	8.027	-7.4001	256.12
hR5	Ni <sub>3</sub> S <sub>2</sub>	D5 <sub>e</sub>	2:3	9.219	-7.1476	208.24
hR5	Bi <sub>2</sub> Te <sub>3</sub>	C33	2:3	7.924	-7.0298	268.73
hP10	Ru <sub>2</sub> B <sub>3</sub>	-	2:3	7.900	-7.6301	274.35
cl80	Mn <sub>2</sub> O <sub>3</sub>	D5 <sub>3</sub>	2:3	8.370	-7.2583	239.62

# A. Appendix

oS16	Pt <sub>5</sub> Ga <sub>3</sub>	-	3:5	7.364	-7.2362	310.33
tl32	Cr <sub>5</sub> B <sub>3</sub>	-	3:5	7.348	-7.2898	257.39
tP6	TiO <sub>2</sub>	C4	1:2	10.163	-6.4382	176.47
tl24	Ga <sub>2</sub> Hf	-	1:2	7.413	-7.2473	277.23
tl12	Fe <sub>2</sub> B	-	1:2	8.471	-7.0714	242.84
tl12	CuAl <sub>2</sub>	C16	1:2	8.470	-7.0715	244.83
tl12	TiO <sub>2</sub>	C5	1:2	9.011	-6.5384	131.61
tl6	ThH <sub>2</sub>	L'2	1:2	8.415	-6.8250	244.67
oS12	HgBr <sub>2</sub>	C24	1:2	7.976	-7.2887	201.62
oS12	Au <sub>2</sub> V	-	1:2	7.047	-7.2740	326.09
oP24	AuTe <sub>2</sub>	C46	1:2	7.286	-7.3352	268.48
oP24	TiO <sub>2</sub>	C21	1:2	7.748	-7.3992	214.90
oP12	FeB <sub>2</sub> *	-	1:2	7.222	-7.5700	307.07
oP12	Co <sub>2</sub> Si	C37	1:2	7.200	-7.3207	275.29
oP12	HgCl <sub>2</sub>	C25	1:2	7.778	-7.3403	273.84
oP12	PbCl <sub>2</sub>	C23	1:2	7.231	-7.4287	305.58
oP6	RuB <sub>2</sub>	-	1:2	7.694	-7.5374	272.58
oP6	CaCl <sub>2</sub>	C35	1:2	7.652	-7.3663	282.32
oP6	FeS <sub>2</sub>	C18	1:2	8.149	-6.9388	232.76
ol6	ReSi <sub>2</sub>	-	1:2	7.047	-7.2738	324.11
oF24	TiSi <sub>2</sub>	C54	1:2	7.080	-7.4127	235.09
mS6	AuTe <sub>2</sub>	C34	1:2	7.263	-7.3211	257.98
hP24	MgNi <sub>2</sub>	C36	1:2	7.379	-7.1745	235.42
hP18	Mg <sub>2</sub> Ni	C <sub>a</sub>	1:2	7.654	-7.4171	281.91
hP12	MgZn <sub>2</sub>	C14	1:2	6.884	-7.0919	309.03
hP9	CrSi <sub>2</sub>	C40	1:2	7.056	-7.3857	324.26
hP9	Fe <sub>2</sub> P	C22	1:2	7.616	-6.9015	268.95
hP9	ηAgZn	B <sub>b</sub>	1:2	7.386	-7.3346	216.80
hP6	ReB <sub>2</sub>	-	1:2	7.654	-7.5393	275.80
hP6	InNi <sub>2</sub>	B8 <sub>2</sub>	1:2	7.258	-6.7749	240.84
hP3	AlB <sub>2</sub>	C32	1:2	7.263	-7.3210	256.36
cP6	Ag <sub>2</sub> O	C3	1:2	12.880	-5.8392	117.53
cF24	Cu <sub>2</sub> Mg	C15	1:2	6.891	-7.0836	318.88
cF12	CaF <sub>2</sub>	C1	1:2	8.430	-6.8203	244.80
oP40	Cr <sub>7</sub> C <sub>3</sub>	D10 <sub>1</sub>	3:7	7.339	-7.2373	288.41
hP20	Th <sub>7</sub> Fe <sub>3</sub>	-	3:7	7.919	-6.9998	203.31
mS28	Mn <sub>5</sub> C <sub>2</sub>	-	2:5	7.852	-7.0675	233.65
tP4	CuTi <sub>3</sub>	L6 <sub>0</sub>	1:3	6.761	-6.6782	322.05
tl32	Ni <sub>3</sub> P	-	1:3	7.362	-6.9952	239.18
tl16	Ir <sub>3</sub> Si	D0' <sub>c</sub>	1:3	7.228	-6.9666	236.16
tl16	SiU <sub>3</sub>	D0 <sub>c</sub>	1:3	6.762	-6.6780	318.90
t16	Al <sub>3</sub> Zr	D0 <sub>23</sub>	1:3	7.135	-6.9302	248.79
oS16	Re <sub>3</sub> B	-	1:3	7.398	-7.0055	245.08
oP16	Fe <sub>3</sub> C	D0 <sub>11</sub>	1:3	7.526	-7.1107	246.59



## A.5. List of Binary Compounds

oP8	$\beta\text{Cu}_3\text{Ti}$	D0 <sub>a</sub>	1:3	6.911	-6.8731	235.51
mP8	$\text{FeB}_3^*$	-	1:3	7.300	-7.3250	272.49
hR8	$\text{BiI}_3$	D0 <sub>5</sub>	1:3	7.966	-7.0314	205.95
hP8	$\text{ReB}_3$	-	1:3	6.922	-6.6879	276.22
hP8	$\text{Fe}_3\text{N}$	-	1:3	7.925	-6.4696	213.12
hP8	$\text{Ni}_3\text{Sn}$	D0 <sub>19</sub>	1:3	6.756	-6.8128	294.27
hP8	$\text{Na}_3\text{As}$	D0 <sub>18</sub>	1:3	7.371	-6.8136	279.91
cP4	$\text{AuCu}_3$	L1 <sub>2</sub>	1:3	6.754	-6.6779	318.53
cP4	$\alpha\text{ReO}_3$	D0 <sub>9</sub>	1:3	12.841	-6.1361	130.13
cF116	$\text{Cr}_{23}\text{C}_6$	D8 <sub>4</sub>	6:23	7.630	-6.7028	227.47
tI10	$\text{MoNi}_4$	D1 <sub>a</sub>	1:4	6.581	-6.6425	287.82
oP20	$\text{MgB}_4$	-	1:4	7.932	-6.8567	160.46
oP10	$\text{FeB}_4^*$	-	1:4	7.189	-7.2029	265.29
oI10	$\text{CrB}_4$	-	1:4	7.301	-7.1766	265.40
mS10	$\text{MnB}_4$	-	1:4	7.312	-7.1754	273.69
hP20	$\text{WB}_4$	-	1:4	7.203	-6.7478	317.50
cP5	$\text{Fe}_4\text{C}$	-	1:4	8.568	-5.8690	174.44
oS20	$\text{PtSn}_4$	D1 <sub>c</sub>	1:5	7.289	-6.7485	256.70
hP6	$\text{CaCu}_5$	D2 <sub>d</sub>	1:5	6.583	-6.1002	254.09
tI18	$\text{NbNi}_8$	-	1:8	6.435	-5.8416	211.15

Table A.1.: List of binary compounds considered in the investigation of phase stability in the Fe-B system. We list the Pearson symbol, prototype, *Strukturbericht* designation if known, composition, volume and energy per atom and bulk modulus. Structures with an asterisk have been identified by the MAISE module [307].

## A.6. Nudged Elastic Band Method

The nudged elastic band (NEB) method is an approach to determine the minimum energy path (MEP) that links two local minima on the potential energy surface. Any point on the path defined by the MEP represents the energy minimum on the plane perpendicular to the path. Thus, with respect to the energy barrier linking the two local minima, the approach yields the minimum energy required to allow the transition from one local minimum to another, the saddle point. Concrete examples for such an energy barrier are the activation energy required for diffusion, where a point defect migrates from its position in the host matrix to an adjacent one, or the energy required to induce a phase transformation.

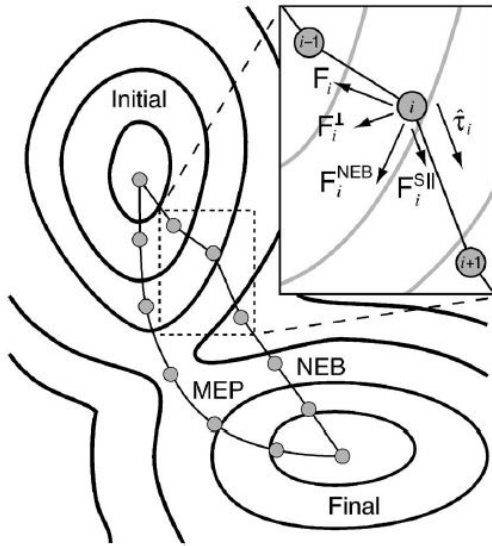


Figure A.8.: The nudged elastic band force  $\vec{F}_i^{\text{NEB}}$  comprises of the spring force  $\vec{F}_i^{\text{S||}}$  parallel and the potential force  $\vec{F}_i^{\perp}$  perpendicular to the tangent (from Ref. [383]).

In this context, the local minimum on the potential energy surface is represented by a stable state, and the energy barrier on the MEP is the minimum energy required to induce the transition between both stable states. For clarification, the stable state does not necessarily include the requirement of being energetically the most stable one, but requires to be stable with respect to small distortions, i.e. the slightly distorted state relaxes towards the stable one.

The NEB method is referred to as chain-of-states method, where the two local minima, representing an initial and final state, are linked by a series of images to represent the pathway between both states. The NEB images are linked by spring forces to ensure an equal distance between two adjacent images. Usually, the images are constructed by simple linear interpolation of the atomic coordinates of the initial and final state. However, in some cases a different scheme might

yield a better initial guess of the path, e.g. when rotation occurs.

The setup of the images provides only a initial guess of the pathway. The converge of the pathway towards the MEP is achieved with a force projection scheme during the actual computation. The total force on each image is represented by the potential force acting perpendicular to the band and the spring forces acting parallel to the band (Fig. A.8). The tangent required for the projections is defined as the unit vector to the neighboring image with higher energy. The usage of the force projection scheme represents an improvement compared to the elastic band method. The perpendicular part of the spring force and parallel part of the potential force are not considered which lead in elastic band calculation to an overestimation of the saddle point energy and a reduction of the path resolution in the area of the saddle point. Upon

convergence of the images towards the MEP, the saddle point can be identified. However, due to the limited number of images usually used, the resolution might be too coarse to clearly identify the saddle point. In these cases, the climbing-image NEB (CI-NEB) method can be used, where no spring force is acting on the image with highest energy, and a reflection of the force along the tangent ensures the climbing of the image towards the saddle point.

The MEP is often visualized using the energy difference with respect to the initial state vs. the reaction coordinate. The latter is defined as sum of the differences between two adjacent images. Referring to the initial state as zeroth image, the reaction coordinate is for image  $m$  is defined as

$$d_m = \sum_{l=1}^m d_{l-1,l} = \sum_{l=1}^m \sqrt{\sum_{i=1}^N \sum_{j=1}^3 \left( x_{ij}^l - x_{ij}^{l-1} \right)^2}, \quad (\text{A.2})$$

where  $N$  represents the number of atoms in the system and  $x_{ij}^l$  represents the  $j$ th component of the atomic position of atom  $i$  in image  $l$ . The reaction coordinate is given in Å.

## A.7. Calculation of Elastic Constants

### A.7.1. Theoretical Background

The elastic constants represent a mechanical property of a crystal describing the stiffness against externally applied strain  $\epsilon$ . According to Hooke's Law, for small deformations the energy of the crystal has a quadratically dependency on the strain, with the elastic constants  $c_{ijkl}$  as pre-factor.

Deformation of a given Bravais lattice results in the displacement of a given point  $\vec{x}$ , whereas the new position  $\vec{u}$  is given by

$$u_i = \sum_{j=1}^3 \frac{\partial u_i}{\partial x_j} x_j = \sum_{j=1}^3 e_{ij} x_j. \quad (\text{A.3})$$

$e_{ij}$  is rewritten in the form

$$\begin{aligned} e_{ij} &= \frac{1}{2} (e_{ij} + e_{ij}) + \frac{1}{2} (e_{ij} - e_{ij}) \\ &= \epsilon_{ij} + \omega_{ij} \end{aligned} \quad (\text{A.4})$$

whereas  $\epsilon_{ij}$  is called the strain tensor and  $\omega_{ij}$  is called the rotation tensor. The usage of the Voigt notation, taking into account the symmetry of the strain tensor, reduces the indexes to  $xx \rightarrow 1$ ,  $yy \rightarrow 2$ ,  $zz \rightarrow 3$ ,  $yz \rightarrow 4$ ,  $xz \rightarrow 5$  and  $xy \rightarrow 6$ , which leads to

$$\underline{\underline{\epsilon}} = \begin{pmatrix} \epsilon_1 & \epsilon_6/2 & \epsilon_5/2 \\ \epsilon_6/2 & \epsilon_2 & \epsilon_4/2 \\ \epsilon_5/2 & \epsilon_4/2 & \epsilon_3 \end{pmatrix} \quad (\text{A.5})$$

A Taylor expansion of the total energy with respect to the components of the strain tensor yields

$$E(V, \{\epsilon_i\}) = E(V) + V \sum_{i=1}^6 \sigma_i \epsilon_i + \frac{V}{2} \sum_{i,j=1}^6 C_{ij} \epsilon_i \epsilon_j + O[\epsilon_i^3] \quad (\text{A.6})$$

with the second-order elastic constants

$$C_{ij} = \frac{1}{V} \left( \frac{\partial^2 E(V, \{\epsilon_n\})}{\partial \epsilon_i \partial \epsilon_j} \right) \bigg|_{\epsilon=0} \quad (\text{A.7})$$

and the volume  $V$  corresponds to the equilibrium volume of the unstrained crystal.

The total number of independent elastic constants  $C_{ij}$  is 21. However, the symmetry of the Bravais lattice reduces the number of the independent elastic constants. Cubic cells have only three independent elastic constants ( $C_{11}$ ,  $C_{12}$ ,  $C_{44}$ ), tetragonal ones have six ( $C_{11}$ ,  $C_{12}$ ,  $C_{13}$ ,  $C_{33}$ ,  $C_{44}$ ,  $C_{66}$ ), orthorhombic ones nine ( $C_{11}$ ,  $C_{12}$ ,  $C_{13}$ ,  $C_{22}$ ,  $C_{23}$ ,  $C_{33}$ ,  $C_{44}$ ,  $C_{55}$ ,  $C_{66}$ ) and

hexagonal ones five ( $C_{11}$ ,  $C_{12}$ ,  $C_{13}$ ,  $C_{33}$ ,  $C_{44}$ ). Monoclinic unit cells have 13 and triclinic ones have 21 independent elastic constants.

The application of a given set of independent strains leads to the determination of the elastic constants. The number of required independent strains is equal to the number of independent elastic constants, as determined by the given Bravais lattice. The strains  $\epsilon_i$  can be individually defined, e.g. in order to make use of the specific symmetry of the supercell or to conserve the volume of the supercell. For the latter, the  $\epsilon_i$  have to fulfill a specific requirement. Application of the strains tensor  $\underline{\epsilon}$  transforms the primitive vectors  $\vec{a}_i$  of the unstrained lattice into the new primitive vectors  $\vec{b}_i$  of the strained lattice via

$$\begin{pmatrix} \vec{b}_1 \\ \vec{b}_2 \\ \vec{b}_3 \end{pmatrix} = \begin{pmatrix} \vec{a}_1 \\ \vec{a}_2 \\ \vec{a}_3 \end{pmatrix} \cdot (\mathbb{1} + \underline{\epsilon}) \quad (\text{A.8})$$

The conservation of the volume requires that

$$|\mathbb{1} + \underline{\epsilon}| \stackrel{!}{=} 1 \quad (\text{A.9})$$

which leads to

$$(1 + \epsilon_1)(1 + \epsilon_2)(1 + \epsilon_3) + \frac{1}{4}\epsilon_4\epsilon_5\epsilon_6 - (1 + \epsilon_1)\frac{\epsilon_4^2}{2} - (1 + \epsilon_2)\frac{\epsilon_5^2}{2} - (1 + \epsilon_3)\frac{\epsilon_6^2}{2} \stackrel{!}{=} 1 \quad (\text{A.10})$$

The used set of strains used throughout the investigation and the corresponding change in the energy are summarized in Tab. A.2 for cubic cells, Tab. A.3 for tetragonal ones, Tab. A.4 for orthorhombic ones and in Tab. A.5 for hexagonal unit cells. The set of strains for the cubic and tetragonal cell follow the procedure described in Refs. [426, 427].

strain	$\epsilon_i$	$E_2$
1	$\epsilon_1 = \delta, \epsilon_2 = -\delta, \epsilon_3 = \delta^2/(1 + \delta^2)$	$V(C_{11} - C_{12})\delta^2$
2	$\epsilon_3 = \delta^2/(4 - \delta^2), \epsilon_6 = \delta$	$VC_{44}/2$
3	$\epsilon_1 = \epsilon_2 = \epsilon_3 = \delta$	$3V(C_{11} + 2C_{12})\delta^2/2$

Table A.2.: Applied parametrized strains to determine the three independent elastic constants for the cubic unit cell. Unlisted  $\epsilon_i$  in the second column are identical to zero.

For the cubic Bravais lattice, the set of strains (Tab. A.2) consist of a volume conserving orthorhombic and monoclinic strain in order to determine a linear combination of  $C_{11}$  and  $C_{12}$ , and  $C_{44}$ , respectively. The last strain is represented by a hydrostatic strain, which does not conserve the volume of the unit cell.

The set of strains for the tetragonal Bravais lattice (Tab. A.3) consist of two non-volume conserving tetragonal strains for the determination of the linear combination of  $C_{11}$  and  $C_{12}$ , and  $C_{33}$ , respectively (strain 1 and 3), but require  $|\vec{a}_1| = |\vec{a}_2| \neq |\vec{a}_3|$ . The set is completed with

## A. Appendix

strain	$\epsilon_i$	$E_2$
1	$\epsilon_1 = \epsilon_2 = \delta$	$V(C_{11} + C_{12})\delta^2$
2	$\epsilon_1 = \epsilon_2 = \delta$ $\epsilon_3 = -(\delta^2 + 2\delta)/(1 + \delta)^2$	$V(C_{11} + C_{12} + 2C_{33} - 4C_{13})\delta^2$
3	$\epsilon_3 = \delta$	$VC_{33}\delta^2/2$
4	$\epsilon_1 = \sqrt{(1 + \delta)/(1 - \delta)} - 1$ $\epsilon_2 = \sqrt{(1 - \delta)/(1 + \delta)} - 1$	$V(C_{11} - C_{22})\delta^2$
5	$\epsilon_3 = \delta^2/2$ $\epsilon_4 = \epsilon_5 = \delta$	$VC_{44}\delta^2$
6	$\epsilon_1 = \epsilon_2 = \sqrt{1 + \delta^2/4} - 1$ $\epsilon_6 = \delta$	$VC_{66}\delta^2/2$

Table A.3.: Applied parametrized strains to determine the six independent elastic constants for the tetragonal unit cell. Unlisted  $\epsilon_i$  in the second column are identical to zero.

two additional volume conserving strains (strain 2 and 4), the former leading to a tetragonal distortion and the latter to an orthorhombic one. The remaining elastic constants  $C_{44}$  and  $C_{66}$  are obtained via two volume conserving monoclinic strains.

strain	$\epsilon_i$	$E_2$
1	$\epsilon_1 = \delta, \epsilon_2 = -\delta/(1 + \delta)$	$V(C_{11} + C_{22} - 2C_{12})\delta^2/2$
2	$\epsilon_1 = \delta, \epsilon_3 = -\delta/(1 + \delta)$	$V(C_{11} + C_{33} - 2C_{13})\delta^2/2$
3	$\epsilon_2 = \delta, \epsilon_3 = -\delta/(1 + \delta)$	$V(C_{22} + C_{33} - 2C_{23})\delta^2/2$
4	$\epsilon_1 = \delta$	$VC_{11}\delta^2/2$
5	$\epsilon_2 = \delta$	$VC_{22}\delta^2/2$
6	$\epsilon_3 = \delta$	$VC_{33}\delta^2/2$
7	$\epsilon_3 = \delta^2/2, \epsilon_4 = \epsilon_5 = \delta$	$V(C_{44} + C_{55})\delta^2/2$
8	$\epsilon_2 = \delta^2/2, \epsilon_4 = \epsilon_6 = \delta$	$V(C_{44} + C_{66})\delta^2/2$
9	$\epsilon_1 = \delta^2/2, \epsilon_5 = \epsilon_6 = \delta$	$V(C_{55} + C_{66})\delta^2/2$

Table A.4.: Applied parametrized strains to determine the nine independent elastic constants for the orthorhombic unit cell. Unlisted  $\epsilon_i$  in the second column are identical to zero.

The set of strains for the orthorhombic Bravais lattice (Tab. A.4) consists of three volume conserving orthorhombic strains, three non-volume conserving strains and additionally three volume conserving monoclinic strains.

Strains 1, 2 and 4 in the set of strains for the hexagonal Bravais lattice (Tab. A.5) make use of the given symmetry of the Bravais lattice, while strain 3 and 5 leads to distortion of the Bravais lattice. Only strains 1,3 and 5 are volume conserving in this case.

strain	$\epsilon_i$	$E_2$
1	$\epsilon_1 = \epsilon_2 = \delta, \epsilon_3 = -(\delta^2 + 2\delta)/(1 + \delta)^2$	$V(C_{11} + C_{12} + 2C_{33} - 4C_{13})\delta^2$
2	$\epsilon_1 = \epsilon_2 = \delta$	$V(C_{11} + C_{12})\delta^2$
3	$\epsilon_1 = \delta, \epsilon_2 = -\delta/(1 + \delta)$	$V(C_{11} - C_{12})\delta^2$
4	$\epsilon_3 = \delta$	$VC_{33}\delta^2/2$
5	$\epsilon_3 = \delta^2/2, \epsilon_4 = \delta$	$VC_{44}\delta^2/2$

Table A.5.: Applied parametrized strains to determine the five independent elastic constants for the hexagonal unit cell. Unlisted  $\epsilon_i$  in the second column are identical to zero.

### A.7.2. Convergence Test for Elastic Constants

Calculations of elastic constants are more demanding with respect to plane wave cutoff and the k-point mesh. This is due to the required distortions of the underlying Bravais lattice, that cause a change of the symmetry of the Bravais lattice and therefore the number of k-points in the irreducible Brillouin zone, and the dependence of the elastic constants on the total energy of the distorted Bravais lattice. Thus, we performed convergence tests of the elastic constants for iron in the ferromagnetic bcc structure, as among the elements that have been considered in the calculation of the elastic constants iron represents the most demanding element with respect to plane wave cutoff and required fineness of the k-point mesh.

The applied procedure is similar to the one described in Sec. A.4 in the appendix, except that the three independent elastic constants  $C_{11}$ ,  $C_{12}$  and  $C_{44}$  are used instead of the total energy difference as convergence criteria. The plane wave cutoff and k-point density for iron as found in the convergence test with respect to total energy differences were used as minimum values, in order to ensure the convergence with respect to total energy. The convergence

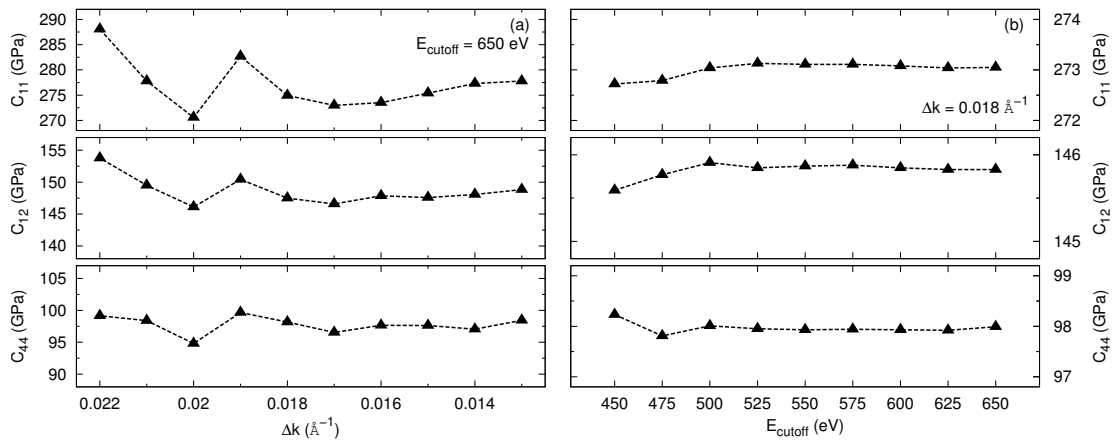


Figure A.9.: Convergence tests with respect to (a) k-point density and (b) plane wave cutoff for elastic constants of ferromagnetic bcc iron.

tests for varying k-point mesh at fixed plane wave cutoff (Fig. A.9(a)) and varying plane wave cutoff at fixed k-point mesh (Fig. A.9(b)) from the previous test yield convergence of the three independent elastic constants within 1% at a plane wave cutoff of  $E_{\text{cut}} = 525$  eV and a k-point density of  $\Delta k = 0.018 \text{ \AA}^{-1}$ . These values were used throughout the investigation for the calculation of elastic constants.



## Bibliography

- [1] T Yukitoshi, K Yoshikawa, T Daikoku, and F Masuyama. Experience of high chromium ferritic steel tubes in power plant. *Journal of Materials for Energy Systems*, 4:99, 1982.
- [2] R Thomson and H Bhadeshia. Carbide precipitation in 12Cr1MoV power plant steel. *Metallurgical and Materials Transactions A*, 23:1171, 1992.
- [3] I Altpeter, G Dobmann, KH Katerbau, M Schick, P Binkele, P Kizler, and S Schmauder. Copper precipitates in 15 NiCuMoNb 5 (WB 36) steel: material properties and microstructure, atomistic simulation, and micromagnetic NDE techniques. *Nuclear Engineering and Design*, 206(2-3):337, 2001.
- [4] PJ Ennis and A Czyrska-Filemonowicz. Recent advances in creep-resistant steels for power plant applications. *Sadhana-Academy Proceedings in Engineering Sciences*, 28(3-4):709, 2003.
- [5] A Baltusnikas, R Levinskas, and I Lukosiute. Kinetics of carbide formation during ageing of pearlitic 12X1M phi steel. *Materials Science-Medziagotyra*, 13(4):286, 2007.
- [6] A Zielinska-Lipiec and A Czyrska-Filemonowicz. Characterisation of the micro- and nanoscale structure of new creep-resistant steels for use in advanced USC steam power plants. *Materials Transactions*, 48(5):931, 2007.
- [7] R Hubo, G Garrigues, F Schroter, and J Flahaut. Heavy plates for bridge construction. *Revue de Metallurgie-Cahiers D Informations Techniques*, 98(6):613, 2001.
- [8] A Samuelsson and F Schroter. High performance steels in Europe. In *Use of Application of High-Performance Steels for Steel Structures*, pages 99–146. IABSE, 2006.
- [9] Y Yoshida, T Obinata, M Nishio, and T Shiwaku. Development of high-strength (780 N/mm<sup>2</sup>) steel for building systems. *International Journal of Steel Structures*, 9:285, 2009.
- [10] M Volz, F Schroeter, and G Steidl. Structural Steels in structural engineering. *Stahlbau*, 77(11):781, 2008.
- [11] HJ Kaiser, A Kern, R Grill, H Schlosser, and F Schroeter. Heavy plates made from special structural steels for highest requirements. *Stahl und Eisen*, 128(4):91, 2008.
- [12] R Hubo, F Martin, and F Schroter. Plates for economic steel and offshore constructions. *Stahl und Eisen*, 120(11):101, 2000.

- [13] F Schroter. Structural steel for the application in offshore, wind and hydro energy production: comparison of application and welding properties of frequently used materials. *International Journal of Microstructure and Materials Properties*, 6:4, 2011.
- [14] M Martins and LC Casteletti. Microstructural characteristics and corrosion behavior of a super duplex stainless steel casting. *Materials Characterization*, 60(2):150, 2009.
- [15] JL Albarran, L Martinez, and HF Lopez. Effect of heat treatment on the stress corrosion resistance of a microalloyed pipeline steel. *Corrosion Science*, 41(6):1037, 1999.
- [16] IG Rodionova, ON Baklanova, ET Shapovalov, NI Endel, II Reformatskaya, AA Podobaev, SD Zinchenko, SV Efimov, EY Kuznetsova, LA Malyshkina, and AV Drandusov. Methods of evaluating the corrosion resistance of low-alloy and carbon tube steels under the service conditions of oil and gas pipelines. *Metallurgist*, 49(5-6):173, 2005.
- [17] R Lewis and RS Dwyer-Joyce. Wear mechanisms and transitions in railway wheel steels. *Proceedings of the Institution of Mechanical Engineers Part J-Journal of Engineering Tribology*, 218(6):467, 2004.
- [18] Y Miyoshi, J Oka, and S Maeda. Fundamental research on corrosion-resistance of precoated steel sheets for automobiles. *Transactions of the Iron and Steel Institute of Japan*, 23(11):974, 1983.
- [19] M Takahashi, A Uenishi, H Yoshida, and H Kuriyama. Advanced high strength steels for automobile body structures. In Chandra, T and Tsuzaki, K and Militzer, M and Ravindran, C, editor, *THERMEC 2006, Pts 1-5*, volume 539-543 of *Materials Science Forum*, pages 4386–4390. Minerals, Met & Mat Soc, 2007. 5th International Conference on Processing and Manufacturing of Advanced Materials, Vancouver, Canada, Jul 04-08, 2006.
- [20] NA Rybkin, IG Rodionova, NG Shaposhnikov, VV Kuznetsov, and PA Mishnev. Development of approaches for selecting the optimum alloying systems and production parameters for manufacturing hot-rolled high-strength low-alloy steels for automobile building. *Metallurgist*, 53(7-8):486, 2009.
- [21] S Takagi, Y Toji, M Yoshino, and K Hasegawa. Hydrogen embrittlement resistance evaluation of ultra high strength steel sheets for automobiles. *ISIJ International*, 52(2):316, 2012.
- [22] J Barry and G Byrne. Cutting tool wear in the machining of hardened steels Part I: alumina/TiC cutting tool wear. *Wear*, 247(2):139, 2001.
- [23] J Barry and G Byrne. Cutting tool wear in the machining of hardened steels Part II: cubic boron nitride cutting tool wear. *Wear*, 247(2):152, 2001.
- [24] P Hedenqvist, M Olsson, P Wallen, A Kassman, S Hogmark, and S Jacobson. How tin coatings improve the performance of high-speed steel cutting tools. *Surface & Coatings Technology*, 41(2):243, 1990.

- 
- [25] RC Glenn and WC Leslie. Nature of white streaks in impacted steel armor plate. *Metallurgical Transactions*, 2(10):2945, 1971.
- [26] MR Edwards and A Mathewson. The ballistic properties of tool steel as a potential improvised armour plate. *International Journal of Impact Engineering*, 19(4):297, 1997.
- [27] F Galvez, D Cendon, N Garcia, A Enfedaque, and V Sanchez-Galvez. Dynamic fracture toughness of a high strength armor steel. *Engineering Failure Analysis*, 16(8):2567, 2009.
- [28] HJ Kaiser, A Kern, S Scharf, and WA Gooch, Jr. Ballistic testing of ThyssenKrupp steel europe armor steel in accordance with US military armor specifications. In Baker, E and Templeton, D, editor, *Ballistics 2011: 26th International Symposium on Ballistics, Vol 1 and Vol 2*, pages 1167–1176. Ballist Div Natl Def Ind Assoc (NDIA), 2011. 26th International Symposium on Ballistics, Miami, FL, Sep 12-16, 2011.
- [29] K Maweja and W Stumpf. Fracture and ballistic-induced phase transformation in tempered martensitic low-carbon armour steels. *Materials Science and Engineering A-Structural Materials Properties Microstructure and Processing*, 432(1-2):158, 2006.
- [30] K Maweja and W Stumpf. The design of advanced performance high strength low-carbon martensitic armour steels - Microstructural considerations. *Materials Science and Engineering A-Structural Materials Properties Microstructure and Processing*, 480(1-2):160, 2008.
- [31] K Maweja and W Stumpf. The design of advanced performance high strength low-carbon martensitic armour steels - Part 1. Mechanical property considerations. *Materials Science and Engineering A-Structural Materials Properties Microstructure and Processing*, 485(1-2):140, 2008.
- [32] H Izumida, N Kawabe, S Takamura, H Morita, and T Murai. Development of high-tensile-strength stainless steel wire. *SEI Technical Review*, 60:24, 2005.
- [33] HKDH Bhadeshia and RWK Honeycombe. *Steels: Microstructure and Properties*. Metallurgy and Materials Science Series. Butterworth-Heinemann, 2006.
- [34] HN Han, CS Oh, G Kim, and O Kwon. Design method for TRIP-aided multiphase steel based on a microstructure-based modelling for transformation-induced plasticity and mechanically induced martensitic transformation. *Materials Science and Engineering A-Structural Materials Properties Microstructure and Processing*, 499(1-2):462, 2009.
- [35] S Shanmugam, NK Ramiseti, RDK Misra, T Mannering, D Panda, and S Jansto. Effect of cooling rate on the microstructure and mechanical properties of Nb-microalloyed steels. *Materials Science and Engineering A-Structural Materials Properties Microstructure and Processing*, 460:335, 2007.
- [36] YY Song, DH Ping, FX Yin, XY Li, and YY Li. Microstructural evolution and low temperature impact toughness of a Fe-13%Cr-4%Ni-Mo martensitic stainless steel. *Materials Science and Engineering A-Structural Materials Properties Microstructure and Processing*, 527(3):614, 2010.

- [37] JQ Wang, A Atrens, DR Cousens, PM Kelly, C Nockolds, and S Bulcock. Measurement of grain boundary composition for X52 pipeline steel. *Acta Materialia*, 46(16):5677, 1998.
- [38] MX Zhang and PM Kelly. Crystallography of carbide-free bainite in a hard bainitic steel. *Materials Science and Engineering A-Structural Materials Properties Microstructure and Processing*, 438:272, 2006.
- [39] J Nowacki, M Urbanski, and P Zajac. FCAW welding of duplex steel in construction of chemical cargo carriers. *Welding International*, 23:34, 2009.
- [40] PE Reynolds. Effect of titanium treatment on grain-size control in low-alloy steels. *Ironmaking & Steelmaking*, 18(1):52, 1991.
- [41] H Adrian and FB Pickering. Effect of titanium additions on austenite grain-growth kinetics of medium carbon V-Nb steels containing 0.008-0.018-%N. *Materials Science and Technology*, 7(2):176, 1991.
- [42] F Penalba, CG DeAndres, M Carsi, and F Zapirain. Austenitic grain size evolution and continuous cooling transformation diagrams in vanadium and titanium microalloyed steels. *Journal of Materials Science*, 31(14):3847, 1996.
- [43] J Degerbeck. Influence of Mn compared to that of Cr, Mo and S on resistance to initiation of pitting and crevice corrosion in austenitic stainless-steels. *Materials and Corrosion-Werkstoffe und Korrosion*, 29(3):179, 1978.
- [44] J-C Kim, S-H Baik, J-H Jun, and Y-K Lee. Effect of chromium addition on damping capacity, mechanical property, and corrosion resistance of Fe-18%Mn alloy. In Igata, N and Takeuchi, S, editor, *High Damping Materials II*, volume 319 of *Key Engineering Materials*, page 73. Japan Soc Promot Sci; Kajima Fdn; Ogasawara Fdn; Suzuki Fdn, 2006. 2nd International Symposium on High Damping Materials, Kyoto, Japan, Sep 09-10, 2005.
- [45] WA Metwally and MK Samy. Evaluation of abrasive-wear and erosion-corrosion resistance of high-Cr cast-steel. *Steel Research*, 65(10):455, 1994.
- [46] M Laribi, AB Vannes, and D Treheux. On a determination of wear resistance and adhesion of molybdenum, Cr-Ni and Cr-Mn steel coatings thermally sprayed on a 35CrMo4 steel. *Surface & Coatings Technology*, 200(8):2704, 2006.
- [47] Y Kawakami, F Tamai, T Enjoji, K Takashima, and M Otsu. Wear resistance properties of tungsten carbide/stainless steel composite materials prepared by pulsed current sintering. In Yoon, DY and Kang, SJL and Eun, KY and Kim, YS, editor, *Progress in Powder Metallurgy, Pts 1 and 2*, volume 534-536 of *Materials Science Forum*, pages 1573–1576. Korean Powder Metallurgy Inst, 2007. Power Metallurgy World Congress and Exhibition 2006, Busan, South Korea, Sep 24-28, 2006.
- [48] K Kimura, K Seki, Y Toda, and F Abe. Development of high strength 15Cr ferritic creep resistant steel with addition of tungsten and cobalt. *ISIJ International*, 41:121, 2001.

- [49] AN Popandopulo, GY Novikova, and EP Danilenko. Solubility of carbides and red hardness of tungsten-molybdenum high-speed steel. *Metal Science and Heat Treatment*, 21(9-10):788, 1979.
- [50] M Calcagnotto, D Ponge, and D Raabe. On the effect of manganese on grain size stability and hardenability in ultrafine-grained ferrite/martensite dual-phase steels. *Metallurgical and Materials Transactions A-Physical Metallurgy and Materials Science*, 43A(1):37, 2012.
- [51] AP Gulyayev. Effect of chromium and nickel on toughness of steel. *Metal Science and Heat Treatment*, 4:491, 1962.
- [52] H Miyaji, A Hoshino, and H Nakajima. Effect of nickel addition on the toughness of 18Cr-1Mo stainless-steels. *Journal of Materials Science*, 25(1B):673, 1990.
- [53] Y Arita and Y Ushigami. Effect of aluminum and titanium content on grain growth, texture and magnetic properties in 3%Si non-oriented electrical steel. In Chandra, T and Tsuzaki, K and Militzer, M and Ravindran, C, editor, *THERMEC 2006, Pts 1-5*, volume 539-543 of *Materials Science Forum*, pages 4428–4433. Minerals, Met & Mat Soc, 2007. 5th International Conference on Processing and Manufacturing of Advanced Materials, Vancouver, Canada, Jul 04-08, 2006.
- [54] E Jimenez-Melero, NH van Dijk, L Zhao, J Sietsma, SE Offerman, JP Wright, and S van der Zwaag. The effect of aluminium and phosphorus on the stability of individual austenite grains in TRIP steels. *Acta Materialia*, 57(2):533, 2009.
- [55] V Ollilainen, W Kasprzak, and L Holappa. The effect of silicon, vanadium and nitrogen on the microstructure and hardness of air cooled medium carbon low alloy steels. *Journal of Materials Processing Technology*, 134(3):405, 2003.
- [56] SS Nayaka, R Anumolu, RDK Misra, KH Kim, and DL Lee. Microstructure-hardness relationship in quenched and partitioned medium-carbon and high-carbon steels containing silicon. *Materials Science and Engineering A-Structural Materials Properties Microstructure and Processing*, 498(1-2):442, 2008.
- [57] MA Krishtal, AA Borgardt, and YD Yashin. Effect of lead on the machinability of free-cutting steel. *Metal Science and Heat Treatment*, 19:178, 1977.
- [58] AN Morozov and YE Goldshtein. Steels containing lead. *Metal Science and Heat Treatment*, 22:779, 1980.
- [59] AY Zaslavskii. Effect of lead on the properties of structural steel. *Metal Science and Heat Treatment*, 22:783, 1980.
- [60] AY Zaslavskii. Mechanism of improving the machinability of steel by inclusions. *Metal Science and Heat Treatment*, 26:665, 1984.
- [61] K Yoshihara, M Tosa, and K Nii. Surface precipitation of boron-nitride on the surface of type 304 stainless-steels doped with nitrogen, boron, and cerium. *Journal of Vacuum Science & Technology A-Vacuum Surfaces and Films*, 3(4):1804, 1985.

- [62] YC Lu and MB Ives. The improvement of the localized corrosion-resistance of stainless-steel by cerium. *Corrosion Science*, 34(11):1773, 1993.
- [63] A Nazeri, PP Trzaskoma-Paulette, and D Bauer. Synthesis and properties of cerium and titanium oxide thin coatings for corrosion protection of 304 stainless steel. *Journal of SOL-GEL Science and Technology*, 10(3):317, 1997.
- [64] MB Whiteman and AR Troiano. Hydrogen embrittlement of austenitic stainless steel. *Corrosion*, 21(2):53, 1965.
- [65] RB Benson, RK Dann, and LW Roberts. Hydrogen embrittlement of stainless steel. *Transactions of the Metallurgical Society of AIME*, 242(10):2199, 1968.
- [66] DP Williams and HG Nelson. Embrittlement of 4130-steel by low-pressure gaseous hydrogen. *Metallurgical Transactions*, 1(1):63, 1970.
- [67] RA Oriani. Hydrogen embrittlement of steels. *Annual Review of Materials Science*, 8:327, 1978.
- [68] RLS Thomas, JR Scully, and RP Gangloff. Internal hydrogen embrittlement of ultrahigh-strength AERMET 100 steel. *Metallurgical and Materials Transactions A-Physical Metallurgy and Materials Science*, 34(2):327, 2003.
- [69] JA Gonzalez, A Molina, E Otero, and W Lopez. On the mechanism of steel corrosion in concrete - The role of oxygen diffusion. *Magazine of Concrete Research*, 42(150):23, 1990.
- [70] G Muller, G Schumacher, and F Zimmerman. Investigation on oxygen controlled liquid lead corrosion of surface treated steels. *Journal of Nuclear Materials*, 278(1):85, 2000.
- [71] EP George, PL Li, and DP Pope. Creep cavitation in iron .1. Sulfides and carbides as nucleation sites. *Acta Metallurgica*, 35(10):2471, 1987.
- [72] CL Briant and PL Andresen. Grain-boundary segregation in austenitic stainless-steels and its effect on intergranular corrosion and stress-corrosion cracking. *Metallurgical Transactions A-Physical Metallurgy and Materials Science*, 19(3):495, 1988.
- [73] EE Bloom and FW Wiffen. Effects of large concentrations of helium on mechanical-properties of neutron-irradiated stainless-steel. *Journal of Nuclear Materials*, 58(2):171, 1975.
- [74] D Kramer, HR Brager, CG Rhodes, and AG Pard. Helium embrittlement in type 304 stainless steel. *Journal of Nuclear Materials*, 25(2):121, 1968.
- [75] O Dremailova, D Emadi, JR Brown, and E Essadiqi. Influence of tin segregation on the intergranular failure of medium carbon steels during continuous casting. *Microscopy and Microanalysis*, 10:760, 2004.
- [76] J Kameda and CJ McMahon. The effects of Sb, Sn, and P on the strength of grain-boundaries in a Ni-Cr steel. *Metallurgical Transactions A-Physical Metallurgy and Materials Science*, 12(1):31, 1981.

- [77] T Yamane, K Hisayuki, Y Kawazu, T Takahashi, Y Kimura, and S Tsukuda. Improvement of toughness of low carbon steels containing nitrogen by fine microstructures. *Journal of Materials Science*, 37:3875, 2002.
- [78] SH Ahn, YS Choi, JG Kim, and JG Han. A study on corrosion resistance characteristics of PVD Cr-N coated steels by electrochemical method. *Surface & Coatings Technology*, 150(2-3):319, 2002.
- [79] RA Mulford, CJ McMahon, DP Pope, and HC Feng. Temper embrittlement of Ni-Cr steels by phosphorus. *Metallurgical Transactions A-Physical Metallurgy and Materials Science*, 7(8):1183, 1976.
- [80] F Jacobs and G Krauss. The effects of phosphorus and carbon on the hardenability of 41XX type steels. *Journal of Heat Treating*, 2:139, 1981.
- [81] K Hirata, O Umezawa, and K Nagai. Microstructure cast strip in 0.1 mass% C steels containing phosphorus. *Materials Transactions*, 43(3):305, 2002.
- [82] A Bedolla-Jacuinde, J Zuno-Silva, S Rojas, I Mejia, and L Bejar-Gomez. High resistance boron treated steels for railway applications. *Materials Science and Technology*, 25(3):361, 2009.
- [83] B Kapadia. Effect of boron additions on the toughness of heat-treated low-alloy steels. *Journal of Heat Treating*, 5:41, 1987.
- [84] CJ McMahon. The role of solute segregation in promoting the hardenability of steel. *Metallurgical and Materials Transactions A*, 11:531–535, 1980.
- [85] E Lopez-Chipres, I Mejia, C Maldonado, A Bedolla-Jacuinde, M El-Wahabi, and JM Cabrera. Hot flow behavior of boron microalloyed steels. *Materials Science and Engineering A-Structural Materials Properties Microstructure and Processing*, 480(1-2):49, 2008.
- [86] LS Lyakhovich and VI Kraevoi. Diffusion saturation and formation of boride coatings on high-strength cast-iron. *Metal Science and Heat Treatment*, 19(5-6):454, 1977.
- [87] MR St.John and AF Sammells. Characterization of an iron boride coating produced by pack boronization of low-carbon steel. *Journal of Materials Science*, 16(8):2327, 1981.
- [88] G Palombarini and M Carbucicchio. Growth of boride coatings on iron. *Journal of Materials Science Letters*, 6(4):415, 1987.
- [89] M Carbucicchio and G Palombarini. Effects of alloying elements on the growth of iron boride coatings. *Journal of Materials Science Letters*, 6(10):1147, 1987.
- [90] M Kulka and A Pertek. Microstructure and properties of borocarbured 15CrNi6 steel after laser surface modification. *Applied Surface Science*, 236(1-4):98, 2004.
- [91] I Campos, M Palomar, A Amador, R Ganem, and J Martinez. Evaluation of the corrosion resistance of iron boride coatings obtained by paste boriding process. *Surface & Coatings Technology*, 201(6):2438, 2006.

- [92] M Eroglu. Boride coatings on steel using shielded metal arc welding electrode: microstructure and hardness. *Surface & Coatings Technology*, 203(16):2229, 2009.
- [93] JA Jiménez, G González-Doncel, and OA Ruano. Mechanical properties of ultrahigh boron steels. *Advanced Materials*, 7(2):130, 1995.
- [94] T Kanaizuka. Phase-diagram of pseudobinary CrB-MnB and MnB-FeB systems - Crystal-structure of the low-temperature modification of FeB. *Journal of Solid State Chemistry*, 41(2):195, 1982.
- [95] T Kanaizuka. Interpretation of Mossbauer-spectra of  $\beta$ -FeB and its low-temperature Modification,  $\alpha$ -FeB. *Physica Status Solidi A-Applied Research*, 69(2):739, 1982.
- [96] VB Nosov and SA Yurasov. Calculation of the hardenability of boron steels. *Metal Science and Heat Treatment*, 37(3-4):105, 1995.
- [97] AI Potapov, IT Malikov, VI Urazov, and AE Semin. Effect of the chemical composition and austenitizing conditions on the hardenability of 35GR steel. *Russian Metallurgy*, 2010:1164, 2010.
- [98] TG Digges, CR Irish, and NL Carwile. Effect of boron on the hardenability of high-purity alloys and commercial steels. *Journal of Research of the National Bureau of Standards*, 41(6):545, 1948.
- [99] RK Guseinov. Structure and properties of medium-carbon martempered steel microalloyed with boron. *Metal Science and Heat Treatment*, 36(9-10):544, 1994.
- [100] BA Miller. Steel hardenability and failure analysis. *Practical Failure Analysis*, 1(3):45, 2001.
- [101] WF Jandeska and JE Morral. Distribution of boron in austenite. *Metallurgical Transactions*, 3(11):2933, 1972.
- [102] WW Cias. Phase transformational kinetics and hardenability of low-carbon, boron-treated steels. *Metallurgical Transactions*, 4(2):603, 1973.
- [103] P Maitrepierre, D Thivellier, and R Tricot. Influence of boron on decomposition of austenite in low-carbon alloyed steels. *Metallurgical Transactions A-Physical Metallurgy and Materials Science*, 6(2):287, 1975.
- [104] GF Melloy, PR Slimmon, and PP Podgursk. Optimizing boron effect. *Metallurgical Transactions*, 4(10):2279, 1973.
- [105] AA Azarkevich, LV Kovalenko, and VM Krasnopolskii. The optimum content of boron in steel. *Metal Science and Heat Treatment*, 37(1-2):22, 1995.
- [106] TI Titova, NA Shulgan, and IY Malykhina. Effect of boron microalloying on the structure and hardenability of building steel. *Metal Science and Heat Treatment*, 49(1-2):39, 2007.
- [107] L Lanier, G Metauer, and M Moukassi. Microprecipitation in boron-containing high-carbon steels. *Mikrochimica Acta*, 114:353, 1994.



- 
- [108] KA Taylor and SS Hansen. The boron hardenability effect in thermomechanically processed, direct-quenched 0.2 pct C steels. *Metallurgical Transactions A-Physical Metallurgy and Materials Science*, 21(6):1697, 1990.
- [109] ZW Zhang, CT Liu, S Guo, JL Cheng, G Chen, T Fujita, MW Chen, YW Chung, S Vaynman, ME Fine, and BA Chin. Boron effects on the ductility of a nano-cluster-strengthened ferritic steel. *Materials Science and Engineering A-Structural Materials Properties Microstructure and Processing*, 528(3):855, 2011.
- [110] SI Bulat, NA Sorokina, and EA Ulyanin. Effect of boron on ductility of austenitic Cr-Ni-Mn steel with nitrogen. *Metal Science and Heat Treatment*, 17(7-8):712, 1975.
- [111] SK Kim, JS Kim, and NJ Kim. Effect of boron on the hot ductility of Nb-containing steel. *Metallurgical and Materials Transactions A-Physical Metallurgy and Materials Science*, 33(3):701, 2002.
- [112] A Deva, BK Jha, and NS Mishra. Influence of boron on strain hardening behaviour and ductility of low carbon hot rolled steel. *Materials Science and Engineering A-Structural Materials Properties Microstructure and Processing*, 528(24):7375, 2011.
- [113] E Lopez-Chipres, I Mejia, C Maldonado, A Bedolla-Jacuinde, and JM Cabrera. Hot ductility behavior of boron microalloyed steels. *Materials Science and Engineering A-Structural Materials Properties Microstructure and Processing*, 460:464, 2007.
- [114] F Zarandi and S Yue. Effect of boron on the hot ductility of the Nb-microalloyed steel in austenite region. *Metallurgical and Materials Transactions A-Physical Metallurgy and Materials Science*, 37A(7):2316, 2006.
- [115] LH Chown and LA Cornish. Investigation of hot ductility in Al-killed boron steels. *Materials Science and Engineering A-Structural Materials Properties Microstructure and Processing*, 494(1-2):263, 2008.
- [116] LL Pyatakova, II Mints, TG Berezina, and MA Sirotkina. Structure and toughness of medium-carbon steel with boron. *Metal Science and Heat Treatment*, 18(1-2):47, 1976.
- [117] LL Pyatakova, MV Mozharov, MA Sirotkina, and TA Dyuzheva. Effect of boron on the cold brittleness of medium-carbon steel. *Metal Science and Heat Treatment*, 13:152, 1971.
- [118] PN Ernst, PJ Uggowitzer, and MO Speidel. Improved boron-containing 9-percent to 12-percent chromium steel with high creep-rupture strength. *Journal of Materials Science Letters*, 5(9):835, 1986.
- [119] P Hofer, MK Miller, SS Babu, SA David, and H Cerjak. Atom probe field ion microscopy investigation of boron containing martensitic 9 Pct chromium steel. *Metallurgical and Materials Transactions A-Physical Metallurgy and Materials Science*, 31(3A):975, 2000.

- [120] F Abe, T Horiuchi, M Taneike, and K Sawada. Stabilization of martensitic microstructure in advanced 9Cr steel during creep at high temperature. *Materials Science and Engineering A-Structural Materials Properties Microstructure and Processing*, 378(1-2):299, 2004.
- [121] F Abe. Behavior of boron in 9Cr heat resistant steel during heat treatment and creep deformation. In Nam, SW and Chang, YW and Lee, SB and Kim, NJ, editor, *Mechanical Behavior of Materials X, Pts 1 and 2*, volume 345-346 of *Key Engineering Materials*, page 569. Korean Inst Metals; Korean Soc Mech Engineers, 2007. 10th International Conference on Mechanical Behavior of Materials, Busan, South Korea, May 27-31, 2007.
- [122] F Abe. Precipitate design for creep strengthening of 9% Cr tempered martensitic steel for ultra-supercritical power plants. *Science and Technology of Advanced Materials*, 9(1):013002, 2008.
- [123] A Zielinska-Lipiec, Koziel T, and A Czyrska-Filemonowicz. Quantitative characterisation of the microstructure high chromium steel with boron for advanced steam power plants. *Journal of Achievements in Materials and Manufacturing Engineering*, 43(1):200, 2010.
- [124] F Abe, H Semba, and T Sakuraya. Effect of boron on microstructure and creep deformation behavior of tempered martensitic 9Cr steel. In Chandra, T and Tsuzaki, K and Militzer, M and Ravindran, C, editor, *THERMEC 2006, Pts 1-5*, volume 539-543 of *Materials Science Forum*, page 2982. Minerals, Met & Mat Soc, 2007. 5th International Conference on Processing and Manufacturing of Advanced Materials, Vancouver, Canada, Jul 04-08, 2006.
- [125] N Shinya and J Kyono. Effect of boron nitride precipitation at cavity surface on rupture properties. *Materials Transactions*, 47(9):2302, 2006.
- [126] N Shinya, J Kyono, and K Laha. Self-healing effect of boron nitride precipitation on creep cavitation in austenitic stainless steel. *Journal of Intelligent Material Systems and Structures*, 17(12):1127, 2006.
- [127] M Fujiwara, H Uchida, and S Ohta. Effect of boron and carbon on creep strength of cold-worked type 316 stainless-steel. *Journal of Materials Science Letters*, 13(8):557, 1994.
- [128] RV Nandedkar and W Kesternich. Influence of boron on creep and microstructural behavior of neutron-irradiated austenitic stainless-steels. *Journal of Nuclear Materials*, 155:1038, 1988.
- [129] RV Nandedkar and W Kesternich. Effect of boron on high-temperature creep-behavior of austenitic stainless-steel DIN-1.4970. *Metallurgical Transactions A-Physical Metallurgy and Materials Science*, 21(12):3033, 1990.
- [130] Y Kurata and Y Ogawa. Internal-stress during high-temperature creep of special grade Hastelloy-X alloys. *Journal of Nuclear Materials*, 158:42, 1988.

- [131] RL Plaut, C Herrera, DM Escriba, PR Rios, and AF Padilha. A Short review on wrought austenitic stainless steels at high temperatures: processing, microstructure, properties and performance. *Materials Research*, 10:453, 2007.
- [132] E Lunarska, J Stabryla, K Nikiforow, and L Starczewski. Boron alloying and laser treatment to improve corrosion and hydrogen resistance of 25G steel. *Materials Science*, 41(4):551, 2005.
- [133] C Menapace, A Molinari, J Kazior, and T Pieczonka. Surface self-densification in boron alloyed austenitic stainless steel and its effect on corrosion and impact resistance. *Powder Metallurgy*, 50(4):326, 2007.
- [134] F Hanguang, S Xuding, L Yongping, and X Jiandong. Effect of boron concentration on the corrosion resistance of cast B-bearing steel in molten zinc. *Materials and Corrosion-Werkstoffe und Korrosion*, 59(12):948, 2008.
- [135] M Sasaki, K Ohsasa, M Kudoh, and K Matsuura. Refinement of austenite grain in carbon steel by addition of titanium and boron. *ISIJ International*, 48(3):340, 2008.
- [136] MI Haq and N Ikram. The effect of boron addition on the tensile properties of control-rolled and normalized C-Mn steels. *Journal of Materials Science*, 28(22):5981, 1993.
- [137] E El-Kashif, K Asakura, T Koseki, and K Shibata. Effects of boron, niobium and titanium on grain growth in ultra high purity 18% Cr ferritic stainless steel. *ISIJ International*, 44(9):1568, 2004.
- [138] W Stumpf and K Banks. The hot working characteristics of a boron bearing and a conventional low carbon steel. *Materials Science and Engineering A-Structural Materials Properties Microstructure and Processing*, 418(1-2):86, 2006.
- [139] Mortimer, DA. Segregation of boron to grain boundaries in iron and a stainless steel. *Journal de Physique*, 36(C4):137, 1975.
- [140] A Chatterjee, JP Hirth, RG Hoagland, A Choudhury, and CL White. Auger analysis of hydrogen embrittled grain-boundaries in a boron containing AISI 1520 steel. *Scripta Metallurgica*, 21(1):79, 1987.
- [141] L Karlsson, H Norden, and H Odelius. Non-equilibrium grain-boundary segregation of boron in austenitic stainless-steel .1. Large-scale segregation behavior. *Acta Metallurgica*, 36(1):1, 1988.
- [142] S Kawasaki, A Hishinum, and R Nagasaki. Behaviour of boron in stainless steel detected by fission track etching method and effect of radiation on tensile properties. *Journal of Nuclear Materials*, 39(2):166, 1971.
- [143] DJ Mun, EJ Shin, and YM Koo. A study on the behavior of boron distribution in low carbon steel by particle tracking autoradiography. *Nuclear Engineering and Technology*, 43(1):1, 2011.

- [144] M Jahazi and JJ Jonas. The non-equilibrium segregation of boron on original and moving austenite grain boundaries. *Materials Science and Engineering A-Structural Materials Properties Microstructure and Processing*, 335(1-2):49, 2002.
- [145] L Karlsson and H Norden. Non-equilibrium grain-boundary segregation of boron in austenitic stainless-steel .2. Fine scale segregation behavior. *Acta Metallurgica*, 36(1):13, 1988.
- [146] K Laha, J Kyono, T Sasaki, S Kishimoto, and N Shinya. Improved creep strength and creep ductility of type 347 austenitic stainless steel through the self-healing effect of boron for creep cavitation. *Metallurgical and Materials Transactions A-Physical Metallurgy and Materials Science*, 36A(2):399, 2005.
- [147] RQ Wu, AJ Freeman, and GB Olson. First principles determination of the effects of phosphorus and boron on iron grain-boundary cohesion. *Science*, 265(5170):376, 1994.
- [148] SP Tang, AJ Freeman, and GB Olson. Local-density studies of the structure and electronic-properties of B and S in an Fe grain-boundary. *Physical Review B*, 50(1):1, 1994.
- [149] P Rez and JR Alvarez. Calculation of cohesion and changes in electronic structure due to impurity segregation at boundaries in iron. *Acta Materialia*, 47(15-16):4069, 1999.
- [150] ZZ Chen and CY Wang. First-principles study on the effects of co-segregation of Ti, B and O on the cohesion of the  $\alpha$ -Fe grain boundary. *Journal of Physics-Condensed Matter*, 17(42):6645, 2005.
- [151] JS Braithwaite and P Rez. Grain boundary impurities in iron. *Acta Materialia*, 53(9):2715, 2005.
- [152] E Wachowicz and A Kiejna. Effect of impurities on grain boundary cohesion in bcc iron. *Computational Materials Science*, 43(4):736, 2008.
- [153] M Yamaguchi. First-principles study on the grain boundary embrittlement of metals by solute segregation: Part I. Iron (Fe)-solute (B, C, P, and S) systems. *Metallurgical and Materials Transactions A-Physical Metallurgy and Materials Science*, 42A(2):319, 2011.
- [154] E Wachowicz and A Kiejna. Effect of impurities on structural, cohesive and magnetic properties of grain boundaries in  $\alpha$ -Fe. *Modelling and Simulation in Materials Science and Engineering*, 19(2):025001, 2011.
- [155] DHR Fors and G Wahnström. Nature of boron solution and diffusion in  $\alpha$ -iron. *Physical Review B*, 77(13):132102, 2008.
- [156] SS Baik, BI Min, SK Kwon, and YM Koo. Boron solution and distribution in  $\alpha$ -Fe: application to boron steel. *Physical Review B*, 81(14):144101, 2010.
- [157] P Villars. Stability diagrams for binary-systems. *Journal of the Less-Common Metals*, 110:11, 1985.

- [158] JC Phillips and JA Van Vecht. Dielectric classification of crystal structures ionization potentials and band structures. *Physical Review Letters*, 22:705, 1969.
- [159] P Villars. A 3-dimensional structural stability diagram for 998 binary AB intermetallic compounds. *Journal of the Less-Common Metals*, 92:215, 1983.
- [160] P Villars. A 3-dimensional structural stability diagram for 1011 binary AB<sub>2</sub> intermetallic compounds. *Journal of the Less-Common Metals*, 99:33, 1984.
- [161] P Villars. 3-dimensional structural stability diagrams for 648 binary AB<sub>3</sub> and 389 binary A<sub>3</sub>B<sub>5</sub> intermetallic compounds. *Journal of the Less-Common Metals*, 102:199, 1984.
- [162] J St. John and AN Bloch. Quantum-defect electronegativity scale for nontransition elements. *Physical Review Letters*, 33:1095, 1974.
- [163] A Zunger. Systematization of the stable crystal-structure of all AB-type binary compounds - A pseudopotential orbital-radii approach. *Physical Review B*, 22:5839, 1980.
- [164] W Gordy and WJO Thomas. Electronegativities of the elements. *Journal of Chemical Physics*, 24(2):439, 1956.
- [165] AI Martynov and SS Batsanov. New approach to electronegativity determination of atoms. *Zhurnal Neorganicheskoi Khimii*, 25(12):3171, 1980.
- [166] RE Watson and LH Bennett. Transition-metals - d-band hybridization, electronegativities and structural stability of intermetallic compounds. *Physical Review B*, 18:6439, 1978.
- [167] E Mooser and WB Pearson. On the crystal chemistry of normal valence compounds. *Acta Crystallographica*, 12:1015, 1959.
- [168] ES Machlin and B Loh. Structural stability of transition-metal binary compounds. *Physical Review Letters*, 45:1642, 1980.
- [169] JK Burdett. Electronic influences on the crystal-chemistry of transition metal-main group MX and MX<sub>2</sub> compounds. *Journal of Solid State Chemistry*, 45:399, 1982.
- [170] X Zhang and A Zunger. Diagrammatic separation of different crystal structures of A<sub>2</sub>BX<sub>4</sub> compounds without energy minimization: a pseudopotential orbital radii approach. *Advanced Functional Materials*, 20:1944, 2010.
- [171] L Guénée and K Yvon. Structure stability maps for intermetallic AB<sub>5</sub> compounds. *Journal of Alloys and Compounds*, 356:114, 2003.
- [172] B Seiser, R Drautz, and DG Pettifor. TCP phase predictions in Ni-based superalloys: Structure maps revisited. *Acta Materialia*, 59(2):749, 2011.
- [173] DG Pettifor. A chemical-scale for crystal-structure maps. *Solid State Communications*, 51:31, 1984.
- [174] DG Pettifor. Phenomenological and microscopic theories of structural stability. *Journal of the Less-Common Metals*, 114:7, 1985.

- [175] DG Pettifor. The structures of binary compounds .1. Phenomenological structure maps. *Journal of Physics C - Solid State Physics*, 19:285, 1986.
- [176] DG Pettifor. Structure maps for pseudobinary and ternary phases. *Materials Science and Technology*, 4:675, 1988.
- [177] DG Pettifor. Structure maps in alloy design. *Journal of the Chemical Society - Faraday Transactions*, 86:1209, 1990.
- [178] P Villars and K Cenzual. Pearson's Crystal Data: Crystal Structure Database for Inorganic Compounds (on CD-ROM). ASM International®, Materials Park, Ohio, USA, Release 2012/13.
- [179] DG Pettifor and R Podlucky. Microscopic theory of the structural stability of pd-bonded AB compounds. *Physical Review Letters*, 53:1080, 1984.
- [180] DG Pettifor and R Podlucky. The structures of binary compounds .2. Theory of the pd-bonded AB-compounds. *Journal of Physics C - Solid State Physics*, 19:315, 1986.
- [181] T Lundström. Structure, defects and properties of some refractory borides. *Pure and Applied Chemistry*, 57:1383, 1985.
- [182] K Girgis and P Villars. Description of Structures in Terms of Polyhedrapacking. *Monatshefte für Chemie*, 116:417, 1985.
- [183] FC Frank and JS Kasper. Complex alloy structures regarded as sphere packing .1. Definitions and basic principles. *Acta Crystallographica*, 11:184, 1958.
- [184] FC Frank and JS Kasper. Complex alloy structures regarded as sphere packing .2. Analysis and classification of representative structures. *Acta Crystallographica*, 12:483, 1959.
- [185] P Villars and F Hulliger. Structural stability domains for single-coordination intermetallic phases. *Journal of the Less-Common Metals*, 132:289, 1987.
- [186] GO Brunner and D Schwarzenbach. Limitation of coordination sphere and determination of coordination coefficient in crystal structures. *Zeitschrift für Kristallographie, Kristallgeometrie, Kristallphysik, Kristallchemie*, 133:127, 1971.
- [187] JLC Daams, JHN Van Vucht, and P Villars. Atomic-environment classification of the cubic intermetallic structure types. *Journal of Alloys and Compounds*, 182:1, 1992.
- [188] JLC Daams and P Villars. Atomic environment classification of the rhombohedral intermetallic structure types. *Journal of Alloys and Compounds*, 197:243, 1993.
- [189] JLC Daams and P Villars. Atomic-environment classification of the hexagonal intermetallic structure types. *Journal of Alloys and Compounds*, 215:1, 1994.
- [190] JLC Daams and P Villars. Atomic environment classification of the tetragonal intermetallic structure types. *Journal of Alloys and Compounds*, 252:110, 1997.

- [191] P Villars and JLC Daams. Atomic-environment classification of the chemical-elements. *Journal of Alloys and Compounds*, 197:177, 1993.
- [192] P Villars, K Cenzual, J Daams, Y Chen, and S Iwata. Data-driven atomic environment prediction for binaries using the Mendeleev number - Part 1. Composition AB. *Journal of Alloys and Compounds*, 367:167, 2004.
- [193] <http://www1.asminternational.org/asmenterprise/apd>, accessed May 16th, 2012.
- [194] VG Kuznetsov, MA Sokolova, KK Palkina, and ZV Popova. The Cobalt-Sulfur system. *Inorganic Materials*, 1:617, 1965.
- [195] KL Komarek and K Wessely. Transition metal-chalcogen systems .1. System Cobalt-Selenium. *Monatshefte für Chemie*, 103(3):896, 1972.
- [196] KO Klepp and KL Komarek. Transition metal-chalcogene systems .3. System Ni-Te. *Monatshefte für Chemie*, 103(4):934, 1972.
- [197] J Hu, C Li, F Wang, and W Zhang. Thermodynamic re-assessment of the V-C system. *Journal of Alloys and Compounds*, 421(1-2):120, 2006.
- [198] H Okamoto. C-Ti (Carbon-Titanium). *Journal of Phase Equilibria*, 19(1):89, 1998.
- [199] <http://www.bopfox.de>.
- [200] T Hammerschmidt, B Seiser, ME Ford, DG Pettifor, and R Drautz. To be published.
- [201] T Schablitzki, J Rogal, and R Drautz. In preparation.
- [202] GF Voronoi. Nouvelles applications des paramètre à la théorie des formes quadratiques. Deuxième mémoire. Recherches sur les paralléloèdres primitifs. *Journal für die reine und angewandte Mathematik*, 134:198, 1908.
- [203] CB Barber, DP Dobkin, and H Huhdanpaa. The Quickhull algorithm for convex hulls. *ACM Transactions on Mathematical Software*, 22(4):469, 1996.
- [204] D Hohnke and E Parthe. AB compounds with Sc, Y and rare earth metals .2. FeB and CrB type structures of monosilicides and germanides. *Acta Crystallographica*, 20(4):572, 1966.
- [205] E Schrödinger. Quantisierung als Eigenwertproblem. *Annalen der Physik*, 384:361, 1926.
- [206] DR Hartree. The wave mechanics of an atom with a non-coulomb central field. Part I. Theory and methods. *Mathematical Proceedings of the Cambridge Philosophical Society*, 24(1):89, 1928.
- [207] V Fock. Näherungsmethode zur Lösung des quantenmechanischen Mehrkörperproblems. *Zeitschrift für Physik A Hadrons and Nuclei*, 61(1):126, 1930.
- [208] JC Slater. Note on Hartree's method. *Physical Review*, 35:210, 1930.
- [209] LH Thomas. The calculation of atomic fields. *Proceedings of the Cambridge Philosophical Society*, 23:542, 1927.

- [210] E Fermi. Eine statistische Methode zur Bestimmung einiger Eigenschaften des Atoms und ihre Anwendung auf die Theorie des periodischen Systems der Elemente. *Zeitschrift für Physik A Hadrons and Nuclei*, 48:73, 1928.
- [211] P Hohenberg and W Kohn. Inhomogeneous electron gas. *Physical Review*, 136(3B):864, 1964.
- [212] W Kohn and LJ Sham. Self-consistent equations including exchange and correlation effects. *Physical Review*, 140(4A):1133, 1965.
- [213] M Born and R Oppenheimer. Zur Quantentheorie der Molekülen. *Annalen der Physik*, 389(20):457, 1927.
- [214] PAM Dirac. Note on exchange phenomena in the Thomas atom. *Proceedings of the Cambridge Philosophical Society*, 26:376, 1930.
- [215] JC Slater. A simplification of the Hartree-Fock method. *Physical Review*, 81:385, 1951.
- [216] E Wigner. Effects of the electron interaction on the energy levels of electrons in metals. *Transactions of the Faraday Society*, 34:678, 1938.
- [217] DM Ceperley and BJ Alder. Ground-state of the electron-gas by a stochastic method. *Physical Review Letters*, 45(7):566, 1980.
- [218] AD Becke. Density-functional exchange-energy approximation with correct asymptotic-behavior. *Physical Review A*, 38(6):3098, 1988.
- [219] JP Perdew, JA Chevary, SH Vosko, KA Jackson, MR Pederson, DJ Singh, and C Fiolhais. Atoms, molecules, solids, and surfaces - applications of the generalized gradient approximation for exchange and correlation. *Physical Review B*, 46(11):6671, 1992.
- [220] JP Perdew, K Burke, and M Ernzerhof. Generalized gradient approximation made simple. *Physical Review Letters*, 77(18):3865, 1996.
- [221] JP Perdew, A Ruzsinszky, GI Csonka, OA Vydrov, GE Scuseria, LA Constantin, X Zhou, and K Burke. Restoring the density-gradient expansion for exchange in solids and surfaces. *Physical Review Letters*, 100(13):136406, 2008.
- [222] CT Lee, WT Yang, and RG Parr. Development of the Colle-Salvetti correlation-energy formula into a functional of the electron-density. *Physical Review B*, 37(2):785, 1988.
- [223] JC Slater. Atomic shielding constants. *Physical Review*, 36:57, 1930.
- [224] JC Slater. Analytic atomic wave functions. *Physical Review*, 42:33, 1932.
- [225] SF Boys. Electronic wave functions. I. A general method of calculation for the stationary states of any molecular system. *Royal Society of London Proceedings Series A*, 200:542, 1950.
- [226] F Bloch. Über die Quantenmechanik der Elektronen in Kristallgittern. *Zeitschrift für Physik*, 52:555, 1929.



- 
- [227] MC Payne, MP Teter, DC Allan, TA Arias, and JD Joannopoulos. Iterative minimization techniques for ab-initio total-energy calculations - Molecular-dynamics and conjugate gradients. *Reviews of Modern Physics*, 64(4):1045, 1992.
- [228] JC Phillips and L Kleinman. New method for calculating wave functions in crystals and molecules. *Physical Review*, 116(2):287, 1959.
- [229] C Herring. A new method for calculating wave functions in crystals. *Physical Review*, 57:1169, 1940.
- [230] DR Hamann, M Schluter, and C Chiang. Norm-conserving pseudopotentials. *Physical Review Letters*, 43(20):1494, 1979.
- [231] DR Hamann. Generalized norm-conserving pseudopotentials. *Physical Review B*, 40(5):2980, 1989.
- [232] D Vanderbilt. Soft self-consistent pseudopotentials in a generalized eigenvalue formalism. *Physical Review B*, 41(11):7892, 1990.
- [233] PE Blöchl. Projector augmented-wave method. *Physical Review B*, 50(24):17953, 1994.
- [234] T Ziegler. Approximate density functional theory as a practical tool in molecular energetics and dynamics. *Chemical Reviews*, 91(5):651, 1991.
- [235] KA Johnson and NW Ashcroft. Corrections to density-functional theory band gaps. *Physical Review B*, 58(23):15548, 1998.
- [236] IN Yakovkin and PA Dowben. The problem of the band gap in LDA calculations. *Surface Review and Letters*, 14(3):481, 2007.
- [237] L Hedin. New method for calculating 1-particle Green's function with application to electron-gas problem. *Physical Review*, 139(3A):796, 1965.
- [238] E Runge and EKU Gross. Density-functional theory for time-dependent systems. *Physical Review Letters*, 52(12):997, 1984.
- [239] U von Barth. Basic density-functional theory - An overview. *Physica Scripta*, 109:9, 2004.
- [240] RO Jones and O Gunnarsson. The density functional formalism, its applications and prospects. *Reviews of Modern Physics*, 61(3):689, 1989.
- [241] L Vocadlo, GA de Wijs, G Kresse, M Gillan, and GD Price. First principles calculations on crystalline and liquid iron at Earth's core conditions. *Faraday Discussions*, 106:205, 1997.
- [242] W Kohn. Nobel Lecture: Electronic structure of matter-wave functions and density functionals. *Reviews of Modern Physics*, 71(5):1253, 1999.
- [243] W Kohn, Y Meir, and DE Makarov. van der Waals energies in density functional theory. *Physical Review Letters*, 80(19):4153, 1998.

- [244] VI Anisimov, F Aryasetiawan, and AI Lichtenstein. First-principles calculations of the electronic structure and spectra of strongly correlated systems: The LDA+U method. *Journal of Physics-Condensed Matter*, 9(4):767, 1997.
- [245] G Kresse and D Joubert. From ultrasoft pseudopotentials to the projector augmented-wave method. *Physical Review B*, 59(3):1758, 1999.
- [246] G Kresse and J Hafner. Ab initio molecular dynamics for liquid metals. *Physical Review B*, 47(1):558, 1993.
- [247] G Kresse and J Hafner. Ab-initio molecular-dynamics simulation of the liquid-metal amorphous-semiconductor transition in germanium. *Physical Review B*, 49(20):14251, 1994.
- [248] G Kresse and J Furthmüller. Efficiency of ab-initio total energy calculations for metals and semiconductors using a plane-wave basis set. *Computational Materials Science*, 6(1):15, 1996.
- [249] G Kresse and J Furthmüller. Efficient iterative schemes for ab initio total-energy calculations using a plane-wave basis set. *Physical Review B*, 54(16):11169, 1996.
- [250] HJ Monkhorst and JD Pack. Special points for Brillouin-zone integrations. *Physical Review B*, 13(12):5188, 1976.
- [251] JD Pack and HJ Monkhorst. Special points for Brillouin-zone integrations - Reply. *Physical Review B*, 16(4):1748, 1977.
- [252] FD Murnaghan. The compressibility of media under extreme pressures. *Proceedings of the National Academy of Science*, 30:244, 1944.
- [253] RF Bunshah, R Nimmagadda, W Dunford, BA Movchan, AV Demchishin, and NA Chursanov. Structure and properties of refractory compounds deposited by electron-beam evaporation. *Thin Solid Films*, 54(1):85, 1978.
- [254] HO Pierson and E Randich. Titanium diboride coatings and their interaction with substrates. *Thin Solid Films*, 54(1):119, 1978.
- [255] E Randich and DD Allred. Chemically vapor-deposited  $ZrB_2$  as a selective solar-absorber. *Thin Solid Films*, 83(4):393, 1981.
- [256] HO Pierson and AW Mullendore. Thick boride coatings by chemical vapor-deposition. *Thin Solid Films*, 95(2):99, 1982.
- [257] JR Shappirio and JJ Finnegan. Synthesis and properties of some refractory transition-metal diboride thin-films. *Thin Solid Films*, 107(1):81, 1983.
- [258] C Mitterer. Borides in thin film technology. *Journal of Solid State Chemistry*, 133(1):279, 1997.
- [259] NB Dahotre, P Kadolkar, and S Shah. Refractory ceramic coatings: processes, systems and wettability/adhesion. *Surface and Interface Analysis*, 31(7):659, 2001.

- [260] S Jayaraman, EJ Klein, Y Yang, DY Kim, GS Girolami, and JR Abelson. Chromium diboride thin films by low temperature chemical vapor deposition. *Journal of Vacuum Science & Technology A*, 23(4):631, 2005.
- [261] Q Gu, G Krauss, and W Steurer. Transition metal borides: superhard versus ultra-incompressible. *Advanced Materials*, 20(19):3620, 2008.
- [262] AL Ivanovskii. Mechanical and electronic properties of diborides of transition 3d-5d metals from first principles: toward search of novel ultra-incompressible and superhard materials. *Progress in Materials Science*, 57(1):184, 2012.
- [263] HY Chung, MB Weinberger, JB Levine, A Kavner, JM Yang, SH Tolbert, and RB Kaner. Synthesis of ultra-incompressible superhard rhenium diboride at ambient pressure. *Science*, 316(5823):436, 2007.
- [264] RB Kaner, JJ Gilman, and SH Tolbert. Materials science - Designing superhard materials. *Science*, 308(5726):1268, 2005.
- [265] JJ Gilman, RW Cumberland, and RB Kaner. Design of hard crystals. *International Journal of Refractory Metals & Hard Materials*, 24(1-2):1, 2006.
- [266] JB Levine, SH Tolbert, and RB Kaner. Advancements in the search for superhard ultra-incompressible metal borides. *Advanced Functional Materials*, 19(22):3519, 2009.
- [267] S Watanabe and H Ohtani. Precipitation behavior of boron in high-strength steel. *Transactions of the Iron and Steel Institute of Japan*, 23(1):38, 1983.
- [268] S Watanabe, H Ohtani, and T Kunitake. The influence of dissolution and precipitation behavior of  $M_{23}(C,B)_6$  on the hardenability of boron steels. *Transactions of the Iron and Steel Institute of Japan*, 23(2):120, 1983.
- [269] M Palumbo, G Cacciamani, E Bosco, and M Baricco. Thermodynamic analysis of glass formation in Fe-B system. *CALPHAD-Computer Coupling of Phase Diagrams and Thermochemistry*, 25(4):625, 2001.
- [270] T van Rompaey, KCH Kumar, and P Wollants. Thermodynamic optimization of the B-Fe system. *Journal of Alloys and Compounds*, 334:173, 2002.
- [271] PK Liao and KE Spear. *Phase Diagrams Of Binary Iron Alloys*. ASM Int., Metals Park, OH, USA, 1993.
- [272] B Hallemans, P Wollants, and JR Roos. Thermodynamic reassessment and calculation of the Fe-B phase-diagram. *Zeitschrift für Metallkunde*, 85(10):676, 1994.
- [273] C Kapfenberger, B Albert, R Poettgen, and H Huppertz. Structure refinements of iron borides  $Fe_2B$  and  $FeB$ . *Zeitschrift für Kristallographie*, 221(5-7):477, 2006.
- [274] KHJ Buschow, PG Vanengen, and R Jongebreur. Magneto-optical properties of metallic ferromagnetic materials. *Journal of Magnetism and Magnetic Materials*, 38(1):1, 1983.

- [275] T Nakamura, H Koshiba, M Imafuku, A Inoue, and E Matsubara. Determination of atomic sites of Nb dissolved in metastable  $\text{Fe}_{23}\text{B}_6$  phase. *Materials Transactions*, 43(8):1918, 2002.
- [276] YD Zhang, JI Budnick, FH Sanchez, WA Hines, DP Yang, and JD Livingston. NMR-studies in orthorhombic  $\text{Fe}_3\text{B}_{1-x}\text{C}_x$  ( $0.1 \leq x \leq 0.4$ ). *Journal of Applied Physics*, 61(8):4358, 1987.
- [277] Y Khan, E Kneller, and M Sostarich. The phase  $\text{Fe}_3\text{B}$ . *Zeitschrift für Metallkunde*, 73(10):624, 1982.
- [278] P Mohn and DG Pettifor. The calculated electronic and structural-properties of the transition-metal monoborides. *Journal of Physics C-Solid State Physics*, 21(15):2829, 1988.
- [279] P Mohn. The calculated electronic and magnetic-properties of the tetragonal transition-metal semi-borides. *Journal of Physics C-Solid State Physics*, 21(15):2841, 1988.
- [280] WY Ching, YN Xu, BN Harmon, J Ye, and TC Leung. Electronic-structures of  $\text{FeB}$ ,  $\text{Fe}_2\text{B}$ , and  $\text{Fe}_3\text{B}$  compounds studied using 1st-principles spin-polarized calculations. *Physical Review B*, 42(7b):4460, 1990.
- [281] Y Kong and FS Li. Cohesive energy, local magnetic properties, and Curie temperature of  $\text{Fe}_3\text{B}$  studied using the self-consistent LMTO method. *Physical Review B*, 56(6):3153, 1997.
- [282] B Xiao, JD Xing, SF Ding, and W Su. Stability, electronic and mechanical properties of  $\text{Fe}_2\text{B}$ . *Physica B-Condensed Matter*, 403(10-11):1723, 2008.
- [283] B Xiao, JD Xing, J Feng, CT Zhou, YF Li, W Su, XJ Xie, and YH Cheng. A comparative study of  $\text{Cr}_7\text{C}_3$ ,  $\text{Fe}_3\text{C}$  and  $\text{Fe}_2\text{B}$  in cast iron both from ab initio calculations and experiments. *Journal of Physics D-Applied Physics*, 42(11):115415, 2009.
- [284] B Xiao, J Feng, CT Zhou, JD Xing, XJ Xie, YH Cheng, and R Zhou. The elasticity, bond hardness and thermodynamic properties of  $\text{X}_2\text{B}$  ( $\text{X}=\text{Cr, Mn, Fe, Co, Ni, Mo, W}$ ) investigated by DFT theory. *Physica B-Condensed Matter*, 405(5):1274, 2010.
- [285] D Tzeli and A Mavridis. Electronic structure and bonding of the 3d transition metal borides, MB,  $\text{M}=\text{Sc, Ti, V, Cr, Mn, Fe, Co, Ni, and Cu}$  through all electron ab initio calculations. *Journal of Chemical Physics*, 128(3):034309, 2008.
- [286] CT Zhou, JD Xing, B Xiao, J Feng, XJ Xie, and YH Chen. First principles study on the structural properties and electronic structure of  $\text{X}_2\text{B}$  ( $\text{X} = \text{Cr, Mn, Fe, Co, Ni, Mo and W}$ ) compounds. *Computational Materials Science*, 44(4):1056, 2009.
- [287] M Mihalkovic and M Widom. Ab initio calculations of cohesive energies of Fe-based glass-forming alloys. *Physical Review B*, 70(14):144107, 2004.

- [288] LG Voroshnin, LS Lyakhovich, GG Panich, and GF Protasevich. The structure of Fe-B alloys. *Metal Science and Heat Treatment [Metal. i Term. Obrabotka Metal.]*, 9:732, 1970.
- [289] L Topor and OJ Kleppa. Enthalpies of formation of 1st-row transition-metal diborides by a new calorimetric method. *Journal of Chemical Thermodynamics*, 17(11):1003, 1985.
- [290] AF Guillermet and G Grimvall. bonding properties and vibrational entropy of transition-metal  $\text{MeB}_2(\text{AlB}_2)$  diborides. *Journal of the Less-Common Metals*, 169(2):257, 1991.
- [291] JK Burdett, E Canadell, and GJ Miller. Electronic-structure of transition-metal borides with the  $\text{AlB}_2$  structure. *Journal of the American Chemical Society*, 108(21):6561, 1986.
- [292] H Okamoto. B-Mn (Boron-Manganese). *Journal of Phase Equilibria*, 14:121, 1993.
- [293] P Duhaj and F Hanic. Metastable  $\text{Fe}_4\text{B}$  phase in amorphous Fe-B alloys. *Physica Status Solidi A-Applied Research*, 62(2):719, 1980.
- [294] P Duhaj and F Hanic. Electron-microscopy and electron-diffraction study of crystallization of metastable phases in amorphous Fe-B alloys. *Physica Status Solidi A-Applied Research*, 76(2):467, 1983.
- [295] KI Portnoi, Levinskaya MKh, and VM Romashov. Constitution diagram of the system iron-boron. *Soviet Powder Metallurgy and Metal Ceramic [Poroshk, Metall.]*, 8:657, 1969.
- [296] VA Barinov, GA Dorofeev, LV Ovechkin, EP Elsukov, and AE Ermakov. Structure and magnetic-properties of the  $\alpha$ -FeB phase obtained by mechanical working. *Physica Status Solidi A-Applied Research*, 123(2):527, 1991.
- [297] K Balani, A Agarwal, and NB Dahotre. Molecular modeling of metastable  $\text{FeB}_{49}$  phase evolution in laser surface engineered coating. *Journal of Applied Physics*, 99(4):044904, 2006.
- [298] JL Hoard, DB Sullenger, CHL Kennard, and RE Hughes. The structure analysis of  $\beta$ -rhombohedral boron. *Journal of Solid State Chemistry*, 1:268, 1970.
- [299] DLVK Prasad, MM Balakrishnarajan, and ED Jemmis. Electronic structure and bonding of  $\beta$ -rhombohedral boron using cluster fragment approach. *Physical Review B*, 72(19):195102, 2005.
- [300] A Masago, K Shirai, and H Katayama-Yoshida. Crystal stability of  $\alpha$ - and  $\beta$ -boron. *Physical Review B*, 73(10):104102, 2006.
- [301] S Shang, Y Wang, R Arroyave, and ZK Liu. Phase stability in  $\alpha$ - and  $\beta$ -rhombohedral boron. *Physical Review B*, 75(9):092101, 2007.
- [302] M Widom and M Mihalkovic. Symmetry-broken crystal structure of elemental boron at low temperature. *Physical Review B*, 77(6):064113, 2008.

- [303] MJ van Setten, VA Popa, GA de Wijs, and G Brocks. Electronic structure and optical properties of lightweight metal hydrides. *Physical Review B*, 75(3):035204, 2007.
- [304] <http://cst-www.nrl.navy.mil/lattice>, accessed April 30th, 2009.
- [305] JP Perdew and A Zunger. Self-interaction correction to density-functional approximations for many-electron systems. *Physical Review B*, 23(10):5048, 1981.
- [306] AN Kolmogorov, S Shah, ER Margine, AF Bialon, T Hammerschmidt, and R Drautz. New superconducting and semiconducting Fe-B compounds predicted with an ab initio evolutionary search. *Physical Review Letters*, 105(21):217003, 2010.
- [307] <http://maise-guide.org>, accessed November 19th, 2010.
- [308] OS Gorelkin, NA Chirkov, OD Kolesnik, and AS Dubrovin. Measurement of heat of formation of intermetallic compounds by sintering method in an isothermal calorimeter. *Russian Journal of Physical Chemistry, USSR*, 46(3):431, 1972.
- [309] S Sato and OJ Kleppa. Enthalpies of formation of borides of iron, cobalt, and nickel by solution calorimetry in liquid copper. *Metallurgical Transactions B-Process Metallurgy*, 13(2):251, 1982.
- [310] H Okamoto. B-Cr (Boron-Chromium). *Journal of Phase Equilibria*, 24(5):480, 2003.
- [311] HY Niu, JQ Wang, XQ Chen, DZ Li, YY Li, P Lazar, R Podloucky, and AN Kolmogorov. Structure, bonding, and possible superhardness of CrB<sub>4</sub>. *Physical Review B*, 85(14):144116, 2012.
- [312] M Carbucicchio, C Grazzi, G Palombarini, M Rateo, and G Sambogna. On the phase transformations in Cr-FeB and Fe-CrB systems at high temperature. *Hyperfine Interactions*, 139(1-4):393, 2002.
- [313] M Carbucicchio, G Palombarini, M Rateo, and G Sambogna. High temperature solid state reactivity between iron and chromium monoborides. *Hyperfine Interactions*, 116(1-4):143, 1998.
- [314] BE Brown and DJ Beerntsen. Refinement of iron chromium boride with Mn<sub>4</sub>B structure. *Acta Crystallographica*, 17(4):448, 1964.
- [315] S Andersson and JO Carlsson. Crystal structure of MnB<sub>4</sub>. *Acta Chemica Scandinavica*, 24(5):1791, 1970.
- [316] Z Liu, X Han, D Yu, Y Sun, B Xu, XF Zhou, J He, HT Wang, and Y Tian. Formation, structure, and electric property of CaB<sub>4</sub> single crystal synthesized under high pressure. *Applied Physics Letters*, 96(3):031903, 2010.
- [317] XD Zhao, XY Liu, F Lin, WN Liu, and WH Su. New route for the synthesis of boron-rich rare-earth boride NdB<sub>6</sub> under high pressure and high temperature. *Journal of Alloys and Compounds*, 249(1-2):247, 1997.

- [318] B Yao, WH Su, FS Li, BZ Ding, and ZQ Hu. Phase transition from  $\text{Fe}_3\text{B}$  to  $\text{Fe}_2\text{B}$  under high pressure. *Journal of Materials Science Letters*, 16(24):1991, 1997.
- [319] AF Bialon, T Hammerschmidt, R Drautz, S Shah, R Margine, and AN Kolmogorov. Possible routes for synthesis of new boron-rich Fe-B and  $\text{Fe}_{1-x}\text{Cr}_x\text{B}_4$  compounds. *Applied Physics Letters*, 98(8):081901, 2011.
- [320] DM Teter. Computational alchemy: The search for new superhard materials. *MRS Bulletin*, 23(1):22, 1998.
- [321] JM Leger, P Djemia, F Ganot, J Haines, AS Pereira, and JAH da Jornada. Hardness and elasticity in cubic ruthenium dioxide. *Applied Physics Letters*, 79(14):2169, 2001.
- [322] VV Brazhkin, AG Lyapin, and RJ Hemley. Harder than diamond: dreams and reality. *Philosophical Magazine A-Physics of Condensed Matter Structure Defects and Mechanical Properties*, 82(2):231, 2002.
- [323] P Lazar and R Podloucky. Cleavage fracture of a crystal: density functional theory calculations based on a model which includes structural relaxations. *Physical Review B*, 78(10):104114, 2008.
- [324] A Simunek and J Vackar. Hardness of covalent and ionic crystals: first-principle calculations. *Physical Review Letters*, 96(8):085501, 2006.
- [325] A Simunek. How to estimate hardness of crystals on a pocket calculator. *Physical Review B*, 75(17):172108, 2007.
- [326] A Simunek. Anisotropy of hardness from first principles: the cases of  $\text{ReB}_2$  and  $\text{OsB}_2$ . *Physical Review B*, 80(6):060103, 2009.
- [327] R Hill. The elastic behaviour of a crystalline aggregate. *Proceedings of the Physical Society of London Section A*, 65(389):349, 1952.
- [328] JJ Wang, FY Meng, XQ Ma, MX Xu, and LQ Chen. Lattice, elastic, polarization, and electrostrictive properties of  $\text{BaTiO}_3$  from first-principles. *Journal of Applied Physics*, 108(3):034107, 2010.
- [329] B Chen, D Penwell, JH Nguyen, and MB Kruger. High pressure X-ray diffraction study of  $\text{Fe}_2\text{B}$ . *Solid State Communications*, 129(9):573, 2004.
- [330] D Golanski, A Marczuk, and T Wierzchon. Numerical modeling of the residual-stresses in borided layers on steel substrate. *Journal of Materials Science Letters*, 14(21):1499, 1995.
- [331] LS Lyakhovich, LN Kosachevskii, AY Kulik, VV Surkov, and YV Turov. Possibility of predetermining the distribution of residual stresses in borided steels. *Soviet materials science : a translation of Fiziko-khimicheskaya mekhanika materialov / Academy of Sciences of the Ukrainian SSR*, 9:272, 1975.
- [332] I Ozbek and C Bindal. Mechanical properties of boronized AISI W4 steel. *Surface & Coatings Technology*, 154(1):14, 2002.

- [333] YA Kunitskii and ÉV Marek. Some physical properties of iron borides. *Soviet Powder Metallurgy and Metal Ceramics*, 10:216, 1971.
- [334] W Zhou, H Wu, and T Yildirim. Electronic, dynamical, and thermal properties of ultra-incompressible superhard rhenium diboride: A combined first-principles and neutron scattering study. *Physical Review B*, 76(18):184113, 2007.
- [335] RF Zhang, S Veprek, and AS Argon. Mechanical and electronic properties of hard rhenium diboride of low elastic compressibility studied by first-principles calculation. *Applied Physics Letters*, 91(20):201914, 2007.
- [336] E Zhao, J Wang, J Meng, and Z Wu. Phase stability and mechanical properties of rhenium borides by first-principles calculations. *Journal of Computational Chemistry*, 31(9):1904, 2010.
- [337] HY Chung, MB Weinberger, JM Yang, SH Tolbert, and RB Kaner. Correlation between hardness and elastic moduli of the ultraincompressible transition metal diborides RuB<sub>2</sub>, OsB<sub>2</sub>, and ReB<sub>2</sub>. *Applied Physics Letters*, 92(26):261904, 2008.
- [338] OS Bobkova and TV Svistunova. Impact of boron on melt properties and structurization of iron and nickel-based steels and alloys. *Metallurgist*, 52(3-4):175, 2008.
- [339] M Djahazi, XL He, JJ Jonas, and WP Sun. Nb(C,N) precipitation and austenite recrystallization in boron-containing high-strength low-alloy steels. *Metallurgical Transactions A-Physical Metallurgy and Materials Science*, 23(8):2111, 1992.
- [340] P Cizek, BA Parker, M Bijok, and P Zuna. The influence of large boride particles on microstructural evolution in AISI-304 steel. *ISIJ International*, 34(8):679, 1994.
- [341] IB Timokhina, AI Nosenkov, AO Humphreys, JJ Jonas, and EV Pereloma. Effect of alloying elements on the microstructure and texture of warm rolled steels. *ISIJ International*, 44(4):717, 2004.
- [342] XL He and YY Chu. The application of the B-10(n, $\alpha$ ) Li-7 fission reaction to study boron behavior in materials. *Journal of Physics D-Applied Physics*, 16(6):1145, 1983.
- [343] L Karlsson and H Norden. Non-equilibrium grain-boundary segregation of boron in austenitic stainless-steel .4. Precipitation behavior and distribution of elements at grain-boundaries. *Acta Metallurgica*, 36(1):35, 1988.
- [344] N Valle, J Drillet, A Pic, and H-N Migeon. Nano-SIMS investigation of boron distribution in steels. *Surface and Interface Analysis*, 43(1-2):573, 2011.
- [345] AF Padilha and G Schanz. Precipitation of a boride phase in 15-%-Cr-15-%-Ni-Mo-Ti-B austenitic stainless-steel (DIN 1.4970). *Journal of Nuclear Materials*, 95(3):229, 1980.
- [346] JF Mansfield. Identification of boron in M<sub>23</sub>X<sub>6</sub> precipitates in 316-stainless steel using electron-energy loss spectroscopy. *Journal of Materials Science*, 22(4):1277, 1987.



- 
- [347] SH Zhang, XL He, YY Chu, and T Ko. Nonequilibrium segregation of solute to grain-boundary .1. Boron segregation in Fe-3%-Si during cooling. *Journal of Materials Science*, 29(10):2633, 1994.
- [348] RB Jones, CM Younes, PJ Heard, RK Wild, and PEJ Flewitt. The effect of the microscale distribution of boron on the yield strength of C-Mn steels subjected to neutron irradiation. *Acta Materialia*, 50(17):4395, 2002.
- [349] RK Wild, PJ Heard, and PEJ Flewitt. Distribution of boron within the microstructure of a ferritic steel determined using secondary ion mass spectrometry. *Philosophical Magazine*, 86(9):1277, 2006.
- [350] BS Seong, YR Cho, EJ Shin, SI Kim, S-H Choi, HR Kim, and YJ Kim. Study of the effect of nano-sized precipitates on the mechanical properties of boron-added low-carbon steels by neutron scattering techniques. *Journal of Applied Crystallography*, 41(5):906, 2008.
- [351] N Wolanska and AK Lis. The deformation analysis of 1008 steel at 0.01/s strain rate. *Journal of Achievements in Materials and Manufacturing Engineering*, 25(1):37, 2007.
- [352] N Wolanska, AK Lis, and J Lis. Investigation of C-Mn-B steel after hot deformation. *Archives of Materials Science and Engineering*, 28(2):119, 2007.
- [353] A Deva, SK De, and BK Jha. Strain hardening behavior and cold reducibility of boron-added low-carbon steel. *Journal of Materials Engineering and Performance*, 18(1):109, 2009.
- [354] YD Litinskii, GA Burakova, NS Kolchenko, NN Nesterova, and PG Budnik. Effect of boron on the structure and ductility of steel 01KH25 after vacuum heat-treatment. *Metal Science and Heat Treatment*, 22(5-6):426, 1980.
- [355] PL Li, EP George, and DP Pope. The effects of boron on the high-temperature ductility of iron and steel. *Scripta Metallurgica*, 20(12):1785, 1986.
- [356] XP Shen and R Priestner. Effect of boron on the microstructure and tensile properties of dual-phase steel. *Metallurgical Transactions A-Physical Metallurgy and Materials Science*, 21(9):2547, 1990.
- [357] N Okubo, E Wakai, S Matsukawa, K Furuya, H Tanigawa, and S Jitsukawa. Heat treatment effects on microstructures and DBTT of F82H steel doped with boron and nitrogen. *Materials Transactions*, 46(2):193, 2005.
- [358] D Isheim, RP Kolli, ME Fine, and DN Seidman. An atom-probe tomographic study of the temporal evolution of the nanostructure of Fe-Cu based high-strength low-carbon steels. *Scripta Materialia*, 55(1):35, 2006.
- [359] PE Busby and C Wells. Diffusion of boron in  $\alpha$ -iron. *Journal of Metals*, 6(9):972, 1954.
- [360] PM Strocchi, BA Melandri, and A Tamba. On nature of boron solid solution in  $\alpha$ -iron. *Nuovo Cimento B*, 51(1):1, 1967.

- [361] R Ray and R Hasegawa. Rapidly quenched metastable iron-boron solid-solutions. *Solid State Communications*, 27(4):471, 1978.
- [362] WR Thomas and GM Leak. Condition of boron in  $\alpha$ -iron. *Nature*, 176(4470):29, 1955.
- [363] WD Wang, SH Zhang, and XL He. Diffusion of boron in alloys. *Acta Metallurgica et Materialia*, 43(4):1693, 1995.
- [364] CQ Guo and PM Kelly. Boron solubility in Fe-Cr-B cast irons. *Materials Science and Engineering A-Structural Materials Properties Microstructure and Processing*, 352(1-2):40, 2003.
- [365] NJ Calos, E Graham, DR Cousens, P Christodoulou, CHL Kennard, LK Bekessy, and SF Parker. Mode of boron solubility in ferrous alloys. *Materials Transactions*, 42(3):496, 2001.
- [366] YN Malinochka, GZ Kovalchuk, and VN Yarmosh. Structure and properties of low-carbon steel alloyed with boron and copper. *Metal Science and Heat Treatment*, 24(11):760, 1982.
- [367] Y Hayashi and T Sugeno. Nature of boron in  $\alpha$ -iron. *Acta Metallurgica*, 18(6):693, 1970.
- [368] FC Frank and D Turnbull. Mechanism of diffusion of copper in germanium. *Physical Review*, 104(3):617, 1956.
- [369] Z Adolf, J Bazan, and L Socha. Thermodynamic conditions for the nucleation of boron compounds during the cooling of steel. *Materiali in Tehnologije*, 45(2):111, 2011.
- [370] G Dubben, MN Chandrasekharaiah, and BH Kolster. Microanalysis of welds using the field-ion microscope atom probe. *Journal of Materials Science*, 27(12):3192, 1992.
- [371] DE Jiang and EA Carter. Diffusion of interstitial hydrogen into and through bcc Fe from first principles. *Physical Review B*, 70(6):064102, 2004.
- [372] DE Jiang and EA Carter. Carbon dissolution and diffusion in ferrite and austenite from first principles. *Physical Review B*, 67(21):214103, 2003.
- [373] CC Fu and F Willaime. Ab initio study of helium in  $\alpha$ -Fe: dissolution, migration, and clustering with vacancies. *Physical Review B*, 72(6):064117, 2005.
- [374] D Simonovic, CK Ande, AI Duff, F Syahputra, and MHF Sluiter. Diffusion of carbon in bcc Fe in the presence of Si. *Physical Review B*, 81(5):054116, 2010.
- [375] C Domain, CS Becquart, and J Foct. Ab initio study of foreign interstitial atom (C,N) interactions with intrinsic point defects in  $\alpha$ -Fe. *Physical Review B*, 69(14):144112, 2004.
- [376] C Domain and CS Becquart. Diffusion of phosphorus in  $\alpha$ -Fe: an ab initio study. *Physical Review B*, 71(21):214109, 2005.

- [377] CC Fu, E Meslin, A Barbu, F Willaime, and V Oison. Effect of C on vacancy migration in  $\alpha$ -iron. In Tikare, V and Murch, GE and Soisson, F and Kang, JK, editor, *Theory, Modeling and Numerical Simulation of multi-physics Materials Behavior*, volume 139 of *Solid State Phenomena*, pages 157–164. Mat Res Soc, 2008. Symposium on Theory, Modeling and Numerical Simulation of Multi-Physics Materials Behavior held at the 2007 MRS Fall Meeting, Boston, MA, Nov 26-30, 2007.
- [378] T Ohnuma, N Soneda, and M Iwasawa. First-principles calculations of vacancy-solute element interactions in body-centered cubic iron. *Acta Materialia*, 57(20):5947, 2009.
- [379] Y You, MF Yan, and HT Chen. Interactions of carbon-nitrogen and carbon-nitrogen-vacancy in  $\alpha$ -Fe from first-principles calculations. *Computational Materials Science*, 67:222, 2013.
- [380] D Psiachos, T Hammerschmidt, and R Drautz. Ab initio study of the modification of elastic properties of  $\alpha$ -iron by hydrostatic strain and by hydrogen interstitials. *Acta Materialia*, 59(11):4255, 2011.
- [381] I Seki and K Nagata. Lattice constant of iron and austenite including its supersaturation phase of carbon. *ISIJ International*, 45(12):1789, 2005.
- [382] H Jónsson, G Mills, and KW Jacobsen. *Classical and Quantum Dynamics in Condensed Phase Simulation*, chapter 16, page 385. World Scientific, Singapore, 1998.
- [383] D Sheppard, R Terrell, and G Henkelman. Optimization methods for finding minimum energy paths. *Journal of Chemical Physics*, 128(13):134106, 2008.
- [384] G Henkelman, BP Uberuaga, and H Jónsson. A climbing image nudged elastic band method for finding saddle points and minimum energy paths. *Journal of Chemical Physics*, 113(22):9901, 2000.
- [385] AF Bialon, T Hammerschmidt, and R Drautz. Ab initio study of boron in  $\alpha$ -iron: Migration barriers and interaction with point defects. *Physical Review B*, 87(10):104109, 2013.
- [386] A Janotti and CL Fu. Aps march meeting abstracts. S16.004, 2003.
- [387] VN Voyevodin, IM Neklyudov, VV Bryk, and OV Borodin. Microstructural evolution and radiation stability of steels and alloys. *Journal of Nuclear Materials*, 271:290, 1999.
- [388] B Cordero, V Gomez, AE Platero-Prats, M Reves, J Echeverria, E Cremades, F Barragan, and S Alvarez. Covalent radii revisited. *Dalton Transactions*, 21:2832, 2008.
- [389] M Kabir, TT Lau, X Lin, S Yip, and KJ Van Vliet. Effects of vacancy-solute clusters on diffusivity in metastable Fe-C alloys. *Physical Review B*, 82(13):134112, 2010.
- [390] T Hejnal. Determination of small concentrations of interstitial carbon and nitrogen in bcc iron. *Czechoslovak Journal of Physics*, 29(10):1149, 1979.
- [391] M Mondino and A Seeger. Interaction of foreign interstitial atoms with vacancies in  $\alpha$ -Fe and group-V transition-metals. *Scripta Metallurgica*, 11(9):817, 1977.

- [392] JRGD Silva and RB McLellan. Diffusion of carbon and nitrogen in bcc iron. *Materials Science and Engineering*, 26(1):83, 1976.
- [393] S Takaki, J Fuss, H Kugler, U Dedek, and H Schultz. The resistivity recovery of high-purity and carbon doped iron following low-temperature electron-irradiation. *Radiation Effects and Defects in Solids*, 79(1-4):87, 1983.
- [394] J Takada and M Adachi. Determination of diffusion-coefficient of oxygen in  $\alpha$ -iron from internal oxidation measurements in Fe-Si alloys. *Journal of Materials Science*, 21(6):2133, 1986.
- [395] C Domain and CS Becquart. Ab initio calculations of defects in Fe and dilute Fe-Cu alloys. *Physical Review B*, 65(2):024103, 2002.
- [396] A Taylor and RM Jones. Constitution and magnetic properties of iron-rich iron-aluminum alloys. *Journal of Physics and Chemistry of Solids*, 6(1):16, 1958.
- [397] A Taylor and RM Jones. Further magnetic and X-ray diffraction studies on iron-rich iron-aluminum alloys. *Journal of Applied Physics*, 29(3):522, 1958.
- [398] M Polcarova, K Godwod, J Bakmisiuk, S Kadeckova, and J Bradler. Lattice-parameters of Fe-Si alloy single-crystals. *Physica Status Solidi A-Applied Research*, 106(1):17, 1988.
- [399] H Zhang, MPJ Punkkinen, B Johansson, S Hertzman, and L Vitos. Single-crystal elastic constants of ferromagnetic bcc Fe-based random alloys from first-principles theory. *Physical Review B*, 81(18):184105, 2010.
- [400] MA Hopcroft, WD Nix, and TW Kenny. What is the Young's modulus of silicon? *Journal of Microelectromechanical Systems*, 19(2):229, 2010.
- [401] J Prohaszka and J Dobranszky. The role of an anisotropy of the elastic moduli in the determination of the elastic limit value. In Gyulai, J, editor, *Materials Science, Testing and Informatics*, volume 414 of *Materials Science Forum*, page 311, 2003. 3rd Hungarian Conference and Exhibition on Materials Science, Testing and Informatics, Balatonfured, Hungary, Oct 14-17, 2001.
- [402] JJ Adams, DS Agosta, RG Leisure, and H Ledbetter. Elastic constants of monocrystal iron from 3 to 500 K. *Journal of Applied Physics*, 100(11):113530, 2006.
- [403] A Machova and S Kadeckova. Elastic-constants of iron-silicon alloy single-crystals. *Czechoslovak Journal of Physics*, 27(5):555, 1977.
- [404] CC Fu, F Willaime, and P Ordejon. Stability and mobility of mono- and di-interstitials in  $\alpha$ -Fe. *Physical Review Letters*, 92(17):175503, 2004.
- [405] A Udyansky, J von Pezold, A Dick, and J Neugebauer. Orientational ordering of interstitial atoms and martensite formation in dilute Fe-based solid solutions. *Physical Review B*, 83(18):184112, 2011.
- [406] Y Tateyama and T Ohno. Stability and clusterization of hydrogen-vacancy complexes in  $\alpha$ -Fe: An ab initio study. *Physical Review B*, 67(17):174105, 2003.

- [407] R Nazarov, T Hickel, and J Neugebauer. First-principles study of the thermodynamics of hydrogen-vacancy interaction in fcc iron. *Physical Review B*, 82(22):224104, 2010.
- [408] SH Zhang, XL He, and T Ko. Nonequilibrium segregation of solutes to grain-boundary .3. Mechanism of nonequilibrium segregation. *Journal of Materials Science*, 29(10):2663, 1994.
- [409] SH Song, RG Faulkner, and PEJ Flewitt. Effect of boron on phosphorus-induced temper embrittlement. *Journal of Materials Science*, 34(22):5549, 1999.
- [410] RG Faulkner. Nonequilibrium grain-boundary segregation in austenitic alloys. *Journal of Materials Science*, 16(2):373, 1981.
- [411] L Kaufman, B Uhrenius, D Birnie, and K Taylor. Coupled pair potential, thermochemical and phase-diagram data for transition-metal binary-systems. *CALPHAD-Computer Coupling of Phase Diagrams and Thermochemistry*, 8(1):25, 1984.
- [412] A Kirfel, A Gupta, and G Will. Nature of the chemical bonding in boron-carbide,  $B_{13}C_2$  .1. Structure refinement. *Acta Crystallographica Section B-Structural Science*, 35:1052, 1979.
- [413] A Gupta, A Kirfel, G Will, and G Wulff. Crystal-structure of D-Mannitol Tris(Benzeneboronic) Ester,  $C_{24}H_{23}B_3O_6$ . *Acta Crystallographica Section B-Structural Science*, 33:637, 1977.
- [414] FH Allen, O Kennard, DG Watson, L Brammer, AG Orpen, and R Taylor. Tables of bond lengths determined by X-Ray and neutron-diffraction .1. Bond lengths in organic-compounds. *Journal of the Chemical Society-Perkin Transactions 2*, 12:1, 1987.
- [415] H Okamoto. B-N (Boron-Nitrogen). *Journal of Phase Equilibria*, 21(2):208, 2000.
- [416] VL Solozhenko, G Will, H Hupen, and F Elf. Isothermal compression of rhombohedral boron-nitride up to 14 GPa. *Solid State Communications*, 90(1):65, 1994.
- [417] OI Gorbatov, PA Korzhavyi, AV Ruban, B Johansson, and YN Gornostyrev. Vacancy-solute interactions in ferromagnetic and paramagnetic bcc iron: Ab initio calculations. *Journal of Nuclear Materials*, 419(1-3):248, 2011.
- [418] L Pauling. The nature of the chemical bond. IV. The energy of single bonds and the relative electronegativity of atoms. *Journal of the American Chemical Society*, 54(9):3570, 1932.
- [419] AL Allred. Electronegativity values from thermochemical data. *Journal of Inorganic and Nuclear Chemistry*, 17(3):215, 1961.
- [420] RS Mulliken. A new electroaffinity scale; Together with data on valence states and on valence ionization potentials and electron affinities. *Journal of Chemical Physics*, 2:782, 1934.
- [421] RS Mulliken. Electronic structures of molecules XI. Electroaffinity, molecular orbitals and dipole moments. *Journal of Chemical Physics*, 3:573, 1935.

- [422] AL Allred and EG Rochow. A scale of electronegativity based on electrostatic force. *Journal of Inorganic and Nuclear Chemistry*, 5(4):264, 1958.
- [423] DN Reshef, YA Reshef, HK Finucane, SR Grossman, G McVean, PJ Turnbaugh, ES Lander, M Mitzenmacher, and PC Sabeti. Detecting novel associations in large data sets. *Science*, 334(6062):1518, 2011.
- [424] <http://www.exploredata.net/Downloads/MINE-Application>, accessed October 12th, 2012.
- [425] SH Vosko, L Wilk, and M Nusair. Accurate spin-dependent electron liquid correlation energies for local spin-density calculations - a critical analysis. *Canadian Journal of Physics*, 58(8):1200, 1980.
- [426] MJ Mehl, BM Klein, and DA Papaconstantopoulos. First principles calculations of elastic properties of metals. In JH Westbrook and RL Fleischer, editors, *Intermetallic Compounds: Principles and Practice, Volume I: Principles*, pages 195–210, London, 1995. John Wiley and Sons.
- [427] O Beckstein, JE Klepeis, GLW Hart, and O Pankratov. First-principles elastic constants and electronic structure of  $\alpha$ -Pt<sub>2</sub>Si and PtSi. *Physical Review B*, 63(13):134112, 2001.

## Curriculum Vitae

05.08.82	born in Tichau, Poland
08/89-06/93	Elementary school Meinolf Grundschule, Hagen
08/93-06/02	Grammar school Hildegardis-Gymnasium, Hagen; General qualification for university entrance
07/02-03/03	Military service
10/03-09/08	Undergraduate studies in physics at the Ruhr-Universität Bochum (RUB), Germany; Diploma thesis with Prof. H. Ruhl: Anharmonic resonance in the interaction of ultra-short intense laser pulses with matter
04/07-07/07	Teaching assistant in problem classes for lecture <i>Fundamentals of Mechanics and Electrodynamics</i> at Department of Physics, RUB
10/07-02/08	Teaching assistant at problem classes for lectures <i>Theoretical Physics 3: Quantum Mechanics</i> and <i>Mathematical Methods in Physics</i> at Department of Physics, RUB
04/08-07/08	Teaching assistant at problem classes for lecture <i>Fundamentals of Quantum Mechanics and Thermodynamics</i> at Department of Physics, RUB
since 11/08	Doctoral candidate at Department of Atomistic Modelling and Simulation, Interdisciplinary Centre for Advanced Material Simulations (ICAMS), RUB
02/09	Tutor at Block lecture <i>Multiscale Modelling of Materials</i> at ICAMS, RUB
02/10	Tutor at module T3 <i>Multiscale Modelling</i> of Max-Planck graduate school SurMat at ICAMS, RUB
03/11-06/11	Participant in the IPAM Long Program: Navigating Chemical Compound Space for Materials and Bio Design, Institute for Pure and Applied Mathematics, UCLA, Los Angeles, CA, USA

## Publications

2010	AN Kolmogorov, S Shah, ER Margine, AF Bialon, T Hammerschmidt, and R Drautz, New superconducting and semiconducting Fe-B groundstates predicted with an ab-initio evolutionary search. <i>Phys. Rev. Lett.</i> , 105:217003, 2010.
2011	AF Bialon, T Hammerschmidt, R Drautz, S Shah, ER Margine, and AN Kolmogorov, Possible routes for synthesis of new boron-rich Fe-B and $\text{Fe}_{1-x}\text{Cr}_x\text{B}_4$ compounds. <i>Appl. Phys. Lett.</i> 98:081901, 2011.

- 2013 AF Bialon, T Hammerschmidt, and R Drautz, Ab initio study of boron in  $\alpha$ -iron: Migration barriers and interaction with point defects. *Phys. Rev. B* 87:104109, 2013.

#### Presentations (selected)

- 06/2009 Hands-on Tutorial on Ab Initio Molecular Simulations, Fritz Haber Institute, Berlin, Germany. Poster: Ab-initio study of boron in iron and steel.
- 01/2010 Workshop on Computational Materials Science on Complex Energy Landscapes, Imst, Austria. Talk: Ab-initio study of structural stability of Fe-B phases.
- 03/2010 German Physical Society Spring Meeting, Regensburg, Germany. Talk: Ab-initio study of structural stability of Fe-B phases.
- 09/2010 Psi-K Conference 2010, Berlin, Germany. Talk: CALPHAD Phase Diagrams from DFT Calculations.
- 04/2011 IPAM CCS2011 Seminar Series Talk, IPAM Long Program: Navigating Chemical Compound Space for Materials and Bio Design, Institute for Pure and Applied Mathematics, UCLA, Los Angeles, California, USA. Talk: DFT study of the iron-boron system: Phase stability of binaries and boron-defect interaction in ferrite.
- 05/2011 Navigating Chemical Compound Space for Materials and Bio Design - Workshop III: Materials Design in Chemical Compound Space, Institute for Pure and Applied Mathematics, UCLA, Los Angeles, California, USA. Poster: Alloying with light elements.
- 07/2011 Mechanics Colloquium, Chair of Technical Mechanics, University of Wuppertal, Wuppertal, Germany. Invited talk: Boron in ferrite: A DFT study of phase stability of binaries and boron-defect interaction.
- 01/2012 1st Austrian-German workshop on Materials Design, Austria. Talk: Ab-initio study of boron in  $\alpha$ -Fe: diffusion barriers and interaction with point defects.
- 03/2012 German Physical Society Spring Meeting, Berlin, Germany. Talk: Point defect interactions of boron in  $\alpha$ -Fe.
- 10/2012 MMM 2012 - 6th International Conference on Multiscale Materials Modeling, Singapore. Talk: Ab-initio study of point defect interactions of boron in  $\alpha$ -Fe: Trends with band-filling and atomic size.
- 03/2013 German Physical Society Spring Meeting, Regensburg, Germany. Talk: Polyhedron-based structure maps for pd-bonded systems.